Fundamental Study of Engineered Cathode and Li-ion Conducting Electrolyte Architectures for High Energy Density Lithium Sulfur Batteries

by

Pavithra Murugavel Shanthi

Bachelor of Technology in Chemical & Electrochemical Engineering, Central Electrochemical Research institute, Karaikudi, India, 2013

Submitted to the Graduate Faculty of the

Swanson School of Engineering in partial fulfillment

of the requirements for the degree of

Doctor of Philosophy

University of Pittsburgh

2020

UNIVERSITY OF PITTSBURGH

SWANSON SCHOOL OF ENGINEERING

This dissertation was presented

by

Pavithra Murugavel Shanthi

It was defended on

December 19, 2019

and approved by

Dr. Robert M. Enick, Ph.D, Professor, Department of Chemical and Petroleum Engineering

Dr. James McKone, Ph.D., Assistant Professor, Department of Chemical and Petroleum Engineering

Dr. Brandon Grainger, Ph.D., Assistant Professor, Department of Electrical and Computer Engineering

Dissertation Director: Dr. Prashant N. Kumta, Ph.D., Professor, Department of Chemical and Petroleum Engineering

Fundamental Study of Engineered Cathode and Li-ion Conducting Electrolyte Architectures for High Energy Density Lithium Sulfur Batteries

Pavithra Murugavel Shanthi, PhD

University of Pittsburgh, 2020

Rapid development in electric vehicle and portable electronic device technologies has made it imperative to identify new higher energy density (~500 Wh/kg) battery systems than currently available Li-ion batteries (~250 Wh/kg). Lithium-sulfur with a theoretical capacity of ~1675 mAh/g has emerged as the leading next generation Li-ion battery system. However, sulfur cathodes are hamstrung by inherent poor electronic conductivity (~1×10^{-15} S/m), volumetric expansion (~80%) and more importantly, soluble polysulfide formation causing inferior cyclability, areal capacities and rate capabilities. This PhD dissertation overcomes these limitations by engineering electron conducting novel cathode architectures using metal organic frameworks (MOFs) and complex framework materials (CFMs) as primary sulfur hosts confining the volume expansion along with composite polymer electrolytes (CPEs) and directly deposited sulfur architectures (DDSA) combining polysulfide trapping agents (PTAs). The sulfur infiltrated MOF (S-MOF) and CFM hosts (S-CFMs) exhibit stable capacities of ~1000-1050 mAh/g with minimal fade rate (~0.12-0.19% loss/cycle) due to Lewis acid-base interactions of the MOF with polysulfides and concomitant sulfur bonding with the CFM carbon architecture yielding complete lithiated polysulfide species retention within the MOF and CFM structures. The CPEs and DDSA-PTA composite systems also exhibit excellent stability (~0.14% loss/cycle) upon extended cycling to (~200 cycles), highlighting the potential of these systems in preventing polysulfide dissolution in Li-S batteries. Fundamental aspects of the different strategies employed to resolve the core sulfur cathode problems of polysulfide dissolution and inferior electronic conductivity of sulfur are outlined. Results from the extensive materials, chemical and electrochemical characterization of these individual systems are also discussed.

Table of Contents

List of Tables

List of Figures

Preface

I would like to thank my parents and husband without their encouragement, I could never have completed my graduate education. I would like to convey my heartfelt gratitude to my committee members Dr. James McKone, Dr. Robert Enick, and Dr. Brandon Grainger for their valuable suggestions and guidance at different stages of my thesis work.

I would like to thank my advisor Dr. Prashant Kumta for his immense guidance and support for my research and innovation. I would also like to gratefully thank the Research Faculty and postdoctoral fellows who have mentored me over the years especially Dr. Moni Datta, Dr. Oleg Velikokhatnyi and Dr. Ramalinga Kuruba.

1.0 Introduction

Lithium battery technology has witnessed revolutionary research developments in the past two decades. Numerous technologies have emerged, and immense progress has been made with various techniques in this field. An ever-increasing demand for portable electronic devices (PEDs), hybrid and electric vehicles (HEVs and EVs) has led to intense research activity in this field. Rechargeable lithium-ion batteries (LIBs) are a key component of portable electronic devices and personal digital assistants (PDA) [1, 2], but LIBs are still not cost-effective for large scale plug-in hybrid and electric vehicle applications. Furthermore, the safety of LIBs is an increasing concern. This has motivated researchers to develop leak-free, high energy density and flexible lithium-ion batteries with enhanced safety [3, 4].

Despite the incredible progress in LIB technology, conventional cathode material-transition metal oxide and phosphate-based systems still show a maximum theoretical capacity of ~200-300 mAh/g. [5, 6]. Fabrication of large-scale devices with high energy densities (≥500 Wh/kg) using materials is hindered by their low specific capacity, high cost, and environmental issues.

In recent years, Lithium-sulfur (Li-S) battery technology has been studied extensively by researchers and is promising to be the appropriate solution to the problems associated with LIBs. Li-S battery is a cost-effective and favorable alternative to current LIBs.[7, 8]. A high theoretical capacity of 1674 mAh/g and a specific energy density of 2600 Wh/kg is observed for inexpensive elemental sulfur. Li-S battery (Lithium metal, sulfur cathode) is approximately 4 times cheaper than the LIB (conventional graphite, lithium nickel magnesium cobalt oxide cathode) ($100/kWh for Li-S battery; $432/kWh for LIB)[9, 10].

The abundance (0.07% of the Earth's crust) and eco-friendliness, in addition to the cost-effective characteristics of sulfur[11] make it a promising cathode material for large scale or grid scale energy storage applications. Nevertheless, the insulating behavior of sulfur leads to the lack of complete utilization of active material in Li-S batteries[12, 13]. During electrochemical cycling of sulfur, lithium polysulfide intermediates are formed that are highly soluble in organic electrolytes. This leads to active material loss and hence poor cyclability[14, 15]. This problem could be rectified by incorporating conducting carbonaceous or polymer matrix-forming composites into electrochemically active sulfur[16-19 20-23]. A conducting sulfur network established from the aforesaid method, enhances the conductivity of the active material composite. Several approaches including the use of transition metal oxides and porous structures have been implemented to prevent the polysulfide's dissolution in Li-S battery. Transition metal oxides chemical interacts with polysulfides, and the porous structures trap the sulfur to restrict its dissolution[24, 25 26-29]. Though these approaches have led to increased active material utilization in sulfur cathodes, they lack entire prevention of the dissolution of polysulfide species in the electrolyte. [30].

This study envisaged the development of various techniques to overcome the above-mentioned problems. It also provided a fundamental understanding of various phenomena. The following strategies are mentioned in this thesis.

In the first strategy, metal organic framework (MOF) was employed as a host for sulfur cathode because of its relatively better chemical properties and more tunable porous structure compared to traditional porous material. The purpose of this research was to explore the reason for irreversible capacity loss as well as to investigate the polysulfide dissolution mechanism through MOF-based sulfur cathodes. Our preliminary results showed that MOF served as a host

for sulfur cathodes which fasten and trap the polysulfides. The second approach mainly focused on preventing polysulfide dissolution by replacing liquid electrolyte with composite polymer electrolyte (CPE), which mitigates the poor cyclability and increases the chemical stability of Li-S batteries. The mechanism by which the MOFs and CFMs prevents polysulfide dissolution was investigated. In the third approach, oxide based solid-state lithium ion conductors were developed and their Li-ion conductivity and electrochemical stability were investigated at room temperature. Also, the usage of substituents was investigated for enhancing their stability and Li-ion conductivity. Finally, high loading sulfur cathodes with novel polysulfide trapping agent (PTA) were employed to improve the stability of high-energy density Li-S batteries.

The thesis is structured into the following sections. Background and significance include a general overview of the state-of-the-art cathodes and polymer electrolytes used in Li-S batteries, followed by the research objectives and specific aims for this proposed research. Specific aim 1 is devoted to our work on carbonate-based metal organic framework (MOF), sulfate-based S-Cu-bpy-CFM, S-Cu-pyz-CFM and sulfonic acid-based SCFM cathodes. Polysulfide trapping properties of the MOF, CFM and SCFM were investigated using several characterizations such as scanning electron microscopy (SEM), transmission electron microscopy (TEM), X-ray diffraction (XRD), X-ray photoelectron spectroscopy (XPS) and other electrochemical characterization methods. Specific aim 2 focuses on high electrochemical conductivity, flame resistance and polysulfide suppressing properties of the composite polymer electrolytes (CPEs). Specific aim 3 discusses in detail about enhancing the lithium ion conductivity of oxide-based solid electrolytes and specific aim 4 focuses on new polysulfide trapping agents (PTAs) for sulfur electrode architectures.

1.1 Background and Significance

1.1.1 Principles of Li-S Battery

A Li–S battery is an electrochemical energy conversion and storage device in which sulfur electrodes store the electrical energy. The components of a single Li-S cell and its working principle (charge/discharge) are schematically depicted in Figure 1-1. [31]

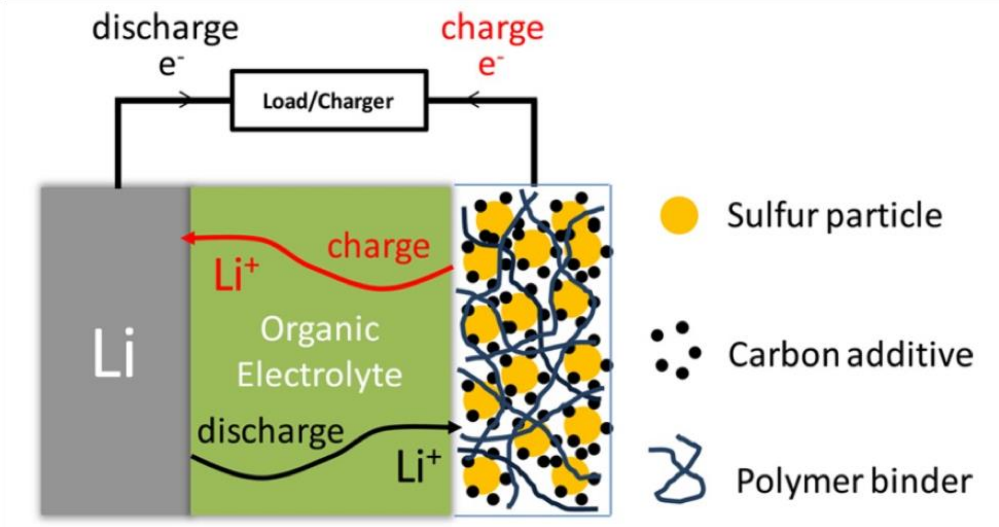

Figure 1-1 Schematic representation of charge/discharge operations in a single Li-S cell (Reprinted with permission from Manthiram et al. [31] . Copyright 2014 by American Chemical Society)

A lithium metal anode, a sulfur composite cathode and an organic electrolyte are the basic components of traditional Li-S cell. The cell function begins with discharge due to sulfur being in charged state. Lithium ions and electrons are formed by the oxidation of lithium metal at the negative electrode during the discharge reaction. The formed lithium ions during the discharge reaction move within the electrolyte to reach the positive electrode. Conversely, the

electrons migrate through the external circuit to reach the positive electrode, thus generating an electrical current. At the positive electrode, the lithium ions and electrons reduce the sulfur into lithium sulfide. The following reactions take place during discharge, and the backward reactions take place during charge.

Lithium metal is oxidized into lithium ions by eliminating electrons at the negative (anode) electrode (equation 1-1).

$$2Li \rightarrow 2Li^{+} + 2e^{-} \quad (1\text{-}1)$$

Sulfur is reduced to Li_2S by accepting lithium ions and electrons at the positive (cathode) electrode (equation 1-2).

$$S + 2Li^{+} + 2e^{-} \rightarrow Li_2S \quad (1\text{-}2)$$

Overall cell reaction of Li-S cell during the discharge process at 2.15 V is mentioned below (equation 1-3)

$$2Li + S \rightarrow Li_2S + 2e^{-} \quad (1\text{-}3)$$

The theoretical cell capacity of 1167 mAh/g is achieved for the Li-S cell because of the theoretically predicted capacities of lithium (3861 mAh/g) and sulfur (1672 mAh/g). An average cell voltage of 2.15 V is obtained from the discharge reaction. Therefore, a gravimetric energy density of 2510 Wh/kg is observed for the Li–S cell. [32].

Sulfur atoms exhibit a pronounced tendency to form long, homoatomic chains or homocyclic rings (catenation) of various sizes. The room temperature (25 ˚C) crystallization of octasulfur (cyclo-S_8) leads to the formation of orthorhombic sulfur (α- S_8)-the most stable allotrope of sulfur, at room temperature. [33] The reduction of octasulfur (cyclo-S_8) causes it to open its rings, which then reacts with lithium to form higher-order lithium polysulfides Li_2S_x (6

< x ≤ 8) during the initial stages of the ideal discharge process. The formation of lower order lithium polysulfides Li_2Sx (2 < x ≤ 6) happens through lithium receival when the discharge continues on longer. The transformation of S_8 to Li_2S_4 and Li_2S_4 to Li_2S occurs at discharge plateaus of 2.3 and 2.1 V in ether-based liquid electrolytes. Li_2S formation takes place during the final stage of discharge process (Figure 1-2). [7].

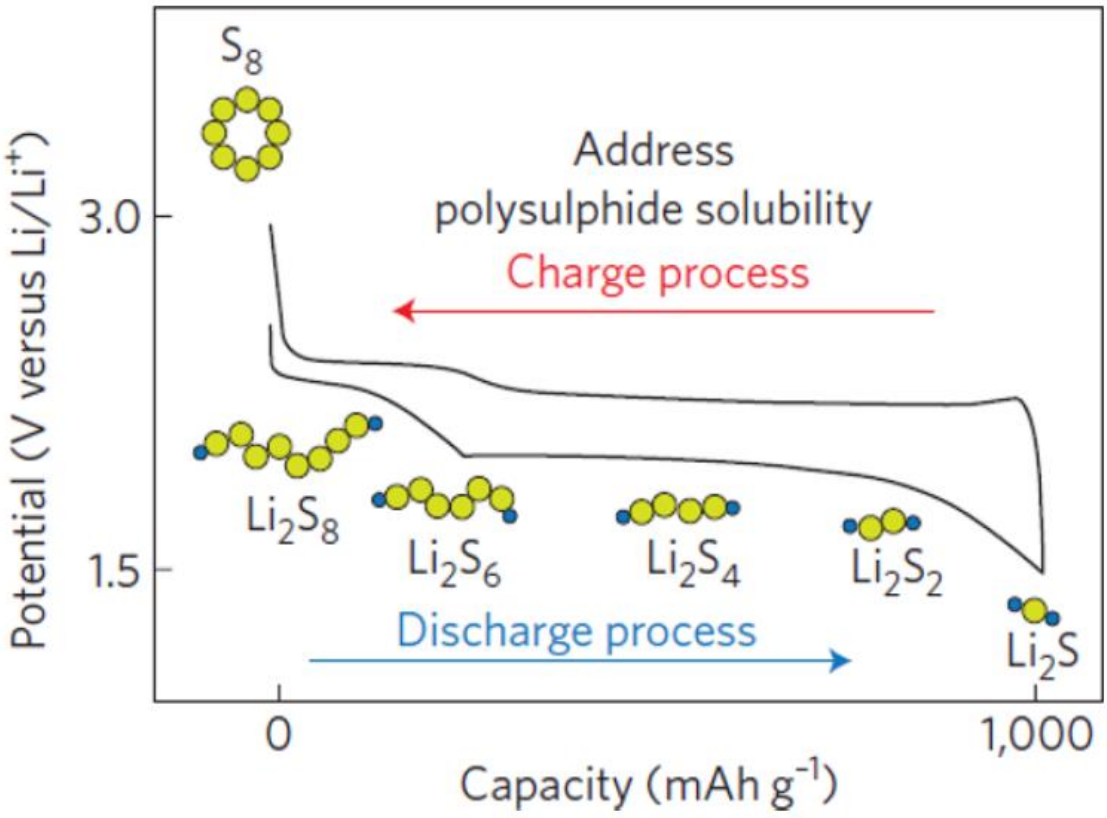

Figure 1-2 Voltage profiles of discharge and charge process in a Li–S cell (Reprinted with permission from Bruce et al. [7]. Copyright 2012 Macmillan Publishers Ltd.)

Li_2S is transformed into S_8 through the formation of lithium polysulfides intermediates during the charging process which thus results in a reversible cycle (Figure 1-2). [34]. Furthermore, the voltage plateaus of the charge/discharge process usually overlay with each other.

1.1.2 Technical Challenges

Several scientific challenges have been encountered for the technological development of Li−S batteries, caused by the materials and/or the system itself. The challenges described below are taken into account.

1. Initially, the low conductivity (~ 10^{-30} S/cm) of sulfur and its formation into intermediates such as lithium polysulfides (Li_2S_x, $3 \leq x \leq 8$) during electrochemical cycling with their morphological and structural changes are challenging issues. This causes an unstable electrochemical contact within the sulfur cathode.
2. Furthermore, the formed polysulfides, dissolve in the electrolyte and migrate within the anode and cathode during cycling as well as react with the anode (Lithium metal) and cathode (Sulfur) (i.e. polysulfide shuttle effect). This effect hinders the practical applications of Li-S system due to the extreme deterioration of cycling performance and fast capacity fading. [35].
3. In addition to this, the formation of lithium sulfide from sulfur through electrochemical cycling leads to morphological and structural changes in the electrode, as well as dissolution and deposition of lithium sulfate, which forms a passivation layer on both electrodes. A substantial increase in impedance is observed for passivated electrodes. These problems reflect ineffective exploitation of the active material, low system efficiency and poor electrochemical cycle life. The traditional Li-S cell depicted in Figure 1-1 is therefore unable to fulfil the requirements for use in commercial applications.

Developing technically and commercially feasible Li-S batteries requires the following problems to be solved. The shuttling effect raised from active cathode material dissolution needs to be

terminated in order to avoid the lower coulombic efficiency and self-discharge behavior. The mitigation of carbon additives in the electrodes is necessary, because the large amount of carbon leads to a decrease in the energy density of Li−S cells. Another major challenge is to achieve a high theoretical capacity of sulfur (1672 mAh/g) through full sulfur exploitation for practical applications. The slow solid-state diffusion reaction occurs during the reduction of low order polysulfide to Li_2S. This leads to a more sluggish lower plateau redox reaction in comparison to the upper plateau redox reaction. [36] Furthermore, surface passivation and dendrite formation on the Li-metal anode needs to be solved. Replacing Li metal anode with another material could be an option to eliminate the disadvantages of lithium metal such as shorting of the cells which leads to fire and explosion and thermal runaway which also causes fire when organic electrolytes are employed in the system.

1.1.3 Sulfur Cathodes

1.1.3.1 Sulfur Composite Electrodes

The Li-S cell model was proposed about 30 years before[37]. Nevertheless, Li−S cell technology was hindered by two major technical problems such as low conductivity of active material and the polysulfide shuttle effect. [12, 38] There is a necessity to solve the problem of high resistance of active material. Choosing a proper electrical conductor (conductive carbon/polymer additives) and embedding it with the active material leads to an increase in conductivity. Also, the electrical conductor should be well dispersed in the active material. This provides charge carrier (electron) transfer within the active material and electrical conductor. Conductive carbons and conductive polymers were introduced into sulfur cathodes to achieve (i) sulfur-carbon composites and (ii) sulfur- conductive polymer composites for nearly a decade. To increase the

conductivity and active material exploitation of electrodes, the conductive carbon was introduced into the sulfur cathodes. Usually in sulfur cathodes, depending on the electronic conductivity of the active material, conductive carbon additives such as Super P is added in varying amounts (~10wt%-30wt%). This carbon additive helps to improve the capacity of the battery by improving the active material utilization. For instance, the cathode resistance was decreased by introducing high conductivity carbon black in the active material mixture. [39] The active carbon possesses micropores with a high surface area for absorbing the polysulfide and which hinders the dissolution in the electrolyte. [40] However, polyacrylonitrile (PAN) conductive polymer was introduced into the sulfur for the formation of sulfur-polymer composite. The system exhibited a high initial discharge capacity of 850 mAh/g.[41] There are several types of conductive polymers and conductive/high surface area porous carbons embedded in the sulfur since the past decade. [39-41]

1.1.3.2 Porous Framework Electrodes

Porous/conductive carbon has attracted great attention among the conductive additives because of its higher electrical conductivity and more porous structure than polymers. It can easily accommodate the active material and it tends to increase the electrical conductivity of cathodes. [26, 42, 43] The change in active material morphology leads to an increase in conductivity of cathodes by two approaches (i) development of conductive carbon network, for instance through carbon nanoparticle clusters and (ii) creation of an internal connection that links conductive framework with the insulating sulfur. Furthermore, the engineered porous carbons such as microporous, mesoporous and macroporous carbon networks enhance the retention of sulfur as well as the migration of charge and electrolyte in the composites. Up till now, several carbon materials and their preparation methods have been devoted to optimizing the composite

configuration to enhance the electrochemical cycling performance of Li-S cells. The mesoporous carbon acts as an ordered encapsulation substrate for sulfur. [26, 44] Li et al. [26] systematically tuned and investigated the pore sizes and pore volumes of several mesoporous carbon materials. They showed that the large pore size of mesoporous carbon can accommodate higher sulfur loading and can exhibit enhanced cell performance under higher sulfur loading situations. This provokes the existing limitation of sulfur content/loading in sulfur-porous carbon (S−PC) composite electrodes. Conversely, the embedded sulfur with mesoporous substrate showed better electrical contact between them through the partial sulfur-filling and surface modification conditions. This can lead to a stable supply of lithium ions and limits dissolution/diffusion of polysulfides.[26] For instance, mesoporous carbon with a pore size of 22 nm and 50 % sulfur loading in the space of mesoporous structure enables S− mesoporous carbon composites. This system shows an initial capacity of 1390 mAh/g and capacity of 840 mAh/g after 100 cycles. The micro/mesopore-decorated porous carbon framework[43, 45, 46] or bimodal micro/mesoporous carbon[42, 47] are a category of engineered hierarchical porous carbon. Initially, Ji et al[48] achieved the ordered nanostructured mesoporous carbon (CMK-3). The carbon network allows controlled sulfur growth on its structure which provides electrical contacts between sulfur and carbon. The exploitation of high sulfur in the system is achieved from complete redox reaction and the electrochemical reaction is stabilized in the nanosized chamber of MPCs. Moreover, MPC acts as an electronic conduit as well as the stockroom for the active material. The above finding motivates the researchers to develop the numerous hierarchical micro/meso/macroporous carbon material with different physical/ chemical properties to enhance the cycling performance of Li-S cell.[48, 49]. In the hierarchically ordered porous carbon material, the active materials could be encapsulated/immobilized in the well-designed pores, so it leads to an improvement in the

electrochemical performance and mitigates the active material loss. The microporous structure acts as the pathway for electrolyte movement and leads to immersion of the electrode. The presence of mesopore helps to enhance the physical properties of the microporous or mesoporous network. Generally speaking, the combined structure of small pore size-based mesoporous with micropore structure, well accommodates the active material. It also acts as a trap for the dissolved polysulfides in the electrolyte, so it tends to decrease the capacity fading. [28, 50]. The presence of large pores in the mesoporous structure leads to an increase in charge transport and allows penetration of electrolyte when it is coupled with microporous structure, so high exploitation of sulfur is achieved.[28, 42, 45]. Therefore, tailored hierarchical porous carbon is a good candidate to trap polysulfides and prevent polysulfide dissolution efficiently among functional micro/meso/macroporous carbons.

1.1.4 Electrolytes and Separators

Ion transport route between positive and negative electrodes happens through the electrolyte. Liquid based electrolytes are the most commonly used in batteries due to their better ionic conductivity. The battery performance was affected by the solubility of polysulfides in the liquid-based electrolyte. Additionally, the composition of liquid electrolytes and the presence of additives led to the formation of passivation at the electrodes by the reduction or oxidation of electrolytes. To overcome this, solid electrolytes are used in the Li-S system. Solid electrolyte reduces the dissolution and polysulfide shuttle effect. Moreover, additional problems occurred when solid based electrolytes were used in Li-S batteries such as lower ionic conductivity, and interfacial stability. The separators physically separate the positive and negative plate at the same time the absorbed ions on the separators move in the liquid electrolyte. Porous polymer

films are mostly used in Li-ion batteries e.g., expanded polypropylene. Ion selective functional separators are promising for Li-S batteries because it reduces the shuttle effect of polysulfides. The following section will discuss the different electrolytes and functional separators used in Li-S batteries.

1.1.4.1 Polymer Electrolytes

In order to reduce polysulfide dissolution and the shuttle effect of polysulfides, polymer and solid-state electrolytes are employed in Li-S batteries instead of liquid-based electrolytes. Furthermore, the safety and cyclic life of the anode was improved using polymer and solid based electrolytes that protect lithium metal and minimize dendrite formation on the anode. This leads to enhanced performance of Li-S batteries. Nevertheless, polymer and solid-state electrolytes are generally suffering from low ionic conductivity due to the high viscous nature of polymers and this hinders the lithium ion transport due to high energy barrier in solid state electrolytes. Due to liquid like properties with better lithium ion transport, the short chain polymers namely polyethylene glycol dimethyl ether (PEGDME) and triethylene glycol dimethyl ether (TEGDME), have been extensively used as an electrolyte for Li-S batteries. For instance, Marmorstein et al.[13] investigated the electrochemical performance of Li-S cells using three polymer electrolytes such as polyethylene oxide (PEO), poly(ethylene−methylene oxide) (PEMO), and TEGDME and identified that TEGDME based Li-S cell exhibited a lower capacity fade rate as compared to the remaining electrolytes. Kim et al.[51] reported the electrochemical performance of Li-S cell with $LiCF_3SO_3$-TEGDME electrolyte and sulfur−mesoporous hard carbon spherule composite cathode. The cell showed a capacity of 750 mAh/g along with better retention during electrochemical cycling. Furthermore, they demonstrated that the cell at lower temperatures (0˚C), exhibits a capacity of 500 mAh/g over 170 cycles. Shim et al.[39] studied the

electrochemical performance of the cell using different electrolytes with lithium (bis)trifluoromethanesulfonate imide salt. They used three different solvents with different molecular weights namely triethylene glycol dimethyl ether (MW 178 g/mol), polyethylene glycol dimethyl ether (PEGDME, MW 250 g/mol) and PEGDME (MW 500 g/mol) for making the electrolyte solution. The Li-S cells with PEGDME 250 and 500 solvents exhibited high columbic efficiency with good reversible charge and discharge behaviors. Conversely, low columbic efficiency was observed for the triglyme solvent due to the shuttle effect of polysulfides. They observed that polymers with higher molecular weights tend to reduce the shuttle effect of polysulfides. Long chain PEO-based polymer electrolytes have been extensively employed as a crucial component in the Li-S batteries. For instance, Shin et al.[52] investigated the ionic conductivity, interfacial stability and electrochemical properties of Li-S cell using $(PEO)_{10}LiCF_3SO_3$ with titanium dioxide additive as a electrolyte. By adding titanium oxide on the composite polymer, ionic conductivity of the electrolyte is enhanced. Also, the interfacial stability and electrochemical performance was significantly improved upon the addition of titanium oxide. Hassoun et al.[53] fabricated a solid-state Li−S battery using a nano composite polymer electrolyte. A PEO/ $LiCF_3SO_3$ complex with nano sized ZrO_2 and Li_2S were used as an electrolyte for the Li-S cell. The presence of ZrO_2 provides an increase in ionic conductivity and lithium transport number. The prevention of polysulfide dissolution and the increase in ionic conductivity of cathode is observed in the presence of Li_2S. The prepared cell exhibited a columbic efficiency of 99 % with a better reversible cycle over 50 cycles at elevated temperatures. Liang et al.[54] showed a Li-S cell containing $PEO_{18}/Li(CF_3SO_2)_2N$ polymer electrolyte with 10 wt % SiO_2 and sulfur−mesoporous carbon sphere composite cathodes. A discharge capacity of 800 mAh/g was observed over 25 cycles at 70 ˚C. The polymer-based electrolytes are good candidates to overcome the limitation of Li-S batteries.

1.1.4.2 Solid-state Electrolytes

Oxide and sulfide-based electrolytes are widely studied as a solid electrolyte for Li-S batteries. Lithium super ionic conductors (LISICON) have attracted attention because of their high ionic conductivity. [55, 56] Oxide based LISICON show ionic conductivity of 10^{-6} S/cm due to the Li^+ hops in the interstitial site of its crystal lattice. Sulfide-based (thio) LISICON exhibit two orders of magnitude higher conductivity than the oxide based LISICON.[55] Glass ceramic materials with thio-LISICON electrolytes were examined for the Li-S batteries that exhibited higher ionic conductivity in Li-S battery. For instance, Hayashi et al.[57] employed $Li_2S–P_2S_5$ electrolyte and fabricated an all solid state Li-S cell. It exhibited Li-ion conductivity of 3.2 mS/cm and maintained a capacity of 650 mAh/g over 20 cycles at room temperature. Hakari et al.[58] in the same research group examined $Li_2S–P_2S_5$ glass ceramic as solid electrolyte. $Li_2S–P_2S_5$ glass ceramic was mixed with acetylene black to form a composite electrode as a working electrode and indium foil was used as a counter electrode for the all-solid-state batteries. The prepared cell exhibited the highest capacity of 240 mAh/g (normalized by the weight of $Li_2S–P_2S_5$). Hayashi et al. [59] also investigated the electrochemical behavior of the cell with aforementioned $Li_2S–P_2S_5$ glass ceramic electrolyte, $Li_2S–Cu$ composite cathodes and Indium metal anode. Li_xC_uS compound formed during the cathode reaction causes a discharge capacity of 490 mAh/g in the first cycle. Nagao et al.[60] investigated sulfur composite cathodes and $Li_2S–P_2S_5$ electrolytes with Li_2S, that exhibited a charge capacity of 1000 mAh/g at 25 ˚C. Kobayashi et al.[61] examined sulfide based LISICON glass ceramic electrolyte ($Li_{3.25}Ge_{0.25}P_{0.75}S_4$), it showed the Li-ion conductivity of 2.2 mS/cm in the solid-state Li-S battery and exhibited some reversible cycles. Yersak et al[62]. fabricated the cells with FeS–S composite cathodes and several glass electrolyte compositions. They revealed that the presence

of Li_2S in the glass electrolyte contributes to the electrochemical process which leads to an increase in the capacity of the cell. [62] Lin et al.[63] reported a lithium poly(sulfidophosphate) based higher sulfur content cathode material exhibiting a Li^+ ion conductivity of 10^{-5}–10^{-6} S/cm. The prepared cell with the above mentioned cathode and solid-state Li_3PS_4 electrolyte showed a reversible capacity of over 1200 mAh/g with 0.1 C rate over 300 cycles at 60 ˚C. Kamaya et al.[64] developed the sulfide based lithium superionic conductor, namely $Li_{10}GeP_2S_{12}$, which exhibited Li^+ ion conductivity of 12 mS/cm at 25 ˚C, so it tends to be promising material for Li–S batteries. Even though the non-oxide (sulfide) based systems are promising in inert atmosphere, the presence of air and moisture will deteriorate its performance due to the sensitive nature of the material. Research must therefore be carried out to develop chemically stable material without losing the high ionic conductivity of Li+ ions.

1.1.4.3 Separators

Expanded polypropylene (PP) is extensively studied as a separator for Li-S batteries. Due to the lack of functionalization, they cannot completely block the shuttling effect of polysulfides. Research has been done to reduce the polysulfide shuttling effect by exploring the functionalized membranes for Li-S System. For instance, Jin et al.[65] used Nafion based separators for Li-S cell. Lithiated Nafion membranes are used as a separator in Li–S batteries, the lithiated Nafion is prepared using the exchange of H^+ ions by Li^+ ions in the sulfonated tetrafluoroethylene-based fluoropolymer-copolymer. Due to the higher ionic conductivity and chemical stability of Nafion membranes (hydrogen form), it is commonly used in proton exchange membrane fuel cells. The proton (H^+) ions in the nafion membrane are exchanged with Li^+ ions and turned into the Li^+ conductor. The lithium ion conductivity of 2.1×10^{-5} S/cm is achieved for lithiated Nafion membranes at 25 ˚C with 0.986 of Li ion transference number and higher selectivity for Li^+ ions.

The Li-S cell prepared using lithiated Nafion membrane showed higher capacity retention of 552 mAh/g at 50 cycles and 97% of coulombic efficiency. Recently, Jin et al.[66] fabricated a cell using perfluorinated polymer membrane with lithium sulfonyl dicyanomethide functional group membrane. It exhibited the Li ion conductivity of 10^{-4} S/cm and the lithium transference number is approximately unity. The prepared cell shows an initial discharge capacity of ~1100 mAh/g and stable discharge capacity of 800 mAh/g over 100 cycles along with higher coulombic efficiency.

1.1.5 Polysulfide Absorbing/Binding Materials

The conductive carbons and polymer based composite materials which are extensively used for Li-S batteries are discussed above. However, other composite materials with additives have also been studied. The additive should possess good absorbing and trapping ability to the dissolved polysulfide and should act as a supporter for the active material to enhance the capacity. In addition, the absorbing agent should exhibit more affinity to polysulfides in order to bind and prevent them from entering into the electrolyte. The absorbing agent should not have an overlapping redox potential with sulfur (1.5−2.8 V vs Li^+/Li^0) because it causes undesirable electrochemical reactions and morphological/structural changes during electrochemical cycling.

In 2001, Gorkovenko et al.[67] patented the usage of silicates, aluminum oxides, vanadium oxides, and transition-metal chalcogenides with sulfur cathodes to decrease the polysulfide diffusion and migration. Even though the absorbing agents exhibited several advantages; absorbing ability and electron transport property were limited by its large particle size which tend to decrease the electrochemical performance.

Song et al.[68] studied the effect of size (30−50 nm) of manganese nickel oxide particles as an absorbing material for the sulfur cathode. This increases the electrochemical cell performance with 85 % capacity retention up to 50 cycles. Also, they studied the criteria for choosing the appropriate absorbing agent such as smaller particle size, high surface area and porous structure. Several nanosized metal oxides including manganese nickel oxide[68], titania[69], γ-alumina[70] and silica[71], satisfy the above addressed criteria.

These nanosized metal oxides enhance the cycling stability through successfully reducing polysulfide dissolution using absorbing effect. The tremendous improvement mainly raised from the addition of small amount of absorbing agents from 3.6 wt % (TiO_2) to 15 wt % ($Mg_{0.6}Ni_{0.4}O$) in the sulfur cathode material. S− metal oxide core−shell composites (sulfur as a core and metal oxide as a shell) are another assembly of materials used to enhance the performance of Li-S cells. Seh et al[72]. prepared yolk−shell composite using S-TiO_2 which showed better cyclability over 1000 cycles. They observed that the metal oxide shell replaces carbon, the polysulfides were trapped by metal oxides. For demonstrating practical applications, there is a necessity to increase the loading of sulfur (0.4−0.6 mg/cm^2). The volume expansion of active material may fracture the TiO_2 spheres during the electrochemical process and lead to the leaking of polysulfides. The yolk−shell structure retards the above-mentioned problem. The presence of an excess large void or pore size in the active material improves polysulfide trapping and also gives it the ability to withstand the volume change during charge/discharge processes.

2.0 Research Objectives and Specific Aims

The overall objective of the PhD thesis is to study and understand the main problems associated with Li-S battery system and to develop new cathodes and separators to address the problems identified. The primary problems of Li-S battery are the poor electronic and ionic conductivity of sulfur and the formation combined with dissolution of the polysulfide in organic battery electrolyte.

In order to address the poor conductivity of sulfur, conducting metal organic framework (MOF) and complex framework material (CFM) hosts were developed for encapsulating sulfur. To overcome polysulfide dissolution, agents capable of trapping the polysulfide by chemically binding onto them were developed. Composite polymer electrolytes (CPEs) and oxides with improved room temperature lithium ionic conductivity were developed and their ability to prevent polysulfide dissolution were studied using materials and electrochemical characterization techniques.

To accomplish the above goals, the broad objectives of this thesis involved executing the following four specific aims:

Specific Aim 1: Understand the Origin of Irreversible Capacity Loss in Li-S Batteries and Address the Mechanisms of Polysulfide Dissolution Using Structurally Distinct Metal Organic Framework (MOF) Based Sulfur Cathodes.

As a part of this specific aim, Zn – MOF – 5, S-Cu-bpy-CFM, S-Cu-pyz-CFM and S-SCFM were synthesized and then infiltrated with sulfur using a vapor infiltration technique. The sulfur infiltrated MOF and CFMs were used as cathodes for Li – S batteries. The specific capacity and the cycling stability of the MOF and CFMs were evaluated using electrochemical

testing. XPS technique was accordingly used to study polysulfide dissolution and to understand S – C bonding providing insight into prevention of the polysulfide dissolution by the MOF. The mechanistic overview provided by the work in this specific aim, could lay the foundations and further identify possible pathways for implementing future design strategies to enhance the capacity and directly aim to resolve polysulfide dissolution problems plaguing the Li-S battery cathodes.

Specific Aim 2: Investigate the Mechanisms of Composite Polymer Electrolytes (CPEs) to Suppress Solid Electrolyte Interphase (SEI) Formation and Prevention of Polysulfide Dissolution in Li-S Batteries

In the aim, poly (vinylidene fluoride – co – hexafluoro propylene) (PVdF – HFP) based CPEs (Composite Polymer Electrolytes) was prepared by a simple electrospinning technique. Further, nanoparticulate SiO_2(nm-SiO_2), TiO_2(nm-TiO_2) prepared using a simple sol – gel based nano fabrication technique and commercially available fumed SiO2(f-SiO_2) was used as fillers to augment the mechanical and Li-ion conducting properties of these CPEs among other necessary ionic transport requirements. These nanofiller incorporated PVdF – HFP composite polymer electrolytes as separator – electrolytes were then tested to demonstrate their improved cycling stability using commercial sulfur as cathodes in Li – S batteries.

Specific Aim 3: Study the Electrochemical Stability and Room Temperature Li-ion Conductivity of New Substituted Solid-state Oxide and Non-oxide Li-ion Conductors.

In this aim, we will investigate the effect of Ca and Mg substitution on Li sites and F substitution on O sites of Li_4SiO_4 on its ionic conductivity. AC impedance spectroscopy measurements was performed on the substituted samples to measure the lithium ionic conductivity of the Li_4SiO_4. By optimizing the substituent concentration, 3-4 order improvement

in room temperature lithium ion conductivity was obtained. Substitution introduces vacancies in the crystal structure that favors the diffusion of lithium ions by creating easy diffusion pathways and hence, increasing the ionic conductivity. These substituted Li_4SiO_4 were then pressed onto S-Cu-bpy-CFM pellets and evaluated for their electrochemical performance.

Specific Aim 4: Develop Novel Composite Sulfur Cathodes Comprising High Sulfur Loadings on Electronically Conducting Platforms with Polysulfide Trapping Agents (PTA) and Understand the Mechanisms Related to Prevention of Polysulfide Dissolution Contributing to High Energy Density.

As a part of this aim, sulfur composite cathodes with high sulfur loadings were prepared using a simple electrodeposition technique. These cathodes have sulfur loadings of >10 mg/cm^2. Slurry-coating technique used for electrode preparation uses PVdF binder (~10wt%), and Super P carbon additive (usually ~20wt% as opposed to ~5-10wt% in conventional cathodes) along with sulfur active material. The binding efficiency of PVdF decreases at such a high Super P content leading to cracks at the electrode at higher loadings. This limits the thickness and sulfur loading of the cathodes to <3mg/cm^2. However, this sulfur loading is not enough to meet the Department of Energy's (DOE) target energy density of 500 Wh/kg for Batt500 program (Batt500 program is directed towards development and commercialization of sulfur cathodes for Li-S battery). In order to achieve this goal, a minimum sulfur loading of 6mg/cm^2 is necessary and this could be achieved only by using modified electrode fabrication techniques such as electrodeposition. The thick electrodes developed as a part of this aim were then coated with a polysulfide trapping agents (PTA) to prevent the polysulfides from dissolving into organic liquid electrolyte. These binder free cathodes were then characterized using XPS and UV-VIS spectroscopy after electrochemical cycling to understanding the nature of bonds between polysulfides and the PTA and the extend of polysulfide trapping by the PTA respectively.

3.0 Specific Aim 1: Understand the Origin of Irreversible Capacity Loss in Li-S Batteries and Address the Mechanisms of Polysulfide Dissolution Using Structurally Distinct Metal Organic Framework (MOF) Based Sulfur Cathodes – (i) Understanding the Origin of Irreversible Capacity Loss in Non-carbonized Carbonate – based Metal Organic Framework (MOF) Sulfur Hosts for Lithium – Sulfur Battery

The results of the work in this specific aim has been published in Electrochimica Acta, 229, 208-218, 2017 (https://doi.org/10.1016/j.electacta.2017.01.115)

Pavithra M Shanthi[a], Prashanth J Hanumantha[b], Bharat Gattu[a], Matthew Sweeney[c], Moni K Datta[a], Prashant N Kumta[a, b, d, e]

[a]Department of Chemical and Petroleum Engineering,

University of Pittsburgh, Pittsburgh, PA 15261 (USA)

[b]Department of Bioengineering,

University of Pittsburgh, Pittsburgh, PA 15261 (USA)

[c]Department of Chemical Engineering,

University of Maryland- Baltimore County, Baltimore, MD 21250 (USA)

[d]Department of Mechanical Engineering and Materials Science,

University of Pittsburgh, Pittsburgh, PA 15261 (USA)

[e]Center for Complex Engineered Multifunctional Materials,

University of Pittsburgh, Pittsburgh, PA 15261 (USA)

3.1 Synopsis

Li-Sulfur (Li-S) batteries are emergent next-generation energy storage devices due to their very high specific energy density (~2567 Wh g^{-1}) but are limited by polysulfide dissolution issues. In this work, chemically synthesized sulfur containing non-carbonized metal organic framework (S-MOF) cathodes show initial specific capacities of 1476 mAh g^{-1} stabilizing at ~609 mAh g^{-1} with almost no fade for over 200 cycles. Post-cycled separators of the S – MOF cathodes display complete absence of polysulfides after cycle 1, 20 and 200. It was identified that the occurrence of carbonate species in the MOF structure resulted in the formation of C-S bonded species causing retention of polysulfide at the electrode surface ensuring long-term stability. However, this observed capacity drop during the first 10 cycles is attributed to the oxidation of some of the infiltrated sulfur by the MOF as determined by electrochemical and X-ray photoelectron spectroscopy (XPS) analyses. Nevertheless, the negligible fade rate (0.0014% $cycle^{-1}$) and complete prevention of polysulfide dissolution renders these cathodes most promising candidates for Li-S batteries. Understanding of this transformation behavior in sulfur-containing MOF is essential to engineer chemically-bonded host-structures capable of efficient polysulfide trapping, a key pathway to establishing novel platforms for achieving high power Li – S batteries.

Key words: Metal organic framework; Lithium-Sulfur; Polysulfide; Encapsulation

3.2 Introduction

In recent years, there is a near exponential increase in the demand for plug – in hybrid vehicles (PHEV) combined with the use of portable electronic devices, together providing the impetus for portable energy storage devices with greater output/mass or volume. Commercial Li – ion batteries since the first Li-ion battery introduced by Sony in 1990 based on lithiation chemistry are limited by a maximum theoretical capacity of ~546 Wh kg^{-1} [73] and are incapable of meeting this ever increasing demand. These limitations make it critical to discover new materials with high specific capacities augmented with the incessant need to engineer the materials exploiting economic scalable approaches to exhibit performance matching the theoretical predictions for rapid commercialization.

The focused search for finding new alternatives to the conventional Li – ion (Li metal oxide cathode-graphite anode) system has led to the identification of the Li-sulfur system with a theoretical specific capacity of 1672 mAh g^{-1} [74] as a promising candidate for high energy density lithium batteries. Sulfur being one of the most abundant elements on the Earth's crust has the additional advantages of being a promising low cost and environmentally benign material.

Despite these advantages, lithium-sulfur batteries suffer from several problems that prevent commercialization of the technology: (i) Sulfur has very low electronic conductivity (~10^{-17} S cm^{-1})[75] which restricts complete utilization of the active material resulting in low specific capacity upon cycling, (ii) Unlike intercalation based Li – ion batteries, sulfur forms a non – intercalation reaction product Li_2S via a series of polysulfide (Li_2S_n ; n = 2 – 8) species leading to complex electrochemical reaction kinetics[14, 15, 76-82], (iii) These polysulfide intermediates show a range of solubility in organic electrolytes resulting in loss of active material[75, 80, 83-86], (iv) In addition, the dissolved polysulfides undergo crossover and coat the

anode resulting in a gradual reduction in the cell voltage and subsequently leading to failure. These problems prevent the Li-S battery technology from being universally adopted and rapidly commercialized.

Extensive research efforts with an objective of solving the problems plaguing Li – S batteries are primarily directed towards addressing the following key aspects: (i) Increasing the active material utilization by improving the electronic and ionic conductivity of sulfur electrodes through the use of conductive coatings or composites[47, 49, 87-103], (ii) Minimizing polysulfide dissolution by replacing the organic liquid electrolyte containing separator with a gel – polymer, composite – polymer or solid polymer electrolyte separator[90, 104-113] (iii) Complete replacement of the liquid based ionic conducting separator systems by solid lithium ion conducting electrolytes[57, 114, 115] (iv) Confinement of sulfur into the porous matrices preventing polysulfide entry into the liquid electrolyte phase[16, 26, 42, 47, 54, 88, 116].

Efforts to improve the conductivity of sulfur are generally focused on either mixing with secondary conducting materials[89, 117, 118] or by utilizing the effect of crystallite size on macroscopic conductivity[18, 91, 119-121]. However, these efforts mostly involve complex synthesis procedures or result in an increase in the inactive materials weight. On the other hand, use of solid and composite – polymer electrolytes [79, 90, 104-106, 122, 123] to replace the liquid electrolyte appears promising in ensuring polysulfide retention and preventing crossover, but is limited by the ionic conductivity of available solid state ionic conductors and the extreme handling issues associated with LISICON (Lithium Super Ionic Conductors) due to their air-sensitive nature and need for external activation[115, 124, 125]. Attempts aimed at preventing polysulfide from entering the liquid electrolyte phase generally focus on exploiting mesoporous and hollow carbonaceous materials as sulfur hosts [42, 47, 126-130].

The strategy with such host-based strategies is two-pronged as described in the following: (a) the host acts as a conductive matrix; and (b) polysulfide species formed during lithiation are trapped within the host matrix. Use of MOF (Metal Organic Framework) derived carbon matrix following high temperature carbonization as a sulfur host [88, 131] has shown considerable improvement in cycling stability along with enhanced capacity. Recent reports on hosting sulfur into the carbon-based hosts have yielded improvement in stability[132-135]. Despite improvements in the improved stability, all these structures exhibit a high initial capacity loss and gradual capacity fade, the origin of which has not been studied.

To rationally design sulfur hosts using complex framework materials (CFM), a basic understanding of the mechanisms involved in trapping polysulfide into the host materials needs to be established. This mechanism would further explain the origin of irreversible capacity loss during the initial cycles. Thus, for the present studies, MOF – 5 was selected as the sulfur host due to its simple scalable synthesis procedure and very small pore size. In the present work, the 3-D sulfur impregnated nanoporous non-carbonized MOF prepared using a solution – infiltration technique is studied as cathodes in Li – S battery system. The electrochemical performance of the S – MOF was investigated using galvanostatic charge – discharge cycling. The work uses XPS analysis as a technique to understand the mechanism involved in masking polysulfide dissolution by directly binding the sulfide species onto the MOF. The proposed concept of using chemical bonding has been reported elsewhere although the complete prevention of polysulfide dissolution and retention by MOF structures has not been reported in the open literature to date, to the best of our knowledge[136].

MOF – 5 is a carbonate – based MOF with an average pore diameter of ~2.5 nm and is expected to bind with lithium polysulfides through a Lewis acid – base interaction[137]. The

carbonization process adopted in previous MOF based framework electrodes eliminates the possibility of such Lewis acid-base interactions, the presence of which is expected to cause binding of sulfur with the MOF structure ensuring polysulfide retention at the electrode surface. Moreover, these non-carbonized MOFs exhibit high pore volumes of ~0.45 cm^3 g^{-1} [138] which can thus accommodate large quantities of sulfur. The use of an easy and facile room temperature synthesis method considerably adds to the scalability of the approach for generation of functional electrodes for entrapment of polysulfide. Figure 3-1 provides a graphical representation of the synthesis and the sulfur encapsulation technique used in this work.

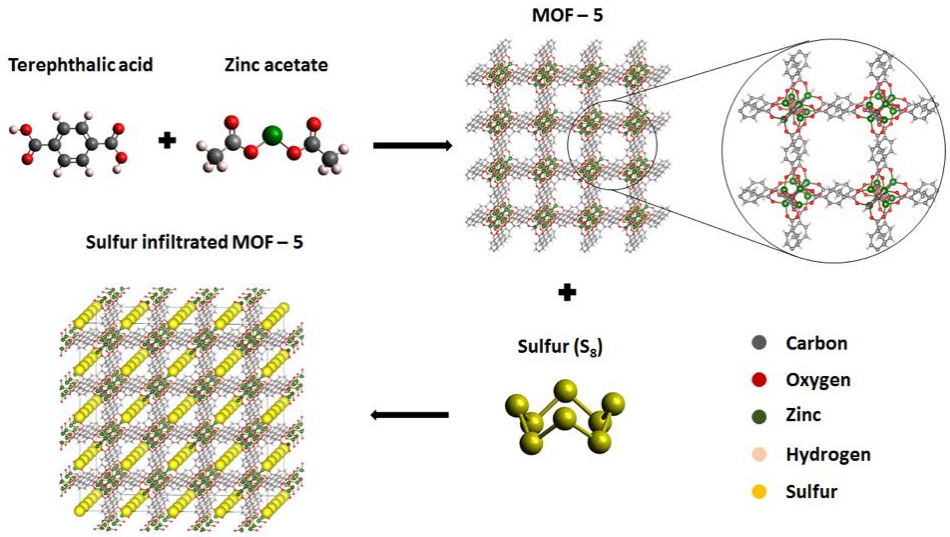

Figure 3-1 Schematic representation of the synthesis of MOF followed by sulfur infiltration.

Zn – MOF – 5 was synthesized at room temperature. However, upon exposure to air, the Zn – MOF – 5 gets transformed into the corresponding air – stable phase, Zn – MOF – 5W. This MOF was then infiltrated with sulfur using a vapor infiltration technique. The sulfur infiltrated MOF, S – Zn – MOF using Zn^{2+} as the metallic center was used as cathodes for Li – S batteries. The S – Zn – MOF shows a very high initial capacity of 1476 mAh g^{-1}, which is one of the

highest capacity values reported in the literature to date[118, 139, 140], stabilizing at 609 mAh g^{-1} over 200 cycles. The almost negligible fade rate (0.0014% $cycle^{-1}$) and complete prevention of polysulfide dissolution makes these cathode systems most promising candidates for Li-S batteries. However, there is an initial loss in capacity observed and to address this initial capacity loss observed in this system, studies related to the understanding of the mechanism involved in the electrochemical lithiation process is very much warranted.

The XPS technique was accordingly used to study polysulfide dissolution and to understand the S – C bonding providing insight into prevention of the polysulfide dissolution in the current work. The mechanistic overview provided in this report we believe could lay the foundations and further identify possible pathways for implementing future design strategies to enhance the capacity and thus directly aim to resolve polysulfide dissolution problems plaguing the Li-S battery cathodes.

3.3 Experimental

3.3.1 Preparation of MOF- 5 and Sulfur Infiltration

Terephthalic acid (C_6H_4 – 1, 4$(COOH)_2$, 98%), Zinc acetate dihydrate (Zn $(CH_3CO_2)_2.H_2O$, >98%), Triethylamine ($(C_2H_5)_3N$), >99%), Dimethylformamide (DMF, 99.8%) and Chloroform ($CHCl_3$, 99.85%) were purchased from Sigma Aldrich and used as received. The Zn – MOF – 5W was synthesized using a modified room temperature precipitation method reported elsewhere [141, 142]. Accordingly, 20 mmoles of Terephthalic acid and 4 ml Triethylamine were dissolved in 200 ml DMF (**Solution 1**) and 50 mmoles zinc acetate dihydrate were

dissolved in 200 ml DMF separately (**Solution 2**). The two solutions were then slowly mixed under stirring over 15 minutes to form a cloudy white solution. The colloidal solution obtained was continuously stirred for 12 h to form white precipitates of the MOF. The precipitates were then filtered and washed in DMF repeatedly. Solvent exchange was performed to ensure low-temperature pore-activation of the resultant MOF materials. DMF was also exchanged with chloroform by immersing in $CHCl_3$ for 7 days with replacement of fresh solvent every 24 h. The resulting white powder (MOF – 5 materials) were activated by heating at 110°C for 12 h.

Sulfur (~325mesh, Sigma Aldrich, Inc., 99% wt) was infiltrated into the MOF [143] under vacuum. Accordingly, pre – calculated weights of sulfur and MOF (50: 50 wt %) were sealed in a quartz tube under vacuum and heated at 300°C for 24 h allowing for impregnation of the sulfur into the MOF to generate the sulfur infiltrated S – Zn – MOF.

3.3.2 Materials Characterization and Electrochemical Measurements

The synthesized MOF – 5W and S – MOF materials were characterized by X- ray diffraction using the Philips XPERT PRO system employing CuK_α (λ = 0.15406 nm). The scans were typically recorded in 2θ range of 5° - 40°, setting the current and voltage constant at 40 mA and 45 kV respectively. The microstructure and morphology of the MOF – 5W and S – MOF materials was analyzed using High Resolution Transmission Microscopy (HRTEM) performed on a JEOL JEM2100F which features high resolution and rapid data acquisition.

The surface chemistry of the MOF and S – MOF was probed by X-ray photoelectron spectroscopy (XPS) using an ESCALAB 250 Xi system (Thermo Scientific) equipped with a monochromated Al Kα X-ray source. Uniform charge neutralization was provided by beams of low-energy (≤10 eV) Ar^+ ions and low-energy electrons guided by magnetic lens. The standard

analysis spot of 400×400 μm^2 was defined by the microfocused X-ray source. The measurements were performed at room temperature in an ultra-high vacuum (UHV) chamber with the base pressure $<5*10^{-10}$ mbar (the charge neutralization device produced $2*10^{-10}$ mbar partial pressure of Ar during measurements). The binding energy (BE) scale of the analyzer was calibrated to produce <50 meV deviations of the three standard peaks from their standard values: 83.98 eV for Au $4f_{7/2}$, 368.26 eV for Ag $3d_{5/2}$, and 932.67 eV for Cu $2p_{3/2}$. The aliphatic C1s peak was observed at 284.6 eV. High-resolution elemental XPS data in C2p, S2p and Zn2p regions were acquired with the analyzer pass energy set to 20 eV (corresponding to energy resolution of 0.36 eV) and the step size set to 0.1 eV. The Avantage software package (Thermo Fisher Scientific) was used to fit the elemental spectra based on calibrated analyzer transmission functions, Scofield sensitivity factors, and effective attenuation lengths for photoelectrons from the standard TPP-2M formalism.

The pore characteristics and specific surface area (SSA) of the samples were analyzed using a Micromeritics ASAP 2020 Physisorption analyzer, utilizing the Brunauer–Emmett–Teller (BET) isotherm generated. The powders were first vacuum degassed and then tested for nitrogen adsorption and desorption for surface area analysis.

Electrodes for battery half-cell characterization were prepared by casting a slurry of 70 wt% S – MOF, 20 wt% carbon black (super-P) and 10 wt% PVdF in N- Methyl Pyrrolidone (NMP) onto aluminum foil followed by drying under vacuum for 24 h. A uniform electrode loading of 1.5 mg – 2 mg cm^2 was maintained for all the electrochemical measurements. Control electrodes of commercially obtained sulfur powder (~325mesh, Sigma Aldrich, Inc, 99% wt) were prepared using identical composition and tested under identical conditions for comparison.

2025 – type coin cells were assembled in an Innovative, Inc. glove box (UHP Argon, <0.1 ppm O_2, H_2O) using S – MOF or commercial sulfur coated electrodes as working electrode, lithium foil as the counter electrode, Celgard polypropylene as the separator and 1.8 M $LiCF_3SO_3$ (lithium trifluoro-methanesulfonate) in 1:1 vol% 1, 3 dioxolane and 1, 2 dimethoxyethane with 0.1 M $LiNO_3$ as the electrolyte. The electrochemical cycling behavior of the cells thus prepared was studied by cycling between 1.7 – 2.6 V (wrt Li^+/Li) at 0.2 C (~300 mA/g) current rate using an Arbin BT200 battery testing system. Finally, cyclic voltammetry (CV) measurements of the electrochemical cells were performed using (VersaSTAT 3, Princeton Applied Research) in the potential range of 1.7V – 2.6V at a scan rate of 0.1mV s^{-1} to obtain mechanistic understanding.

3.4 Results and Discussion

Crystallographic information file (CIF) obtained from MOFiomics (CCDC number 256965) was used to simulate the XRD pattern of MOF – 5 which was used for comparison with the experimentally observed patterns. Figure 3-2 compares the experimental XRD patterns obtained for Zn – MOF – 5 (damp) with chloroform against the simulated pattern of Zn-MOF-5. The perfect fit between the simulated and experimental patterns indicates the single crystallinity and phase purity of the synthesized MOF – 5 materials, which is in-line with previous reports on MOF-5 materials[138, 142, 144-146]. The short-range order offered by the synthetic metal organic nanostructures can be observed from the presence of the crystalline diffraction peaks observed at low 2θ values[147-150].

However, upon exposure to ambient atmosphere i.e. complete desiccation and removal of the solvent, the MOF – 5 systems adsorb atmospheric moisture and undergoes slow transformation into hydrated phase MOF – 5W [151] through partial cleavage of the Zn-O bonds. This transformation is observed in Zn – MOF – 5 samples occurring because of handling in air during analysis and sample processing for infiltration.

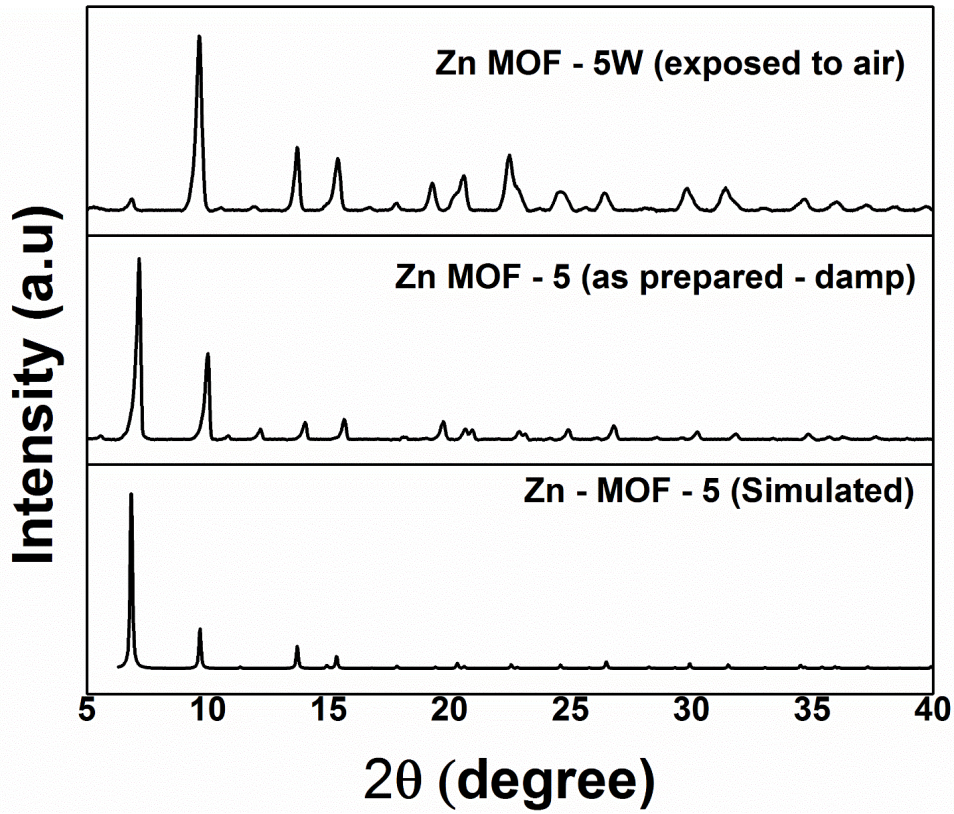

Figure 3-2 XRD patterns of Zn – MOF – 5 predicted by simulation, experimentally synthesized Zn MOF – 5 post-exposure to atmospheric air.

Figure 3-2 shows the XRD profile of the MOF exposed to atmosphere compared with the damp or wet sample. The patterns of the MOF, MOF – 5W closely match those of published patterns for MOF – 5W [151] indicating the initial stages of hydration of MOF – 5. However, the

Lewis – acid base interactions are observed in both MOF – 5 and MOF – 5W due to the presence of identical ligands irrespective of hydration[151] These MOF – 5W materials were further characterized and infiltrated with sulfur.

Table 3-1 BET surface area and pore size analysis of Zn – MOF – 5W exposed to atmospheric moisture.

	BET Surface Area/m^2 g^{-1}	Langmuir Surface Area/ m^2 g^{-1}	Total Pore Volume/cm^3 g^{-1}	Adsorption average pore width/ nm	BET Surface Area/ m^2 g^{-1} (literature)
Zn – MOF – 5W	684.25	1083.07	0.422	2.47	1100 – 2500 [152-155]

Table 3-1 represents the BET specific surface area and average pore sizes of the MOF – 5W materials. Zn – MOF – 5W exhibit a very high surface area of ~684.25 m^2 g^{-1}, with an average pore size of ~2. 47 nm. The MOF was found to have high pore volume of and ~0.422 cm^3 g^{-1}. These values are in accordance with the values reported in the literature for MOF materials[153-155] shown in Table 3-1, though the values are somewhat lower than the Langmuir surface areas[142] reported for pure MOF-5 materials due to the transformation into MOF-5W.

It is however, noteworthy that these specific surface areas are greater than those of most carbonaceous host materials that have reportedly been used as sulfur hosts in Li – S batteries[26, 42, 88, 127]. The large pore volume of the MOF materials is expected to facilitate in ensuring larger amounts of sulfur encapsulation and thus, resulting in high sulfur loading in the electrodes. Another unique advantage yielded using MOF materials to encapsulate sulfur is the small

average pore diameter of the MOF (2.46 nm) that aids in minimizing polysulfide dissolution by offering a better mode for trapping and confining the polysulfide species.

The thermal stability of MOF – 5W has been extensively studied and reported in the literature [156-158]. MOF – 5W exhibits exceptional stability up to 450°C (Appendix A Figure 1), and hence, no denaturing is expected to occur during sulfur infiltration at 300°C which is confirmed by XRD analysis (Figure 3-3).

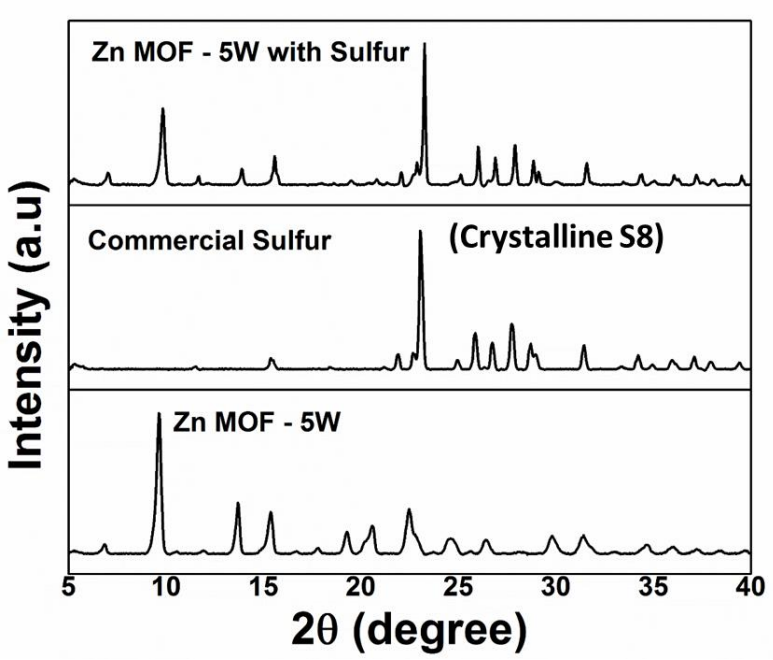

Figure 3-3 XRD patterns of commercial Sulfur, MOF – 5W predicted by simulation, experimentally synthesized S – Zn – MOF.

XRD pattern of S – MOF show peaks corresponding to the MOF – 5 materials (after exposure to air) (see Figure 3-2) along with sulfur peaks confirming the presence of crystalline S_8 sulfur in S – MOF and that the MOF is indeed not denatured during the sulfur infiltration process. It can be seen from above that the XRD analysis confirms the presence of sulfur along

with the MOF. However, no detailed information regarding the chemical interaction of sulfur with the MOF host could be ascertained from the XRD patterns. The nature of sulfur in the S – MOF was thus, studied using XPS analysis (Figure 3-4).

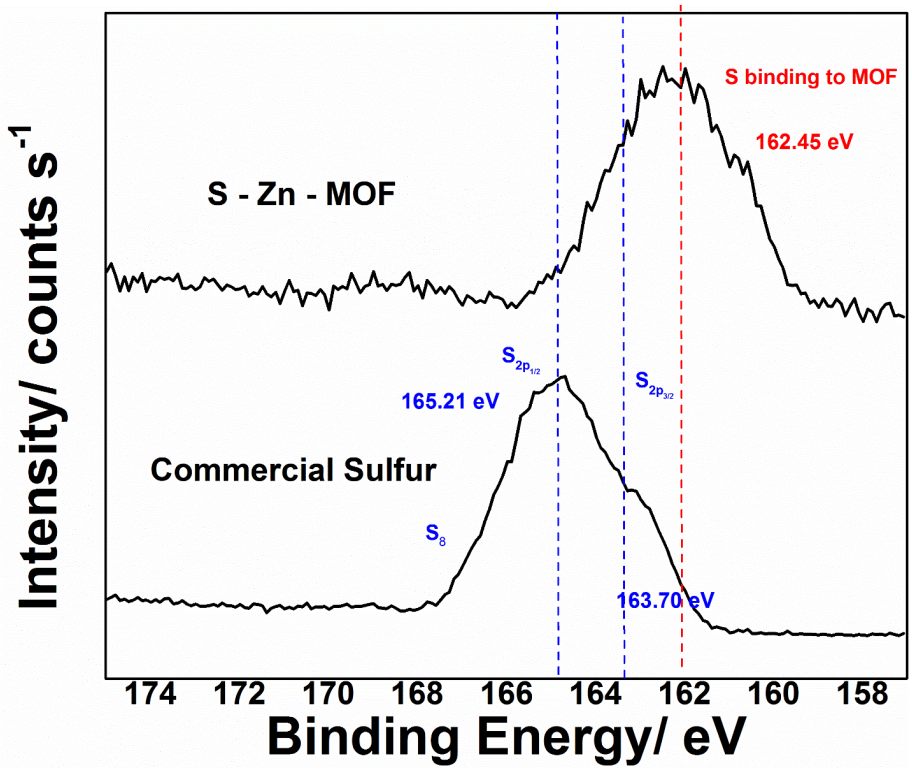

Figure 3-4 XPS S2p Binding Energy profile of Commercial Sulfur and S – Zn – MOF.

XPS analysis was performed on a Thermo ESCALAB 250Xi with suitable background correction. It can be observed that the characteristic $S2p_{1/2}$ peak is observed for the commercial sulfur powder at 165.21 eV in line with previous reports for orthorhombic sulfur (S_8) [143, 159-161]. The XPS spectra of S-MOF however, show a shift in the S2p peak as compared to commercial sulfur indicating the absence of free elemental sulfur suggesting binding of sulfur to the MOF structures. The $S2p_{3/2}$ peak position at 162.45 eV corresponding to the binding of sulfur onto the MOF is similar to values observed in chemically-bound sulfur studied by Chehimi et al.,[162]

further confirming the bound nature of sulfur onto the MOF. The nature of this interaction could be explained by the acidic nature of MOF – 5 precursors that tend to interact with the basic molecules of sulfur[137]. This interaction is more pronounced in gases even at room temperature [138, 163-166], because of which MOF – 5 is widely used for gas storage. This chemical binding of sulfur along with the nanoporous nature of the MOF would result in minimal sulfur dissolution into the organic liquid electrolyte. The shift in $S2p_{3/2}$ peaks in S – MOF could alternatively be attributed to the distortion of sulfur within the MOF structures due to constraints imposed by the nanopores which could restrict the departure of sulfur from the pore during lithiation/delithiation[167]. This effect has also been observed in sulfur entrapped in single wall carbon nanotubes (SWCNTs) of ~1.5nm diameter by Fujimori et al [143] wherein sulfur adopts either a linear or a zig-zag orientation as opposed to the conventional cyclic S_8 rings of S. Due to an average pore size of 2 nm, comparable to the SWCNTs (~2 nm) used[143], the sulfur strands might experience strain from the MOF pore walls thus yielding a lower S2p binding energy.

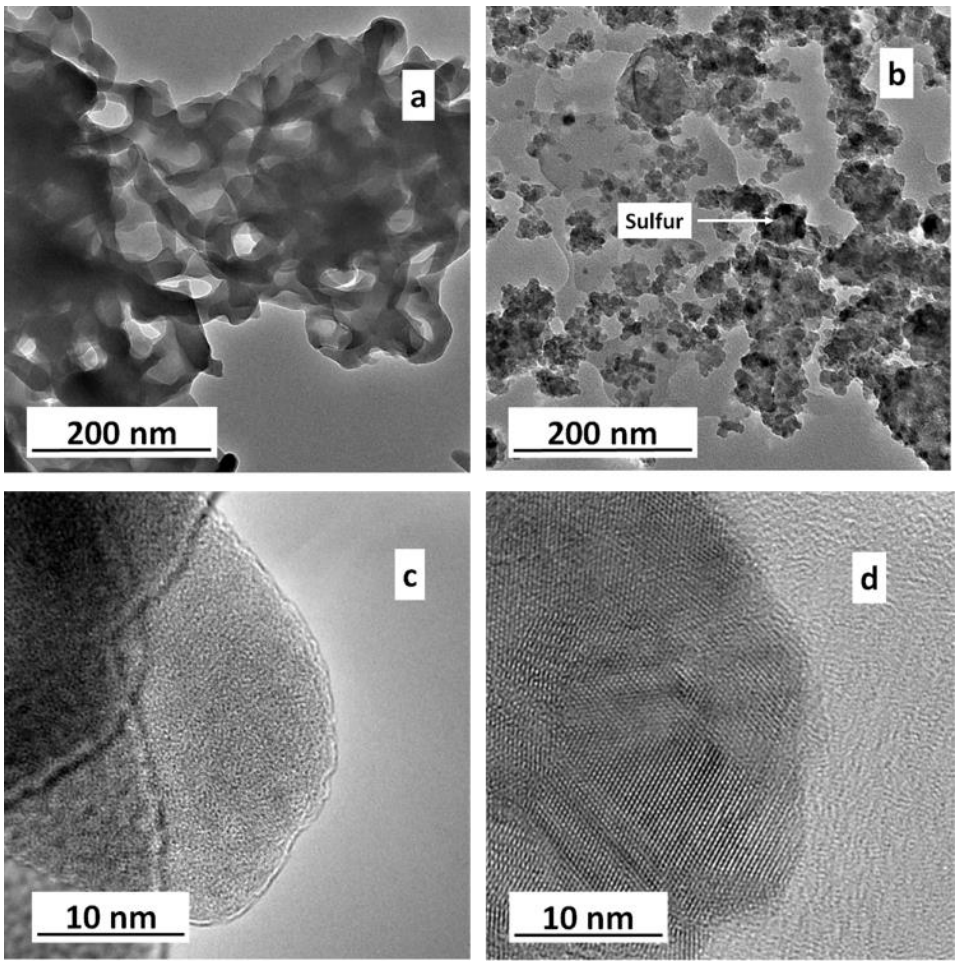

Figure 3-5 TEM images of (a) Zn – MOF– 5W at higher magnification, (b) S - Zn – MOF at lower magnification, (c) S–Zn-MOF – 5W at lower magnification, (d) S–Zn-MOF at higher magnification

MOF -5W, being derived from dicarboxylic acid molecules linking metal oxide cage, undergoes Lewis acid – base interaction with the polysulfides eventually binding them[137]. This kind of acid – base interactions have been reported in different systems involving molecular binding onto MOF[168, 169]. The complete trapping of the polysulfide in a host matrix however, has not yet been reported in the literature to the best of our knowledge and it is expected that further optimization of the MOF materials using a mechanistic understanding gained from the rest of this study would help engineer very high capacity cathodes with almost no capacity fade. To

prove the nanoporous nature of MOF and the binding of sulfur to MOF, TEM analysis was conducted (Figure 3-5). The TEM images of Zn-MOF – 5W at a lower magnification (Figure 3-5a) shows the highly porous nature of the MOF. Phase contrast image of S – Zn – MOF **(**Figure 3-5b**)** clearly shows ~5nm islands of sulfur inside the parent MOF structure thereby supporting the results from XRD analysis indicating sulfur infiltration into the MOF. Figure 3-5c demonstrates the local-ordering in the MOF structure resulting in the low-angle peaks observed in the X-ray diffraction pattern of Zn-MOF-5W in Figure 3-2. The nature of sulfur inside the MOF structure can be seen in Figure 3-5d wherein clear lattice fringes corresponding to crystalline sulfur infiltrated within the MOF structure are observed. Having identified the clear presence of chemical bonding between the sulfur and the MOF matrix, the effect of this binding on the electrochemical performance of S – MOF was studied by performing electrochemical charge – discharge cycling. The electrochemical cycling performance of S – MOF is shown in Figure 3-6. The S – MOF and commercial sulfur electrodes were cycled at 0.2C with an average electrode loading of 1.5 – 2 g cm^{-2} electrode area. The S – Zn – MOF shows an initial discharge capacity of 1476 mAh g^{-1} which stabilizes at 624 mAh g^{-1} after the 10^{th} cycle. Upon prolonged cycling, the S – Zn – MOF shows a very stable capacity of 609 mAh g^{-1} for over 200 cycles.

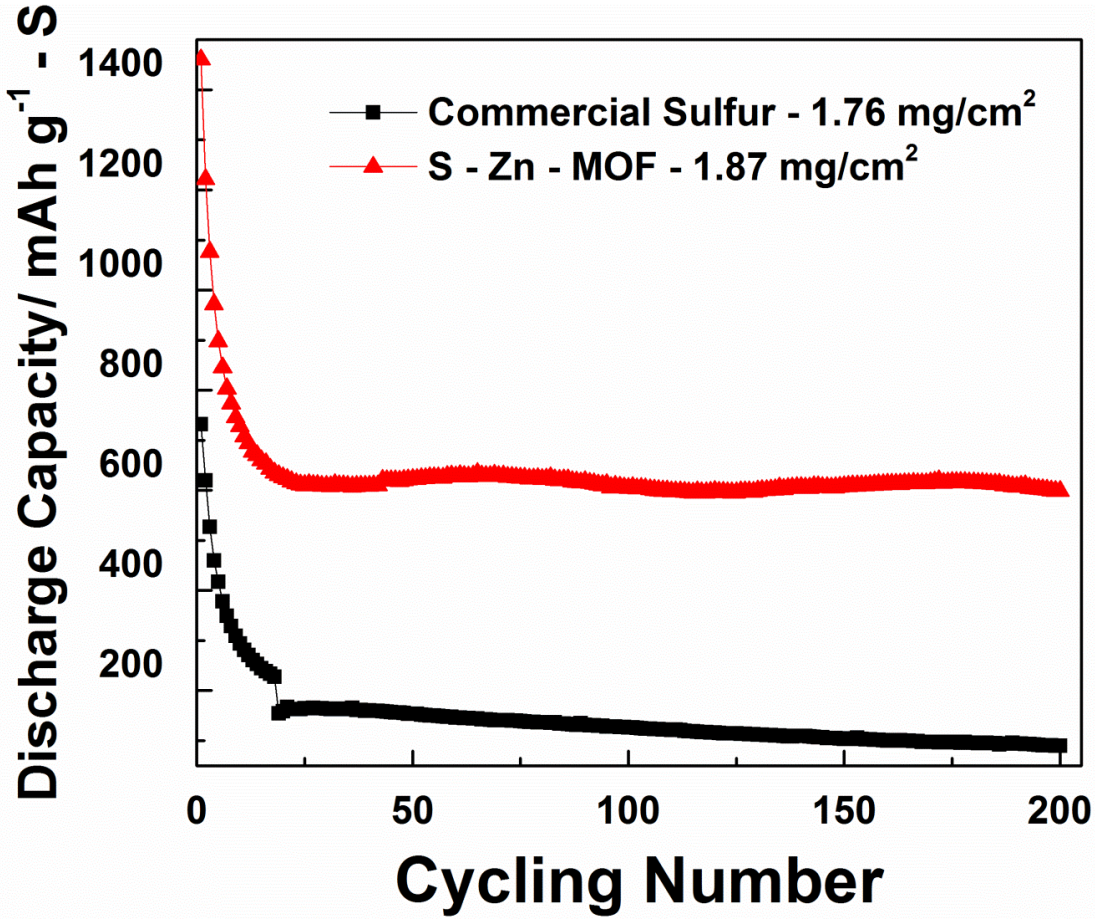

Figure 3-6 Cycling performance of S – Zn-MOF and commercial sulfur at 0.2C rate.

However, commercial sulfur showed an initial capacity of 800 mAh g^{-1} which fades to less than 100 mAh g^{-1} in less than 20 cycles. The nature of the cycling behavior is quite disparate between the two different electrodes with commercial sulfur failing almost instantaneously due to the well-known polysulfide formation and lack of entrapment of the same. The S-MOF electrodes on the other hand, undergo an initial fade followed by stabilization with the S-Zn-MOF demonstrating a superior fade-free cycling behavior (0.0014 % $cycle^{-1}$. The S-MOF electrode, thus demonstrate exceptional stability[137] which could possibly be attributed to sulfur binding with the MOF (evidenced by XPS and TEM-Figure 3-4 and Figure 3-5d) and resulting in effective trapping of polysulfide inside the nanopores of the MOF.

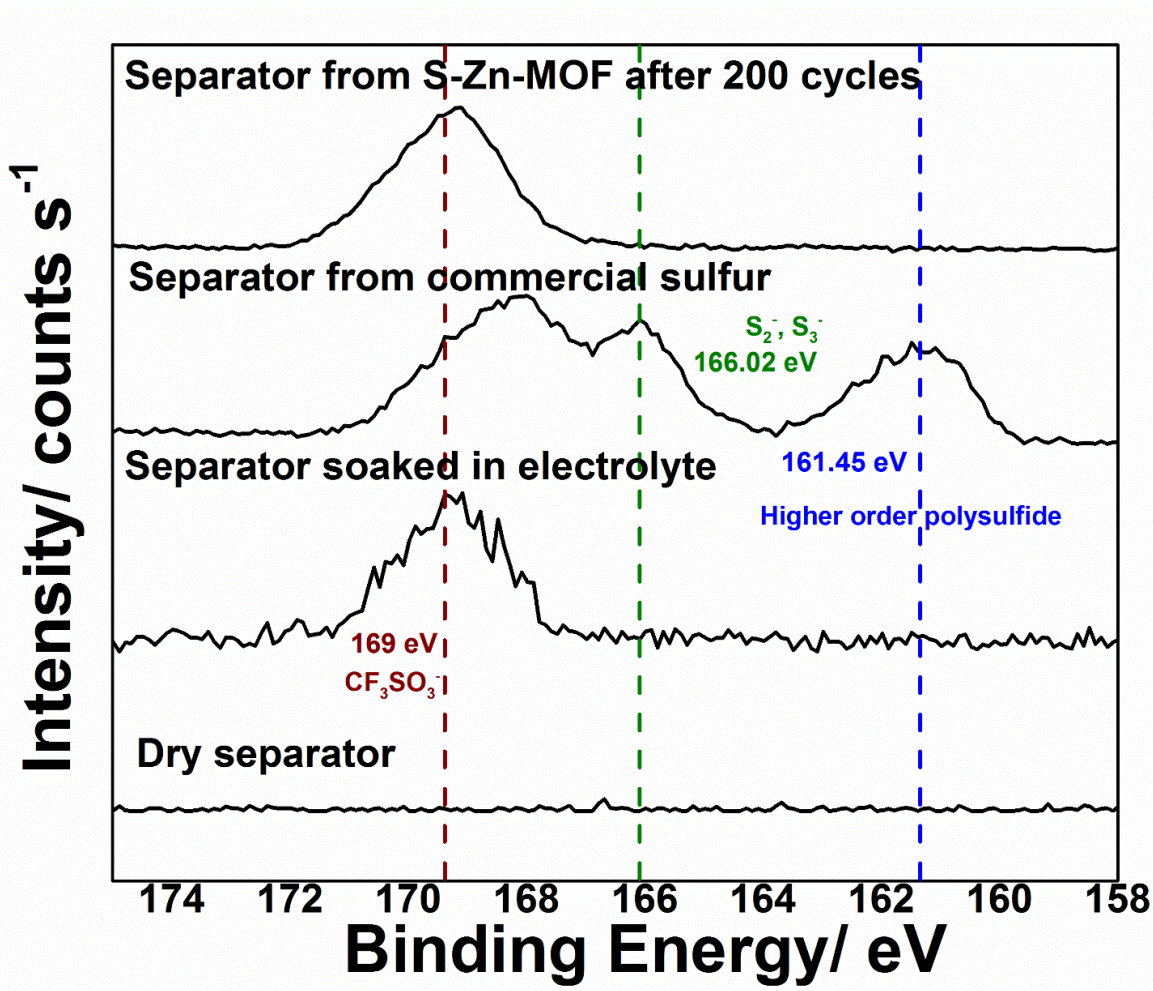

Figure 3-7 XPS S2p binding energy profile of commercial separator, commercial separator soaked in electrolyte; separators of commercial sulfur electrode and S –Zn– MOF (after 200 cycles at 0.2 C rate).

Though the MOF material exhibits excellent cycling stability after initial stabilization, a significant portion of the initial observed capacity is lost within the 1st ten cycles. This loss is typically attributed to the dissolution of sulfur into the electrolyte and loss of the eventual polysulfide species. However, the stabilization of the capacity following the initial loss appears to draw credence to the possibility of the confinement occurring but also alluding to the possible existence or evidence of other extraneous sacrificial or parasitic reactions. This result thus implied that the origin of the initial capacity loss in these S – MOF needs to be better understood

warranting better characterization to be conducted to be able to improve the overall performance of the MOF based sulfur electrode system. The effect of sulfur encapsulation within the MOF structures on the cycling performance of S – MOF was studied by analyzing the separators retrieved using XPS after 200 charge – discharge cycles. S2p peaks were analyzed to understand the nature of the sulfur/polysulfide species present in the various separators. As control experiments, the commercial separator and commercial separator dipped in the lithium electrolyte were also analyzed and the resultant XPS plots are shown in Figure 3-7. As expected, the Celgard separator does not display an S2p peak before cycling while a distinct peak corresponding to the electrolyte species (Trifluoro methyl sulfonate lithium salt) is seen in Figure 3-7 [170]. The XPS plot for the post-cycled separator for the commercial sulfur electrode clearly shows S2p peaks at 169eV, 166.02 eV and 161.45 eV. The peak at 169eV corresponds to S2p peak of electrolyte $CF_3SO_3^-$. On the other hand, the peaks at 166.02 eV and 161.45 eV are due to lower and higher order polysulfide, respectively [80, 171-173]. This indicates and validates the well-known phenomenon of the commercial sulfur electrode (Figure 3-7) undergoing rapid loss in capacity as seen in Figure 3-6 due to the rapid dissolution of polysulfide species formed because of a lack of any medium or mechanism to retain/constrict the same at the electrode surface.

However, the separators corresponding to the S – MOF electrodes (post-cycling) (Figure 3-7) distinctly display only a single S2p peak at 169 eV which corresponds to the sulfur corresponding to the $LiCF_3SO_3$ from the electrolyte[170] as observed in the case of Figure 3-7 for the commercial separator soaked in the electrolyte. The absence of any detectable polysulfide and elemental sulfur in the post-cycled separators cycled from the electrode generated with S-Zn-MOF, after cycle 1 (Appendix A Figure 4), cycle 20 (Appendix A Figure 4) and after 200 cycles (Figure 3-7) indicates complete constriction of the formed polysulfide within the MOF

structures possibly due to chemical-binding of S to the MOF architecture as observed in the TEM images (Figure 3-5) and XPS (Figure 3-4). In addition, spatial confinement (Table 3-1) possibly aids in ensuring polysulfide retention at the electrode. Furthermore, absence of polysulfide species on the counter electrode (lithium) (Appendix A Figure 7) after cycle 1, and 20 corroborates the constriction of electrochemically active sulfur species in the S-MOF electrode architecture. Porous structures have previously been shown to result in improved cycling behavior[28, 42, 88, 127]. However, complete masking of polysulfide dissolution using a porous host has seldom or never been reported to the best of our knowledge. The unique cage-like structure of the MOF along with the chemical binding occurring therein thus results in a very stable cycling performance with a remarkably low fade rate of ~0.0014% $cycle^{-1}$.

To understand the reasons for the observed electrochemical behavior and superior capacity retention, XPS analysis was performed on the S-Zn-MOF electrodes before cycling and after 200 charge-discharge cycles at a 0.2 C rate. Figure 3-8 represents the C1s spectrum of slurry cast S – MOF electrodes and the same electrodes post cycling. S – Zn – MOF (Figure 3-8) electrode sample have peaks corresponding to – (CF_2 – CF_2) – bonds from PVdF binder (289.87 eV)[174], -C_6H_5S- bond corresponding to ring C – S interactions (285.59 eV)[175] and –$C_6H_4S_2$- (284.4 eV)[176]. The presence of the C-S peaks herein confirms the observations in the S2p spectrum (Figure 3-4) and corroborates the hypothesis that sulfur-carbon bonding aids in ensuring superior polysulfide retention within the MOF structure. The S – MOF post-200 cycles showed two C_{1s} peaks at 292.41 eV and 289.55 eV in addition to the peaks observed before cycling. The peak at 292.41 eV corresponds to the $CF_3SO_3^-$[170] group of the lithium salt $LiCF_3SO_3$ used with the organic electrolyte.

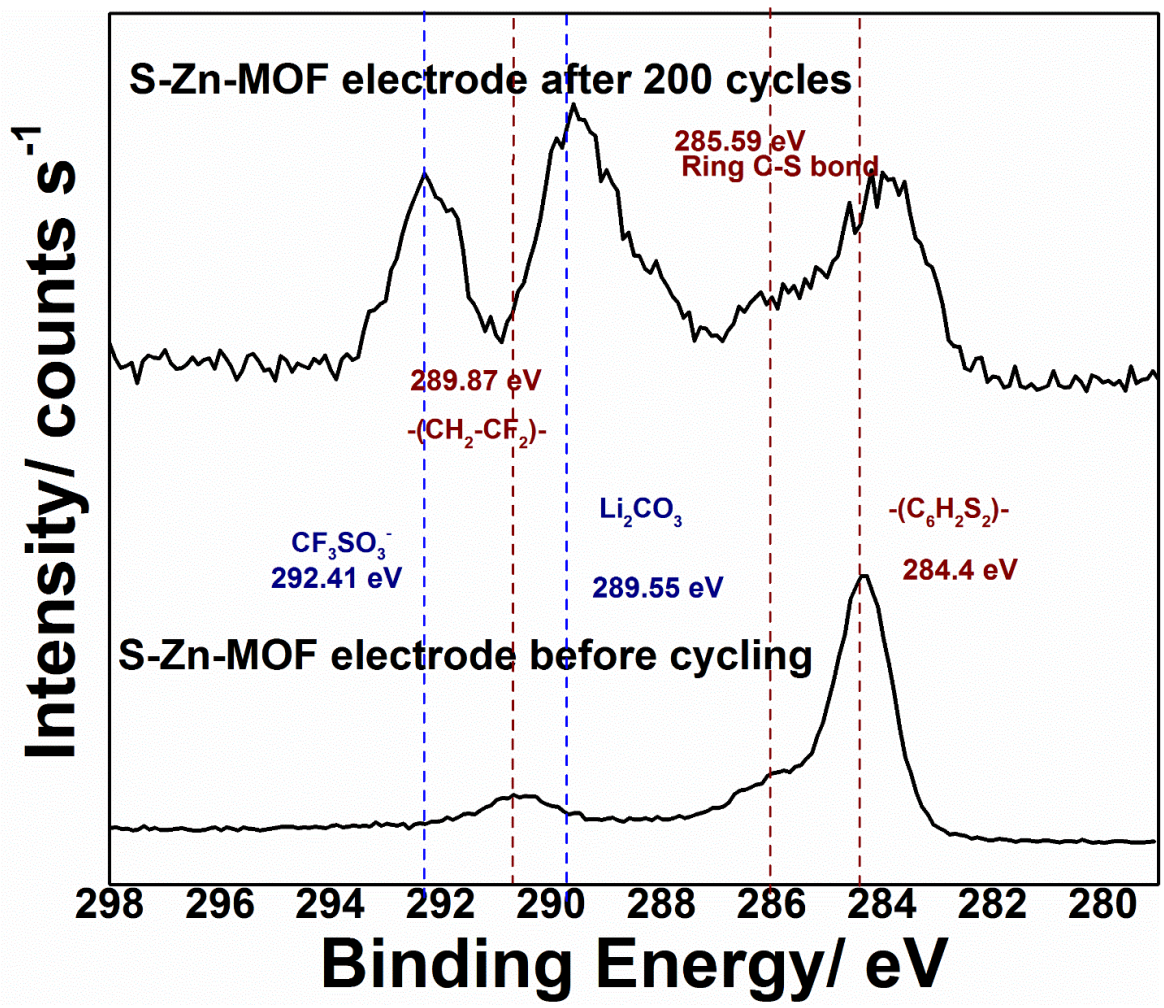

Figure 3-8 XPS C1s Binding Energy profile of slurry coated electrodes of S – Zn – MOF before cycling and S – Zn – MOF after 200 cycles at 0.2 C rate.

The peak at 289.55 eV (Figure 3-8) corresponds to Li_2CO_3[177] resulting from the irreversible reaction of Li^+ ions with the –(CO_3)- groups of the MOF [Appendix A Figure 8 depicts the C1s spectra of the MOF powders before and after sulfur infiltration indicating the presence of –(CO_3)- bonds therein which is to be expected given the structure of the MOF materials (Figure 3-1)]. The lithium carbonates may also be arising from the formation of a solid electrolyte interphase (SEI) layer at the electrode surface. The existence of carbonate moieties in the MOF materials both before and after cycling (occurs during cycles 1, 20 as well-see

Appendix A Figure 5) plays a role in the electrochemical characteristics of the MOF materials as will be discussed below. Though the S-Zn-MOF material exhibit very stable cycling, they undergo an unusual initial loss in capacity. The XPS results discussed above clearly indicate that this loss is not related to polysulfide dissolution as evidenced by the lack thereof of any sulfur species detected on the separators (Figure 3-7). The presence of C-S bonding (Figure 3-4**,** Figure 3-8) in the MOF structure has been shown to result this unique behavior causing the very stable cycling after initial fade (Figure 3-6**)**.

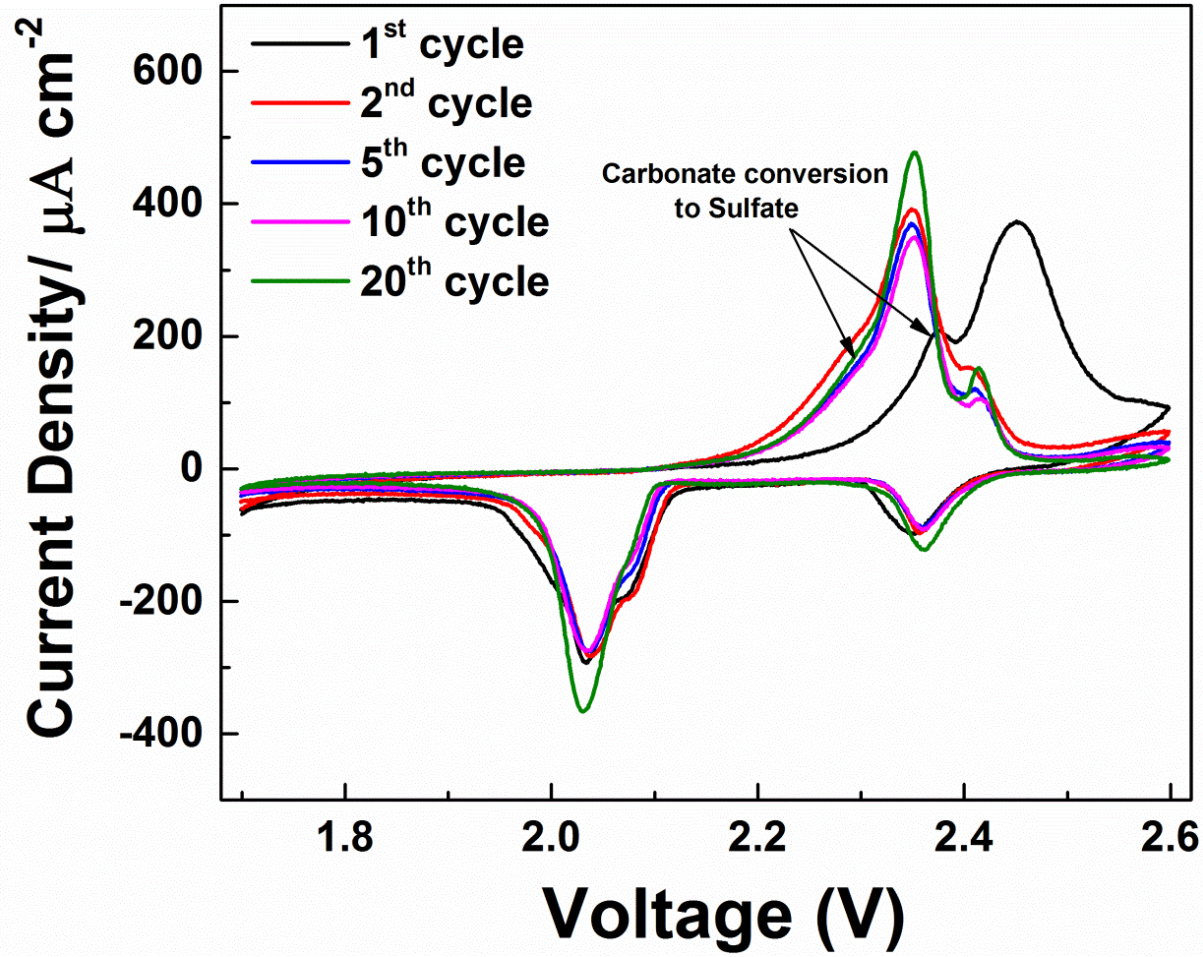

Figure 3-9 Cyclic Voltammetry Plot of S – Zn – MOF at 1st, 2nd, 10th and 20th cycles at a scan rate of 0.1mV s^{-1}.

To understand the origin of this observed initial capacity loss, cyclic voltammetry was performed in the S-Zn-MOF (see Figure 3-9) electrodes at a very slow scan rate of 0.1 mV/s. A distinct change in peak position and height is observed in the cyclic voltammograms of S-Zn-MOF during cycling, especially between the 1st and 2nd cycles. In the case of the MOF material, a third anodic peak appears after the first cycle. This is actually the result of overlap of the two sulfur anodic processes (Reactions (i), (ii)) during the 1st cycle which has been known to result in the formation of one large peak at about 2.55 V[178]. A slight drop in overpotentials (Appendix A Table 1) for the four reactions listed below (Reaction (i-iv)) is also observed, which is the result of a slight decrease in overpotentials for lithation and delithation, after the 1st cycle as reported elsewhere[178]. A third peak at ~2.28 V (Appendix A Table 1) appears as a minor shoulder in S-Zn-MOF. The intensity of this shoulder peak stabilizes before the 10th cycle in the case of the S-Zn-MOF (Figure 3-9).

Reaction (i): $Li_2S_8 \rightarrow Li_2S_p + xLi^+ + xe^-$; $2 \leq p \leq 8$; $2 \leq x \leq 8$

Reaction (ii): $Li_2S_p \rightarrow S_8 + xLi^+ + xe^-$; $2 \leq p \leq 8$; $2 \leq x \leq 8$

Reaction (iii): $Li_2S_n + xLi^+ + xe^- \rightarrow Li_2S_m$; $4 \leq n \leq 8$; $2 \leq m \leq 4$; $2 \leq x \leq 8$

Reaction (iv): $S_8 + 2Li^+ + 2e^- \rightarrow Li_2S_8$

Though the third peak at ~2.28 V has not been explicitly reported in cyclic voltammograms in the literature, we believe the origin for this peak is the result of electrochemical oxidation of sulfur by the carbonate species present in the MOF structure. The chemical oxidation of sulfur to $S_2O_3^{2-}$ species and sulfate species has been reported in the literature[179]. Several studies[180] have also reported consumption of sulfur polysulfides to form –SCO– compounds in carbonate based electrolytes and this phenomenon, we believe, is reflected in the cyclic voltammograms as an electrochemical oxidation of the active sulfur as seen in Figure 3-9.

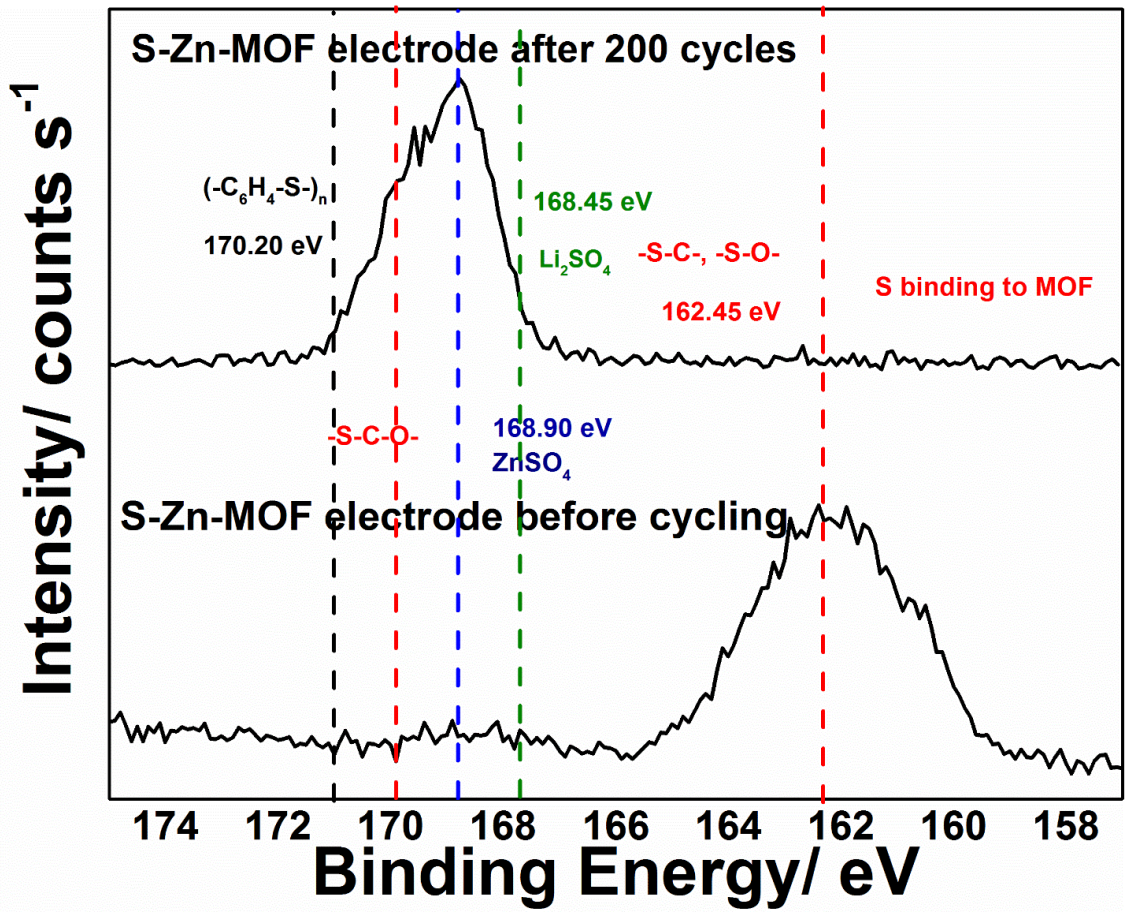

Figure 3-10 XPS S2p Binding Energy profile of slurry coated electrodes of S – Zn – MOF-before cycling and S – Zn – MOF after 200 cycles at 0.2 C rate.

This hypothesis was further examined by XPS performed on the S – MOF coated electrodes before and after 200 cycles. Figure 3-10 depicts the S2p profiles of the S-MOF electrodes before and after cycling. S – Zn – MOF electrode before cycling shows S2p peak at 162.45 eV representing the bonding of sulfur to MOF (as also observed in Figure 3-4). The S – Zn – MOF electrode post-cycling however, shows the presence of a satellite peak at 170.20 eV, corresponding to the occurrence of sulfur-carbon bonding [175, 181]. This indicates that sulfur is bound to the carbon before cycling as well as through the various stages of cycling preventing the loss of sulfur through the traditional polysulfide run-away to bulk electrolyte during cycling

resulting in the exceptional stability observed in Figure 3-6. In addition to the peaks corresponding to C-S bonding, there are unique peaks observed in the post-cycled electrodes corresponding to the formation of -SCO- bonding[170] and a mixture of sulfate species (Li_2SO_4 at 168.45 eV[182] and $ZnSO_4$[183, 184] represented by the peak at 168.90 eV). The irreversible loss in capacity observed in Figure 3-6 could thus be attributed to irreversible consumption of sulfur through the formation of lithium, zinc sulfates during electrochemical cycling. The peak observed in the cyclic voltammograms at~2.28 V in S-Zn-MOF material (Figure 3-9 and Appendix A Table 1**)** indicates that the formation of sulfates is an electrochemical process with no reversibility in the cycling window. The deactivation of the electrochemically active sulfur occurs through the formation of sulfate species and -SCO- compounds during the initial cycling resulting in irreversible capacity loss. This process occurs predominantly during the 1st ten cycles over which the cyclic voltammograms stabilizes as seen in Figure 3-9. The same is confirmed by examining the S2p peaks during the 1st, 20th and 200th cycle-see Figure 3-10 and Appendix A Figure 6 where the occurrence of sulfate and sulfite species is seen in the 1st and 20th cycle as also seen to occur in the 200th cycle.

Thus, from the above it can be construed that the initial loss in capacity is attributed to phase transformation associated with chemical reaction between the polysulfide and the carbonate groups of the terephthalic sub – units of the MOF rather than the traditionally well-known polysulfide dissolution. Jie et al [185] used sulfur K – edge X-ray absorption spectroscopy to explain the chemical reaction of polysulfide with carbonate based ether electrolytes which was later confirmed by Zhe et al[186] in their work on cycling FeS_2 cathodes with ether based electrolytes. Taeeun et al[180] observed decomposition of carbonate electrolytes by inter/intra molecule nucleophilic substitution to form -SCO- bonding[180].

The amount of sulfur that gets converted to sulfate corresponds [indicated by the initial irreversible loss in capacity (~59%)] well with the S: O ratio (2:1) based on the initial nominal composition used for the synthesis of the S-MOF (indicating that ~50% of the sulfur is rendered inactive through binding with oxygen existing within the MOF) (see **Appendix A** for possible reaction mechanism **Reactions S1 and S2**).

A detailed study to overcome this oxidation phenomenon is currently ongoing and will be published shortly. Nevertheless, the results presented herein clearly demonstrate that the embedding of sulfur into the nanoporous MOF frameworks directly in the as-prepared form without any carbonization step ensures minimal polysulfide transport out of the electrode into the separator ensuring minimal capacity loss due to chemical bonding of carbon in the MOF structure with sulfur; and possible constriction of the lithium polysulfide species within the porous matrix. This is indeed reflected resulting in stable capacity of ~609 mAh g^{-1} with a fade rate of only ~0.0014% $cycle^{-1}$ demonstrating the promise of this novel synthetic strategy.

However, what is distinctly evident and observed from the results discussed in the present study is the presence of carbonate groups in the MOF that contribute to the formation of metal sulfate type compounds during the initial charge – discharge cycle, resulting in the irreversible capacity loss during the initial cycling stages and not due to the hitherto accepted occurrence of dissolved polysulfide species. The results discussed herein also suggest that the use of carbonate – free MOF as potential hosts for sulfur in Li – S battery could result in electrodes with high capacity and exceptional stability. This discovery of sulfur interacting with MOF as outlined in the current study during synthesis and upon lithiation provides the framework outlining the pathway for a better understanding of the mechanism involved in the lithiation of sulfur encapsulated in the non-carbonized metal organic framework structures.

3.5 Conclusions

Nanoporous non-carbonized MOF were synthesized using a simple, scalable room temperature method. Sulfur was directly infiltrated into the as-synthesized MOF with no subsequent carbonization and tested as cathodes for Li – S batteries. The resultant S – MOF display very high initial capacity (1476 mAh g^{-1}) that is rendered stable at 609 mAh g^{-1} for over 200 cycles with an impressive very minimal fade rate (0.0014 % $cycle^{-1}$). The study reveals that the use of non-carbonized MOF resulting in Lewis acid-base interactions is vital for ensuring the carbon-sulfur bonding with the MOF architecture resulting in complete retention of lithiated polysulfide species within the porous MOF structure. Furthermore, the results conclusively indicate that the use of a porous sulfur host is a critical factor for masking the generated polysulfide from escaping into the bulk electrolyte, resulting in the continuous loss in capacity ubiquitous to Li-S electrodes. There is however, an initial loss in capacity which is attributed to sulfur oxidation via reaction with carbonate groups in the MOF architecture to form sulfate species as confirmed by XPS and electrochemical studies. The absence of polysulfide species on the separators and counter electrodes following cycling clearly highlights the potential of nanoporous non-carbonized MOF materials as hosts for sulfur while establishing the importance of chemical bonding as well as pore-driven constriction in stabilizing the electrochemically active sulfur. The study also provides insights into preventing polysulfide dissolution using porous carbon-sulfur containing hosts. This understanding could pave the wave for better engineering of metal organic frameworks as effective polysulfide traps ensuring the generation and stabilization of high capacity Li-S electrodes.

3.6 Acknowledgments

Research supported by the U.S. Department of Energy OVT-DE-EE0006825. PNK thanks the Edward R. Weidlein Chair Professorship Funds and the Center for Complex Engineered Multifunctional Materials (CCEMM) as well as NSF-CBET 1511390 for partial assistance and help with procuring the electrochemical equipment and facilities used in this research work. The authors acknowledge Dr. Joel Gillespie, PPG Materials Characterization Laboratory, and the Department of Chemistry for graciously providing access to the use of XPS instrumentation. The authors also acknowledge the help of Mr. Karthikeyan Saravanan and Dr. John Keith, Department of Chemical Engineering, University of Pittsburgh for their help with the simulation of XRD profiles from CIF (Crystallographic Information File**)** information.

4.0 Specific Aim 1: Understand the Origin of Irreversible Capacity Loss in Li-S Batteries and Address the Mechanisms of Polysulfide Dissolution Using Structurally Distinct Metal Organic Framework (MOF) Based Sulfur Cathodes - (ii) Effective Bipyridine and Pyrazine-based Polysulfide Dissolution Resistant Complex Framework Materials (CFM) Systems for High Capacity Rechargeable Lithium – Sulfur Battery

The results of the work in this specific aim has been published in Energy Technology, 7, 1900141 (1-12), 2019 (https://doi.org/10.1002/ente.201900141)

Pavithra M Shanthi[a], Prashanth J Hanumantha[b], Ramalinga Kuruba[b], Bharat Gattu[a], Moni K Datta[b], Prashant N Kumta[a, b, c,d*]

[a]Department of Chemical and Petroleum Engineering,

University of Pittsburgh, Pittsburgh, PA 15261 (USA)

[b]Department of Bioengineering,

University of Pittsburgh, Pittsburgh, PA 15261 (USA)

[c]Department of Mechanical Engineering and Materials Science,

University of Pittsburgh, Pittsburgh, PA 15261 (USA)

[d]Center for Complex Engineered Multifunctional Materials,

University of Pittsburgh, Pittsburgh, PA 15261 (USA)

4.1 Synopsis

Lithium−sulfur (Li-S) batteries with high theoretical capacity (~1650 mAh/g) and specific energy density (~2567 Wh/g) are not yet commercialized due to low cycling stability arising from dissolution of lithium polysulfides. This work follows our previous work on carbonate-based MOFs. In the current study, sulfur infiltrated non-carbonized non-carbonate containing metal organic complex framework materials (CFM) systems (S-Cu-bpy-CFM and S-Cu-pyz-CFM) were developed as sulfur cathodes for the first time. The S-Cu-bpy-CFM and S-Cu-pyz-CFM show an initial capacity of 1626 mAh/g and 1565 mAh/g with stable capacities of 1063 mAh/g and 1025 mAh/g, respectively after 150 cycles. XPS analysis after sulfur infiltration shows the occurrence of -C-S- bonds arising from the Lewis acid-base interaction of the CFMs with sulfur. The separators from the batteries cycled with the CMF cathodes displayed complete absence of polysulfides after 150 cycles. These CFM cathodes exhibit an initial fade in capacity during the first ~25 cycles that was attributed to the irreversible reaction of nitrogen with sulfur (-N-S-) during cycling. A clear understanding of this chemical interaction between sulfur and nitrogen present in the sulfur-infiltrated CFMs is essential for engineering nitrogen containing hosts capable of trapping polysulfides effectively. Understanding reported here will help develop novel materials that could achieve the high specific energy densities characteristic to Li – S batteries.

Key words: Non – carbonized sulfate CFM; Li-S battery; Polysulfide encapsulation

4.2 Introduction

Rapid progress in the development of next-generation electric vehicles (EVs) and hybrid EVs (HEVs) are largely limited by the saturated energy storage capacity of existing Lithium-ion Batteries (LIBs). Commercial LIBs as is ubiquitously known store energy by reversibly intercalating lithium ions from a layered oxide cathode into a graphite anode exhibiting an energy density of 400 Wh/kg[75, 187], which is less than half of the current EV energy requirements[188, 189]. Research focused into developing new battery chemistries that can bypass the limitations of current LIBs has led to the identification and subsequent development of lithium-sulfur batteries (LSBs) as a promising technology. LSBs work based on a non-insertion type crystallographic system presenting a two-electron redox reaction of one sulfur atom with two lithium ions, enabling the system to exhibit a high theoretical capacity and specific energy of 1675 mAh/g[190] and 2600 Wh/g[191], respectively. In addition, elemental sulfur offers additional advantages of low cost[192], natural abundance[14], and environmental compatibility[193]. Such benefits render the LSB to be a strong candidate for next-generation energy storage devices used for transportation and grid storage.

Despite the above-mentioned advantages, LSBs face several challenged that need to be addressed which include poor cyclability[194], low electrochemical utilization[195], inferior shelf-life[35], and serious issues of self-discharge[196]. These challenges arise primarily from the reaction of sulfur with lithium at the sulfur cathode and the successive changes in the physiochemical properties of the active materials and the electrolyte. Sulfur, as an electrode material has poor electrical conductivity ($\sim\times10^{-15}$ S/m)[197] greatly limiting the utilization as an active material at the cathode, hence resulting in low electrochemical utilization[198]. In addition, sulfur undergoes significant volume expansion (80%)[117] during electrochemical discharge-charge process that

eventually leads to cracking and delamination of the cathode resulting in poor cyclability[199]. Sulfur reacts with lithium ions to form a series of polysulfide intermediates (Li_2S_x, x = 1-8) during the discharge cycle. These polysulfides, especially the species characterized by longer chain lengths are highly soluble in the organic liquid electrolytes used in LSBs[200]. This solubility of polysulfides is undesirable and results in uncontrolled leaching of active sulfur from the sulfur cathode leading to crossover of the dissolved polysulfides towards the anode adding to the electrochemical impedance, ensuing polarization and finally, lowering the capacity and stability[180]. The deposition of Li_2S and resulting polysulfides on the anode surface can impede the reversible charge transfer, thus limiting the overall capacity and power density[201, 202]. Polysulfide diffusion continues, even as the cell rests resulting in significant self-discharge contributing to poor shelf-life that may not even last a single day[196].

To overcome these issues, significant amount of research has been focused on the design and engineering of sulfur cathodes. The sulfur cathodes have shown significant improvement in electrochemical performance by the use of: a) porous and functionalized conducting sulfur host[203-205], b) additives to optimize the electrolyte properties[206, 207], c) modification of current collector architecture[208, 209] and d) replacing the electrolyte/separator complex with a gel/composite/solid polymer electrolyte[210-213]. By implementation of these techniques, there has been reports of satisfactory improvements achieved in cell performance with stable capacities[214-218], albeit attaining the theoretical capacity of sulfur discussed above still remains elusive and largely impractical to achieve.

Of all the above-mentioned strategies, the most effective and widely applied strategy is the impregnation of sulfur into a high surface area, electrical conductive carbon host[219]. Use of conventional mesoporous[43, 44, 54] and microporous[220] carbonaceous materials with high surface

area[28, 47] and larger pore volume[43] has demonstrated ability to hold large amounts of sulfur. However, the pores of these carbonaceous materials are subject to clogging very easily after sulfur infiltration limiting the penetration of electrolyte, thus consequently reducing lithium ion diffusion, and eventually leading to poor cycling performance[221-223]. Carbon Nano Tube (CNT) and graphene forms an open pore structure and have been found to be effective due to their high surface area[224] and electrical conductivity[118]. However, all these porous architectures exhibit a highly disordered[26] and non-tunable[16] porous structure which hinders complete prevention of polysulfide dissolution. Due to their highly tunable and ordered porous structure, Metal Organic Frameworks (MOFs) have emerged as promising precursors for preparation of porous carbon electrode hosts[46]. MOFs are well designed assemblies of metal nodes coordinated to organic ligand linkers to form a one-, two- or three-dimensional structures. Hierarchical porous carbon templates derived from MOFs have been used as sulfur hosts in LSBs with considerable improvement in battery performance[46, 220, 225]. Despite the highly-tuned porous structure of these hosts derived from MOFs, they are inefficient in their ability to prevent the dissolution of polysulfide completely, primarily due to a lack of chemical interaction between the host and the resultant polysulfides.

Recently, the use of non-carbonized MOFs as sulfur immobilizing hosts in LSBs has attracted more interest[134, 137, 214]. Compared to traditional porous carbon structures, the metal nodes of the MOFs forms Lewis acidic sites and the functional groups from the organic moieties link to the Lewis basic sites serving as effective binding sites for the lithium polysulfides and strongly confining them within the MOFs, especially those nano-sized porous framework complexes with rich cage-like structures, offering a platform for scientists to design materials for effectively restraining the dissolution and diffusion of polysulfides at the molecular level. Reports on using MOF as sulfur hosts has taken advantage of the Lewis acid-base interaction of

polysulfides with the binding functional sites[134, 137, 226]. However, all these work on using non-carbonized MOFs reporting on the use of carboxylic acid (-CO_3-) functionalized organic linkers, and the corresponding electrochemical cycling plots show a significant drop in capacity during the first few cycles. For example, Wang et al[134] used HKUST-1 MOF derived from benzene-1,3,5-tricarboxylic acid linkers as sulfur hosts in LSBs. The MOFs showed an initial capacity of ~1500 mAh/g which quickly faded to ~500 mAh/g in the first 25 cycles. In order to explain this drop in capacity, we in our previous publication, Shanthi et al[29] used XPS to analyze the chemical nature of the MOF-5 electrodes after electrochemical cycling and discovered irreversible chemical interaction of -CO_3- groups from the MOFs with sulfur to form -SO_4- moieties, rendering the MOFs electrochemically unstable. MOFs generated with presence of -SO_4- groups could be a possible solution to this issue. Accordingly, in this manuscript we have synthesized new chemically complexed framework materials (CFM) utilizing sulfate containing precursors.

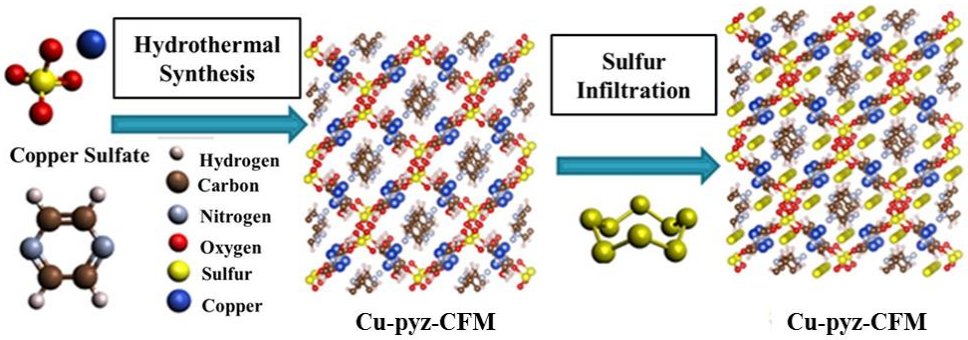

Figure 4-1 Scheme of the synthesis of Cu-pyz-CFM and sulfur infiltration.

Copper-sulfate-pyrazine CFM (Cu-pyz-CFM)[227] and copper-sulfate-bipyridine-CFM (Cu-bpy-CFM)[228] are two such CFMs generated containing the -SO_4 groups and were studied as sulfur hosts in the present study for the first time. The CFMs were synthesized using simple

hydrothermal techniques followed by sulfur infiltration under vacuum (Figure 4-1). The cathodes made from these sulfur infiltrated CFMs were tested for Li – S batteries. The S-CFMs upon testing, exhibits an initial capacity of 1626 mAh/g(S-Cu-bpy-CFM) and 1565 mAh/g (S-Cu-pyz-CFM) and stable capacity of >1000 mAh/g after 150 cycles. A loss in capacity is albeit observed during the initial stages of cycling warranting further studies to be conducted that will help in understanding the underlying mechanisms involved in the cycling process. In the present study therefore, the cycling performance and the reasons contributing to the initial capacity loss along with the mechanisms responsible for the polysulfide dissolution was studied using XPS spectroscopy. The scientific findings from this study will help in not only designing but also developing new techniques to further enhance the cycling capacity as well as prevent the dissolution of polysulfides in Li-S battery cathodes.

4.3 Experimental

4.3.1 Materials

Copper(II) sulfate pentahydrate ($CuSO_4.5H_2O$, ≥98.0%, Sigma Aldrich), pyrazine (pyz, $C_4H_4N_2$, ≥99%, Sigma Aldrich), 4,4'-bipyridine (4,4'-bpy, $C_{10}H_8N_2$, ≥98.0%, Alfa Aesar), L-aspartic acid (L-asp, $C_4H_7NO_4$, ≥98%, Sigma Aldrich), benzoic acid (C_6H_5COOH, ≥99.5%, Sigma Aldrich) and sulfur (S, ≥99.5%, Sigma Aldrich) were the reagents used in the chemical synthesis of the CFMs, and all were used without further purification.

4.3.2 Synthesis of Cu-bpy-CFM

The Cu-bpy-CFM ($Cu_2(4,4'\text{-bpy})_2SO_4$) was synthesized following a previous report by Shi et al[228]. 4.6 mmol (1.153 g) $CuSO_4.5H_2O$, 6.6 mmol (1.030 g) 4,4'-bpy and 5.9 mmol (0.0787 g) L-asp were mixed in 160 ml of DI (deionized) water. The mixture was transferred to a microwave-assisted hydrothermal reactor and heated at 120°C for 24 h. After the reaction, greenish yellow crystals obtained was filtered and washed with DI (deionized) water repeatedly before air-drying under ambient conditions.

4.3.3 Synthesis of Cu-pyz-CFM

The Cu-pyz-CFM ($Cu_2(pyz)_2(SO_4)$) was synthesized per earlier report by Amo-Ochoa et al[227]. A precursor mixture of 6.264 mmol (1.564 g) $CuSO_4.5H_2O$, 6.264 mmol (0.502 g) pyz and 6.264 mmol (0.762 g) C_6H_5COOH were mixed in 30 ml deionized water. The reaction mixture was heated at 180°C for 12 h in a microwave-assisted hydrothermal furnace to obtain red crystals of Cu-pyz-CFM. The resulting red crystals were filtered on a glass frit, washed with warm water, and dried under ambient air.

4.3.4 Sulfur Infiltration into the CFMs

The CFMs were dried under vacuum conditions at 100°C for 12 hours to remove residual solvent and the water of crystallization from the synthesis process. The synthesized CFMs were infiltrated with sulfur under vacuum following the procedure reported by the authors earlier in their previous work on S-Zn-CFM[29]. Sulfur and CFM weights ((70: 30 wt %) were calculated

considering stoichiometry and pore volume data (**see supplementary information**)) were sealed under vacuum into a quartz tube and then heated at 300°C for 24 hrs to prepare the sulfur infiltrated S-Cu-pyz-CFM and S-Cu-bpy-CFM.

4.3.5 Chemical and Electrochemical Characterization

4.3.5.1 Materials Characterization

The crystal structure of the Cu-bpy-CFM and Cu-pyz CFM before and after sulfur infiltration were analyzed using X- ray diffraction (XRD) spectroscopy in a Philips XPERT PRO system that employs CuKα (λ = 0.15406 nm) radiation. The samples were scanned from 10°-90° (2θ) range under a constant current and voltage of 40 mA and 45 kV respectively. The scanning electron microscopy (SEM) images of the CFMs were obtained using a Philips XL30 machine at 10 kV. An attenuated total reflectance Fourier Transform Infrared Spectroscope (ATR-FTIR, Nicolet 6700 Spectrophotometer, Thermo Electron Corporation) which employs a diamond ATR smart orbit was used to obtain the FT-IR spectra of the samples. The FT-IR spectra are collected at a resolution of 1 cm^{-1}, averaging 32 scans between the frequency of 400-4000 cm^{-1}. X-ray Photoelectron Spectroscopy (XPS) analysis of the CFMs and S-CFMs were performed using ESCALAB 250 Xi system (Thermo Scientific). This XPS system consists of a monochromated Al Kα X-ray source and low energy (≤10 eV) argon ions and low-energy electrons beams that provide the charge neutralization. The XPS measurements were carried out at room temperature, under an ultra-high vacuum (UHV) chamber ($<5*10^{-10}$ mBar) and a spot size of 200×200 μm^2. The surface area and pore characteristics of all the CFM samples were analyzed using a Micromeritics ASAP 2020 Physisorption analyzer, using the Brunauer–Emmett–Teller (BET) isotherm generated.

4.3.5.2 Electrochemical Characterization

The S-CFMs were cycled between 1.7-2.6 V (wrt Li+/Li) at a current rate of 0.2 C (~330 mA/g) in a 2025-coin cell using Arbin BT200 battery testing station to evaluate their electrochemical performance. The cathodes for electrochemical evaluation were prepared by manually coating a dispersion of 70 wt% S-CFMs, 20 wt% Acetylene black and 10 wt% PVdF dispersed in N- Methyl Pyrrolodine (NMP) on an aluminum foil, followed by vacuum drying for 12 hours at 60°. All the cathodes that were tested had a uniform sulfur loading of 1.5 – 2 mg cm/cm^2. Accordingly, 2025-coin cells were assembled with the S-CFM coated cathodes as working electrode, a lithium foil as the counter electrode and Celgard 2400 polypropylene (PP) as the separator in an Innovative, Inc. glove box (UHP Argon, <0.1 ppm O_2, H_2O). A 1 M $LiCF_3SO_3$ (Lithium trifluoromethanesulfonate) and 0.2 M $LiNO_3$ dissolved in 50:50 vol% 1,3 dioxolane and 1,2 dimethoxyethane was used as the electrolyte. The Cyclic voltammetry (CV) measurements were performed on the cells in VersaSTAT3, Princeton Applied Research in the voltage range of 1.7 V − 2.6 V at a slow scan rate of 0.1 mV s^{-1}.

4.4 Results and Discussion

XRD analysis was performed on the as synthesized Cu-pyz and Cu-bpy CFMs to confirm their phase purity. Figure 4-2 presents the XRD patterns of synthesized Cu-pyz-CFM and Cu-bpy-CFM compared with that simulated from their crystallographic information file (. cif) data. The crystallographic data files CCDC 636375[227] and CCDC 805893[228] corresponding to Cu-pyz-CFM and Cu-bpy-CFM respectively were extracted from the Cambridge Crystallographic Data Center (CCDC) (https://www.ccdc.cam.ac.uk/structures/) and used to simulate the XRD patterns

of the CFMs using Materials Studio Materials Modelling and Simulation application by Accelrys Inc. The XRD pattern of the experimentally synthesized Cu-bpy-CFM and Cu-pyz-CFM matches well with the simulated patterns, confirming the single crystalline and phase-pure nature of the synthesized CFMs.

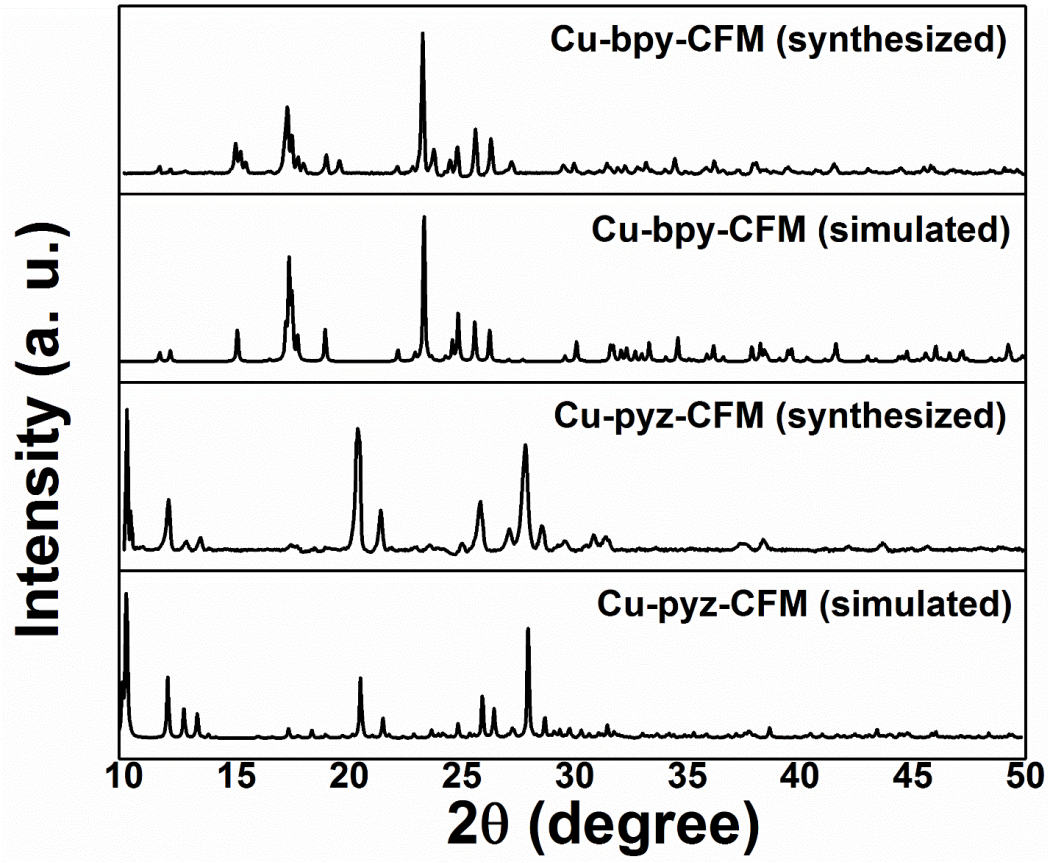

Figure 4-2 XRD patterns of experimentally synthesized Cu-pyz-CFM and Cu-bpy-CFM compared to the simulated XRD patterns.

The synthesized CFMs similar to metal organic framework systems, MOFs, due to their highly ordered structure and fine-tuned porous nature, exhibit high surface area[229, 230]. The surface area of the CFMs is a critical factor in accessing the extent of Lewis acid-base interaction between the CFMs and the polysulfides as well as eventual prevention of polysulfide

dissolution[137, 231, 232]. In addition, data derived from surface are analysis such as pore size and pore volume are important factors that decide the extent of successful infiltration of sulfur into the CFMs. BET surface area analysis was performed on the CFMs to understand their microporous properties. Table 4-1 represents the results of the pore size and surface area analysis and Appendix B Figure 1 represents the adsorption isotherms corresponding to the Cu-bpy-CFM and Cu-pyz-CFM. The Cu-bpy-CFM and Cu-pyz-CFM exhibit a high BET surface area of ~290.20 m^2/g and ~215.31 m^2/g, respectively. These values are typical of porous hosts used in Li-S battery[43, 214, 220, 223], however the CFMs synthesized herein have the additional advantage of exhibiting strong Lewis acid-base interaction characteristics. In addition, these CFMs have a very small pore size of ~2.4-2.9 nm which is in accordance with the values reported in literature for nanoporous MOFs[233-236]. This nano-sized pore of the CFMs is expected to potentially aid in trapping and preventing the polysulfide species formed from dissolving into the electrolyte.

Table 4-1 Results of the BET surface and pore analysis of Cu-bpy-CFM and Cu-pyz-CFM. (Each datum is an average of three experiments conducted on three independent batches of synthesized Cu-bpy-CFM and Cu-pyz-CFM).

	BET Surface Area (m^2/g)	Langmuir Surface Area (m^2/g)	Total Pore Volume (cm^3/g)	Adsorption average pore width (nm)
Cu-bpy-CFM	290 ± 12	471 ± 22	0.31 ± 0.02	2.94 ± 0.22
Cu-pyz-CFM	215 ± 14	344 ± 34	0.32 ± 0.01	2.43 ± 0.18

Sulfur was infiltrated into the CFMs using a vapor phase infiltration process[237]. To confirm the nanoporous characteristic of the CFMs and the presence of crystalline sulfur inside the CFMs, TEM analysis was conducted on the Cu-bpy-CFM and Cu-pyz-CFM following

infiltration of sulfur. High and low resolution TEM micrographs of the CFMs are shown in Figure 4-3. The low resolution TEM images of the CFMs (Figure 4-3**a&c**) clearly show islands of sulfur generated inside the Cu-bpy-CFM and Cu-pyz-CFM crystals.

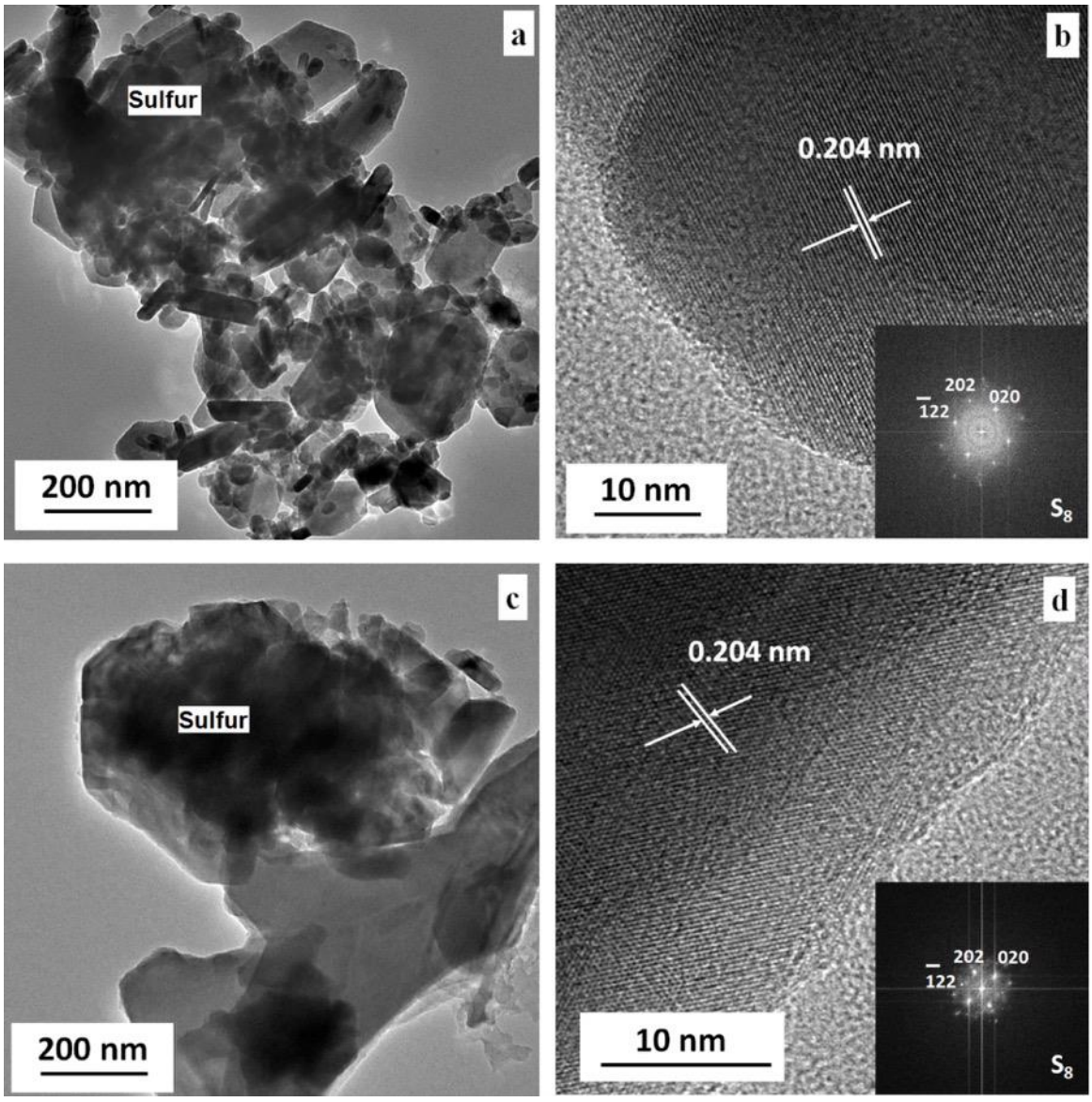

Figure 4-3 TEM images of S-Cu-bpy-CFM (a & b) at two different magnifications along with the corresponding SAED pattern (Figure 4-3b inset); TEM images of S-Cu-pyz-CFM (c&d) at two different magnifications along with the corresponding SAED pattern (Figure 4-3d inset).

The high-resolution images (Figure 4-3b&d), on the other hand, additionally clearly shows the fringe patterns with a d-spacing of 0.204nm corresponding to crystalline sulfur[237] confirming the infiltration of sulfur into the two CFM structures. In addition, the SAED pattern of the sulfur infiltrated CFMs (inset of Figure 4-3b&d) also shows diffraction pattern corresponding to crystalline sulfur planes of [122], [202] and [020][238]. The synthesized CFMs were imaged using SEM while the sulfur infiltrated CFMs were also analyzed using SEM and EDS, and the results indicating the presence of sulfur validating the results of the TEM analyses presented above are shown in Appendix B Figure 2 and Appendix B Table 1.The TEM and BET analyses presented above indicate that the sulfur infiltrated is likely present within the nanopores of the synthesized CFM. However, the presence of sulfur within and around the nanopores of the synthesized CFM cannot be discounted. The Lewis acid-base interactions generated indeed serve to preserve the electrochemical activity of the infiltrated sulfur as indicated by the electrochemical results discussed in the sections to follow.

FT-IR analysis was performed on the CFMs after sulfur infiltration to understand the effect of the infiltration process and the nature of chemical bonding in the CFMs before and after sulfur infiltration. The comparison of the FT-IR spectra of Cu-bpy-CFM and Cu-pyz-CFM before and after sulfur infiltration is shown in Figure 4-4. The FT-IR spectra of both the CFMs after sulfur infiltration retained all the peaks observed before sulfur infiltration confirming the chemical stability of the CFMs after the sulfur infiltration process. The CFMs show peaks at 1479.23 cm^{-1} (-C-C- stretching vibrations[239]), 1411.91 cm^{-1} (-C-H- bending vibrations[240]), 809.09 cm^{-1} (-C-C- stretching and coupled -C-H- deformation[241]), 1036.28 cm^{-1} (-C-H- bending in ring plane[242]) and 809.209 cm^{-1}, (-C-C- asymmetric stretching band[243]).

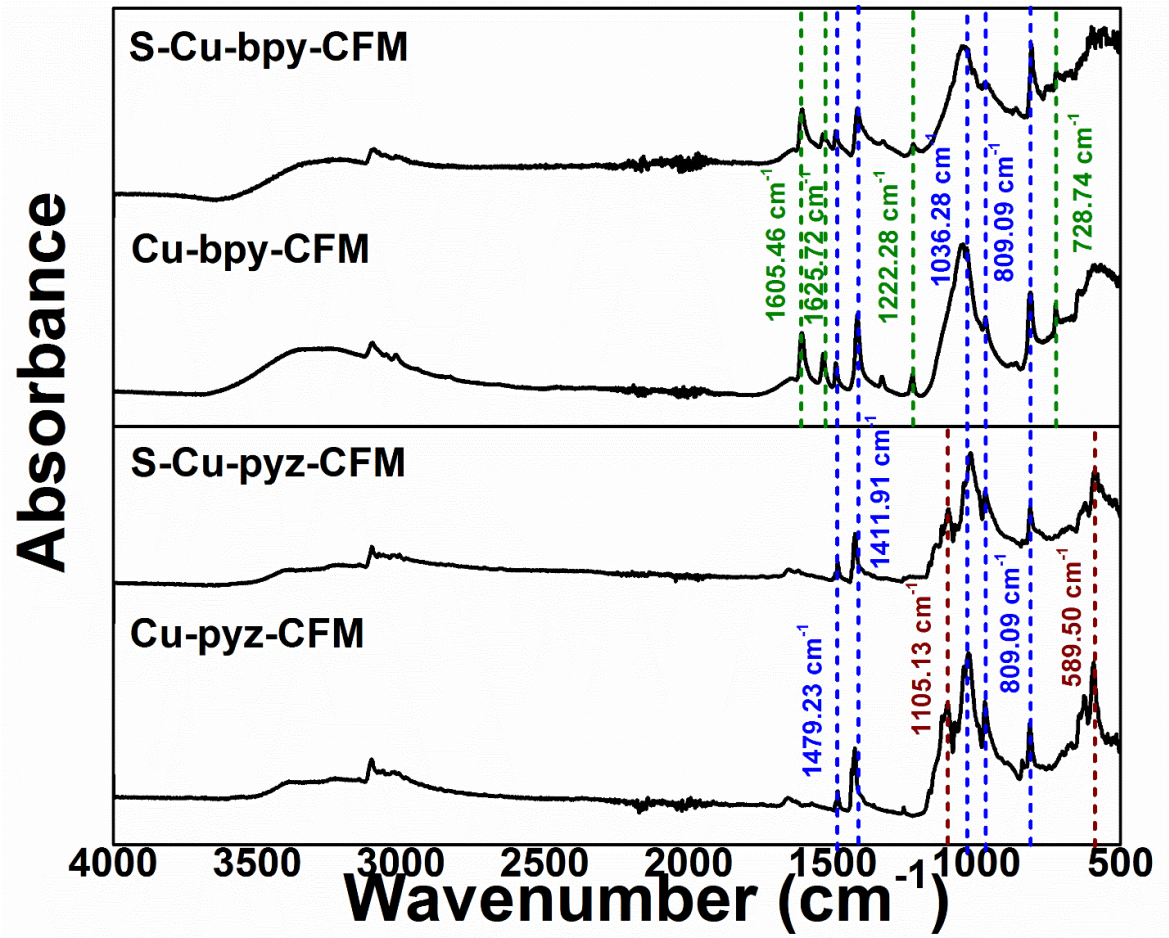

Figure 4-4 FT-IR comparison of Cu-pyz-CFM and Cu-bpy-CFM before and after sulfur infiltration process.

In addition to the common peaks, the Cu-bpy-CFM showed FT-IR peaks at 1605.46 cm^{-1}, 1625.72 cm^{-1}, 1222.28 cm^{-1} and 728.74 cm^{-1} corresponding to -C-O- stretching vibration[244], H-bonds involving -C-O- groups[245], symmetric stretching of -C-N-[246] and out of plane -C–H-deformations[247] respectively. On the other hand, the Cu-bpy-CFM exhibited peaks at 1105.13 cm-1 and 589.50 cm^{-1} arising from the -C-O-stretching[248] and -C-N-C- vibrations[249] respectively. The absence of any anomalous peaks in the FT-IR spectra validates the chemical stability of the CFMs after sulfur infiltration.

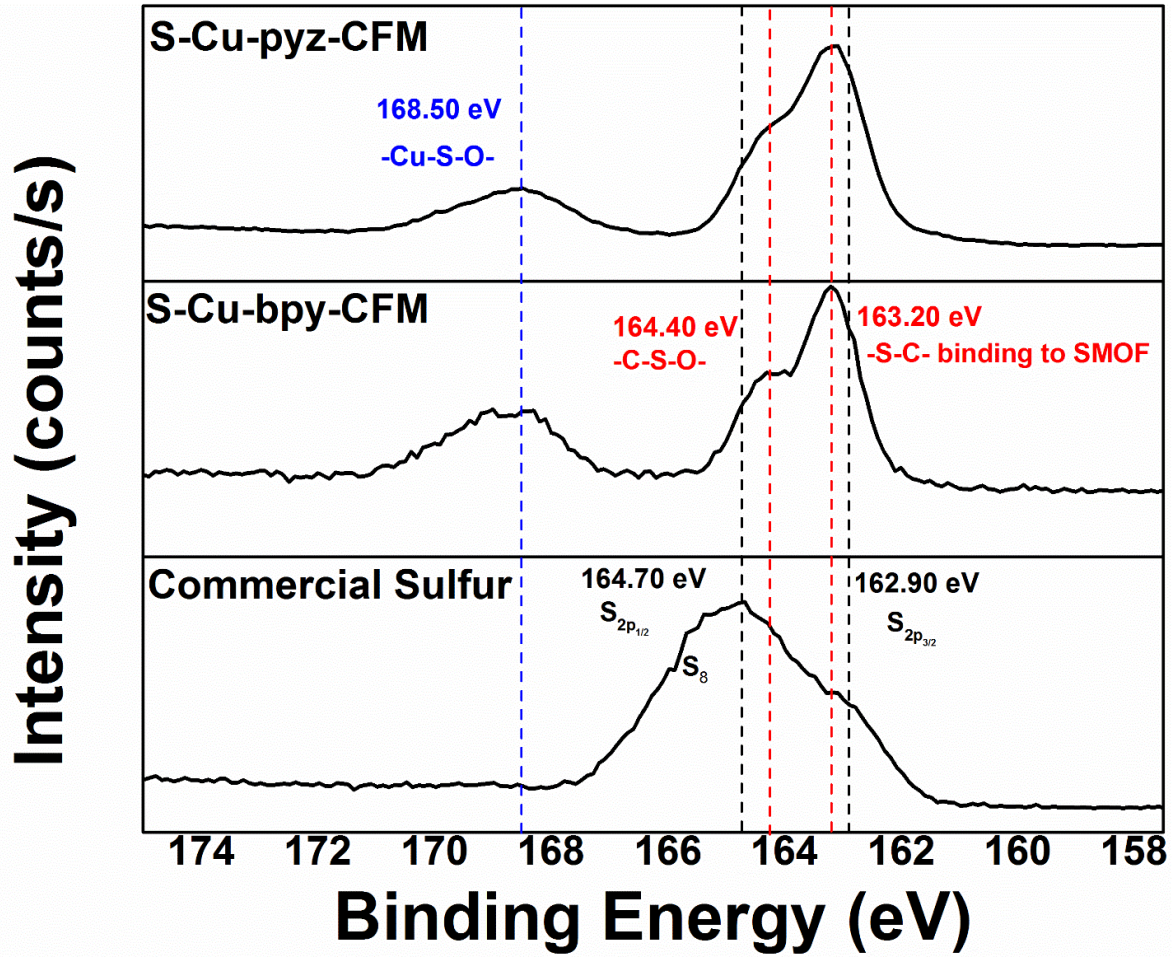

Figure 4-5 XPS S2p spectra of Commercial Sulfur, S-Cu-bpy-CFM and Cu-pyz-CFM.

TEM and SEM analysis of the S-Cu-bpy-CFM and S-Cu-pyz-CFM discussed above shows the presence of crystalline sulfur inside the CFMs. The nature of sulfur binding was analyzed using XPS spectroscopy, Figure 4-5 shows the S2p spectra of commercial sulfur compared with that of S-Cu-bpy-CFM and S-Cu-pyz-CFM. Commercial sulfur exhibits $S2p_{1/2}$ and $S2p_{3/2}$ peak at 164.70 eV[161] and 162.9 eV[160], respectively.

However, the XPS spectra of the S-Cu-bpy-CFM and S-Cu-pyz-CFM shows a shift in the S2p peaks which upon carful comparison with literature confirms the binding of sulfur to the carbon backbone of the CFM. Accordingly, the peaks at 164.40 eV and 163.20 eV corresponds

to –(C-S-O)–[250] binding and –(S-C)–[170, 251] binding respectively. The XPS analysis confirms the presence of a chemical binding between sulfur and carbon which attribute to the likely binding and prevention of polysulfide dissolution. The absence of S2p at 164.7 eV in the XPS spectra collected on both, the Cu-bpy-CFM and Cu-pyz-CFM confirms the absence of free sulfur S_8 in the synthesized CFMs and hence, confirm the complete binding of the infiltrated sulfur to carbon backbone in the synthesized CFM.

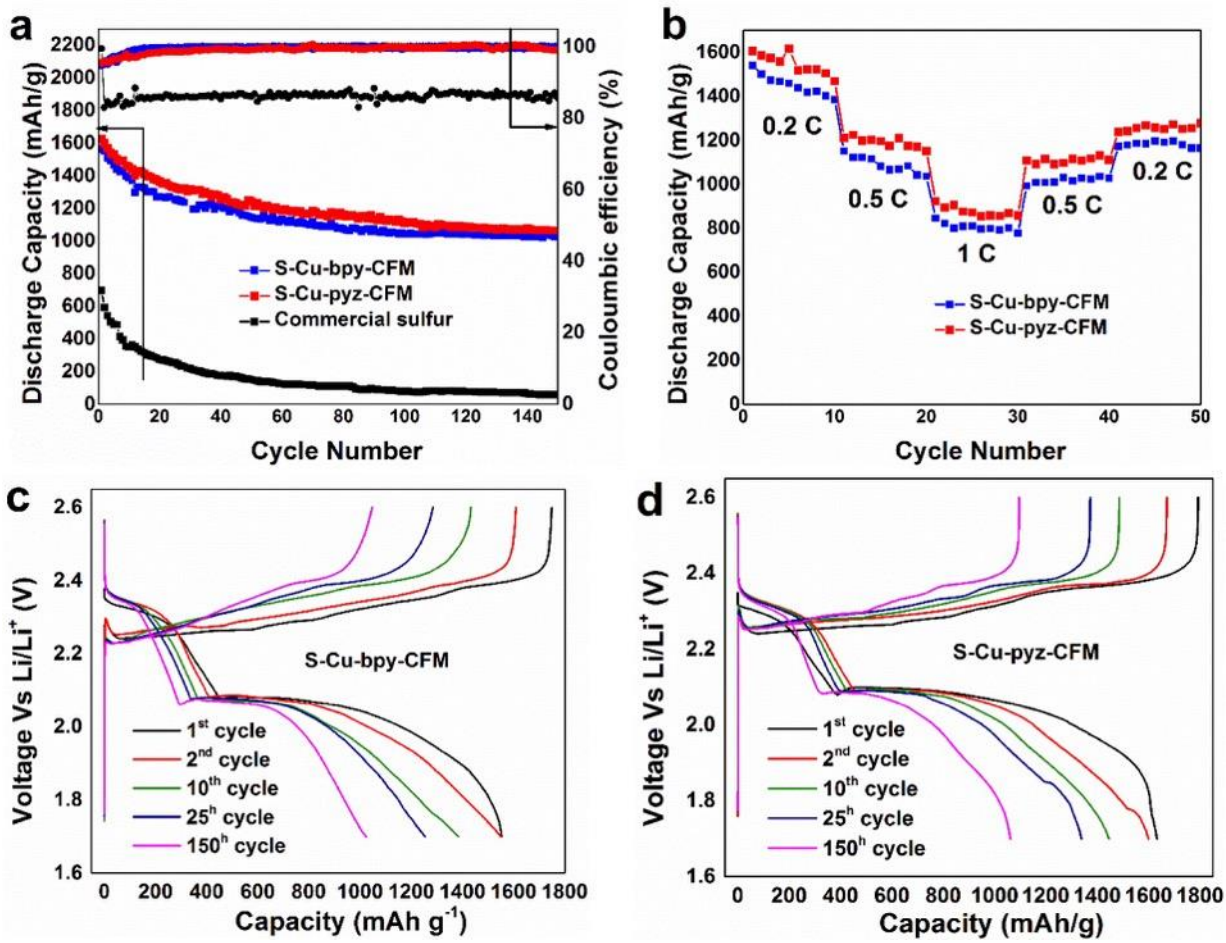

Figure 4-6 a) Cycling performance of S-Cu-bpy-CFM and S-Cu-pyz-CFM cycled at 0.2C rate, b) rate capability plot of S-Cu-bpy-CFM and S-Cu-pyz-CFM, c) charge-discharge plot of S-Cu-bpy-CFM and d) charge-discharge plot of S-Cu-pyz-CFM.

The effect of chemical binding between the CFMs and sulfur on the electrochemical performance of the S-CFMs was further studied by electrochemically cycling the S-Cu-bpy-CFM and S-Cu-pyz-CFM. Figure 4-6a represents the results of the electrochemical cycling experiments and Figure 4-6b the rate capability experiments of S-Cu-bpy-CFM and S-Cu-pyz-CFM (The cycling and rate capability experiments were performed on three batches of sulfur infiltrated S-Cu-bpy-CFM and S-Cu-pyz-CFM samples prepared independently from three batches of CFM samples. The difference in capacity observed in all the three runs were determined to be within ±5%. Extended cycling of the S-Cu-bpy-CFM and S-Cu-pyz-CFM for 200 cycles are shown in Appendix B Figure 4). The S-Cu-bpy-CFM shows an initial discharge capacity of 1565 mAh/g and stabilizes to a discharge capacity of 975 mAh/g after 200 cycles (fade rate of 0.19%/ cycle). The S-Cu-pyz-CFM also shows a high initial discharge capacity of 1626 mAh/g and a stable 1020 mAh/g discharge capacity after 200 cycles (fade-rate of 0.18%/cycle). Both, the S-Cu-bpy-CFM and S-Cu-pyz-CFM show good rate capability as seen from Figure 4-6b. This result is a significant improvement in performance as compared to the commercial sulfur cathodes that show an initial capacity of 697 mAh/g which rapidly fades down to 57 mAh/g by the end of 150 charge-discharge cycles. Appendix B Table 3 represents a comparison of the performance of all the non-carbonized MOF-based cathode systems reported in the literature thus far. The current work on S-Cu-bpy-CFM and S-Cu-pyz-CFM system has the highest sulfur contents (49 wt%) in the cathode next to that reported by Zhao et al[252] in their work reported on MIL-101 (58.8% wt) and Zheng et al[137] on using Ni-MOF DUT-23 (60 wt%). The S-Cu-bpy-CFM and S-Cu-pyz-CFM system used in the present work reported herein also shows a very high stable discharge capacity of 975 mAh/g and 1020 mAh/g, which is the highest value reported in literature thus far to the best of our knowledge. The cycling stability of the S-Cu-bpy-CFM (0.19%/cycle) and S-Cu-pyz-CFM (0.18%/cycle) is also one of the lowest values

reported in literature so far. However, it is important to note that both the CFMs (S-Cu-bpy-CFM and S-Cu-pyz-CFM) exhibit a fade of ~35% of the initial discharge capacity during the initial ~25 cycles followed by a stable cycling performance. To understand better and determine the exact reasons contributing to this fade in capacity, comprehensive XPS and FT-IR analyses were performed on the electrodes and the separators before and after cycling. The results of the XPS analysis conducted on the separators clearly indicates absence of polysulfides on the separators (Figure 4-7) thereby suggesting possible other reasons responsible for this observed initial loss in capacity. The separators following electrochemical cycling appeared identical in color to the pristine separators before cycling visually also confirming the absence of polysulfides on the separators. The results of the XPS and FT-IR analysis on the electrodes will be explained in detail in later sections of the paper.

To further understand the electrochemical charge storage behavior of the S-CFMs and to identify the source of initial irreversible capacity loss, the charge-discharge profiles of the S-CFMs were evaluated and are shown in Figure 4-6c (S-Cu-bpy-CFM) and Figure 4-6d (S-Cu-pyz-CFM). Figure 4-6c&d corresponds to the specific capacity plots of 1^{st}, 2^{nd}, 10^{th}, 25^{th} and 150^{th} charge – discharge profiles of S-Cu-bpy-CFM and S-Cu-pyz-CFM, respectively at 0.2C rate. The discharge profiles of both the CFMs show a smaller plateau at 2.35 V[199] corresponding to the formation of the higher order polysulfide during the initial stages of lithiation Li_2S_n (n = 4-8) and a wider plateau at 2.05 V[253] that in turn corresponds to the formation of lower order lithium sulfides Li_2S_n (n<4). Similar plateaus at 2.4 V and 2.25 V are observed in the charge cycles corresponding to the delithiation of Li_2S to form the lower order polysulfides and corresponding higher order polysulfides, respectively ultimately resulting in the formation of sulfur.

The cycling stability of the CFMs could be attributed to the nanoporous nature of their pores (Table 4-1) and chemical binding of sulfur to the carbon moieties of the CFMs as is evident from the XPS analysis Figure 4-5. Though the S-CFMs exhibit excellent initial discharge capacity and good cycling stability, an initial loss of capacity is observed in the first 25 cycles. Similar kind of loss in capacity has been observed in the literature and is usually attributed to polysulfide dissolution into the electrolyte[30, 49, 254]. However, the stable cycling performance observed after ~25 cycles indicates the possibility of sulfur confinement by binding to the CFMs. This result implies that the origin of initial capacity loss needs to be studied in detail using XPS and FT-IR spectroscopy to understand the effectiveness of the Cu-bpy-CFM and Cu-pyz-CFM serving as effective polysulfide trapping agents in Li-S batteries. To confirm the polysulfide trapping ability of the CFMs via Lewis acid-base interactions, the separators from the S-CFMs were analyzed using XPS spectroscopy after 150 charge-discharge cycles. Figure 4-7 represents the S2p spectra of separators obtained from the cells cycled against commercial sulfur electrode compared with separators from the S-Cu-bpy-CFM and S-Cu-pyz-CFM electrodes after cycling for 150 cycles at 0.2 C rate. The XPS spectra of the separator cycled against cathodes made from commercial sulfur (Figure 4-7) shows S2p peaks at 168.90 eV, that corresponds to the $CF_3SO_3^-$ group from the electrolyte, along with peaks at 166.72 eV and 163.08 eV, clearly corresponding to the presence of lower and higher order polysulfides, respectively[80, 171-173, 255]. This result confirms the ubiquitous and characteristic typical phenomenon of polysulfide dissolution observed in commercial sulfur cathodes during electrochemical charge-discharge cycles.

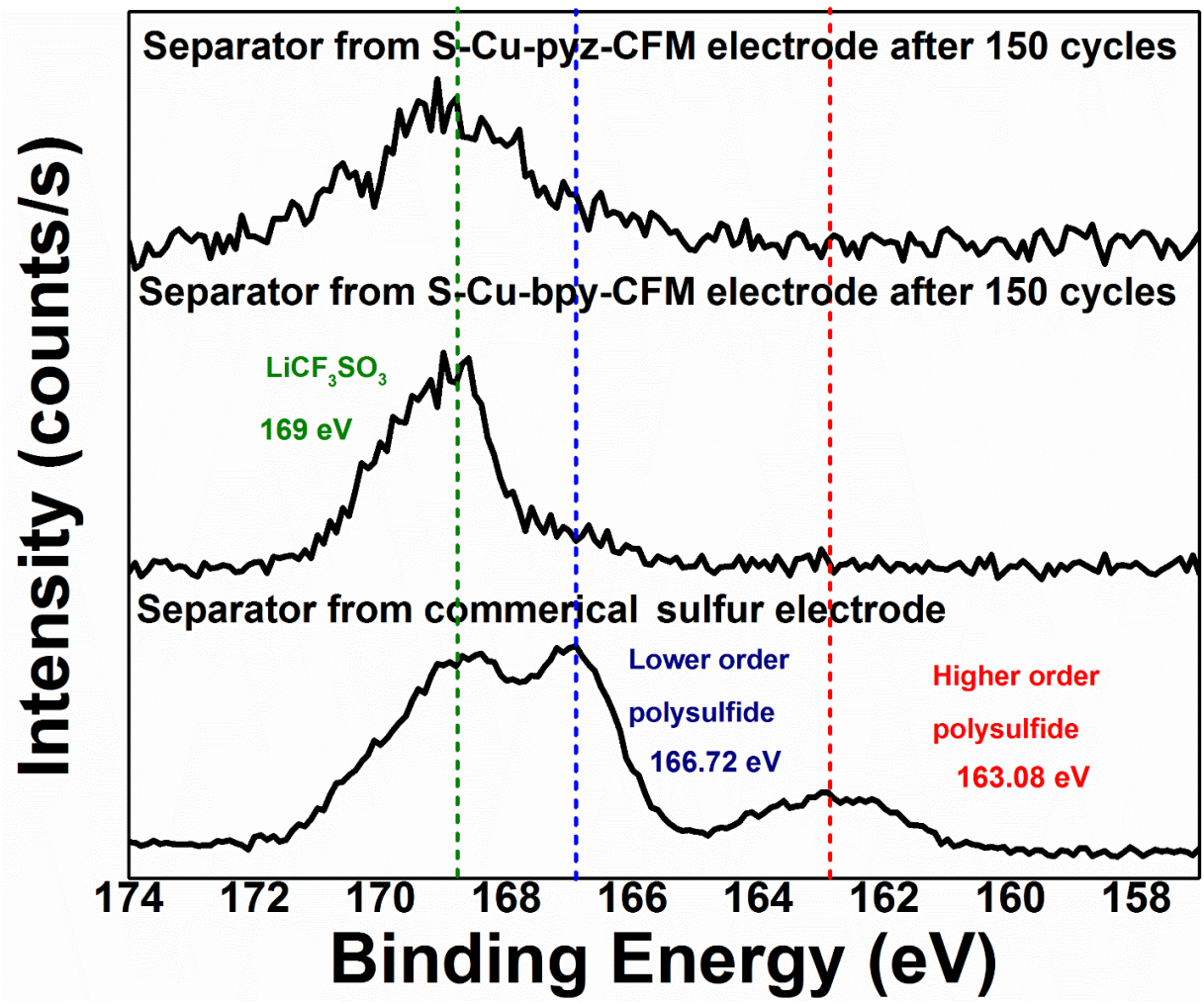

Figure 4-7 XPS S2p binding energy profile of 6a) separators of commercial sulfur electrode and 6b) S-Cu-bpy-CFM and 6c) S-Cu-pyz-CFM (after 150 cycles at 0.2 C rate).

On the other hand, the separators corresponding to S-Cu-bpy-CFM and S-Cu-pyz-CFM after 150 cycles shows only one S2p peak at 168.90 eV corresponding to the sulfur binding in $LiCF_3SO_3$ salt used in the electrolyte[170]. The absence of peaks corresponding to the polysulfides in the S-CFM separators post cycling indicates the complete entrainment of the polysulfide species by the CFMs,. This can can be attributed to the binding of the polysulfides due to the Lewis acid-base interactions between the synthesized CFMs and sulfur, as well as the entrapment effect provided by the nanoporous nature of the CFMs as is evident from the BET analysis (Table 4-1). There are

also reports on the use of carbonaceous porous matrix[27, 28, 43, 44, 54] including conventional carbonate based MOFs[134, 137] as sulfur hosts that have shown improvement in electrochemical cycling. However, it should be noted that complete prevention of polysulfide dissolution has not been reported thus far, except for our previous work on the use of Zn-MOF-5[29] as sulfur hosts in Li-S battery. In our previous work we unequivocally demonstrated total prevention of polysulfide dissolution, which was further confirmed by XPS spectroscopy using a sulfur infiltrated carbonate-based MOF, namely Zn-MOF-5. However, despite being successful in trapping the polysulfide species, the Zn-MOF-5 was unstable under electrochemical charge-discharge conditions exhibiting a large capacity fade particularly during the first ~10 cycles attributed to consumption of sulfur leading to sulfate species formation as indicated earlier. The total absence of polysulfides confirmed by the XPS analysis conducted on the separators corresponding to S-Cu-bpy-CFM and Cu-pyz-CFM indeed makes them promising hosts for sulfur. However, the initial capacity loss observed during the charge-discharge cycling in these CFMs needs to be understood to effectively engineer these porous materials for further use as electrodes in Li-S battery. The results of these studies are described in the following sections. In order to explain the electrochemical cycling behavior of the CFMs, the electrodes from the Cu-bpy-CFM and Cu-pyz-CFM were further characterized using XPS spectroscopy, both before and after 150 charge-discharge cycles. C1s spectra of the CFM electrodes before and after 150 charge-discharge cycles at 0.2 C-rate is shown in Figure 4-8. Both the CFM electrodes exhibits peaks at 290.40 eV that represents the –(CF_2-CF_2)- group arising from the PVdF binder (289.87 eV)[174], the peak at 286.10 eV corresponds to -(C_6H_4S)- bond[175] arising from the binding of sulfur to the ring carbon atoms and the peak at 284.2 eV[176] corresponding to other ring –(C-S)- bonds.

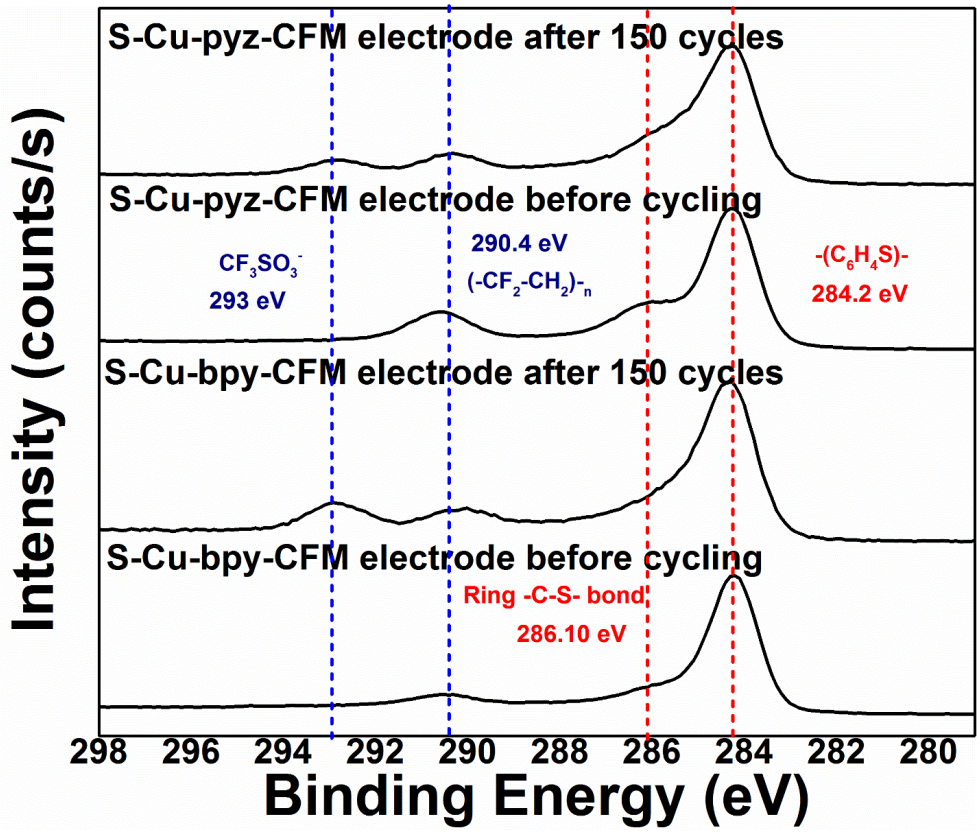

Figure 4-8 XPS C1s spectra of of S-Cu-bpy-CFM and S-Cu-pyz-CFM electrodes before and after 150 cycles at a rate of 0.2 C.

The presence of these C-S peaks confirms the existence of sulfur-carbon binding observed in the S2p spectrum (Figure 4-5) and supports the findings that this chemical linkage between the sulfur and carbon species created during the sulfur infiltration process aids in polysulfide retention within the CFM structures. However, the CFM electrodes after 150 charge-discharge cycles at 0.2 C- rates also show a peak at 293 eV in addition to the above discussed peaks. This peak corresponds to the presence of the $-CF_3SO_3^{-170}$ group originating from the lithium salt $LiCF_3SO_3$ used in the organic electrolyte. These results from the XPS analysis on the electrodes clearly show that there is no observable change in the binding of carbon atoms in the electrode, hence validating the stability of the carbon atoms in the synthesized CFM structures.

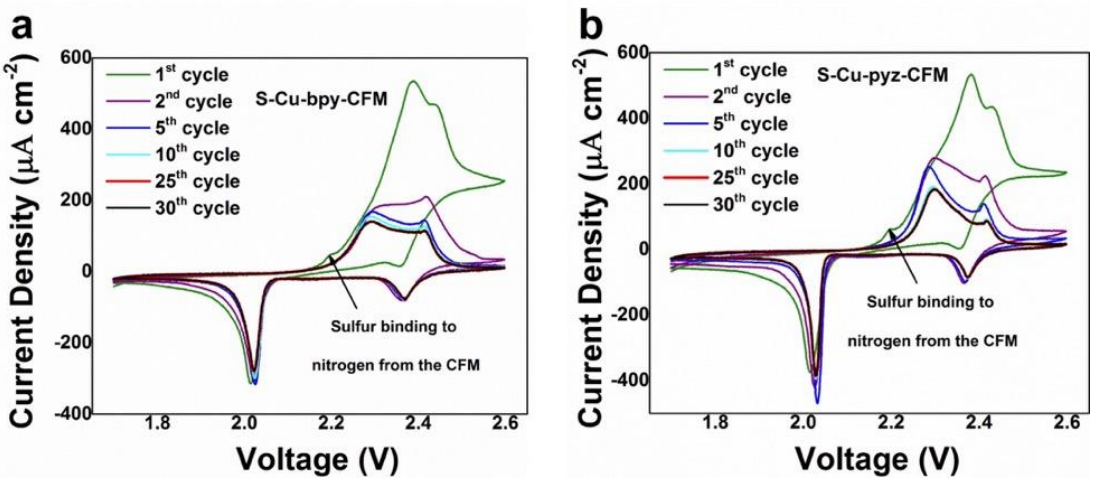

Figure 4-9 Cyclic Voltammograms of (a) S-Cu-bpy-CFM and (b) S-Cu-pyz-CFM at different cycles performed at 0.05mV s-1 scan rate.

Cyclic voltammetry measurements were made on the S-Cu-bpy-CFM and S-Cu-pyz-CFM electrodes to provide a reasoning for the initial capacity loss. Figure 4-9 a&b show the CV of S-Cu-bpy-CFM and S-Cu-pyz-CFM electrode performed at 0.05 mV/s scan rate. A change in the height of the peaks was observed in the CVs of both, the S-Cu-bpy-CFM and the S-Cu-pyz CFM electrodes during the initial 25 charge-discharge cycles. This change in height could be related to polarization in the electrodes due to the possible insulating nature of the CFM structures and the observed loss in capacity during the first 25 cycles (see Appendix B Table 4 for a tabulated list of the peaks observed in both electrodes). However, the peaks corresponding to the 25th cycle and 30th cycle completely overlap each other indicating that the loss in capacity is limited largely to the first 25 cycles only. The CV profiles show two cathodic peaks at 2.36 V and 2.1 V corresponding to the lithiation of sulfur to form the higher and lower order polysulfides, respectively[256]. The two anodic peaks at 2.38 eV and 2.43 eV correspond to the delithiation of the polysulfides[257] to elemental sulfur and lithium through a series of higher and lower order polysulfides. The CV also shows an additional anodic peak at 2.19 eV, the intensity

of which decreases and eventually disappears after 25th cycle. This peak is however, not observed in the cathodic scan indicating the irreversible nature of the reaction corresponding to this peak. This reaction, if identified could explain the initial irreversible capacity loss during the first 25 cycles.

The third peak at ~2.19 V in the CVs is believed to be arising from the irreversible binding of sulfur to the nitrogen moieties present in the CFMs. N1s scans of the XPS analysis was also collected and analyzed to ascertain if there is any evidence of -N-S- bonds. Figure 4-10 shows the N1s spectra collected on the S-Cu-bpy-CFM and S-Cu-pyz-CFM electrodes before and after 150 charge-discharge cycles. The N1s spectra corresponding to the S-Cu-bpy-CFM and S-Cu-pyz-CFM after 1st, 2nd,10th and 25th cycles are shown in Appendix B Figure 4a&b.

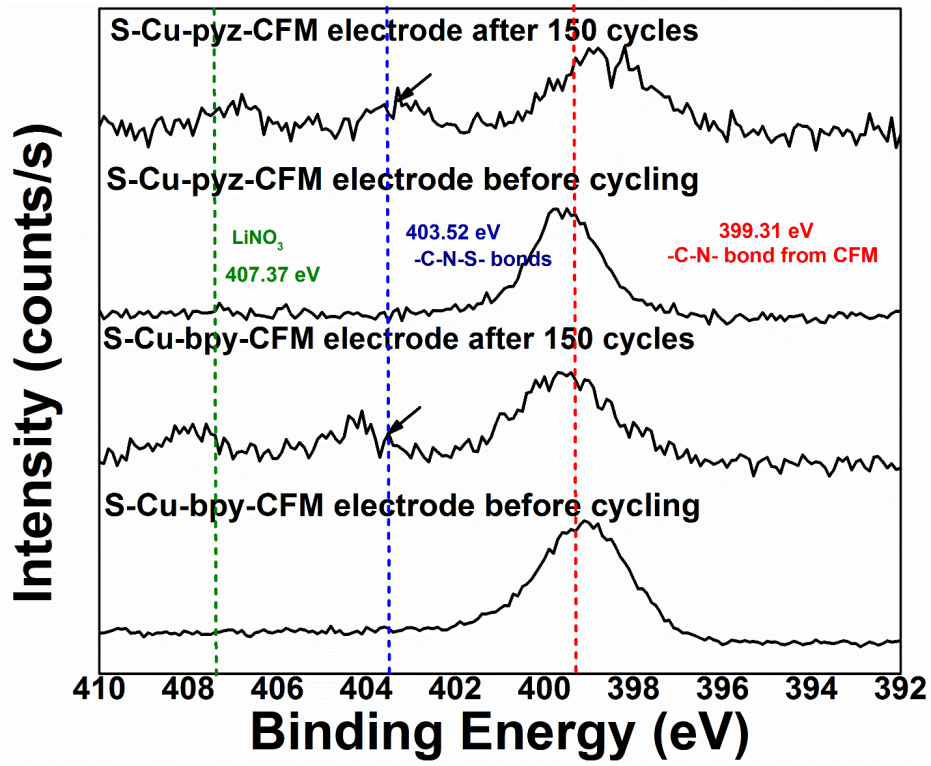

Figure 4-10 N1s spectra of S-Cu-bpy-CFM and S-Cu-pyz-CFM before and after 150 cycles (cycled at 0.2C rate).

The N1s spectra of both S-Cu-bpy-CFM and S-Cu-pyz-CFM show a peak at 399.31 V that corresponds to the binding of carbon to nitrogen arising from the -C-N-[258-260] bonds of pyrazine and bipyridine present in the synthesized CFMs. A peak at 407.37 eV corresponding to $LiNO_3$[261] added to the electrolyte is also observed in the electrodes cycled for 150 cycle and the corresponding electrodes after 1st, 2nd, 10th and 25th cycles (Appendix B Figure 4a&b). In addition to these peaks, the cycled electrodes show a peak at 403.52 eV, analysis of which indicates its origin to the -N-S- bonds[262]. Lalitha et al also observed similar peaks between nitrogen and sulfur while studying ditholate complexes[263]. Occurrence of this peak corresponding to the presence of -N-S- binding confirms our hypothesis and explains the initial loss in capacity to be attributed to the irreversible loss of sulfur caused by binding of the sulfur to nitrogen atoms from the CFM background. Appendix B Figure 4c also shows the presence of the peak at 403.52 eV in both Cu-bpy-CFM electrode and Cu-pyz-CFM electrode after first charge and discharge confirming the irreversible nature of the -N-S- bond and justifies corresponding loss in capacity.

From the results of the XPS analysis, the initial loss in capacity could arise from the irreversible chemical reaction between the sulfur and nitrogen atoms present in the two synthesized CFM structures (originating from the pyrazine and bipyridine sub-units of the synthesized CFMs) rather than polysulfide dissolution. The amount of sulfur that is trapped by this irreversible -S-N- bond formed with the nitrogen in the CFMs on the basis of the initial stoichiometry used for sulfur infiltration into the CFMs indicates that ~10-15 wt% of the sulfur becomes inactive through binding with nitrogen present in the CFMs (**Reactions S1 and S2, and** Appendix B Table 6). This binding results in a ~10-15% loss in capacity during the initial 25 charge-discharge cycles.

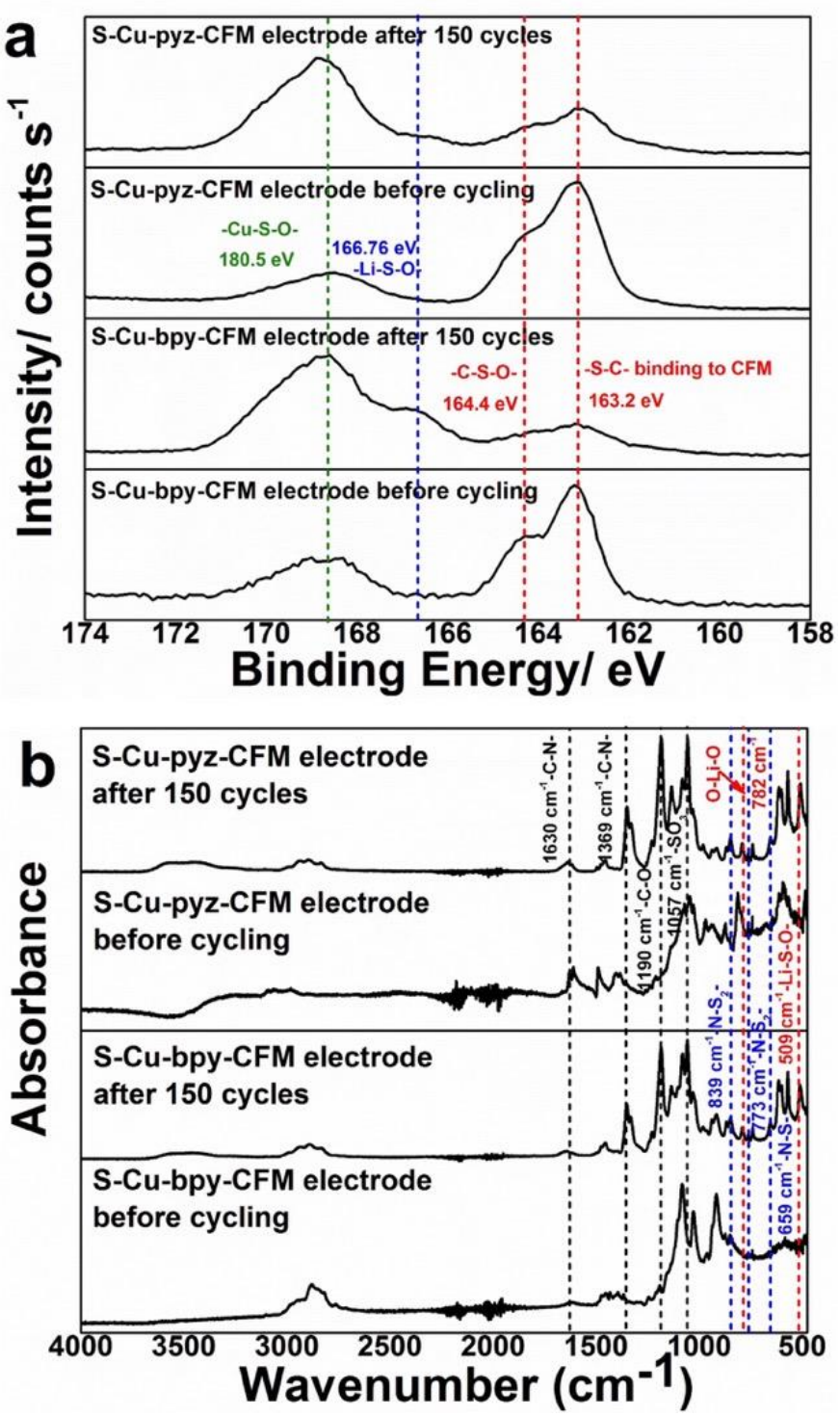

Figure 4-11 (a) S2p spectra of S-Cu-bpy-CFM and S-Cu-pyz-CFM before and after 150 cycles (0.2C rate) and (b) FT-IR spectra of the S-Cu-bpy-CFM and S-Cu-pyz-CFM before and after 150 cycles (0.2C rate).

XPS experiments were accordingly performed on the S-Cu-bpy-CFM and S-Cu-pyz-CFM electrodes before cycling and after the 1st, 2nd, 10th, 25th and 150th cycles. Figure 4-11a represents the XPS S2p spectra collected on the S-Cu-bpy-CFM and S-Cu-pyz-CFM electrodes before and after 150 charge discharge cycles. The S2p spectra of the S-Cu-bpy-CFM and S-Cu-pyz-CFM electrodes after 1st, 2nd, 10th, 25th cycles are shown in Appendix B Figure 5 a&b. The S2p spectra collected on the S-Cu-bpy-CFM and S-Cu-pyz-CFM electrodes before cycling shows peaks at 168.6 eV corresponding to the -Cu-S-O-[264] linkages which is characteristic of the synthesized CFMs. The peaks observed at 163.2 eV and 164.4 eV in the spectra of S-Cu-bpy-CFM and S-Cu-pyz-CFM corresponds to -C-S- bonds[265] and -C-S-O-[170, 266, 267] bonds formed due to the chemical interaction of sulfur with the carbon in the SCFM. The S2p spectra collected on both the CFMs after 150 cycles (Figure 4-11a) (and after the1st, 2nd, 10th and 25th cycles as shown in Appendix B Figure 5a&b) shows all the peaks observed before cycling, along with one additional peak at 166.76 eV corresponding to -Li.S-O-[268, 269]. This peak at 166.76 eV is likely due to the loss of active sulfur from the electrode due to formation of the well-known solid electrolyte interphase (SEI) layer, which could explain the additional ~20% loss in capacity in addition to the ~15% loss due to the formation of the -N-S- bonds. This SEI formed during the initial cycle is expected to stabilize the electrode, hence explaining the absence of a significant change in peak height in the CVs of the S-Cu-bpy-CFM and S-Cu-pyz-CFM (Figure 4-9 a&b) after the 25th cycle. The presence of this peak at 166.76 eV in both, the Cu-bpy-CFM electrode and the Cu-pyz-CFM electrode after the first charge and discharge (Appendix B Figure 5c) cycles confirms the irreversible nature of the SEI formed.

To further confirm the formation of the stable SEI layer in the form of -Li-S-O- compounds, FT-IR analysis was also performed on the S-Cu-bpy-CFM and S-Cu-pyz-CFM electrodes before and after the 1^{st}, 2^{nd}, 10^{th}, 25^{th} and 150^{th} cycles. Figure 4-11b represents the FT-IR spectra collected on the S-Cu-bpy-CFM and S-Cu-pyz-CFM electrodes before and after 150 cycles. The FT-IR spectra collected on the S-Cu-bpy-CFM and S-Cu-pyz-CFM electrodes after the 1^{st}, 2^{nd}, 10^{th}, and 25^{th} cycles are shown in Appendix B Figure 6a&b. The FT-IR spectra collected on the S-Cu-bpy-CFM and S-Cu-pyz-CFM electrodes shows peaks characteristic of the CFMs at 1027 cm^{-1}, 1079 cm^{-1}, 1395 cm^{-1} and 1470 cm^{-1} corresponding to C-H rocking[270], C-C stretching[271], C-N[272] bond stretching and C-H bending vibrations[273] respectively. FT-IR peaks from Figure 4-11a are indexed in Appendix B Table 5. The S-Cu-bpy-CFM and S-Cu-pyz-CFM electrodes after cycling show peaks at 574 cm^{-1} and 1057 cm^{-1} corresponding to CF_2 bending vibrations[274], [275], [276] from the PVdF binder and $-SO_3$ groups from the $LiCF_3SO_3$ salt, respectively[277] . These are in addition to the peaks characteristic of the CFMs. Additionally, the electrodes after cycling shows peaks at 659 cm^{-1}, 773 cm^{-1} and 839 cm^{-1} corresponding to the N-S symmetric stretching[278], N-S_2 asymmetric stretching[278] and N-S_2 stretching vibrations[279] respectively. These peaks arise from the binding of sulfur to nitrogen as demonstrated from the XPS N1s spectra from Figure 4-10. Two additional peaks are observed at 782 cm^{-1} and 509 cm^{-1} that corresponds to O-Li-O stretching[280] and Li-S-O from cationic interaction with $-SO_4$ groups[281] respectively. The occurrence of these peaks corresponding to Li-S-O bonds in the FT-IR spectra and XPS S2p spectra (Figure 4-11a and Appendix B Figure 6a&b) confirms the formation of SEI and subsequent loss of sulfur and ~20% loss in capacity. Appendix B Figure 6c shows the FT-IR spectra collected on the S-Cu-bpy-CFM and S-Cu-pyz-CFM after the 1^{st} charge and 1^{st} discharge. The presence of peaks corresponding to -N-S- bonds and Li-S-O bond in the

FT-IR spectra after the 1st charge and 1st discharge indicates the irreversible nature of N-S bonds and the SEI formed during cycling. The results presented in this study therefore demonstrates the benefits of infiltrating sulfur into the nanoporous, metal sulfate derived pyrazine and bipyridine CFM structures to ensure minimal polysulfide dissolution into the electrode warranting minimal loss in capacity. This is due to the binding of carbon atoms from the CFM backbone with sulfur atoms; resulting in prevention of the formed lithium polysulfide species from leaving the porous CFM matrix. However, it is also distinctly evident that the presence of nitrogen atoms in these two CFM structures contributes to the formation of -N-S- bonds during the initial charge-discharge cycles and SEI formation (Li-S-O), resulting in loss of capacity during the initial stages of cycling and not due to the dissolved polysulfide species. The use of nitrogen-free sulfate/sulfonic CFMs as cathodes in Li – S battery could help in improving the capacity along with cycling stability. Confirmation of the interaction between sulfur and the nitrogen from the CFM structures aids in obtaining a better understanding of the mechanisms involved in the lithiation of sulfur infiltrated into the chemically complexed metal organic framework structures. The results presented in this study thus can further support the design of more efficient polysulfide-entrapping framework structures for achieving high energy density batteries in the Li-S system.

4.5 Conclusions

Metal sulfate containing, nanoporous CFMs (Cu-bpy-CFM and Cu-pyz-CFM) were synthesized using microwave-assisted hydrothermal synthesis, infiltrated with sulfur, and used as cathodes to study their performance in Li-S battery. The S-Cu-bpy-CFM shows an initial

discharge capacity of 1565 mAh/g and stabilizes at a discharge capacity of 975 mAh/g after 200 cycles (**fade rate of 0.19%/ cycle**). The S-Cu-pyz-CFM also shows a high initial discharge capacity of 1626 mAh/g and a stable 1020 mAh/g discharge capacity after 200 cycles (**fade rate of 0.18%/cycle**). These CFMs interacts with polysulfides via Lewis acid-base interactions and thereby effectively restrain the polysulfides from diffusing and dissolving into the electrolyte. In addition, the carbon atoms of the CFMs bind with sulfur during the sulfur infiltration process, further aiding in preventing the polysulfides from dissolving into the electrolyte. XPS analysis of the CFM separators further confirms the absence of polysulfide dissolution. However, the observed loss in initial capacity is due to the irreversible binding of nitrogen from the CFMs to sulfur and SEI formation at the cathode as validated and explained by XPS and FT-IR analyses. This study presented thus provides an understanding of the ability of nitrogen containing porous synthesized chemically complexed metal organic frameworks (CFMs) to prevent polysulfide dissolution. The chemical insight gained from this work could help in employing these CFM systems as effective polysulfide trapping agents in the development of stable high capacity Li-S batteries in the near future.

4.6 Acknowledgements

This research was funded by the U.S. Department of Energy (DE-EE0006825, DE-EE0007797 and DE-EE0008199), the Edward R. Weidlein Chair Professorship Funds, and the Center for Complex Engineered Multifunctional Materials (CCEMM), Swanson School of Engineering at the University of Pittsburgh. The authors acknowledge Dr. Joel Gillespie from the PPG Materials Characterization Laboratory (Department of Chemistry, University of Pittsburgh)

for providing access to the XPS instrumentation. Mr. Louis Wang (Department of Energy, Environmental and Chemical Engineering, Washington University in St. Louis) is also acknowledged for his assistance in conducting experiments during the initial stages of this research. Additionally, Dr. John A Keith and Mr. Karthikeyan Saravanan from the Department of Chemical Engineering, University of Pittsburgh are acknowledged for their help with simulating the XRD patterns collected of the CFMs from the CIF (Crystallographic Information File**)** information.

5.0 Specific Aim 1: Understand the Origin of Irreversible Capacity Loss in Li-S batteries and Address the Mechanisms of Polysulfide Dissolution Using Structurally Distinct Metal Organic Framework (MOF) Based Sulfur Cathodes - (iii) Sulfonic Acid Based Complex Framework Materials (CFM) – New Nanostructured Polysulfide Immobilization Systems for Rechargeable Lithium – Sulfur Battery

The results of the work in this specific aim has been published in the Journal of The Electrochemical Society, 166, A1827-A1835, 2018 (https://doi.org/10.1149/2.0251910jes)

Pavithra M Shanthi[a,c,d], Prashanth J Hanumantha[b], Kuruba Ramalinga[b,c,d], Bharat Gattu[a,c,d], Moni K Datta[b,c,d], Prashant N. Kumta[a, b, c, d,e,*]

[a]Department of Chemical and Petroleum Engineering,
University of Pittsburgh, Pittsburgh, PA 15261 (USA)

[b]Department of Bioengineering,
University of Pittsburgh, Pittsburgh, PA 15261 (USA)

[c]Center for Energy, University of Pittsburgh, Pittsburgh, PA 15261 (USA)

[d]Center for Complex Engineered Multifunctional Materials,
University of Pittsburgh, Pittsburgh, PA 15261 (USA)

[e]Department of Mechanical Engineering and Materials Science,
University of Pittsburgh, Pittsburgh, PA 15261 (USA)

5.1 Synopsis

Lithium−sulfur (Li-S) secondary batteries with sulfur cathodes and theoretical energy density of ~2600 Wh/kg, are promising high energy-density systems for next-generation electric-vehicles (EVs) potentially mitigating the gravimetric and volumetric energy density limitations of existing lithium-ion (Li-ion) batteries. Herein, a chemically synthesized sulfonic acid-based complex framework materials (CFM) termed as (SCFM), was used as sulfur host (S-SCFM) to prevent polysulfide dissolution in Li-S batteries. The S-SCFM based CFM cathodes show an initial capacity of 1190 mAh/g and a capacity of 1044 mAh/g after 100 cycles. In addition, the S-SCFM based CFM exhibited good cycling stability with a minimal fade rate of ~0.0012% per cycle. XPS analysis of the cycled separators with the S-SCFM electrodes shows complete absence of polysulfide species after 100 charge-discharge cycles. It was also identified that the SCFM based CFM chemically binds sulfur via -C-S- linkages thereby exhibiting an affinity for the polysulfide species formed during the charge-discharge cycles. As a result, the SCFM based CFM prevent polysulfide species from dissolving and diffusing into the electrolyte. A thorough understanding of these engineered SCFM based CFM sulfur host in Li-S battery outlined herein will be vital in designing promising sulfur hosts for next generation sulfur cathodes in Li-S batteries.

Key words: Sulfonic Acid CFM; Lithium-Sulfur battery; Polysulfide dissolution; Sulfur-host

5.2 Introduction

The rapid evolution of electric vehicles, combined with the emergence of large scale stationary and portable electronic devices has given rise to an urgent demand for rechargeable batteries with high energy densities and long cycle life and low cost[8, 190]. Owing to their high volumetric[282] and high gravimetric energy densities[283], lithium-ion (Li-ion) batteries are the principal source of power source in portable electronic devices such as cell phones and laptops[284]. However, the energy density (80-170 Wh/kg) and power density (800-200 W/kg)[285] of currently available rechargeable Li-ion batteries are inferior, requiring significant improvements in gravimetric and volumetric performance with adequate cost match to power electric vehicles in order to meet the DOE target of $125/kWh by 2020[286]. Despite much improvement since the commercialization of the Li-ion battery in 1991, the specific capacities of most commonly used layered oxide-based cathodes $LiMO_2$, M=Ni, Co, Mn (~150 mAh/g)[287] and M=Fe (~170 mAh/g)[288] are significantly lower than those of graphite (370mAh/g)[289] and silicon (~4200 mAh/g)[290] anodes. It is therefore, extremely important to develop new cost-effective cathode and anode chemistries for rechargeable Li-ion batteries.

Among different lithium battery cathodes explored, sulfur exhibits a theoretical capacity of 1672 mAh/g[7], significantly higher than hitherto insertion-based cathode materials. Lithium-Sulfur (Li-S) batteries operate via a two-electron reaction pathway, presenting exceptionally high theoretical energy densities of 2600 Wh/kg[51]. In addition to the high energy and power densities, sulfur exhibits other advantages. These include low cost ($100/kWh of Li-S batteries comprising lithium metal anode and sulfur cathode)[9] compared to conventional cathodes ($432/kWh graphite anode and lithium nickel magnesium cobalt oxide (NMC) cathode)[9, 10], natural abundance (0.07% of the Earth's crust)[291], and environmental friendliness. Thus, Li-S batteries

can be established as a promising candidate to satisfy the extensive requirements of the energy storage market. However, the insulating nature of sulfur results in low active material utilization[292]. Furthermore, conversion of sulfur to Li_2S causes a large volume expansion(~80%)[30]. More importantly, the reaction of sulfur with lithium leades to polysulfide intermediates (S_n^{2-}, $3 \leq n \leq 8$)[35] that are highly soluble in organic battery electrolytes, resulting in loss of energy-bearing active materials yielding poor cycling stability. Polysulfide dissolution also causes a change in the electrolyte composition during cycling and its impact on the solid electrolyte interphase (SEI)[35, 69, 293], a major contributor to performance decay, additionally being poorly understood. These challenges have hindered the commercial progression of Li-S batteries for practical applications.

In order to address the obstacles facing Li-S batteries, extensive research is conducted in recent years. These include designing composite nanostructured architectures to immobilize sulfur and polysulfides within the cathode[28, 42-44, 54], thus increasing active material utilization and controlling polysulfide dissolution. Introducing a carbon interlayer between the cathode and the separator[294-296] has helped contain the polysulfides within the cathode serving as an extended current collector. Furthermore, solid, composite, and gel polymer electrolytes have also been used to block polysulfide dissolution, diffusion, and migration. The addition of $LiNO_3$ as an electrolyte additive[199, 297, 298] to promote the formation of a passivation film at the lithium/electrolyte interface has also proven to be effective in preventing polysulfide dissolution. Additionally various nano-sized metal oxides, such as manganese nickel oxide[68], γ-alumina[70], silica[71], and titania[69] have shown to improve the Li-S battery performance by absorbing and trapping the soluble polysulfides.

Amongst all the reported approaches, the most popular method documented is the employment of nanoporous carbon hosts to improve the Li-S battery performance [42, 51, 209, 299] while ensuring that the sulfur particles are nano-sized with the ability to encapsulate sulfur and polysulfides within their pores during cycling. Numerous porous carbonaceous materials have been used as sulfur hosts, including microporous and mesoporous carbons[26-28, 42-44, 47, 54, 300], porous carbon spheres[54], activated carbon fibers[301], carbon nanotubes[19] and graphene nanosheets[302]. All these approaches have had a positive impact on the cycling stability of Li-S batteries.

In general, carbon hosts confine sulfur and polysulfides within the pores or interlayers by physically interacting with the sulfur. The weak physical interaction however, can only retain polysulfides partially and for only a short period. Consequently, the dissolved polysulfides will eventually diffuse out of the cathode during the charge-discharge process. Recently, it has been proven that the use of metal oxides[24, 72], metal sulfides[303, 304] and metal organic frameworks (MOFs)[29, 226, 305] immobilize polysulfide species by chemical adsorption. MOFs are a new class of crystalline porous materials made of metal ions or cluster nodes linked by organic ligands in infinite arrays. MOFs are also easy to design with the ability to add chemical moieties on the surface for further functionalizing the system with potential applications in gas storage, separations, catalysis, detection, and electrochemistry. In recent years, the use of MOFs as hosts for immobilizing sulfur in Li-S batteries has also attracted much interest[46, 214, 225]. Metal nodes within the MOF form Lewis acid sites, and the functional groups from the organic linkers form Lewis base sites, together with the nanoporous architecture providing effective binding sites for the lithium polysulfides[137] and hence, strongly confining them within the pores. The nanoporous framework also offers a platform for researchers to design materials for effectively restraining

the dissolution and diffusion of polysulfides at the molecular level. Until now, most reports on MOFs for Li-S batteries exploited the pore size of carbonized MOFs to limit the polysulfide dissolution[46, 220, 225, 306-308]. Only few reports reflect the use of Lewis acid and Lewis base sites within the MOFs to serve as active binding sites for polysulfide dissolution[134, 137, 214, 226, 305]; noteworthy being Wang et al[134] and Zheng et al[137] reporting on carbonate-based MOFs used as sulfur hosts for Li-S batteries. It is important to note that there is a significant initial loss in capacity in both reports with no adequate scientific explanation. We have previously reported extensively on the reason for the observed irreversible loss in capacity in carbonate based MOFs used in Li-S batteries[29]. The observed loss in irreversible capacity in carbonate-based MOFs is attributed to the reaction of sulfur with the carbonate functional groups of the MOFs during cycling. With this understanding, putatively using a sulfonate functionalized MOF as a sulfur host forming a complex framework material (CFM), could essentially mitigate this observed initial capacity loss.

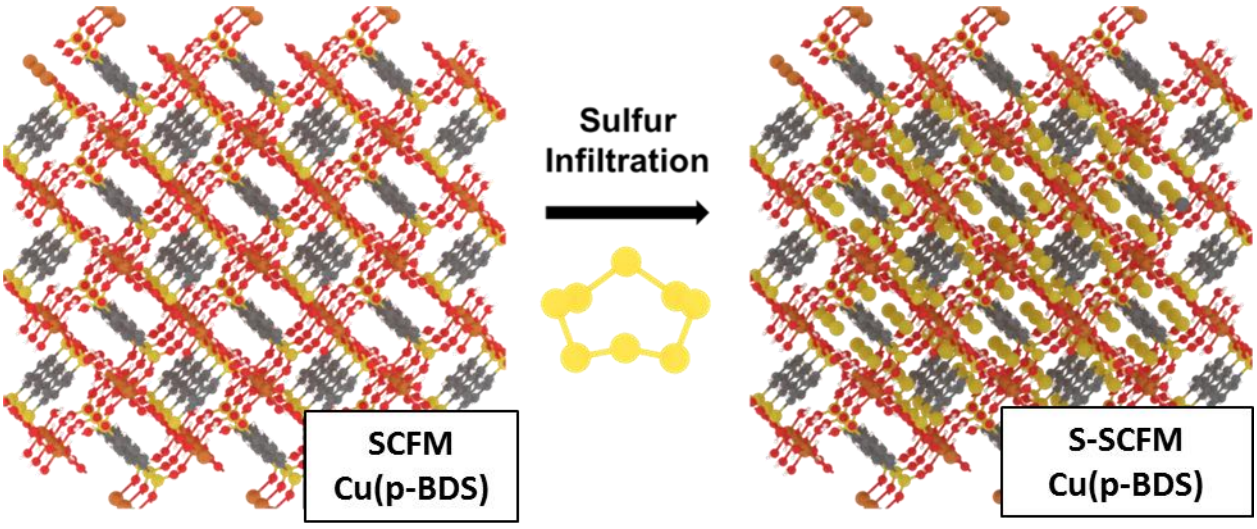

Figure 5-1 Schematic representation of the CFM derived SCFM before and following sulfur infiltration.

In this work, accordingly, we report on the use of a novel complex framework material (CFM) based CFM synthesized from sulfonic acid analogues of carboxylic acid, reported by Metrach et al,[309] as sulfur hosts for Li-S batteries. A simple room temperature method was used to synthesize the sulfonic acid-based CFM termed SCFM, followed by infiltration of sulfur using a vapor phase based infiltration process before using it as cathode in Li-S batteries. (Figure 5-1). The sulfur infiltrated CFM termed S-SCFM cathodes, when tested in Li-S battery shows an initial capacity of 1190 mAh g^{-1} with a stable capacity of at 1044 mAh g^{-1} for over 100 cycles. In addition, these cathodes exhibit a total prevention of polysulfide dissolution along with negligible fade rate (0.0014% $cycle^{-1}$) (evident from XPS analysis and electrochemical cycling testing respectively) making these cathode systems promising candidates for Li-S batteries. X-ray photoemission spectroscopy (XPS) was subsequently used to further understand the S-C bonding characteristics and provide additional insights into the prevention of polysulfide dissolution. Results of these studies are accordingly described in detail in the following sections.

5.3 Experimental

5.3.1 Preparation of Sulfonic Acid CFMs and Sulfur Infiltration

Benzene-1,4-dithiol (99% (GC)), hydrogen peroxide solution (30 wt. % in H_2O, ACS reagent), methanol (≥99.8%, ACS reagent), copper (II) carbonate (basic, ACS reagent) and sulfur (-325 mesh particle size, ACS reagent) were purchased from Sigma-Aldrich and used without any further treatment.

1,4-benzenedisulfonic acid dihydrate (p-$BDSH_2 \cdot 2H_2O$) was prepared by dissolving 9.0mM (1.3g) 1,4-benzene dithiol in warm methanol (18ml) and H_2O_2 (15ml) as reported by Mietrach et al[309]. The suspension was stirred for 16 h at 25°C. All volatile materials were then removed under high vacuum to yield a colorless solid of (p-$BDSH_2.2H_2O$).

Copper(II) (1,4-benzenedisulfonate) tetrahydrate [Cu(p-BDS) -$(H_2O)_4$/Sulfonic – CFM/SCFM] was prepared by mixing copper II carbonate (40 mg) and 1,4-benzenedisulfonic acid (0.1 g) in 5 ml water and heating at 50°C under stirring for one day as reported by Mietrach et al[309]. The resulting solution was then filtered and after a few days in air at room temperature in a small petri dish blue crystal of Cu(p-BDS) -$(H_2O)_4$ were obtained from the blue solution.

The CFM derived SCFM was infiltrated with sulfur [143] under vacuum. The sulfur weight infiltrated into the CFM derived SCFM was calculated from the pore volume of the SCFM (70:30 wt% S: SCFM) and was sealed in a quartz ampoule under vacuum. The ampoule was then heated at 300°C for 24 h to impregnate sulfur into the CFM derived SCFM to obtain the sulfur infiltrated-SCFM, referred as (S-SCFM) henceforth in this manuscript[29].

5.3.2 Chemical and Electrochemical Characterization

X-Ray diffractometry (XRD) was used to characterize the SCFM using a Philips XPERT Pro X-Ray diffractometer. The diffractometer employs CuK_α radiation with a wavelength of 0.15406 nm to record 2θ scans in the 10-50° range. The current and voltage were set constant at 40 mA and 45 kV, respectively during the measurements. High-Resolution Transmission Microscopy (HRTEM) imaging of the CFM derived SCFM and S-SCFM was performed in a JEOL JEM2100F equipment to derive a better understanding of the morphology.

X-Ray Photoelectron Spectroscopy (XPS) analysis of CFM derived SCFM and S-SCFM was performed in an ESCALAB 250 Xi system employing Al Kα as the X-Ray source. A sample spot of 200×200 μm^2 was defined for XPS analysis under uniform charge neutralization conditions established using a beam of Ar^+ ions and enactors guided using magnetic lens. The XPS measurements were performed under a pressure of $<5\times10^{-10}$ mbar. The analyzer was calibrated to provide <50 meV deviation in binding energy of Au $4f_{7/2}$ (83.98 eV), Ag $3d_{5/2}$ (368.26 eV) and Cu $2p_{3/2}$ (932.67 eV). The data collected from the spectrometer was analyzed using Avantage software package.

A Micromeritics ASAP 2020 analyzer was used to analyze the specific surface area and the pore characteristics of the CFM samples. The Brunauer–Emmett–Teller (BET) isotherms were obtained after vacuum degassing followed by conducting the nitrogen adsorption-desorption experiments on the samples.

The cathodes for electrochemical charge-discharge cycling evaluation were prepared by coating a homogeneous slurry of the CFM derived S-SCFM (80 wt%), super P (10 wt%) and PVdF (10 wt%) dispersed in N-methyl pyrrolidone (NMP) onto aluminum foil (MTI corporation). The slurry coated foils were then dried under ambient conditions for 24 hours. The loading of the slurry coated electrodes was maintained uniformly at 1.5 – 2 mg cm^{-2}. Commercial sulfur (Sigma Aldrich, Inc, 99%) was also used to generate the control electrodes of identical composition to compare the electrochemical performance of the S-SCFM.

The sulfur infiltrated sulfonic acid derived CFM termed S-SCFM cathodes (working electrode) were assembled into 2025-coin cells in a glove box under Argon (H_2O <0.1 ppm, O_2 <0.1 ppm). The coin cell contained lithium metal counter electrode using a Celgard polypropylene (PP) separator and 1.8 M $LiCF_3SO_3$ (lithium trifluoro-methanesulfonate) + 0.2 M

$LiNO_3$ in 50:50 vol% 1, 3 dioxolane and 1, 2 dimethoxyethane electrolyte. The coin cells were tested in an Arbin BT200 battery tester between 1.7-2.6 V (w.r.t. Li^+/Li) at 0.1 C current rate. Cyclic Voltammetry (CV) and Electrochemical Impedance Spectroscopy (EIS) experiments on the batteries were performed using a VersaSTAT (Princeton Applied Research) potentiostat. The CV experiments were carried out at a scan rate of 0.1 mVs^{-1} between 1.7 V-2.6V. The impedance spectra were performed by varying the frequency between 100 kHz and 10 mHz at an amplitude of 10 mV w.r.t the open circuit potential. The obtained EIS data were then fitted using the ZView software (Scribner and Associates).

5.4 Results and Discussion

The crystal structure of the CFM derived SCFM was studied using XRD. Experimentally obtained XRD patterns of the SCFM was compared with the corresponding pattern simulated using the crystallographic information file (CIF) of the SCFM[309] obtained from the Cambridge Crystallographic Data Centre (via www.ccdc.cam.ac.uk/data_request/cif.) (CCDC number 738978) to ascertain the phase-purity of the synthesized SCFM. Figure 5-2 represents a comparison of the XRD patterns of experimentally obtained SCFM against the simulated pattern for the corresponding SCFM. A good fit between the simulated and the experimentally obtained XRD patterns implies that the SCFM[309] is phase pure and indeed crystalline in nature. Pore size and pore volume of the experimentally synthesized SCFM is a critical factor in determining the amount of sulfur that can be completely infiltrated into the SCFM structure. The porosity of the experimentally synthesized SCFM and S-SCFM were accordingly analyzed using BET and the results of the pore size and surface area analysis are shown in Table 5-1 **(**Appendix C Figure

1shows the corresponding adsorption isotherms). The experimentally obtained SCFM structure exhibits a specific surface area (SSA) of ~452.6 m^2g^{-1}, an average pore size of ~3.2 nm and a pore volume of ~0.623 cm^3g^{-1}. The experimentally determined specific surface area values are comparable with the specific surface area corresponding to conventional CFMs or MOFs studied and reported for gas storage and energy storage applications for Li – S batteries[26, 42, 88, 127, 153-155].

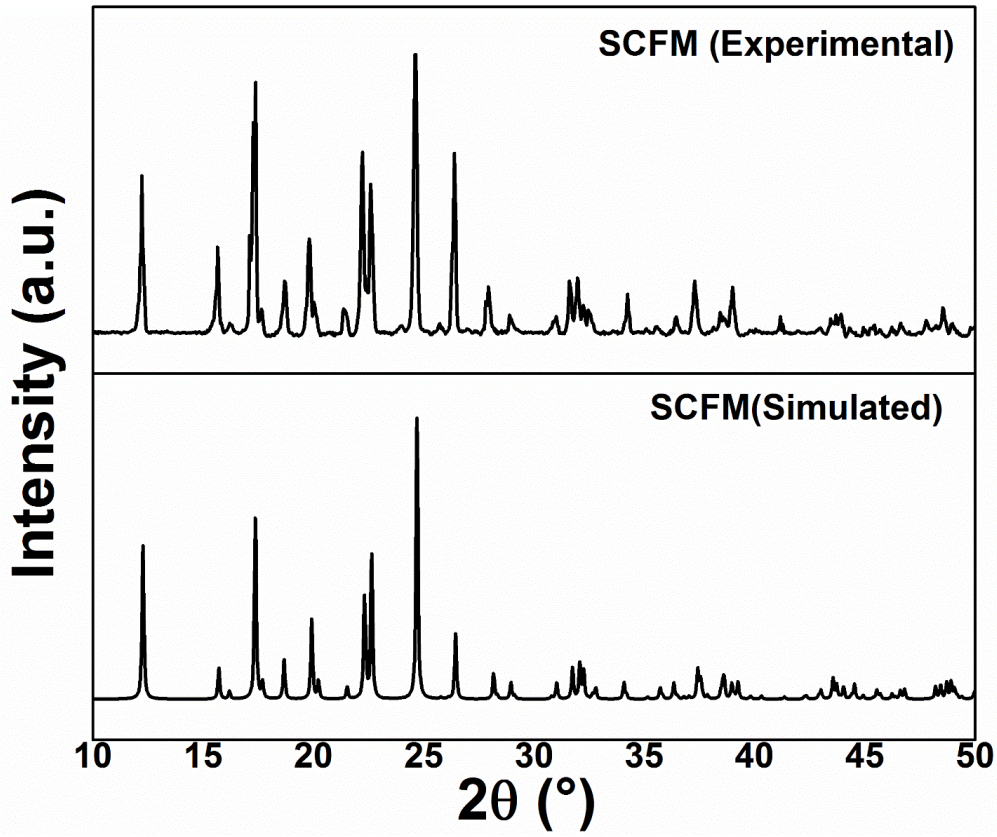

Figure 5-2 XRD patterns of the SCFM structure predicted by simulation and synthesized experimentally showing a positive match.

The small average pore diameter of the SCFM (~3.2 nm) is expected to aid in preventing polysulfide dissolution by facilitating improved trapping of the polysulfides formed during electrochemical cycling. The sulfur infiltrated CFM derived S-SCFM, on the other hand, shows a

drastic reduction in surface area (12.36 m^2g^{-1}) which is clearly indicative of the pores being filled by sulfur and is thus, attributed to sulfur infiltration into the porous channels of the chemically derived CFM based SCFM which results in filling up of the pores. Pore closure in CFMs upon interaction with other molecules similar to sulfur herein is a well-studied phenomenon and our results are thus consistent with reports in the literature[310, 311].

Table 5-1 Results of BET analysis of SCFM and S-SCFM. (Each datum represents an average of three independent tests run on three different samples prepared under identical conditions).

	BET Surface Area (m^2/g)	Langmuir Surface Area (m^2g^{-1})	Total Pore Volume (cm^3g^{-1})	Adsorption average pore width (nm)
SCFM	266.4±17.84	452.6±21.54	0.623±0.07	3.2±0.12
S-SCFM	7.60±1.42	12.36±0.94	0.0018±0.0002	11.19±0.44

TEM analysis was subsequently performed on the experimentally synthesized SCFM to confirm the nanoporous nature and on the sulfur infiltrated CFM structures, namely, S-SCFM to confirm that the infiltrated sulfur had indeed entered and occupied the pores within the experimentally generated SCFM structure (Figure 5-3). The HR-TEM image of the CFM derived S-SCFM at low magnification shows the macroscopic structure of the SCFM and the high-resolution image (Figure 5-3b) further shows the highly ordered nature of the SCFM while the corresponding SAED diffraction pattern of the SCFM (inset Figure 5-3b) indicates the expected long-range order of the SCFM channels. Figure 5-3c represents the corresponding HR-TEM image of the sulfur-infiltrated SCFM (S-SCFM). HR-TEM of the S-SCFM at a higher

magnification (Figure 5-3d) shows the presence of fringe patterns with an inter-planar spacing value of 0.2046 nm corresponding to that of crystalline sulfur (α-S_8)[237]. The inset in Figure 5-3d also shows the SAED pattern corresponding to S-SCFM. Upon further analysis, the SAED pattern shows spots corresponding to (202), (020) and ($\bar{1}22$) crystalline planes of α-S_8[238], thus confirming the presence of crystalline sulfur inside the SCFM. The SEM images of the sulfonic acid derived CFM structures comparing the morphology of the experimentally synthesized SCFM before and following infiltration with sulfur, S-SCFM are shown in Appendix C Figure 2a-d. Appendix C Figure 2e and Appendix C Table 1 represents the EDS pattern and the composition of the SCFM after sulfur infiltration. Appendix C Table 1 clearly shows that the experimental composition of the sulfur infiltrated S-SCFM is in accordance with the calculated composition, thus confirming complete sulfur infiltration and the presence of ~70 wt% sulfur in the S-SCFM following sulfur infiltration.

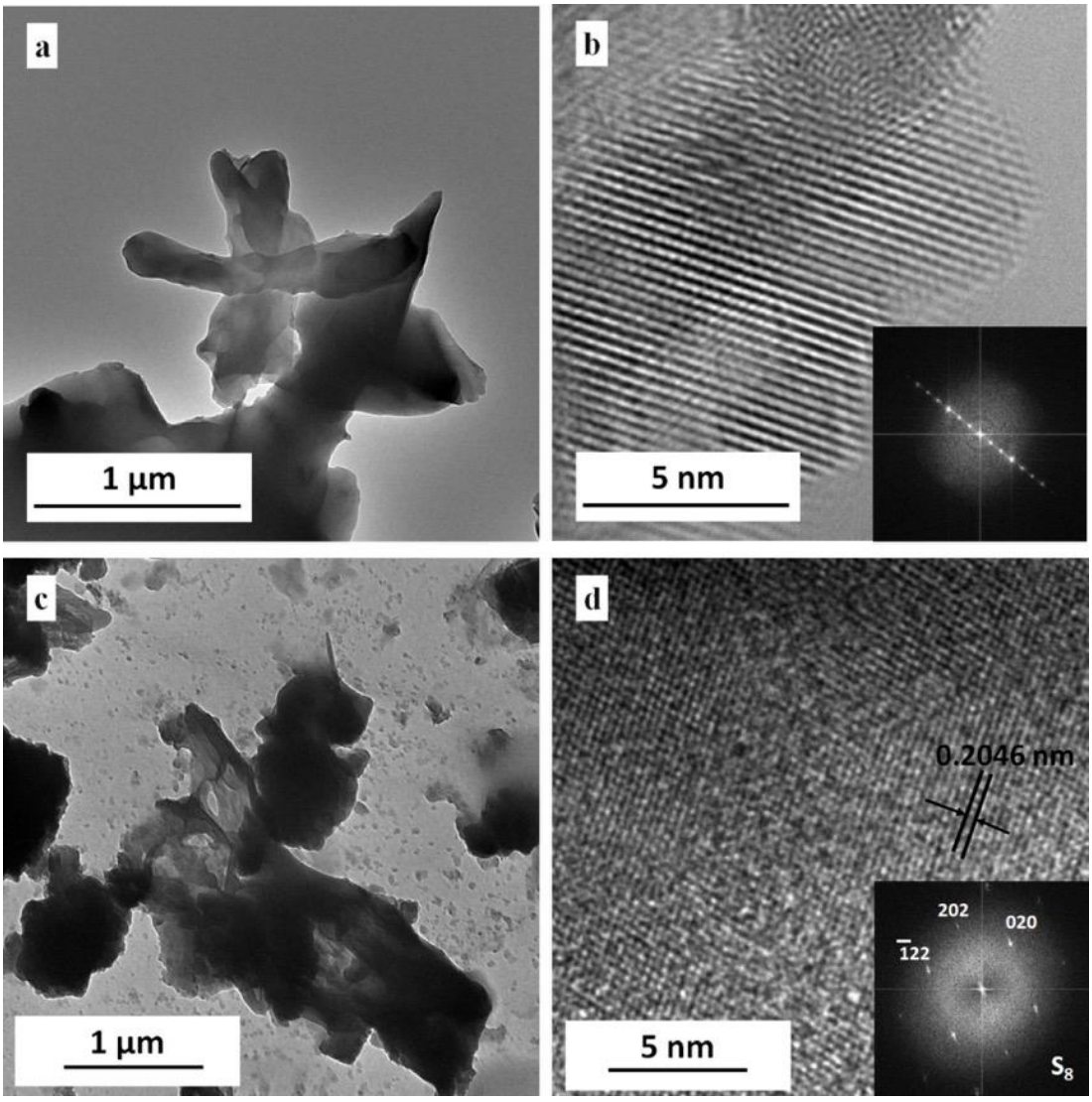

Figure 5-3 TEM images of Sulfonic acid based CFM derived SCFM at (a) low magnification and (b) high magnification, (c) Sulfur incorporated sulfonic acid based CFM derived S-SCFM at low magnification and (d) Sulfur incorporated sulfonic acid based CFM derived S-SCFM at high magnification (Inset: SAED pattern of the S-SCFM confirming the presence of sulfur in the S-SCFM).

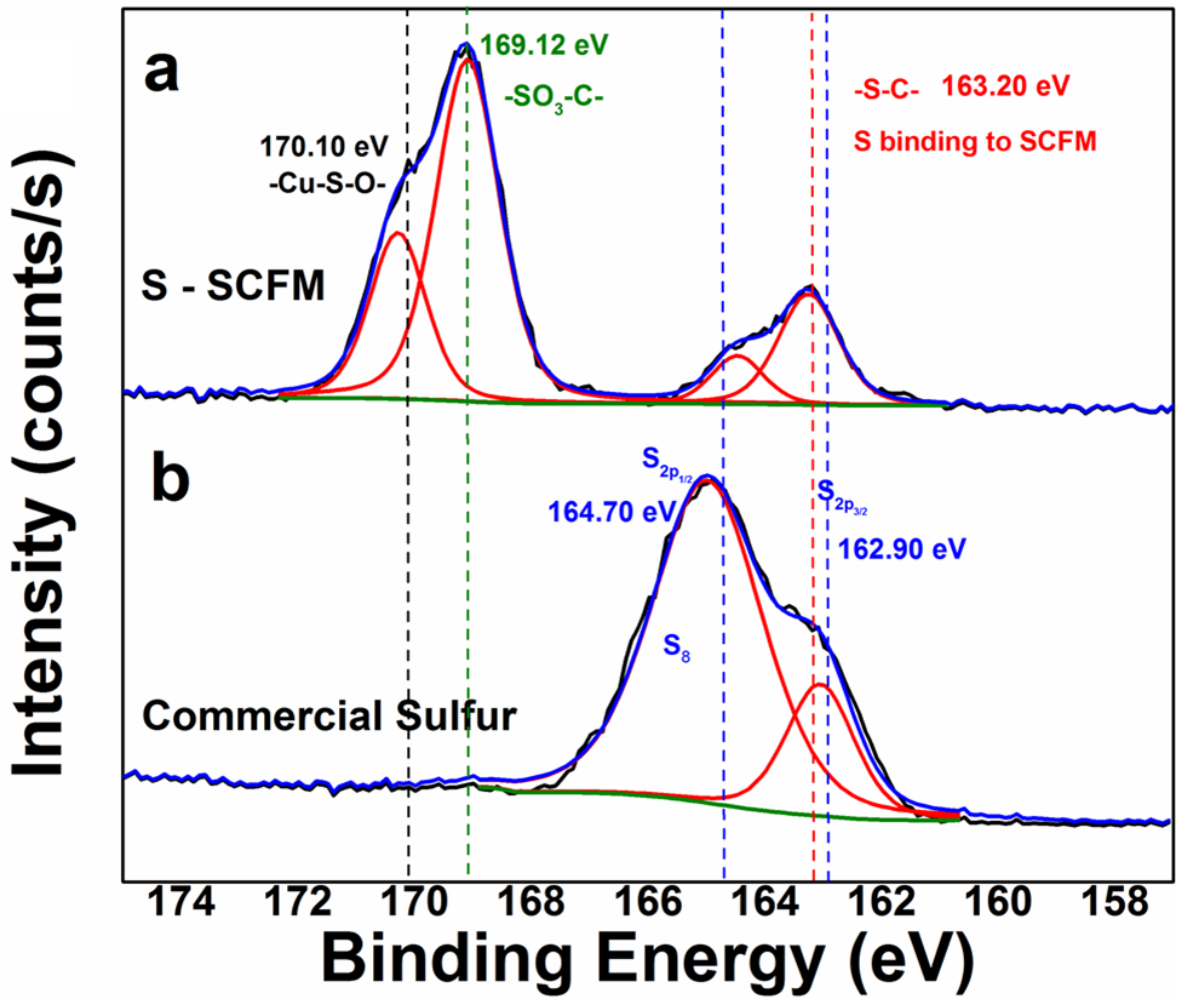

Figure 5-4 XPS S2p Binding Energy profile corresponding to (a) sulfur infiltrated SCFM, S -SCFM and that of (b) commercially obtained Sulfur.

In order to confirm the presence of sulfur and to understand the nature of the binding between the infiltrated sulfur and the sulfonic acid-based CFM derived SCFM, the experimentally synthesized S-SCFM was analyzed using XPS on a background corrected Thermo ESCALAB 250Xi after sulfur infiltration. Figure 5-4represents the S2p spectra collected on the sulfur infiltrated into the SCFM, namely, S-SCFM (Figure 5-4a) compared with that of commercial sulfur (Figure 5-4b). The characteristic S2p peaks of S_8, $S2p_{1/2}$ and $S2p_{3/2}$ were observed at 164.70eV and 162.90 eV [143, 159-161], respectively for commercial sulfur. On the other

hand, the XPS spectra collected on S-SCFM following sulfur infiltration shows S2p peak at 163.20 eV as opposed to the spectra collected on commercial sulfur (S_8) (which usually occurs at 164.70 eV and 162.90 eV) indicating the absence of free elemental sulfur. The peaks at 170.10 eV and 169.12 eV corresponds to the -Cu-S-O-[264] and -SO_3-C-[170] bonds that are characteristics of the SCFM. The $S2p_{3/2}$ peak observed at 163.20eV in the spectra of S-SCFM corresponds to -C-S- bonds as shown by Wagner et. al.[265] confirming the chemical binding of sulfur to the CFM derived SCFM arising from the infiltration of sulfur into the chemically derived sulfonic acid based CFM, i.e. SCFM to form the S-SCFM. This binding of the acidic SCFM chemical linkages with the basic sulfur is due to the acidic nature of the synthesized SCFM [137]. This chemical binding of sulfur to the carbon atoms from the sulfonic acid based CFM derived SCFM, along with the nanoporous nature of the SCFM (~3.2 nm from BET (Table 5-1)) would help to immobilize and thereby prevent the dissolution of polysulfide species formed as a result of electrochemical cycling into the electrolyte solution. Further, the SCFM, being derived from sulfonic acid (-SO_3-) groups, will interact with the basic polysulfides (via Lewis acid-base interaction) that are generated during electrochemical cycling, thereby preventing them from dissolving into the electrolyte. This type of acid – base interaction has been reported in various systems that involves molecular binding onto various CFMs[168, 169].

We have also demonstrated complete binding and subsequent trapping of the polysulfide in a carbonate-based MOF (MOF-5) in our previous publication[48]. However, the carbonate-based system showed a very high loss in capacity in the first ~20 cycles due to the chemical reaction of sulfur with the -CO_3- group of the MOF-5 forming sulfate species. The absence of -CO_3- groups in the currently synthesized sulfonic acid based CFM derived SCFM is evidently expected to reduce the loss in capacity and lead to improved cycling stability.

Having confirmed the presence of sulfur infiltrated into the sulfonic based CFM derived SCFM and the corresponding chemical binding between the synthesized SCFM and infiltrated sulfur, electrochemical charge-discharge cycling was performed on the synthesized sulfur infiltrated SCFM namely, the S-SCFM electrodes to study the effect of this binding on the electrochemical performance of the generated S-SCFM structure. The results of the electrochemical charge-discharge response on the S-SCFM at 0.1C rate (~1.5-2 $mgcm^{-2}$ sulfur loading) and the corresponding rate capability response is shown in Figure 5-5a. The S-SCFM electrode shows an initial discharge capacity of 1190 mAh g^{-1} which stabilizes at 1044 mAh g^{-1} after the 100^{th} cycle. Moreover, following cycling of the electrode at 1C rate yielding a capacity of 669 mAh g^{-1}, the electrode regains the capacity of 1066 mAh g^{-1} when cycled at 0.1C. Commercial sulfur cathodes on the other hand, when cycled at similar conditions (0.1C rate against lithium metal anode) shows a much lower initial capacity of 557 mAh/g that fades rapidly to 81 mAh/g (Appendix C Figure 3). At the same time, this initial discharge capacity value is lower than the initial capacity reported by us in our previous work using Zn-MOF-5 as sulfur hosts (1476 mAh/g at 0.2C rate)[29]. It is worthy to note that, in our previous work, 50 wt.% sulfur was infiltrated into 50wt.% Zn-MOF-5 and the electrodes had a total sulfur loading of 36 wt.%. This could be attributed to the comparatively lower electrical and ionic conductivity of the CMF derived SCFM and S-SCFM as compared to the earlier reported MOF-5 and S-MOF-5 resulting in a lower capacity despite utilizing a higher sulfur loading in the electrodes used in our current S-SCFM cathodes (56 wt%) (see Appendix C Table 2).

The experimentally synthesized sulfonic acid based CFM derived S-SCFM exhibits electrical conductivity ($7.64\pm0.73\times10^{-10}$ Scm^{-1}) and ionic conductivity ($4.03\pm0.12\times10^{-10}$ Scm^{-1}) which is an order of magnitude lower than the electrical conductivity ($1.83\pm0.21\times10^{-8}$ Scm^{-1}) and

ionic conductivity ($1.37\pm0.08\times10^{-9}$ Scm^{-1}) of S-MOF-5. The lower ionic and electronic conductivity of the CFM derived S-SCFM could limit the complete utilization of the infiltrated sulfur, hence resulting in specific capacities lower than the theoretical capacity of sulfur (1672 $mAhg^{-1}$). The voltage versus specific capacity plot of S-SCFM is shown in Figure 5-5b**.** The specific capacity plot of the S-SCFM system shows a difference of ~10% difference between the first cycle charge and discharge capacities, which is accordingly reflected in the coulombic efficiency plot (Figure 5-5a). This difference is similar to the observations made by Zhao et al[137] and Zhao et al[252] on their work on different non-carbonized MOF-based sulfur cathode systems. Both the authors cite the absence of polysulfide dissolution in their respective systems due to Lewis acid-base interaction between the MOF and polysulfides, however, a scientific explanation for this observed difference between the charge and discharge capacity is lacking. In order to additionally prove and provide scientific insights into the observed differences between the first cycle charge and discharge capacities, we have characterized the system extensively by conducting XPS analysis on the separator and the cycled electrodes respectively, the results of which will be discussed in the following sections outlined below.

It should be noted that the sulfonic acid based CFM derived S-SCFM, however, exhibits an exceptionally low fade-rate of 0.0012%/cycle along with good rate-capability and coulombic efficiency (~99.9%). In our previous work reporting the use of carbonate-based S-MOF-5, the capacity was observed to fade rapidly during the first 10 cycles only to stabilize at a capacity of 609 $mAhg^{-1}$ after 200 cycles with comparable fade rate of 0.0014%$cycle^{-1}$.

CFM-based cathode systems reported in the literature thus far. The current work on sulfur infiltrated sulfonic acid based CFM derived S-SCFM system has the highest sulfur contents (56 wt%) in the cathode next to that reported by Zhao et al[252] in their work on chromium MOF MIL-

101 (58.8% wt) and Zheng et al[137] who describe using Ni-MOF DUT-23 (60 wt%). The sulfur infiltrated sulfonic acid based CFM derived S-SCFM system used in the work reported herein also exhibits exceptionally high stable discharge capacity of 1044 mAh/g which is the highest value reported in the cited literature thus far to the best of our knowledge. The cycling stability (0.0012%) is also one of the lowest values reported in literature so far. The exceptional electrochemical cycling stability of the sulfur infiltrated sulfonic acid based CFM derived S-SCFM cathodes is due to sulfur binding with the SCFM (confirmed by XPS analysis - Figure 5-4a) subsequently resulting in effective trapping of polysulfide species inside the nanopores of the sulfonic acid based CFM derived sulfur infiltrated SCFM, S-SCFM architectures.

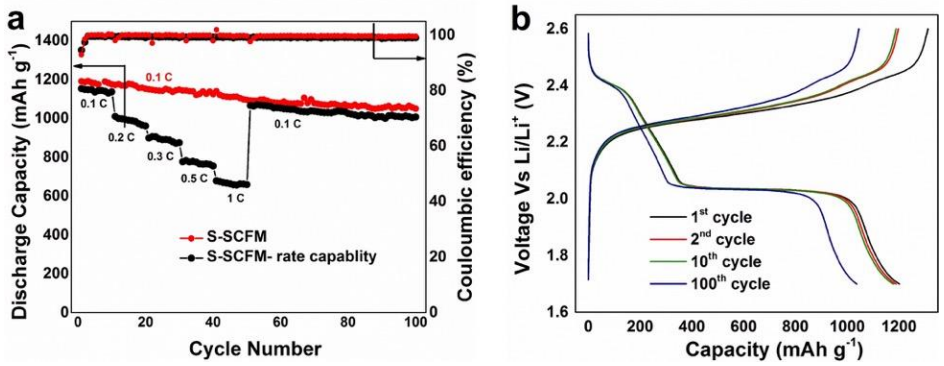

Figure 5-5 (a) Electrochemical cycling performance of S-SCFM with coulombic efficiency and (b) Specific capacity plots of S-SCFM (The cycling experiment was performed on three batches of S-SCFM samples prepared independently from three batches of CFM derived SCFM samples. The difference in capacity in all the three runs were within ±5%).

Confirmation of the complete encapsulation of sulfur and the polysulfide species inside the sulfonic acid based CFM derived sulfur infiltrated SCFM, S-SCFM architectures during the electrochemical charge-discharge cycle, was achieved by conducting XPS. Accordingly, XPS analysis was performed on the separators retrieved from the electrochemically cycled batteries

containing the S-SCFM electrodes after 100 cycles and compared with the XPS spectra collected on the separators obtained from electrochemically cycled batteries made from commercially obtained sulfur electrodes. The Celgard separators corresponding to dry and another separator accordingly dipped in the electrolyte were used as the corresponding control samples allowing for suitable comparison. The results of the XPS analysis are accordingly shown in Figure 5-6a.

In the case of the polypropylene (PP) separator that is dry, no S2p peak was observed before cycling, but in the PP separator dipped in electrolyte, a single peak corresponding to the -SO_3- group from the lithium salt present in the electrolyte (Trifluoro methyl sulfonate lithium salt) is observed at 168.93 eV as seen in Figure 5-6a [170]. In addition to this peak, the XPS spectra of the separator cycled with the commercial sulfur electrode shows the characteristic S2p peaks at 166.72 eV and 163.08 eV, arising from the lower and higher order polysulfide species, respectively[80, 171-173]. This validates the fact that the commercial sulfur electrode undergoes polysulfide dissolution into the electrolyte during electrochemical cycling depositing on the separator. The commercial sulfur cathode, when cycled electrochemically (Appendix C Figure 3) shows an initial capacity of 557 mAh/g that rapidly fades to 81 mAh/g in the first 100 cycles along with a low coulombic efficiency (~80%). This result confirms and supports our XPS observation indicating clearly the presence of polysulfide dissolution contributing to the characteristic loss in capacity and rapid fade rate. However, the separator corresponding to the sulfonic acid based CFM following sulfur infiltration namely, S-SCFM electrode after 100 cycles shows only one S2p peak at 168.93 eV (see Figure 5-6a) corresponding to the sulfur binding in the $LiCF_3SO_3$ salt present in the electrolyte[170].

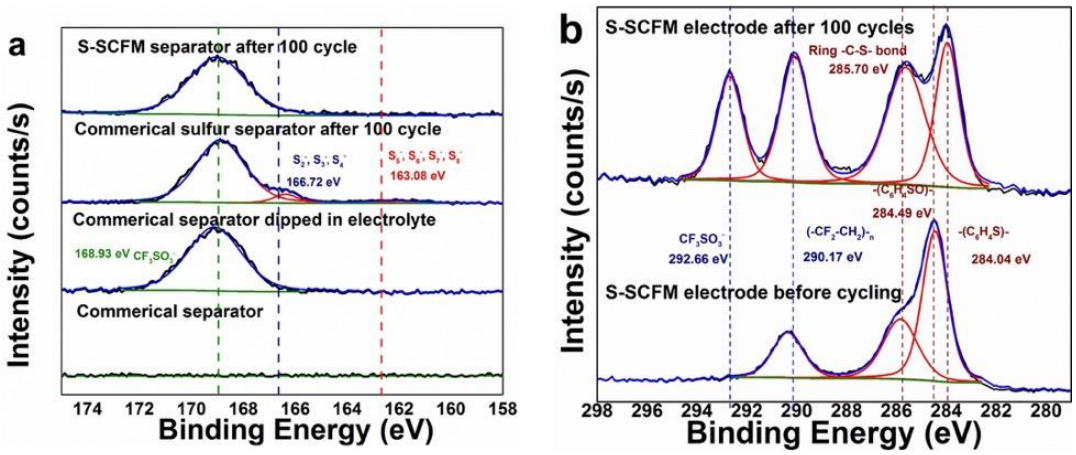

Figure 5-6 (a) XPS S2p spectra of commercial separator (Celgard PP), separator soaked in liquid electrolyte, separators cycled with commercial sulfur electrode and sulfonic acid based CFM following sulfur incorporation namely, S-SCFM (after 100 cycles at 0.1 C rate), (b) XPS C1s spectra of pristine S-SCFM electrodes before cycling and the electrodes after 100 charge-discharge cycles at 0.1 C rate.

The clear absence of polysulfide species related peaks in the sulfonic acid based CFM following sulfur infiltration namely, S-SCFM separator and the lithium counter electrode (see Appendix C Figure 4) post cycling clearly shows and validates the complete entrainment of the polysulfide species by the S-SCFM architecture. This observation can be attributed to the binding of polysulfide species due to the Lewis acid-base interactions between the synthesized sulfonic acid based CMF derived SCFM and the infiltrated sulfur, as well as the entrapment effect provided by the nanoporous nature of the SCFM as is evident from the TEM (Figure 5-3) and BET analysis (Table 5-1). Use of a carbonaceous porous matrix[27, 28, 43, 44, 54] and conventional carbonate CFMs[134, 137] as sulfur hosts reported previously has shown improvement in electrochemical cycling. However, a complete prevention of polysulfide dissolution in the CFM synthesized as outlined herein has not been reported thus far. The unique -SO_3- functional groups present in the precursor used to synthesize the SCFM in the current study, and its chemical inertness to sulfur preventing the formation of any unwanted sulfate species during

electrochemical cycling as opposed to our previously published work[29] is clearly responsible for this observed result. As a result, the chemically synthesized sulfonic acid based CFM derived SCFM following sulfur incorporation, S-SCFM is not only effective in entrapping the polysulfides but also contributes to elimination of the formation of any metal sulfate species that is responsible for the large first cycle irreversible loss as reported by us in the carbonate derived CFM structures. Furthermore, the sulfonic acid based CFM derived sulfur infiltrated S-SCFM architecture owing to the presence of the sulfonic acid species leads to exceptional low fade rates of ~0.0012%/cycle.

Following confirmation of no observable and detectable polysulfide species in the separators collected from the S-SCFM electrodes after cycling, the electrodes were further analyzed using XPS both before and after 100 cycles. The C1s spectra collected on the sulfonic acid based CFM following sulfur infiltration, namely, S-SCFM electrodes before cycling and after cycling for 100 cycles are shown in Figure 5-6b. The S-SCFM electrode before cycling shows a peak at 290.17 eV corresponding to $(-CF_2-CH_2)-_n$ bonding from the PVdF binder used in the electrode[174]. The electrode before cycling also shows peaks at 285.70 eV and 284.04 eV corresponding to the different types of chemical interactions between the carbon and sulfur in the sulfonic acid based CFM, $-C_6H_4S-$ bonding[175] and –C-S- bonding[176], respectively. The presence of the C-S bond in the XPS spectra validates the observations from Figure 5-4, that the formation of the sulfur-carbon bonding during infiltration of the sulfur ensures complete retention of the polysulfide species formed within the S-SCFM structure.

The S-SCFM electrode after completing 100 charge-discharge cycles shows the characteristic –C-S- binding peaks in the sulfur infiltrated S-SCFM electrode as discussed earlier, along with a peak at 292.66 eV corresponding to $CF_3SO_3^-$[170] group from the lithium salt ($LiCF_3SO_3$) present in the organic electrolyte used for battery testing. Another additional peak is

observed at 284.04 eV that corresponds to the presence of (-C_6H_4S-)[175], which is a slight variation to the binding observed in the electrode before cycling. There is no significant change in the binding state of C1s observed indicating the chemical stability of the S-SCFM upon electrochemical cycling. In our previous work reporting the use of MOF-5 as sulfur host for Li-S battery[29], we observed peaks corresponding to the reaction of the -CO_3- groups with sulfur and lithium. However, the absence of any such anomalous peaks in the C1s spectra and the presence of -C-S- peaks even after 100 charge-discharge cycles is a convincing validation supporting the strong Lewis acid-base interaction of the SCFM with infiltrated sulfur and the polysulfide species[137].

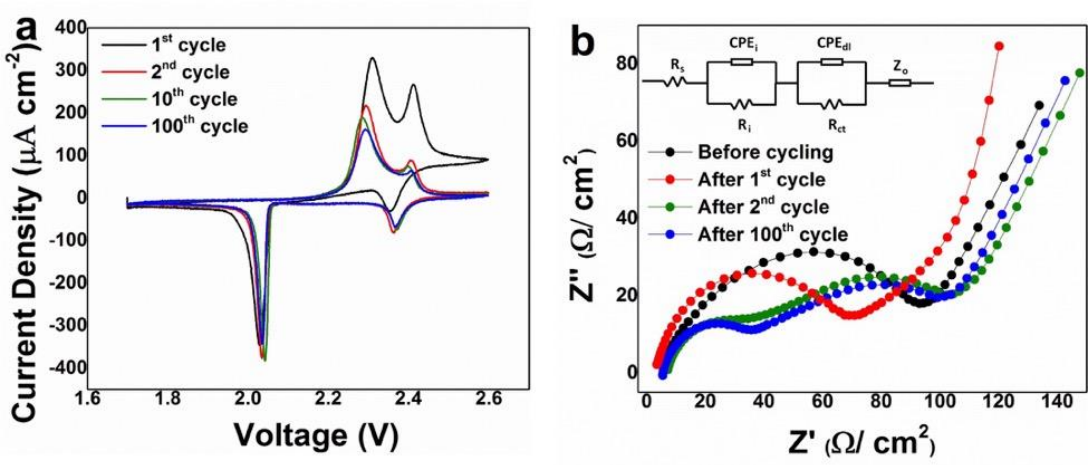

Figure 5-7 a) Cyclic Voltammograms (CV) and b) Electrochemical Impedance Spectroscopy (EIS) plot of S-SCFM at various cycles (scan rate: 0.1mV/s).

For further better understanding of the good cycling stability and low fade-rate observed for the sulfur infiltrated S-SCFM electrodes discussed above, cyclic voltammetry (CV) and electrochemical impedance spectroscopy (EIS) measurements were performed (Figure 5-7a&b). The CVs were performed employing a very slow scan rate of 0.1 mV/s. The two reduction peaks

at 2.36 V and 2.03 V correspond to the two discharge plateaus[257] observed in the specific capacity plots (Figure 5-5b), which results from the transformation processes corresponding to the conversion of linear S_8 chain to soluble polysulfides Li_2S_x (x = 4–8) and Li_2S_4 to insoluble Li_2S, respectively[312]. Similarly, the two oxidation peaks observed at 2.40 eV and 2.30 eV corresponds to the two charge plateaus observed in the specific capacity plots (Figure 5-5b) attributable to the conversion of the insoluble Li_2S to Li_2S_4 and Li_2S_4 to S_8 via the formation of the ubiquitous soluble polysulfides Li_2S_x (x=4-8), respectively[100]. It should be noted that there is also no observable change in the peak positions in the charge and discharge peaks (Appendix C Table 4) indicating lack of any observable irreversible polarization occurring in the assembled electrode suggesting the reversible nature of the CFM derived S-SCFM system. However, there is indeed a change in the peak height observed between the first and second cycle. This change in the peak height has been reported in the literature as well and is believed to be due to the formation of the solid electrolyte interphase (SEI) as is well-known in all electrochemical systems and is also discussed below[313].

The Electrochemical Impedance Spectroscopy (EIS) measurement was employed to understand further the behavior observed in the CV experiments. Figure 5-7b represents the results of the EIS analysis conducted on the S-SCFM system (before and after the 1st, 2nd and 100th cycles) between a frequency range of 0.01Hz to 100,000Hz at an applied amplitude of 10mV at the open circuit potential. The EIS spectra were fitted to the Randal's circuit model (Figure 5-7b inset) comprised of two semicircles in the low frequency regime corresponding to the charge transfer reaction (R_{ct} and CPE_{ct}) [15] with the medium frequency region corresponding to the resistances and capacitances at the interface (R_i and CPE_{dl}) [314]. Additionally, the characteristic sloping line in the very low frequency region is attributed to the Warburg

impedance (Z_o), the values of which are tabulated in Appendix C Table 5. Before cycling, the initial resistance is very high at 107.2 Ω due to the relatively poor conductivity of the S-SCFM (as discussed in Appendix C Table 5). During the first discharge process, lithium reacts with sulfur to form polysulfides that exhibit higher conductivity. Hence, there is a decrease in the charge transfer resistance, R_{ct} to 89.5Ω. These results are in accordance with the results reported in the literature in experiments conducted on CFM-based systems[137]. However, after the second cycle there is a considerable decrease in the R_{ct} (70.1Ω), which almost remains constant up until after 100 cycles (68.8Ω). The change in the value of R_{ct} between the first discharge and the second discharge also hints to the formation of a SEI layer on the electrode surface, which requires further chemical characterization as is discussed below.

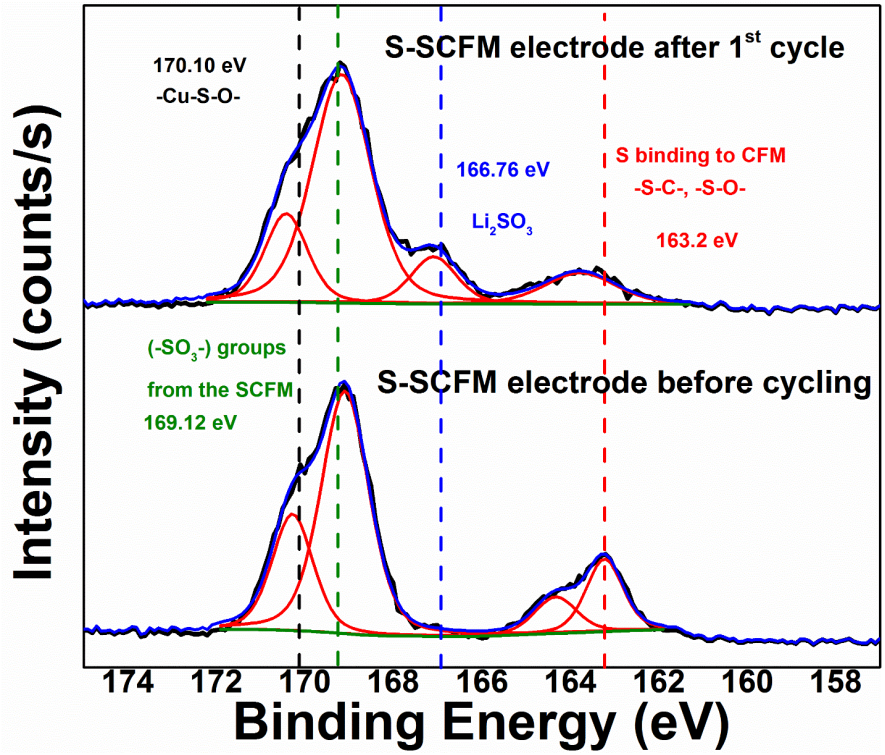

Figure 5-8 XPS S2p spectra of slurry coated electrodes of the CFM derived S-SCFM-before and after 1st cycle (0.1 C rate).

For further explaining the difference observed in the peak heights between the first and the second cycle observed in the CV (Figure 5-7a), XPS analysis was carried out on the pristine uncycled sulfonic acid based CFM derived sulfur infiltrated S-SCFM electrode as well as on the electrode after the first discharge cycle. A comparison of the S2p spectra is shown in Figure 5-8. The S2p spectra of the S-SCFM electrode before cycling shows peaks at 170.10 eV and 169.12 eV corresponding to the -Cu-S-O-[264] and -SO_3-C-[170] bonds, respectively, both of which are characteristic of the SCFM. In addition, a peak at 163.20eV is observed in the spectra of the S-SCFM corresponding to -C-S- bonds[265] formed due to the chemical interaction of sulfur with the carbon in the SCFM as discussed earlier. The S2p spectra of the S-SCFM after the 1st charge-discharge cycle shows all the peaks observed before cycling, along with a new peak at 166.76 eV corresponding to Li_2SO_3[268, 269]. This peak at 166.76 is likely arising from the decomposition of the liquid electrolyte containing $LiCF_3SO_3$ at the electrode surface to form the characteristic SEI. This SEI formed during the initial cycle confirms the observed change in peak height seen in the CV and the characteristic EIS signature discussed above. The formation of this SEI layer is however, expected to stabilize the electrode. Formation and stabilization of the electrode indeed explains the absence of a significant change in the peak height in the CV (Figure 5-7a) after the 1st cycle.

From the results of our previous study on carbonate-based CFM host for sulfur, it is indeed evident that the presence of electrochemically unstable carbonate groups in the CFM resulted in the formation of metal sulfate complexes during the initial charge-discharge cycles. These sulfate complexes lead to irreversible loss in capacity despite its ability to successfully prevent polysulfide species from dissolving into the electrolyte[29]. Hence, by generating a CFM architecture as outlined herein using a sulfonic acid-based CFM (SCFM), this problem of the

initial capacity loss that we previously observed in our carbonate derived CFM is indeed overcome in the present study. The results discussed in this work herein further suggests that the use of this sulfonic acid based CFM derived from a non-carbonate species containing CFM could ably serve as potential hosts for sulfur thus serving as a promising pathway towards the fabrication of stable and reversible Li-S battery electrodes exhibiting better capacity and exceptional stability. The results of this study described herein indeed could serve to provide better insights into the designing of next generation complex framework materials (CFM) type CFM based sulfur hosts serving as effective architectures for entrapment of polysulfide species leading to high energy density Li-S batteries. The efficient polysulfide trapping as evinced from the results here combined with the elimination of the metal sulfate species provides an elegant pathway for further modification of the system to demonstrate the creation of the next generation electrodes with high sulfur loading while still demonstrating the excellent capacity retention. The results of the current study will nevertheless provide insights for these studies to be conducted in the near future.

5.5 Conclusions

A sulfonic acid-based complex framework materials (CFM), termed as SCFM was effectively synthesized at room temperature and infiltrated with sulfur using a vapor-phase infiltration technique to form S-SCFM. The S-SCFM electrode was then tested as a cathode for Li-S batteries. The S-SCFM electrode demonstrated a high initial capacity of 1190 $mAhg^{-1}$, with stable capacity of 1044 $mAhg^{-1}$ for up to 100 cycles when cycled at 0.1C rate while also exhibiting reversible capacity of 669 $mAhg^{-1}$ at 1C rate. The electrode regains the capacity of

1066 $mAhg^{-1}$ when cycled back at 0.1C. The S-SCFM also exhibited good cycling stability along with a low fade rate of ~0.0012%/cycle. The higher discharge capacity along with impressive cycling stability makes the sulfonic acid based CFM namely, SCFM an appealing sulfur host to form S-SCFM serving as effective operational electrodes for Li-S batteries. XPS analysis of the S-SCFM separators post-cycling shows the absence of any polysulfide species, which is attributed to the binding of the infiltrated sulfur with the carbon from the SCFM backbone and the ability of the SCFM to interactively bind polysulfide species through the characteristic Lewis acid-Lewis base interactions. These interactions accordingly, prevent the polysulfide species from dissolving and diffusing into the electrolyte. The study also provides insights into stabilizing and entrapping the polysulfide species using the porous, non-carbonized sulfonic acid based polymeric complex framework materials (CFM) as sulfur hosts. The results of this study demonstrate the promise of designing and developing new sulfonic acid, based CFM derived SCFM serving as effective sulfur hosts with potentially maintaining higher sulfur loadings that are capable of efficiently preventing polysulfide dissolution. At the same time, these systems will likely demonstrate the ability to deliver a high energy density in the range of ~500 $Whkg^{-1}$ needed and desired for next generation Li-S batteries.

5.6 Acknowledgements

This research was supported by the Department of Energy (DOE) grant OVT-DE-EE0006825, DE-EE0007797, and DE-EE0008199. The authors also acknowledge the Edward R. Weidlein Chair Professorship Funds, the Center for Complex Engineered Multifunctional Materials (CCEMM) and NSF-CBET 1511390 for supporting the research while also providing

the required equipment for characterization as needed for this study. The authors also further acknowledge Dr. Joel Gillespie, PPG Materials Characterization Laboratory (Department of Chemistry, University of Pittsburgh) for providing access to the use of XPS instrumentation. Finally, the authors acknowledge the help of Mr. Karthikeyan Saravanan, Dr. John Keith and Mr. Brian Day (Department of Chemical Engineering, University of Pittsburgh) for their help in simulating the XRD pattern from CIF (Crystallographic Information File**)** information as well as generation of the schematic plots of the SCFM and S-SCFM structures.

6.0 Specific Aim 2: Investigate the Mechanisms of Composite Polymer Electrolytes (CPEs) to suppress solid electrolyte Interphase (SEI) Formation and Prevention of Polysulfide Dissolution in Li-S Batteries – Novel Composite Polymer Electrolytes (CPEs) of PVdF – HFP Derived by Electrospinning with Enhanced Li-ion Conductivities for Rechargeable Lithium – Sulfur Batteries

The results of the work in this specific aim has been published in the ACS Applied Materials & Interfaces, 1, 483−494, 2018 (https://doi.org/10.1021/acsaem.7b00094)

Pavithra M Shanthi[a], Prashanth J Hanumantha[b], Taciana Albuquerque[c], Bharat Gattu[a], Prashant N Kumta[a, c, d, e]

[a]Department of Chemical and Petroleum Engineering,
University of Pittsburgh, Pittsburgh, PA 15261 (USA)

[b]Department of Bioengineering,
University of Pittsburgh, Pittsburgh, PA 15261 (USA)

[c]Department of Chemical Engineering,
Arizona State University, Tempe, AZ 85287 (USA)

[d]Department of Mechanical Engineering and Materials Science,
University of Pittsburgh, Pittsburgh, PA 15261 (USA)

[e]Center for Complex Engineered Multifunctional Materials,
University of Pittsburgh, Pittsburgh, PA 15261 (USA)

6.1 Synopsis

Composites of poly (vinylidene fluoride – co – hexafluoro propylene) (PVdF – HFP) incorporating 10 wt. % Bis(trifluoromethane)sulfonimide lithium salt (LiTFSI) and 10 wt. % particles of nanoparticulate silica (nm-SiO_2), nanoparticulate titania (nm-TiO_2) and fumed silica (f-SiO_2) were prepared by electrospinning. These membranes served as host matrix for the preparation of composite polymer electrolytes (CPEs) following activation with lithium sulfur battery electrolyte comprising 50/50 vol% Dioxolane/Dimethoxyethane with 1 M LiTFSI and 0.1 M $LiNO_3$. The membranes consist of layers of fibers with average fiber diameter of 0.1–0.2 μm. CPEs with f-SiO_2 exhibited higher ionic conductivity with a maximum of 1.3×10^{-3} S cm^{-1} at 25 °C obtained with 10 wt. % filler compositions. The optimum CPE based on PVdF – HFP with 10 wt% f-SiO_2 exhibited enhanced charge–discharge performance in Li – S cells at room temperature eliminating polysulfide migration, delivering initial specific capacity of 895 mAh g^{-1} at 0.1 C-rate and a very low electrolyte/sulfur (E/S) ratios between 3:1 to 4:1 ml.g^{-1}. The CPEs also exhibited very stable cycling behavior well over 100 cycles (fade rate ~0.056%/cycle), demonstrating their suitability for Li – S battery applications. In addition, the interconnected morphological features of PVdF – HFP result in superior mechanical properties (200-350% higher tensile strength). Higher Li-ion conductivity, higher liquid electrolyte uptake (>250%) with dimensional stability, lower interfacial resistance and higher electrochemical stability are some of the attractive attributes witnessed with these CPEs. With these improved performance characteristics, the PVdF – HFP system is projected herein as suitable polymer electrolytes for high-performance Li – S rechargeable batteries.

Key words: Lithium sulfur battery; composite polymer electrolyte; nanoparticle fillers; polymer membranes; low electrolyte (E)/sulfur (S) ratio; mechanical properties; electrochemical stability

6.2 Introduction

Lithium battery technology over the last two decades has witnessed unprecedented development due to the incessant increased demand for ever – increasing portable electronic devices and the all-pervading reality of hybrid electric vehicles. Portable electronic devices and the personal digital assistants (PDAs) in use today are already utilizing secondary lithium – ion batteries (LIBs)[1, 2], which are as yet not economical for large scale plug – in hybrid applications. In addition, there is an increasing concern associated with the safety of LIBs drawing considerable attention of researchers targeting the development of high energy density, leak – free and flexible lithium polymer batteries with improved safety [3, 4].

Though the field of LIBs has witnessed tremendous progress, transition metal oxide and phosphate – based systems are still the dominant archetypical systems used as cathodes exhibiting a maximum theoretical capacity of ~200-300 mAh/g[5, 6]. This specific capacity limitation, along with the ensuing high costs and ecological concerns associated with these materials restricts their application in large – scale devices.

Lithium – sulfur battery (Li – S) technology has in recent years been considered and widely investigated as a potential alternative and more importantly, a much more economically favorable system that could realize expedient technology translation for use in current LIBs. The system also boasts superior theoretical capacity (1674 mAh/g) and specific energy density (2600 Wh/kg)[315] of the cost effective elemental sulfur in comparison with conventional cathode materials. In addition to the low cost, the large abundance, and environmentally friendly attributes of sulfur make it a promising candidate cathode material for large scale energy storage applications. However, lithium – sulfur batteries suffer from inefficient utilization of the active material due to the insulating nature of sulfur[12, 13]. The lithium polysulfides formed during the

electrochemical cycling of sulfur are highly soluble in organic liquid electrolytes leading to loss of active material which in turn results in poor cyclability[14, 15]. Improved active material utilization can be achieved by embedding the electrochemically active sulfur into a conducting carbonaceous[16-19] or polymer matrix forming composites[20-23]. This technique provides a conducting network for sulfur hence, improving the conductivity of the composite. Other approaches to improve the capacity of Li – S battery involve the use of chemical interactions of polysulfides with transition metal oxides[24, 25] and trapping of sulfur into porous structures[26-29] preventing their dissolution. Though these approaches can increase the active material utilization of sulfur cathodes, they unfortunately, do not completely prevent the polysulfide species from dissolving into the electrolyte[30].

Another approach to reduce the dissolution of sulfur is to modify the electrolyte by replacing it with an ionic liquid electrolyte[16, 196, 202, 316], polymer electrolyte[13, 79, 211, 317-319] or even Li-ion conducting solid electrolytes [320-323]. Among these approaches addressing modification of the electrolyte, replacing the liquid organic liquid electrolytes with polymeric electrolytes is certainly a highly promising and has proven to be an effective approach[210]. In general, a polymer electrolyte may be defined as a membrane with transport properties similar to liquid ionic electrolytes[4, 324]. Polymer electrolytes, originally developed for the lithium ion battery system[325-328] could be modified for application in lithium sulfur batteries. All the polymer systems are conveniently grouped into two broad categories namely, solid polymer electrolytes (SPE) and gel polymer electrolytes (GPE).

Solid polymer electrolytes (SPE) are composed of a lithium salt (e.g., $LiPF_6$, $LiCF_3SO_3$, $LiC(CF_3SO_2)_3$) dissolved in high molecular weight polymers such as polyethylene oxide (PEO) or polypropylene oxide (PPO), with the polymer acting as a solid solvent[212, 329]. SPE conducts

ions through local segment motion of polymer unfortunately, resulting in poor ionic conductivities. The second class of polymer electrolyte, GPE on the other hand, is obtained by incorporating liquid electrolyte into a polymer matrix that forms a stable gel polymeric host, resulting in high ionic conductivities[324, 330]. Other unique advantages of GPEs over liquid electrolyte includes no internal short – circuiting and moreover, allowing minimal electrolyte leakage that is highly conducive to prevention of polysulfide dissolution, an inherent problem of Li-S batteries as outlined above [331-334]. The prerequisites of GPEs for lithium – sulfur batteries includes the following: high ionic conductivity at ambient and non – ambient temperatures, high transference number[335], good mechanical strength[332], good thermal and electrochemical stability as well as compatibility with electrodes[333, 334]. In addition GPEs have the ability to act as a physical barrier to prevent the dissolution of polysulfide ions from the cathode and subsequently depositing at the anode[336]. Identification of an effective system combined with a suitable and yet very effective fabrication process could catapult the system into being a highly attractive vehicle for translational implementation in commercial Li-S rechargeable battery systems. An approach that is highly amenable for generation of GPE, electrospinning which is an efficient fabrication process that gives porous and fibrous membranes with average diameters ranging from 100 nm to 5 μm[337], which are at least one or two orders of magnitude smaller than the fibers produced from other fiber fabrication processes such as melt and solution spinning. Electrospinning technology has recently made strides into various fields such as preparation of porous filters, myriad biomedical scaffold and device materials, reinforcing components, cloths for electromagnetic wave shielding, sensors, electronic devices, etc., [338, 339]. Electrospun mats of conventional polymer composites have also been used as electrolytes for lithium batteries[326, 328, 330, 340, 341]. These electrospun polymer electrolytes show superior mechanical and ionic properties

due to their unique fibrous structure. However, to date, there is no known reports on using electrospun polymer membranes as electrolytes for lithium – sulfur batteries. In the present study, poly (vinylidene fluoride – co – hexafluoro propylene) (PVdF – HFP) based CPEs (Composite Polymer Electrolytes) were prepared by a simple electrospinning technique. Further, nanoparticulate SiO_2(nm-SiO_2), TiO_2(nm-TiO_2) prepared using a simple sol – gel based nano fabrication technique[342, 343] and commercially available fumed SiO_2(f-SiO_2) were also used as fillers to augment the mechanical and Li-ion conducting properties of these CPEs among other necessary ionic transport requirements. These nanofiller incorporated PVdF – HFP composite polymer electrolytes as separator – electrolytes were then tested to demonstrate their improved cycling stability using commercial sulfur as cathodes in Li – S batteries, the results of which are described and discussed in the present manuscript.

6.3 Experimental Section

6.3.1 Materials

The polymer Poly (vinylidene fluoride – co – hexafluoropropylene) (PVdF – HFP) (Mw ~400,000, Aldrich), solvents N, N – Dimethylformamide (DMF) (ACS reagent, ≥99.8%, Aldrich), Acetone (ACS reagent, ≥99.5%, Aldrich) and lithium salt, Bis(trifluoromethane)sulfonimide lithium salt (LiTFSI) (99.95% trace metals basis, Aldrich) used for the electrospinning process were vacuum dried for 12 h at 60ºC before further use. Commercially available fumed silica, f-SiO_2 (0.007 μm powder, Aldrich) was used as-received in this work without any further treatment. Reagents for synthesizing nm-sized SiO_2 and nm-

sized TiO_2 nanoparticles which include, Tetraethyl orthosilicate (TEOS) (99.99%, Aldrich), Titanium(IV) isopropoxide (TTIP) (97%, Aldrich), ethanol (99.99%, Aldrich), 2-Propanol (ACS reagent, ≥99.5%, Aldrich), Hydrochloric acid (ACS reagent, 37%, Aldrich) and ammonium hydroxide (ACS reagent, 28.0-30.0% NH_3 basis, Aldrich) were used without any further purification. Finally, Milli-Q water (18.2 Ω) was used throughout the entire experiment.

6.3.2 Preparation of PVdF-HFP Nanofiber Membrane

The composite polymer electrolytes, CPEs of PVdF – HFP (10 w%) and LiTFSI (0.1 w%) were prepared by dissolving the components in a mixed solvent of DMF/acetone (7:3, w/w) at 50ºC for 12 h until a homogeneous solution was formed. The resulting solution was dispersed with (0.1 wt. %) nano – filler (nm-SiO_2/nm-TiO_2/f-SiO_2) under sonication for 12 h. The CPEs were prepared by a typical electrospinning method at room temperature. Electrospinning of the nano – filler dispersed solution was performed at a flowrate of 1 ml/h and a high voltage of 20 kV at room temperature with 15 cm distance maintained between the tip of the syringe and the rotating drum. The nanofibers deposited onto the rotating drum were then collected, dried under vacuum for 12 h at 60ºC at 1 atm. The nanofiber mats were then heat pressed at 80ºC for 30 min at 1 atm. pressure and activated by soaking in 1.8 M LiTFSI and 1 M $LiNO_3$ in 1:1 vol% Dioxolane/Dimethoxy ethane for 30 min before use as separator – electrolyte complex in Li – S battery.

6.3.3 Preparation of SiO_2 Nanoparticles

The nanoparticles of SiO_2, were prepared by hydrolysis of TEOS in ethanol medium in the presence of ammonium hydroxide as reported by Roy et al[342]. Initially, 3ml TEOS was mixed with 20 ml ethanol under sonication. 20 ml ammonium hydroxide solution (28-30%) was then added to this solution under sonication to promote the condensation reaction. The white turbid solution of SiO_2 nanoparticles was centrifuged and then dried under vacuum for 12 h. The SiO_2 nanoparticles was heated at 700^oC for 4 h to remove any carbon residues.

6.3.4 Preparation of TiO_2 Nanoparticles

The nanoparticles of TiO_2 were also similarly prepared by the hydrolysis of TTIP in propyl alcohol following the published method[344]. Accordingly, 5 ml TTIP was dissolved in 10 ml isopropyl alcohol, and then the solution is added dropwise into 40 ml water containing 2.5 ml HCl under sonication. The colloidal solution is then filtered and dried under vacuum for 12 h. The fine powders of TiO_2 obtained after drying are then calcined at 800^oC for 3 h.

6.3.5 Materials Characterization and Electrochemical Measurements

It is important to understand the nature of the nanoparticulate fillers and the electrospun CPE membranes to explain the observed cycling stability. Accordingly, to investigate the microstructure of the nanofillers and electrospun CPE membranes, scanning electron microscopy (SEM) analysis was conducted on a Philips XL30 machine operating at 20 kV. The crystal structure of the synthesized nm-TiO_2, nm-SiO_2 and f-SiO_2 nanoparticles were characterized by

X- ray diffraction using Philips XPERT PRO system employing CuKα (λ = 0.15406 nm). The scans were recorded in 2θ range of 10° - 90°, at a constant current of 40 mA and voltage of 45 kV. The average particle size of nm-SiO_2 and nm-TiO_2 was determined by conducting Dynamic light scattering (DLS) experiments in a Malvern Zetasizer Nano ZS90. Samples for the DLS experiment were prepared by dispersing in DI water (0.01 g/ml) after being wetted in iso-propanol to determine the average particle size. The nature of chemical bonding in the CPEs were further analyzed by attenuated total reflectance Fourier transform infrared spectroscopy (ATR-FTIR, Nicolet 6700 spectrophotometer, Thermo Electron Corporation) using a diamond ATR Smart orbit. Spectra were obtained at 1 cm^{-1} resolution averaging 64 scans in the 400–4000 cm^{-1} frequency range. The surface chemistry of the CPEs were probed by X-ray photoelectron spectroscopy (XPS) using an ESCALAB 250 Xi system (Thermo Scientific) equipped with a monochromated Al Kα X-ray source. Beams of low-energy (≤10 eV) Ar^+ ions and low-energy electrons guided by magnetic lens were used to provide uniform charge neutralization. The standard analysis spot of 400×400 μm^2 was defined by the microfocused X-ray source. The measurements were performed at room temperature in an ultra-high vacuum (UHV) chamber with the base pressure $<5*10^{-10}$ mbar (the charge neutralization device produced $2*10^{-10}$ mbar partial pressure of Ar during measurements). The Avantage software package (Thermo Fisher Scientific) was used to fit the elemental spectra based on calibrated analyzer transmission functions, Scofield sensitivity factors, and effective attenuation lengths for photoelectrons from the standard TPP-2M (Tanuma Powell and Penn -2M) formalism. The mechanical properties of the CPEs also need to be evaluated in order to explain the improved electrochemical performance of the CPEs. Accordingly, the stress–strain behavior of the polymer membranes was studied using Instron Universal Tensile Tester, Model 1123. The pore characteristics and

specific surface area (SSA) of the nano filler samples were analyzed on a Micromeritics ASAP 2020 Physisorption analyzer, using the Brunauer–Emmett–Teller (BET) isotherm generated. The powders were first vacuum degassed and then tested for Nitrogen adsorption and desorption for the specific surface area analysis.

6.3.6 Electrochemical Characterization

Electrodes for battery half-cell characterization were prepared by casting a slurry of 70 wt. % commercial sulfur, 20 wt. % acetylene black and 10 wt. % PVdF in N- Methyl Pyrrolidone (NMP) onto aluminum foil followed by drying under vacuum for 24 h. A uniform electrode sulfur loading varying between 1.5 mg – 2 mg cm/cm^2 was utilized for all the electrochemical measurements. 2025 – type coin cells were assembled in Innovative, Inc. glove box (UHP Argon, <0.1 ppm O_2, H_2O) utilizing slurry coating approach. Accordingly, sulfur electrodes formed the working electrode, lithium foil as the counter electrode, and the electrospun CPE membranes soaked in liquid electrolyte (1:1 vol% 1, 3 dioxolane and 1, 2 dimethoxyethane with 1.8 M LiTFSI (Bis(trifluoromethane)sulfonamide lithium salt) and 0.1 M $LiNO_3$) as the electrolyte/separator complex. The E/S ratios used in the CPE membranes was between 3:1 and 4:1 ml g^{-1}. Control samples were prepared under identical conditions replacing the CPE with 100 µl liquid electrolyte and Celgard 2400 polypropylene (PP) membrane as the separator. The E/S ratio in the control samples was maintained between 50:1 to 65:1 ml g^{-1}. The electrochemical cycling behavior of the cells thus prepared was studied by cycling between 1.7 – 2.6 V (w.r.t. Li^+/Li) at 0.1 C (~162 mA/g) current rate using an Arbin BT200 battery testing system. Ionic conductivity of CPEs was studied using AC impedance spectroscopy in Gamry Potentiostat. The

polymer membranes were accordingly secured between two steel disks and data was collected in the high frequency range (10–100 kHz). Equivalent circuit modeling was performed using the Z-view 2.0 (Scribner Associates Inc.) to obtain the CPE ionic conductivity values.

6.4 Results and Discussion

6.4.1 SEM Analysis of Nanofiller Particles

Figure 6-1 shows the morphology of nm-SiO_2, nm-TiO_2 and f-SiO_2 nanoparticles studied using Scanning Electron Microscopy (SEM). The nm-SiO_2 and nm-TiO_2 **(**Figure 6-1a, b**)** were observed to be spherical with a uniform particle size distribution similar to the observations reported in the reference method followed[342]. The nm-SiO_2 nanoparticles had an average particle diameter of ~200 nm which was further confirmed by Dynamic Light Scattering (DLS) technique. The nm-TiO_2 particles were almost spherical shaped with ~150 nm diameter. The SEM of f-SiO_2 was performed at a higher magnification **(**Figure 6-1c**)**, showing agglomerates of nano – meter sized individual particles. This is similar to the observations made by Zhou et al [345] confirming the extremely small (~7nm) particle size of f-SiO_2 mentioned in the product specification (Sigma Aldrich, Inc.). The XRD patterns obtained from both nm-SiO_2 and f-SiO_2 showed patterns that correspond to amorphous structures, indicating the amorphous nature of both the SiO_2 samples. However, the XRD pattern of TiO_2 showed crystalline peaks corresponding to the anatase structure. (Appendix D Figure 1).

6.4.2 Specific Surface Area Analysis

Specific surface area of the nanofillers is an important factor deciding the electrochemical performance of the CPEs. It has been observed that smaller size particles for a similar volume fraction of the ceramic filler phase would impart an improved performance as compared to larger size particles because of their ability to cover more surface area[346]. The BET surface area analysis of the nanofillers are presented in Table 6-1. The BET surface area results indicate that f-SiO_2 has a high BET surface area of 191.61 m^2/g which is closer to the value (175-225 m^2/g) from the product specifications. f-SiO_2 also exhibits a high pore volume of 0.417 cm^3/g.

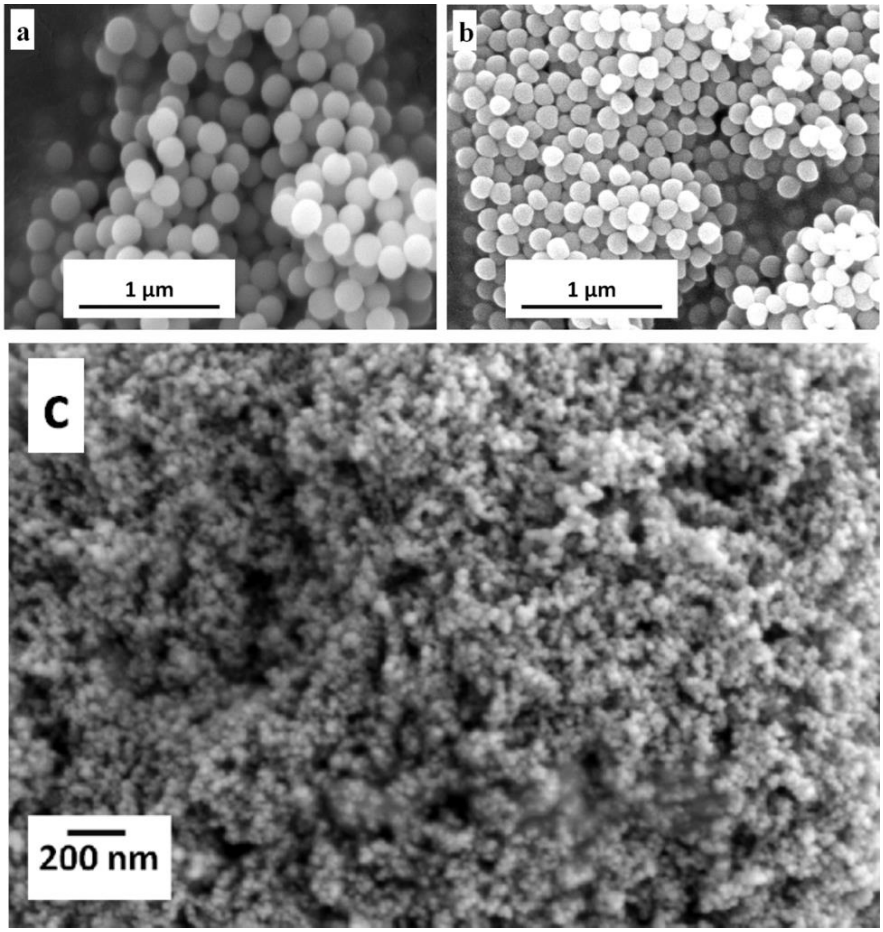

Figure 6-1 SEM images of a) nm-SiO_2 and b) nm-TiO_2 and c) f-SiO_2.

Table 6-1 BET surface area analysis of nm-SiO_2, nm-SiO_2 and f-SiO_2. Each data represents an average of three independent tests run on three different samples under identical conditions.

Sample	BET Surface Area (m^2/g)	Langmuir Surface Area/ (m^2/g)	Total Pore Volume (cm^3/g)	Adsorption average pore width (nm)
f-SiO_2	191.61±7.23	329.19±9.14	0.42±0.06	8.72±1.04
nm-SiO_2	18.03±1.16	22.36±1.92	0.21±0.02	7.96±0.92
nm-TiO_2	6.47±0.72	10.18±0.65	0.17±0.03	10.90±0.75
Celgard 2400	46.42±3.54	52.62±6.91	0.12±0.01	24.64±1.62
Electrospun PVdF-HFP	63.56±2.34	71.92±5.68	0.18±0.03	14.24±0.56
PVdF-HFP + f-SiO_2	217.20±6.25	342.5±11.68	0.53±0.06	14.42±0.86
PVdF-HFP + nm-SiO_2	99.04±5.83	100.02±6.98	0.25±0.04	15.20±0.49
PVdF-HFP + nm-TiO_2	72.60±3.76	86.50±5.63	0.21±0.03	12.20±0.21

On the other hand, the nm-SiO_2 and nm- TiO_2 showed lower surface area of 18.03 and 6.47 m^2/g respectively. The very high surface area of f-SiO_2 is expected to improve the performance of CPEs over other fillers. Table 6-1 also shows the specific surface areas and porosities of nm-SiO_2, f-SiO_2 and nm-TiO_2 incorporated PVDF – HFP hybrid membranes. For

comparison, the porosity of a commercial polypropylene (PP) membrane separator (Celgard 2400) is also shown. The BET surface area of the polypropylene membrane is 46.42 m^2/g comparable to the values reported in the literature[347, 348]. The porosities of these hybrid membranes are significantly greater than that of microporous PP membrane. The PVDF – HFP nanofibers form free-standing nonwoven membranes that have relatively high porosities. The introduction of nm-SiO_2 and nm-TiO_2 nanoparticles further increases the porosity values due to the extra surface area of nanoparticles. However, owing to the very high surface area of f-SiO_2 the BET surface area of f-SiO2 incorporated PVdF – HFP membrane was found to be 217.2 m^2/g, almost twice higher than that of the other nanofiller counterparts.

6.4.3 SEM Analysis of the Nanofibers

The electrospun polymer mats are usually required to be of uniform fiber thickness with a bubble – free morphology to serve as effective battery separators for use in battery applications, [327]. Formation of bubble-like structures usually results in non – uniform pore distribution in the mats and a decrease in the nanofiller exposure on the surface[50]. To understand the morphological characteristics of the membranes, the electrospun polymer mats were analyzed using the scanning electron microscopy technique. The SEM micrographs of PVDF-HFP membranes with 10 wt. % dissolved LiTFSI **(**Figure 6-2a**)** shows an inter – penetrated fibrous network possibly resulting in an improvement in the mechanical strength of the CPEs. The membranes also exhibit a uniform and bead free morphology with fibers of ~175 nm diameter. SEM images of PVdF-HFP + LiTFSI membranes with dispersed 10 wt. % f-SiO_2 **(**Figure 6-2b**)** indicates that the introduction of nanofillers does not change the morphology of the electrospun PVDF nanofibers. The nanoparticles of f-SiO_2 (~7nm) are both embedded inside the nanofibers and dispersed on

the fiber surface which is clearly observed in the SEM EDS mapping of the filler incorporated polymer mats **(**Appendix D Figure 2**)**, similar to the observations of Sethupathy et al.[349] in their reported studies on SiO_2 incorporated electrospun PVdF-HFP membranes. However, with PVdF-HFP + LiTFSI membranes containing 10wt% nm-SiO_2 and nm-TiO_2 nanofillers, the surface of the membranes (Figure 6-2c&d) appears to show larger aggregates of the nanofiller particles. This is mainly attributed to the larger particle size of the nm-SiO_2 (~200nm) and nm-TiO_2 (~150nm), respectively in comparison with f-SiO_2 (~7nm). Correspondingly, the small particle size of f-SiO_2 render it more amenable to be uniformly distributed, as a result, the SEM image correspondingly shows the matt morphology with the f-SiO_2 nanoparticles more uniformly dispersed and integrated into the surface structure. The surface roughness increased upon introduction of nanofillers, while the average diameter of nanofibers was largely unaffected. The exposure of nm-TiO_2, nm-SiO_2 and f-SiO_2 nanofillers on the fiber surfaces results in increasing the accessible surface area and form extensive Lewis acid/base interactions with the ionic species in the liquid electrolyte possibly resulting in higher ionic conductivities[350].

Solairaj et al studied the effect of SiO_2 nanofiller composition on the surface morphology, electrolyte uptake, membrane porosity and ionic conductivity[351]. Their study indicates that the ionic conductivity and electrolyte uptake of the polymer membranes increases with nanofiller concentration, decreasing steadily beyond 10wt% SiO_2 composition. Similar observations were made by Stephan et al and Angiah et al in their study on the effect of aluminum oxyhydroxide, $(AlO[OH]_n)$[352] and ZrO_2[353], respectively. Accordingly, in order to obtain high electrolyte uptake, membrane porosity and ionic conductivity, considering the results of the above explained researchers, a nanofiller composition of 10wt% of the selected nanofillers (f-SiO_2, nm-SiO_2, and nm-TiO_2) was also used in this study.

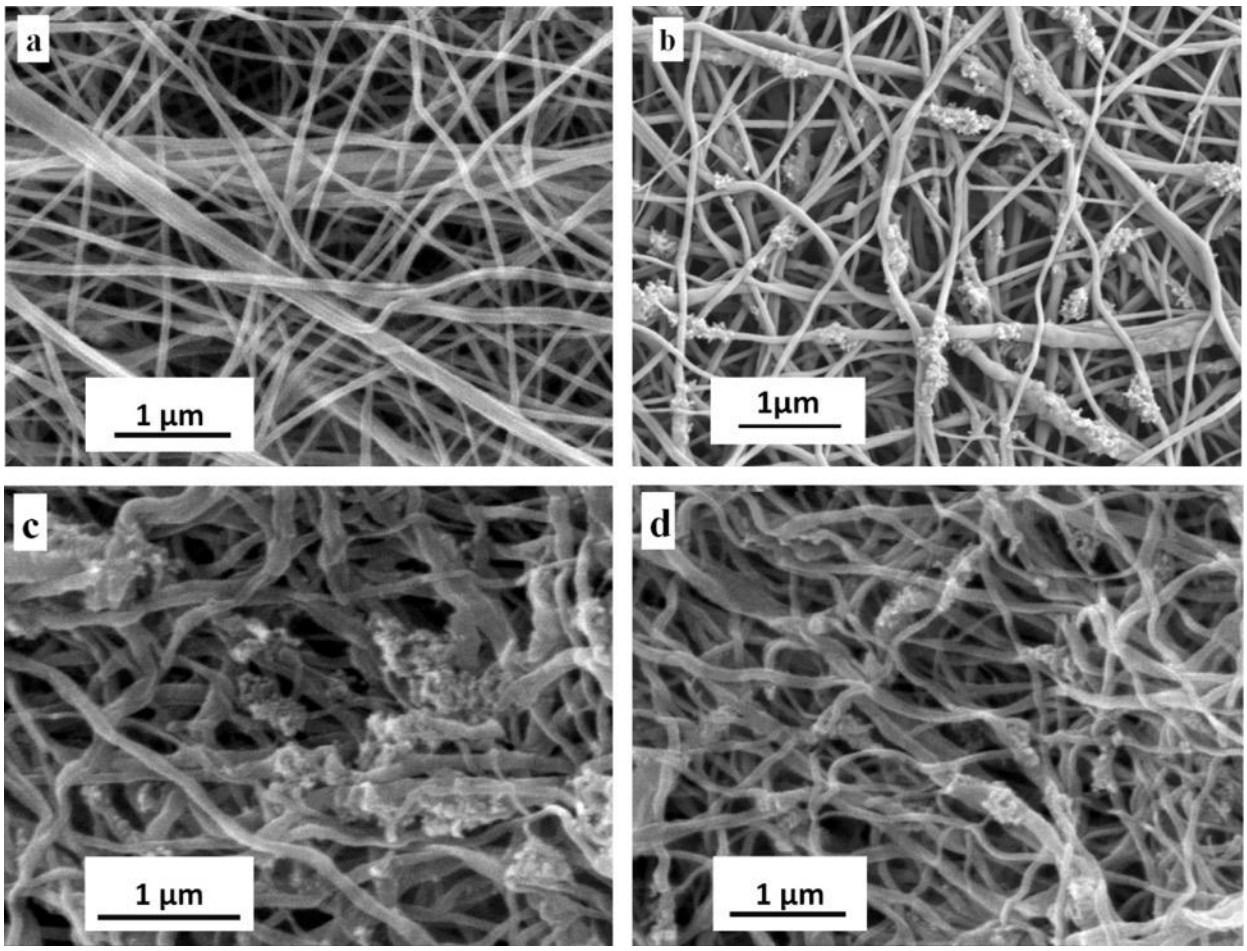

Figure 6-2 SEM images of a) electro spun PVdF-HFP polymer membranes with dissolved LiTFSI, b) electro spun PVdF-HFP with dissolved LiTFSI(10 wt%) and dispersed f-SiO_2(10 wt%) c) electro spun PVdF-HFP with dissolved LiTFSI(10 wt%) and dispersed nm-SiO_2(10wt%) and d) electro spun PVdF-HFP with dissolved LiTFSI(10wt%) and dispersed nm-TiO_2(10wt%).

6.4.4 FTIR Analysis

Any change in the chemical nature of PVdF-HFP membranes upon addition of LiTFSI salt and nanofillers (f-SiO_2, nm-SiO_2 and nm-TiO_2) needs to be understood in order to predict the chemical stability of the CPEs during electrochemical cycling[354]. The nature of the chemical bonding in PVdF-HFP and LiTFSI **(**Figure 6-3 and Appendix D Figure 3**)** was accordingly

analyzed using FTIR spectroscopy for comparison with LiTFSI incorporated polymer membranes. PVdF-HFP being a semi-crystalline polymer, the FTIR spectra of pure PVdF-HFP contains some crystalline (α-phase) and amorphous (β-phase) phase related peaks. The bands of pure polymer PVdF-HFP due to the crystalline phase (α-phase) are observed at 489, 532, 614, 762, 796 and 976 cm^{-1}, while the bands related to the amorphous phase (β-phase) are observed at 839 cm^{-1} and 879 cm^{-1}[327] which are individually indexed and explained in Appendix D Table 1.

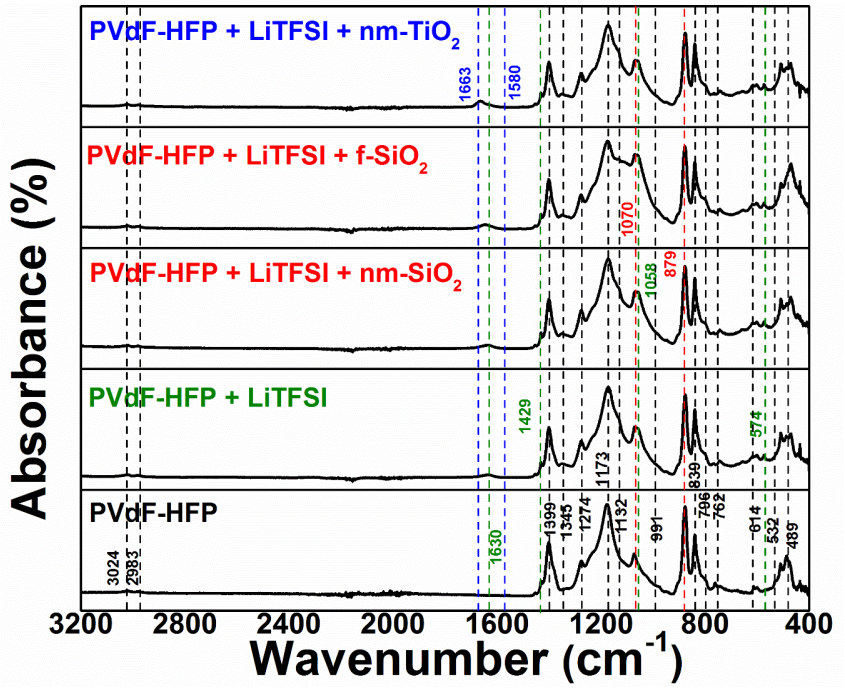

Figure 6-3 FTIR spectra of pure PVDF-HFP, PVDF-HFP with 10 wt. % LiTFSI and various nanofillers (10 wt. %).

Addition of LiTFSI to the PVdF-HFP membranes introduces three distinct peaks at 1058, 1630 and 574 cm^{-1}[327] in the FTIR spectrum, in addition to the peaks corresponding to PVDF-HFP polymer. These observations exactly overlap with the findings of Shalu et al. related to the FTIR analysis of the interaction of LiTFSI with PVdF-HFP[327] according to which the

peaks at 1058 and 574 cm^{-1} are due to the asymmetric -S-N-S- stretching of LiTFSI and asymmetric CF_3 bending vibrations of LiTFSI salt, respectively. Furthermore, the peak at 1630 cm^{-1} is due to the complexation between the polymer backbone and LiTFSI salt. The retention of all the characteristic peaks of PVdF-HFP even upon addition of LiTFSI indicates the absence of any form of chemical reaction between the polymer and the salt.

Comparing the spectra of PVdF–HFP before and after incorporation of the nano fillers (Figure 6-3), the intensity of the broad band centered at 1070 cm^{-1} clearly increases for SiO_2 incorporated PVdF–HFP using the C–F symmetric stretching band at 879 cm^{-1} as reference[355]. This is due to the overlap of the band from the F–C–F symmetric stretching vibration at 1072 cm^{-1} and the band from the Si–O–Si antisymmetric stretching vibration at 1070 cm^{-1}[1356], indicating the binding of Si-O- to the polymer.

In the case of the PVDF–HFP membranes incorporated with TiO_2, the NH_2 group usually observed at 1600 cm^{-1} is shifted to the lower wave number around 1580 cm^{-1}[1357]. In addition, the peak at 1663 cm^{-1} becomes prominent due to enhanced -C=O stretching owing to the interaction with TiO_2[358].This indicates the fact that a greater number of ions coordinate with $–NH_2$. The new interaction of the nanofiller, $–TiO_2$ and TiO_2–polymer in the FTIR spectra of PVDF–HFP hybrid membranes can be expected to improve the ionic conductivity of the system on the fiber surface.

6.4.5 Mechanical Properties

The mechanical properties of the electrospun polymer membranes are very important for effective application in batteries as separators. In the electrospun membranes, mechanical properties are expected to be improved due to entanglement of singular fibers aided by the

presence of nanoparticle fillers [328]. The mechanical properties of the electrospun membranes were compared with that of solution cast membranes of the same composition to demonstrate the superior properties attained by the electrospinning method. The thickness of both electrospun and solvent cast membranes used for mechanical property measurements was maintained uniformly at 0.035±0.005 mm. The Strain Vs Stress and Tensile Strength of the hybrid membranes characterized by tensile measurements are represented in Figure 6-4a. Both the solvent cast and electrospun samples exhibited a linear elastic behavior comparable to the results from similar systems reported in literature [354, 359]. The tensile strength of the electrospun membranes is uniformly superior to that of solvent cast membranes due to the enhanced elastic nature of the electrospun membranes as explained by Blond et al on his work comparing the mechanical properties of electrospun and solvent – cast membranes[360]. For example, the tensile strength increased from 650.73 MPa for solvent cast PVdF – HFP + LiTFSI + nm-TiO_2 membrane to 1409.92 MPa for electrospun membranes, **(**Figure 6-4b**)** confirming the effect of electrospinning on improving the tensile properties of the hybrid membranes.

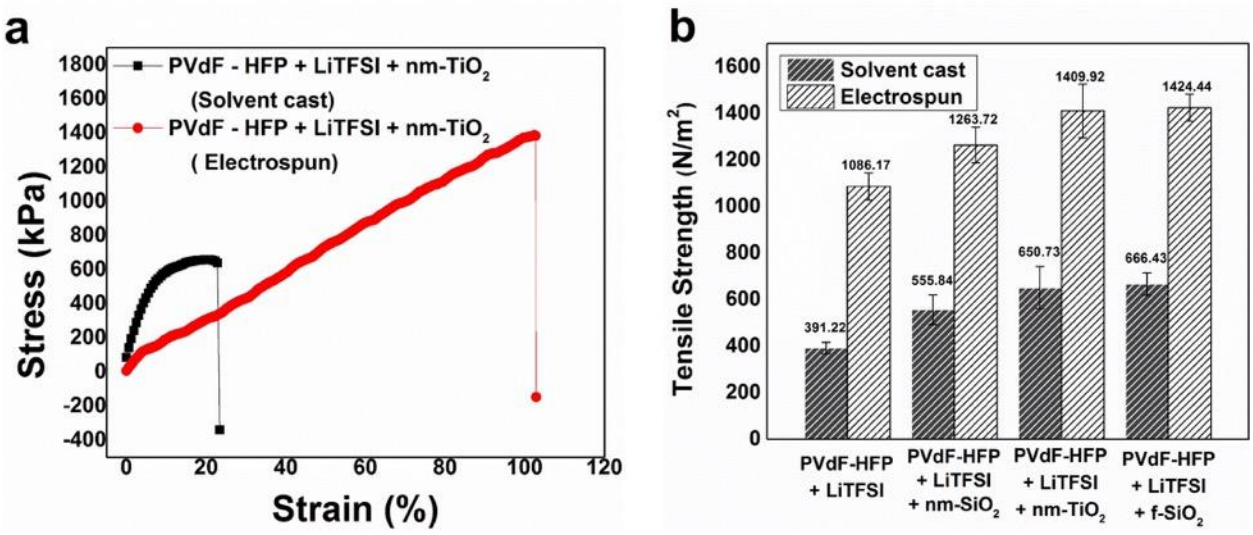

Figure 6-4 a) Stress Vs Strain relationship of nm-TiO2 incorporated membranes and b) Comparison of Tensile strengths of various electrospun and solvent cast membranes. Each data represents an average of three independent tests run on three different samples under identical conditions.

In addition to the improved mechanical properties, flame retarding ability of the CPEs is an important factor that determine the safety of the lithium ion battery[361, 362]. The CPEs soaked in electrolyte were thus, subjected to combustion test by exposing them to heat for 60 seconds. Commercial Celgard 2400 PP separators soaked in electrolyte was also exposed to the same conditions, the results of which are shown in Appendix D Figure 4. The commercial separator shrunk immediately after exposing to the flame. However, the CPEs remained unaffected by the heat exposure generated by the flame for more than 60s and the dimensions of the CPE membranes also remained unaltered confirming the absence of shrinkage due to the high temperature exposure generated from the flame. These results show that the CPE membranes show better flame retarding properties and thermal stability, which would subsequently make them a safer alternative for use in lieu of commercial separators and electrolytes.

6.4.6 Electrolyte Uptake

Appendix D Figure 5 represents the relationship of electrolyte uptake of the nanofiber membranes with time, obtained by soaking the nanofiber membranes in the liquid electrolyte of 1.8 M LiTFSI and 0.1 M $LiNO_3$ in 1:1 vol% dioxolane and dimethoxyethane for a period of 30 min. The electrolyte uptake is observed to stabilize within the initial 10 minutes of exposure to electrolyte of all the hybrid polymer membranes[363]. The electrolyte uptake of f-SiO_2 membranes is ~219% which is about four times higher than the uptake of commercial polypropylene (PP) separator which is ~63%[364]. As expected, the higher pore volume of the f-SiO2 material (Table 6-1) results in the highest electrolyte uptake for the same (Table 6-2). Though the electrolyte uptake of these membranes were high, the E/S ratio in these membranes was considerably low, ranging between 3:1 to 4:1 ml g^{-1}. The high retention ability and faster penetration of liquid electrolyte into the fibrous membranes are due to the unique pores generated from the interconnected fibers, which in turn increase the ionic conductivity. PVDF – HFP + LiTSI membranes showed a very high uptake value ~550%, due to uncontrolled swelling of the membranes and lack of mechanical integrity owing to the absence of filler particles.

Table 6-2 Electrolyte uptake studies on the polymer membranes. Each data represents an average of three independent tests run on three different samples under identical conditions.

Sample	Electrolyte uptake after 10 min (%)	Electrolyte uptake after 30 min (%)	Electrolyte uptake after 60 min (%)
PVdF – HFP + LiTFSI	436.6±10.2	550±11.3	551.5±14.3
PVdF-HFP + LiTFSI + nm-SiO_2	182.5±7.8	190.5±8.6	190.5±9.2
PVdF-HFP + LiTFSI + f-SiO_2	207.5±13.4	219±14.9	220±10.7
PVdF-HFP + LiTFSI + nm-TiO_2	253.5±6.2	266.5±9.6	270±7.6
Commercial PP separator	59.5±2.5	63±4.1	63±2.7

6.4.7 Ionic Conductivity Studies

The most important requirement of CPEs is their room temperature Li-ion conductivity which needs to be closer to liquid electrolytes to display better electrochemical properties for potential applications in Li-ion batteries. EIS analysis of the CPEs was performed using stainless steel blocking electrodes on both sides. Nyquist plot of the EIS analysis of CPEs are shown in Figure 6-5a, b. The impedance plots were modeled to the general equivalent circuit using Z-view 2.0, shown in Figure 6-5c[365], where R_s represents the electrolyte resistance, C_{dl} represents the capacitive coupling between the ionic conduction in the electrolyte and the electronic conduction in the measuring circuit. Additionally, C_g is the geometrical capacitance representing the capacitive effects of the cell hardware and of the electrical leads[366]. The electrolyte conductivity was thus, calculated using R_s, thickness of the polymer membrane (t) and the surface are of the electrolyte sample, A using the equation (6-1) given below:

$$\sigma = \frac{t}{R_s A} \tag{6-1}$$

The room temperature conductivities of the polymer electrolytes are about ~10^{-3} S cm^{-1} which is in line with several reports[4, 324, 333, 367]. From the conductivity value of the electrolyte, it is seen that there is an increase in ionic conductivity of the CPE systems in comparison with the liquid electrolyte based separator. This is due to the enhanced electrolyte uptake due to the nanoporous structure of the electrospun membranes. The PVdF – HFP membranes with nm-SiO_2 fillers shows the highest room temperature conductivity of 9.48×10^{-3} S cm^{-1} (Table 6-3). This is slightly unexpected due to the higher uptake seen in the case of f-SiO_2 indicating that ionic conductivity in the composite polymer electrolytes depends not only on the electrolyte uptake (Appendix D Figure 5) and pore volume (Table 6-1) but also on the nature of the bonding of filler particles with the liquid electrolyte. Further studies are indeed warranted to obtain a good understanding of this unique phenomenon.

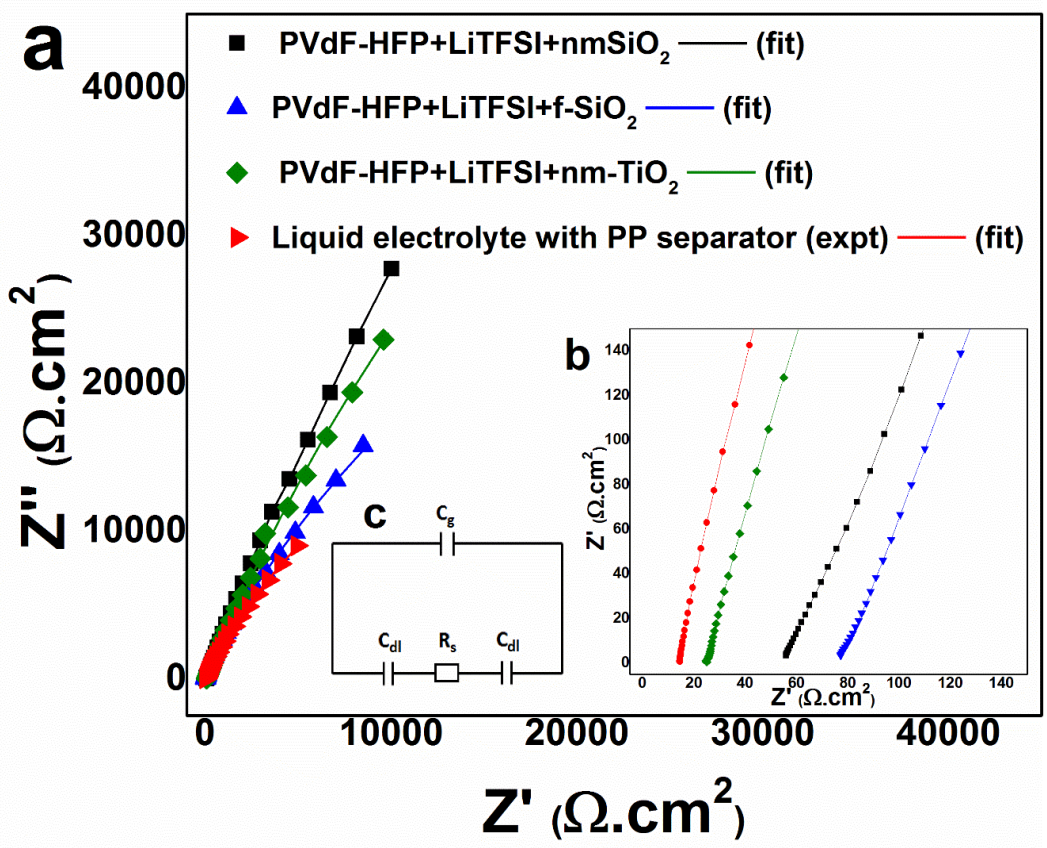

Figure 6-5 a) Fitted Nyquist plot of the polymer membranes, b) enlarged Nyquist plot (inset) and c) equivalent circuit used to fit the Nyquist plots (inset).

Table 6-3 Ionic conductivity of commercial electrolyte and various polymer membrane electrolytes. Each data represents an average of three independent tests run on three different samples under identical conditions.

Sample Composition	Conductivity (S cm^{-1})
Commercial separator with liquid electrolyte	$1.283 \pm 0.26 \cdot 10^{-3}$
PVdF-HFP + LiTFSI +nm-TiO_2	$1.881 \pm 0.14 \cdot 10^{-3}$
PVdF-HFP + LiTFSI + f-SiO_2	$3.009 \pm 1.65 \cdot 10^{-3}$
PVdF-HFP + LiTFSI + nm-SiO_2	$9.48 \pm 0.87 \cdot 10^{-3}$

6.4.8 Electrochemical Cycling Performance

The electrochemical performance of the PVdF – HFP composite polymer electrolytes were studied by performing electrochemical charge – discharge cycling against commercial sulfur cathodes. The electrochemical cycling performance and coulombic efficiencies of the polymer electrolytes are shown in Figure 6-6a**.** The PVdF – HFP – f-SiO_2 hybrid polymer separator shows an initial capacity of 895 mAh g^{-1} and a stable capacity of 845 mAh g^{-1} after 100 cycles (fade rate 0.055%/cycle). On the other hand, the PVdF – HFP – nm-SiO_2 shows an initial discharge capacity of 860 mAh g^{-1} which stabilizes at 734 mAh g^{-1} after the 100 cycles cycle (0.146%/cycle). The PVdF – HFP nm-TiO_2 separators showed an initial capacity of 915 mAh g^{-1} and stabilized at 749 mAh g^{-1}(0.18%/cycle). Accordingly, all the CPEs exhibited average coulombic efficiencies of 98-99% indicating the absence of capacity loss due to polysulfide dissolution. However, the cells containing the commercial separator along with liquid electrolyte cycled opposite commercial sulfur cathode gave an initial capacity of 557 mAh g^{-1} which quickly faded to 132 mAh g^{-1} in less than 10 cycles. The commercial separator containing cells exhibit an initial coulombic efficiency of 94.6% which quickly fades to 80% within the first 50 cycles, clearly indicating the presence of polysulfide dissolution resulting in loss in capacity and coulombic efficiency. The charge – discharge profiles of the cell with PVdF-HFP+LiTFSI+f-SiO_2 CPE membrane is also shown in Figure 6-6b. The charge – discharge profiles of the other two CPE membranes are shown in Appendix D Figure 6 a&b. The voltage profiles of all the CPEs at 1^{st}, 2^{nd}, 10^{th} and 100^{th} cycles feature the two characteristic discharge plateaus, the plateau at around 2.4 V corresponds to the transformation from the S_8 molecular forms of the polysulfide to a series of soluble polysulfides. On the other hand, the plateau at 2.1 V corresponds to the transformation of the L_2S_4 species to insoluble Li_2S_2 and Li_2S[100, 254]. The enhanced electrochemical

cycling performance of the f-SiO_2 incorporated CPE is attributed to the higher surface area and pore volume of the filler particles that facilitated the formation of an insulated layer of ceramic particles at the electrode surface serving to impede electrode reactions as explained by Kumar et al[346]. This phenomenon has been observed by Capuano et al when excessive amounts of the passive ceramic phase were introduced into the polymer matrix[368]. This insulation layer, in addition to impeding surface reactions facilitates prevention of polysulfide dissolution in Li- S battery, which explains the superior performance of the f-SiO_2 CPE over other fillers.

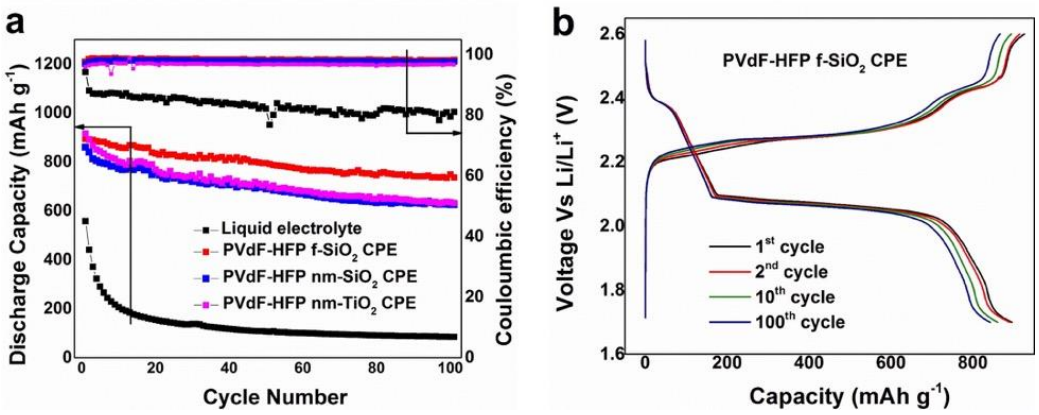

Figure 6-6 a) Electrochemical cycle performance and coulombic efficiencies of the different polymer membranes and b) charge – discharge profile of PVdF-HFP+LiTFSI+f-SiO_2 polymer membrane

6.4.9 XPS Analysis of Separators Post Cycling

X-ray photoelectron spectroscopy (XPS) analysis was performed on the polymer electrolyte separators after 100 cycles to understand the origin of the cycling stability of the hybrid polymer membranes. XPS was performed on both the side facing the sulfur cathode and the side facing lithium anode. Figure 6-7 represents the XPS of the polymer electrolyte membranes post cycling. The peak at 169.61 eV represents S2p peak corresponding to sulfur

binding in LiTFSI, the peak at 167.65 eV and 163.10 eV corresponds to the higher order polysulfide and Li_2S respectively. Commercial separator and liquid electrolyte cycled with sulfur cathodes shows peaks corresponding to both higher and lower order polysulfide confirming polysulfide dissolution in liquid electrolyte system. However, it should be noted that these polysulfide peaks are absent in polymer electrolyte membranes facing lithium anode confirming the absence of polysulfide dissolution into the electrolyte. On the other hand, the side of the fumed SiO_2 and TiO_2 incorporated polymer membrane facing the sulfur cathode shows very mild peak at 163.1 eV corresponding to Li_2S. This might be due to the surface adsorbed Li_2S molecules and not the dissolution of polysulfide.

6.4.10 FTIR Analysis Post Cycling

It is well-known that the structural and chemical stability of the polymer membranes are two important parameters that decide the long-time performance of polymer electrolytes. The XPS analysis of the CPE membranes after electrochemical cycling provided information about the binding energy changes on the surface of the membranes. To ascertain the changes in chemical properties occurring in the bulk of the membrane and to confirm the absence of polysulfides, FTIR analysis was performed on the membrane surface facing the lithium anode and the surface facing the sulfur cathode. Accordingly, the FTIR spectrum of PVdF – HFP + LiTFSI + SiO_2 separator (activated by soaking in 1.8 M LiTFSI and 1 M $LiNO_3$ in 1:1 vol% dioxolane and dimethoxy ethane for 30 min) before and after 100 charge – discharge cycles is shown in Figure 6-8**.** Similar studies on the f-SiO_2 and TiO_2 incorporated membranes showed identical results and are correspondingly tabulated in Appendix D Table 2**.**

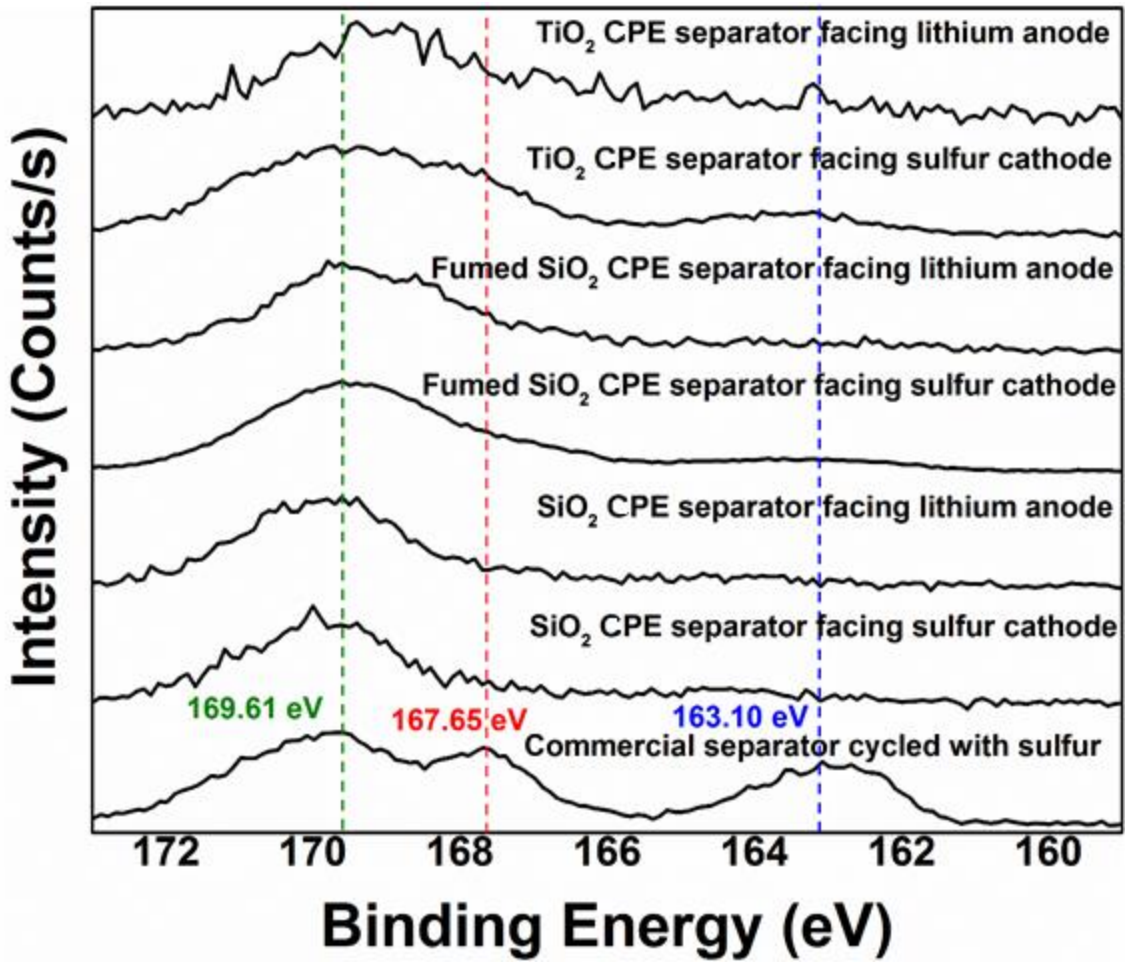

Figure 6-7 S2p spectrum of different separators before and after cycling.

The FTIR spectrum of PVDF – HFP + LiTFSI + SiO_2 membrane soaked in electrolyte shows peaks corresponding to PVdF – HFP as explained in Appendix D Table 2. In addition, the peak at 1032 cm^{-1} and 1070 cm^{-1} corresponds to the introduction of SO_3^- group and overlap of F-C-F symmetric stretching vibrations and Si-O-Si asymmetric stretching vibrations resulting from LiTFSI and SiO_2 respectively[369]. In addition, spectrum for the polymer membranes collected prior to cycling shows peaks at 509, 570, 684, 762, 1229, 1355, 2829 and 2960 cm^{-1}.

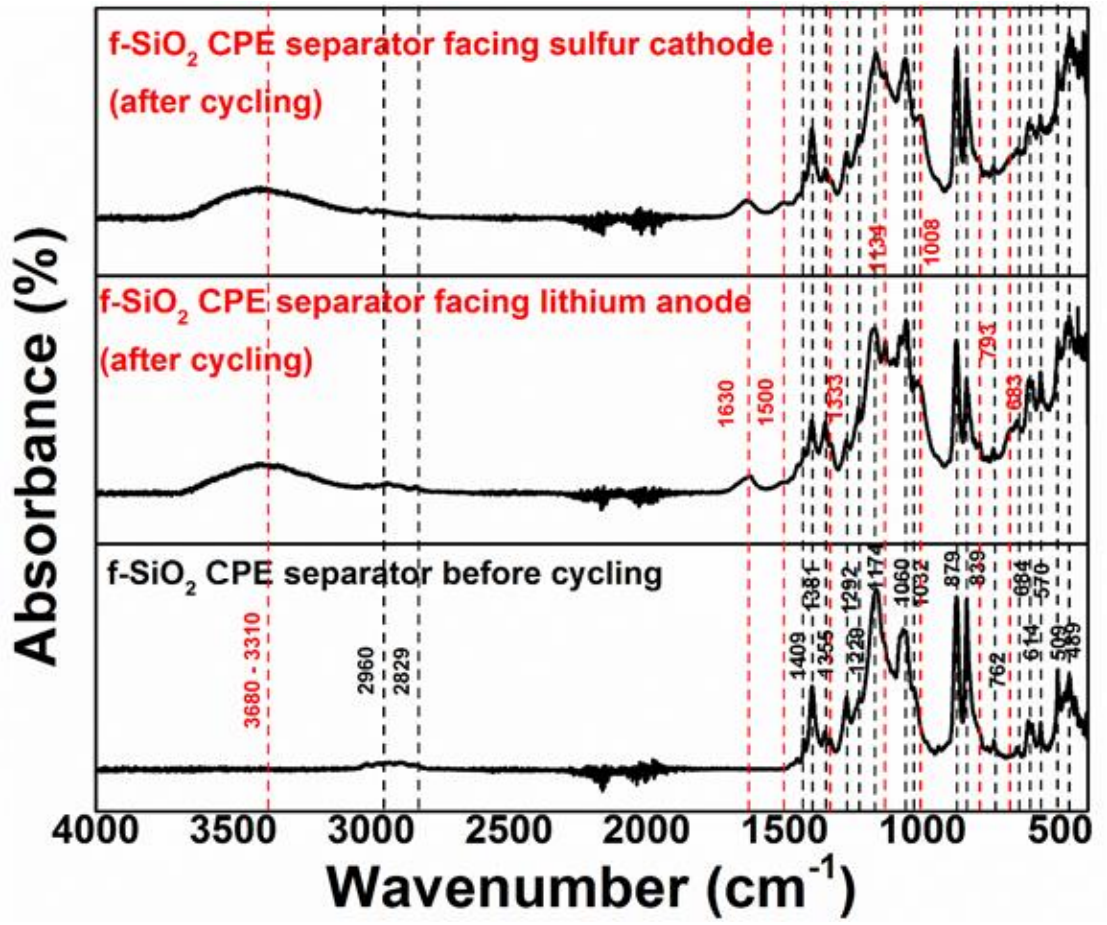

Figure 6-8 FTIR spectrum of the SiO_2 polymer electrolyte membrane before and after 100 cycles (side exposed to lithium anode and sulfur cathode).

These peaks correspond to the out of plane -C-C- bending of the ring structure of dioxolane[370], symmetric deformation mode of $-CF_3$ group from interaction with dioxolane[371], -N-H bending vibrations from the imide group of LiTFSI, -C=O vibrations (ester) [372], -C-N- stretching vibration[373], $-CH_3$ vibration from dimethoxyethane, $-CH_2$ symmetric stretching vibrations[374] and -C-H stretching vibrations, respectively.

After 100 charge – discharge cycles, both sides of the polymer membrane showed almost the same pattern with peaks at 3680-3130 cm^{-1} indicating the presence of exchangeable protons, from amide group of LITFSI. The peaks at 1630 and 1500 cm^{-1} corresponds to -C=O bond from

carbonyl group of dimethoxyethane. The band around 1333 cm^{-1} corresponds to the -C-H ring bending vibrations of dioxolane ring[375]. The peak at 1134 cm^{-1} corresponds to stretching vibrations of carbonate group[376]. The peaks at 1008, 793, 683 cm^{-1} corresponds to -Si-O stretching vibrations[377], $-SO_3$ group from LiTFSI[378] and Si–O–Si stretching vibration modes respectively. Polysulfide peaks arising due to -S-S- stretching vibrations usually occurring between 500 – 540 cm^{-1}[379, 380]. The absence of these peaks indicates the absence of dissolved polysulfide in the CPE membranes after cycling, thus confirming the results from XPS. The absence of any anomalous peaks further confirms the chemical stability of the polymer membranes even after prolonged cycling. The chemical stability of the CPEs suggests their potential to replace PP separators in commercial sulfur batteries.

6.5 Conclusions

In this work, f-SiO_2, nm-SiO_2 and nm-TiO2 incorporated novel electrospun PVdF – HFP CPEs were tested as electrolytes in Li – S battery. The 10 wt. %f- SiO_2 CPE exhibited an initial discharge capacity of 895 mAh g^{-1} and very low fade rate of 0.055%/cycle when cycled for over 100 cycles at 0.1C rate against commercial sulfur cathode. The study also conclusively indicates that the electrospinning technique improves the mechanical properties of the CPEs which in turn helps suppress dendrite formation on the lithium anode. The nanofiller incorporated CPEs also exhibit excellent room temperature ionic conductivity 9.48×10^{-3} S cm^{-1}**,** with values comparable to that of liquid electrolytes. The CPEs also exhibits excellent chemical stability upon cycling for over 100 cycles confirmed using FTIR and XPS analysis. The study also highlights the advantage of high surface area f-SiO_2 filler in preventing polysulfide dissolution by forming an

insulating film over the cathode. This has been confirmed using XPS analysis, which indicates the absence of polysulfide species on the surface of cycled separators. Polysulfide shuttling is usually observed in Li–S cells containing liquid electrolytes and commercial separators. In contrast, the CPE membrane described herein can suppress the dissolution and migration of the polysulfides generated and deposition on the surface of the lithium metal. This is primarily due to the small pore size of the CPE membranes (~15nm) in comparison with commercial PP separators (~25nm), which facilitates blocking and restricts the migration of polysulfide molecules through the membranes. The polysulfide species, upon entering the highly porous CPE membranes are easily trapped in these nanopores preventing further dissolution of the polysulfides. In addition, the extremely low E/S ratio (3:1 and 4:1 ml g^{-1}) of the CPE membrane cells contrasted with Li-S cells containing liquid electrolyte with commercial separators (50:1 to 65:1 ml g^{-1}) greatly restricts the mobility of polysulfides despite the high ionic conductivities. The result described herein is of significant value that will help initiate future research in GPE systems to be conducted focused on preventing polysulfide dissolution and dendrite formation using CPE separators.

6.6 Acknowledgements

The authors acknowledge the financial support of DOE grant DE-EE 0006825, Edward R. Weidlein Chair Professorship funds and the Center for Complex Engineered Multifunctional Materials (CCEMM). PNK also acknowledges support of the National Science Foundation, CBET – Grant 0933141 and CBET – Grant 1511390 for partial support of this research.

7.0 Specific Aim 3: Study the Electrochemical Stability and Room Temperature Li-ion Conductivity of New Substituted Solid-state Oxide and Non-oxide Li-ion Conductors - Theoretical and Experimental Strategies for New Heterostructures with Improved Stability for Rechargeable Lithium Sulfur Batteries

The results of the work in this specific aim has been submitted to the Journal of The Electrochemical Society (Manuscript ID: JES-100043)

Pavithra M. Shanthi[a], Ramalinga Kuruba[b], Oleg I. Velikokhatnyi[b], Prashanth J. Hanumantha[b], Bharat Gattu[a], Moni K. Datta[b,d], Shrinath D Ghadge[a], Prashant N. Kumta[a, b, c, d, *]

[a]Department of Chemical and Petroleum Engineering,

University of Pittsburgh, Pittsburgh, PA 15261 (USA)

[b]Department of Bioengineering,

University of Pittsburgh, Pittsburgh, PA 15261 (USA)

[c]Department of Mechanical Engineering and Materials Science,

University of Pittsburgh, Pittsburgh, PA 15261 (USA)

[d]Center for Complex Engineered Multifunctional Materials,

University of Pittsburgh, Pittsburgh, PA 15261 (USA)

7.1 Synopsis

The prowess of Li_4SiO_4, a known Li-ion conductor for effectively trapping solvents while enabling Li-ion migration contributing to Li-S battery stability was previously demonstrated. Herein Li-ion conductivity enhancement of Li_4SiO_4 was investigated using first principles calculations and correspondingly, Ca, Mg and F were shown to yield ~3 – 4 order improvement in room temperature Li^+ ion conductivities with reduced activation barriers via vacancy mechanism favoring easy diffusion. To demonstrate effects on Li-S battery performance, high sulfur loading cathodes (~3.8 mg S/cm^2) were generated by coating substituted silicates onto sulfur infiltrated copper bipyridine complex framework material (S-Cu-bpy-CFM) electrodes. These ions substituted Li_4SiO_4 coated sulfur electrodes demonstrated high areal capacities (~2.21-2.67 mAh/cm^2), good capacity retention (~0.19-0.33%/cycle) and rate capabilities (~800 mAh/g-700 mAh/g @100 mA/g, 600 mAh/g- 500 mAh/g @300 mA/g, 400 mAh/g-300 mAh/g @ 500 mA/g and ~250mAh/g – 190 mAh/g @1000 mA/g) contrasted with unsubstituted Li_4SiO_4. Post cycle electrochemical impedance spectroscopy analysis of the batteries also shows that the difference in charge-transfer resistance (R_{ct}) between the 1st and the 100th cycle is 49.7Ω for the pristine Li_4SiO_4 coated electrodes while only 2.14Ω is observed for the calcium substituted Li_4SiO_4 coated cathodes justifying the cycling performance improvements using the ion-substituted Li_4SiO_4 coating.

7.2 Introduction

Lithium ion batteries (LIBs) are currently the established predominant energy storage systems for use in all portable and handheld electronic devices as well as automotive systems including the prevalent plug – in hybrid vehicles, and the much awaited all-electric vehicles (EVs)[7, 381, 382]. Despite significant advances, current LIBs are still unable to meet the large energy storage demands of prevalent portable devices due to the low theoretical capacity offered by the traditional graphitic anodes (372mAh/g) while all the much researched advanced cathodes at present still very much rely on the use of transition metal oxides offering only marginal improvements in capacity [289, 383-385]. Furthermore, use of organic liquid electrolytes and polymeric separators greatly limits the safety and operating voltage of the present day LIBs[15]. Moreover, carbonate – based liquid electrolytes are susceptible to decomposition at higher temperatures[386] and voltages releasing toxic compounds and gases [387] posing extreme flammability hazards. In addition, long term cycling of LIBs using metallic lithium anodes inevitably result in formation of dendrites causing deleterious short – circuit conditions promoting thermal run away causing catastrophic combustion of organic liquid electrolytes leading to potential explosion hazards[388, 389]. These adverse situations of fire and explosion hence, compromise the safety and reliability of LIBs, potentially limiting their large-scale application as well as universal adoption in small-scale devices.

Research in recent months has witnessed considerable efforts in the area of development of all solid – state electrolytes as a replacement to the traditional liquid electrolyte used in current LIBs[61, 390, 391]. These solid – state electrolytes could emerge as alternative systems should they meet the high Li-ion conductivity demands along with low leakage currents over a wide electrochemical operating window combined with chemical compatibility with electrodes[392-394].

The materials also need to be conducive to be easily manufactured in a scalable fashion utilizing environmentally benign approaches commensurate with large scale scalability. Research focused on solid electrolytes have identified a number of different classes of materials that partially caters to the above demands [55, 61, 325, 391, 392, 395]. Single crystalline, polycrystalline and amorphous ceramics are found to exhibit good ionic conductivity. These solid electrolytes generally contain monovalent protons, divalent ions, lithium and/or fluoride ions[392]. These ceramic compounds conduct ions by the movement of ionic point defects, the creation and movement of which requires energy. As a result, the conductivity of these compounds increases with increase in temperature. However, ionic conduction in some compounds is reasonably high even at relatively low temperatures. As a result, several types of lithium-ion conducting inorganic ceramic sulfides[55], phosphates[396] and oxides[387, 397] have been investigated in recent years for use in LIBs.

Phosphate based inorganic ceramic electrolytes of LIPON and NASICON – type compounds exhibit a wide electrochemical stability window and are chemically compatible with lithium electrodes. However, the Li-ion conductivity of these compounds is low ($\sim 10^{-6}$ S cm^{-1}) at room temperature. Sulfide based ceramic Li-ionic conductors (LIC) fall under the $Li_2S - Li_2P_5$ and the LiSICON class of compounds. On the other hand, $Li_{10}GeP_2S_{12}$ (LGPS)[55], and different variants of the superionic conductor, have a reported Li-ion conductivity of ~12 mS cm^{-1} at room temperature that rivals many liquid electrolytes, and appears to be stable over a relatively wide operating voltage range. However, the expensive nature of germanium and the rapid hydrolysis at room temperature accompanied by decomposition of these sulfides upon exposure to atmospheric moisture forming toxic H_2S gas restricts the handling of these materials in ambient air. The identification of perovskite (La,Li)TiO_3 (LLTO)[398] and garnet type oxides based

on $Li_5La_3Ta_2O_{12}$[399, 400] of late, are promising solid-state ionic conductors. However, these oxides tend to be brittle and moreover, suffer from very complex and tedious synthesis procedures to form the desired stable crystallographic phases that are very sensitive to temperature and sintering conditions that may pose scalability limitations.

Lithium orthosilicate (Li_4SiO_4) and its derivatives are probably one of the most conventional and well-studied solid-state lithium ion conductors (LIC)[397, 401]. The unit cell of Li_4SiO_4 consists of two SiO_4^{-4} tetrahedra linked by 8 lithium ions, which are distributed over 18 possible sites. The advantage of lithium orthosilicate– based compounds are their compatibility with lithium metal electrodes and exceptional chemical stability at ambient atmospheric conditions rendering it an important component for Li batteries. Moreover, these oxide – based ionic conductors are compatible with commercial organic lithium battery electrolytes that further aids in the development of heterogeneous sulfur cathode structures preventing the characteristic polysulfide dissolution, a major limitation of the Li-S battery system.

In our previous publication, Hanumantha et al[30] demonstrated the ability of these orthosilicate structures to serve as an effective impermeable membrane to solvent molecules thus preventing polysulfide dissolution ubiquitously prevalent in Li-S batteries. They prepared the unsubstituted pristine form of Li_4SiO_4 based composite multilayer heterostructured electrodes for sulfur cathodes in Li-S systems and tested them in commonly used organic liquid electrolytes (Dioxane and Dimethoxyethane) successfully demonstrating the use of a solvent impermeable layer of lithium ion conducting Li_4SiO_4 to effectively prevent polysulfide dissolution into the electrolyte[30]. Although improvement in capacity retention using the Li-ion conducting layer was achieved, the Li ion conductivity of pure Li_4SiO_4 is rather low ($\sim 10^{-12}$ S cm^{-1}) at room temperature. To achieve higher initial capacities close to the theoretical capacity and enhanced

rate capability of the sulfur cathodes without compromising on the innate ability to prevent polysulfide dissolution, the Li ion conductivity of Li_4SiO_4 needs to be improved further (~10^{-8} S cm^{-1} and higher). A 3 to 4 orders of magnitude improvement in ionic conductivity could be obtained by forming simple solid solutions with Li_3PO_4 though at 100°C with no significant improvement in room temperature ionic conductivity[401]. A strategy widely used to significantly improve the Li-ion conductivity for other Li ion conductor (LIC) ceramic materials is the introduction of ions into the various cationic and anionic sites of the corresponding crystal lattice[402]. Cation substitution of $LaFeO_3$[403], $RbNO_3$[404], lanthanum silicates[405], ZrO_2[406] and $Li_7La_3Zr_2O_{12}$[399] have all demonstrated significant improvement in ionic conductivity of these respective compounds. It has also been demonstrated that the activation energy for lithium ion hopping is lowered by the introduction of vacancies during substitution which results in an increase in the ionic conductivity [399, 402, 404, 405].

Research focused on improving the ionic conductivity of Li_4SiO_4 has shown that substitution of Sn[407], Cr and Zr[408] into the Si sites and N[409] onto the O sites improve the ionic conductivities. However, these reports were focused primarily on addressing the total ionic conductivity of the system at high temperatures instead of purely focusing on improving the room-temperature Li-ion conductivity. Moreover, the substituents used were multivalent in nature which makes it difficult to explain their form/state of existence in the substituted solid solution. In addition, Cr and Zr are expensive elements rendering the syntheses processes for incorporating Cr and Zr ions uneconomical. In order to improve the room temperature Li-ion conductivity of Li_4SiO_4, non-expensive earth abundant substituents exhibiting a constant valence state need to be identified and used.

In this work, first principles calculations were therefore performed to understand the crystal structure of Li_4SiO_4 and explore the strategies for introduction of possible substitute ions that could improve the room-temperature Li-ion conductivity. Using the density functional theory (DFT) the effect of several monovalent and divalent cations and anions on the Li^+ conductivity of the crystal was studied, and suitable substituent elements were correspondingly, identified. To validate the calculations, experimental studies were subsequently conducted to incorporate cations and anions as substituents in the Li_4SiO_4 crystalline lattice to obtain the final structures corresponding to the chemical formula shown by i and ii below.

i. $(Li_y[\ ]_xX_x)_4SiO_4$, where X – Ca, Mg, [ ] – vacancy, x – 0.025 to 0.15

ii. $Li_4Si(O_y[\ ]_xF)_4$, where F – Fluorine, [ ] – vacancy, x – 0.025 to 0.15

Lithium orthosilicate was then experimentally substituted systematically with six different concentrations of each substituents using a facile solid-state diffusion technique. Electrochemical Impedance Spectroscopy (EIS) analysis results show that the introduction of the substitute ions improved the Li-ion conductivity of Li_4SiO_4 by 3 – 4 orders of magnitude. In fact, the introduction of divalent, Ca^{2+} on the Li site resulted in maximum improvement in the Li-ion conductivity increasing from 1.18×10^{-12} S cm^{-1} to an impressive value of 2.90×10^{-8} S cm^{-1}, a 4-order improvement in Li-ion conductivity.

In addition, a simple solid-state fabrication method was used to create architectures similar to the original design demonstrated in our previous work by Hanumantha et al[30]. By implementing such composite multilayer heterostructured architectures, the ions-substituted Li_4SiO_4 with high room-temperature lithium ion conductivity were used to demonstrate thick electrodes (~3.8 mg S/cm^2) possessing excellent cycling stability, areal capacity and rate capability. Sulfur infiltrated copper bipyridine complex framework material (S-Cu-bpy-CFM)

capable of preventing polysulfide dissolution previously reported by Shanthi et al earlier[410] was used to fabricate the thick electrode (~400-500 μm) architectures. The slurry coated S-Cu-bpy-CFM demonstrated an initial capacity of 1626 mAh/g and a stable capacity of 1063 mAh/cm^2 after 150 cycles at an electrode sulfur loading of 1.5 mg/cm^2 and hence, was selected as a sulfur cathode active material of choice in this study. When used along with S-Cu-bpy-CFM and the ions substituted-Li_4SiO_4 coated sulfur cathode, the characteristic fade issues typically known to occur with these electrodes associated with the sulfur battery cathodes were overcome justifying the impermeable nature of the orthosilicate membrane along with demonstration of good rate capability performance justifying the favorable influence of the improved Li-ion conductivity of the substituted Li_4SiO_4 coatings. Further, electrochemical impedance spectroscopy (EIS) was employed to study the effect of the ions substituted-Li_4SiO_4 on the charge transfer resistance (R_{ct}) of the pristine electrodes and the electrodes after electrochemical charge-discharge cycling experiments. Results of these studies are documented in the sections to follow.

7.3 Computational Methodology

7.3.1 Crystal Structure

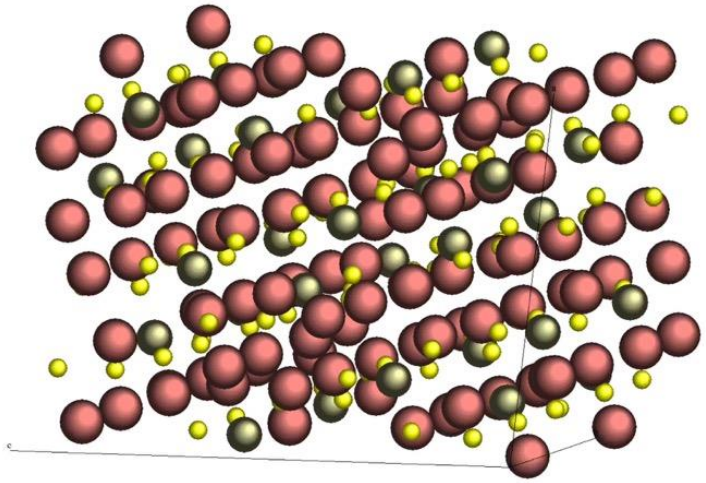

Figure 7-1 The unit cell of Li4SiO4 crystal structure. Large red balls – Si; medium gold – O; small yellow – Li.

Li_4SiO_4 is a complex ternary lithium silicate with monoclinic symmetry and space group *P*21/*m*. The unit cell contains 14 formula units (56 Li, 14 Si, and 56 O atoms) with the following lattice parameters: *a*=11.546 Å, *b*=6.090 Å, *c*=16.645 Å, and β=99.5^{o} [411] shown in Figure 7-1. The 126-atom crystal structure has isolated SiO_4 tetrahedra and Li atoms positioned around silicate tetrahedra.

The density of electronic states and the electronic structure of the studied materials were calculated using density functional theory (DFT) from the Vienna Ab-initio Simulation Package (VASP) within the projector-augmented wave (PAW) method[412-414]. The exchange-correlation energy function was used to calculate the spin-polarized generalized gradient approximation (GGA) as described by Perdew and Wang[415]. The electronic structure was analyzed by the

computational package using the Hellmann-Feynman theorem and the first principles was used to calculate the inter-atomic forces. The standard PAW potentials were used for the elemental components and accordingly, Li, Si, O, Mg, Ca, V, Nb, and F potentials thus contained one, four, six, two, two, five, eleven and seven valence electrons, respectively. In the present theoretical analysis, in order to maintain high precision for the total energy calculations for all the Li-ion conducting compositions, a plane wave cutoff energy of 520 eV was chosen. The internal positions and lattice parameters of the atoms were optimized by employing the double relaxation method.

In addition, the minima of the total energies with respect to the inter-ionic positions and the lattice were determined. The geometry was optimized by using conjugate gradient method to minimize the Hellman–Feynman force leading to zero net forces applied on every ion in the lattice. The total electronic energies converged within 10^{-5} eV/un.cell leading to lower than 0.01 eV/Å/atom residual force components on each atom and an accurate internal structural parameters determination. The Monkhorst-Pack scheme was used to sample the Brillouin Zone (BZ) and to create the k-point grid for the solids and different isolated atoms investigated in this study. The selection of an appropriate number of k-points in the irreducible part of the BZ was made based on the converging the total energy to 0.1 meV/atom. The climbing-image nudged elastic band (CNEB) method [416, 417] also implemented in VASP has been used to determine the various diffusion pathways and migration energy barriers of Li^+-ions in the Li_4SiO_4 structure.

7.3.2 Electronic Structure

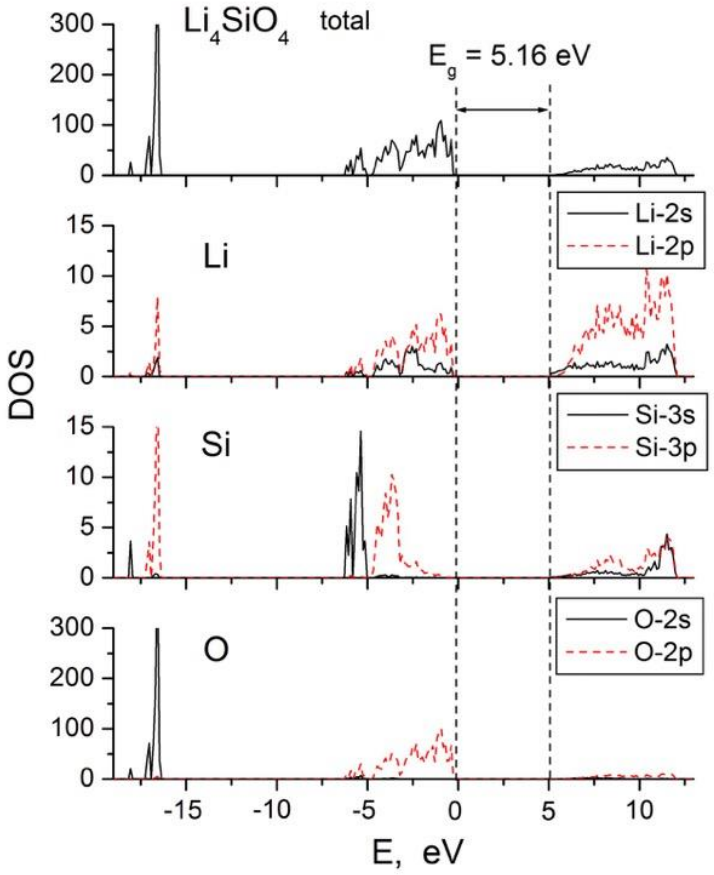

Figure 7-2 Electronic density of states of Li_4SiO_4. Zero energy corresponds to Fermi level.

At the outset, the electronic structure of Li_4SiO_4 was deemed essential to be considered. Figure 7-2 depicts the calculated total and projected density of valence electronic states with the Fermi energy set to zero. It can be seen that the Li_4SiO_4 bulk ground properties are mainly determined by the 2*p* orbital electrons of oxygen atoms. The 3*s* and 3*p* bands of the silicon atoms are overlapped slightly with each other and are strongly hybridized with the 2*p* states of oxygen causing covalency in this material. Strong peaks occur at -1.1, -2.5, -3.7 and -5.2 eV in the upper

valence band while the lower valence band contains peaks at -16.8, -17.1, and -18.0 eV. Tang *et al*.[418] reported similar results except for the small difference in the energy values. The -1.1 and -2.5 eV peaks mainly result from the contributions of O 2*p*, Li 2*s* and Li 2*p* orbitals, -3.7 eV peak comes from the O 2*p*, Si 3*p* and Li 2*s* orbital, while -5.2 eV is composed of O 2*p*, Si 3*s* and Li 2*p* orbital. A strong peak at -16.8 eV results from the contribution of O 2*s*, Si 3*p* and Li 2*p*, while peaks at -17.1 and -18.0 eV come from O 2*s* and Si 3*s* states. The conduction band mainly consists of Li 2*s*, 2*p* orbitals hybridized with Si 3*s*, 3*p* states and are separated from the upper valence band with a band gap of 5.16 eV. Of course, this value cannot be very accurate due to the well-known inability of the density functional methods to accurately predict band gaps in semiconductors and insulators with systematic underestimation in the 30-50% range. However, in the present study this shortcoming does not play a critical role since the goal is to observe trends and hence, the calculated value can be considered to be satisfactory and acceptable.

7.3.3 Ionic mobility of pure Li_4SiO_4

In order to estimate the Li-ion conductivity, there is a need to consider various pathways for migration of the Li-ions during the propagation of the Li-ions through the bulk of the materials. Assuming that the Li-ion diffusion occurs by a hopping mechanism from the occupied Li-site to the neighboring Li-vacancy, it would be prudent to calculate the activation energy barriers for the various hopping pathways occurring between the fixed Li-ion vacancy and the various closest Li-ions in the crystal lattice. Knowing the activation barrier values and using the Arrhenius equation, the Li-diffusion coefficient can be expressed as follows: where *D* is the diffusion coefficient, *a*- the hopping distance (~3.0A in this case), v^* - hopping frequency ($\sim 10^{13} s^{-1}$).

$$D(T) = a^2 v^* \exp[-E_a/k_b T] \quad (7\text{-}1)$$

Figure 7-3 shows the Li-vacancy in the center marked with 0 and the six closest Li-ions from which the six different hopping pathways will be considered to the central fixed vacancy. Also, silicon and oxygen atoms are shown in the vicinity of the Li-vacancy.

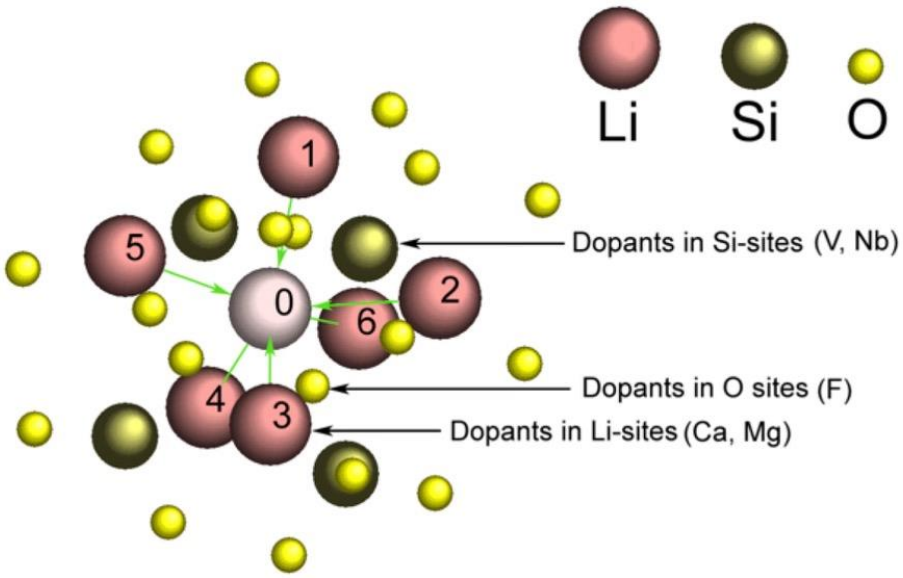

Figure 7-3 Li-vacancy and the various neighboring sites in the vicinity for consideration of the different hopping pathways.

Each pathway has been divided into 8 equal parts reflecting the intermediate positions of the Li-ion hopping between the occupied and the vacant lattice sites. The total energies of the distorted crystal structures have been calculated for all the 9 consecutive intermediate images where each image was relaxed until the maximum residual force was less than 0.1 meV/A. The energy difference between the initial configuration and the maximum energy obtained for some of the intermediate positions of the specific pathway has been considered as an activation barrier E_a for each of the six possible hopping pathways as shown in Figure 7-3**.**

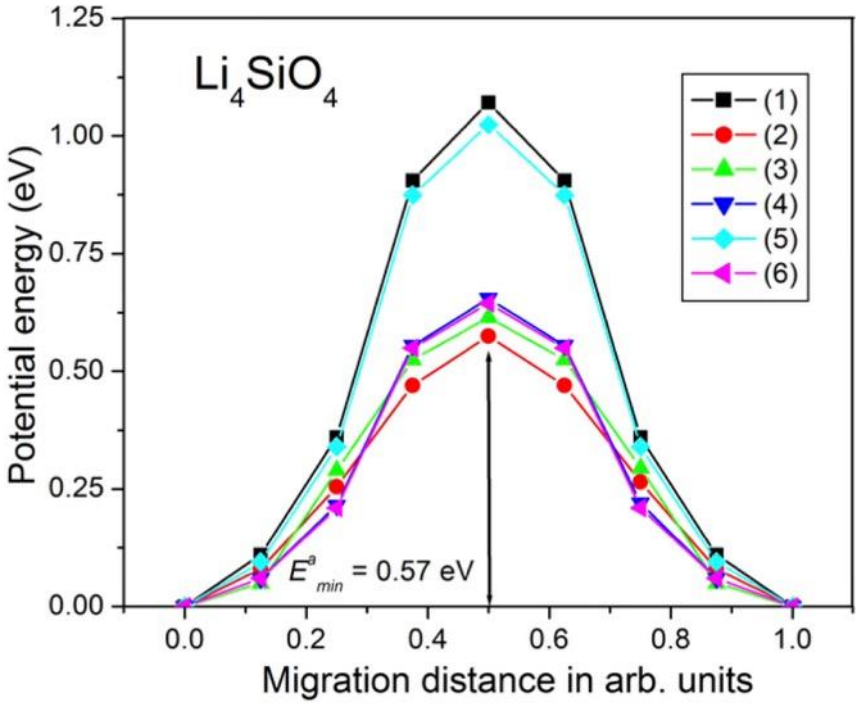

Figure 7-4 Potential energy for different migration pathways of Li-ions in pure Li_4SiO_4.

The calculated potential energies for the different pathways in pure Li_4SiO_4 are shown in Figure 7-4. It can be seen that, depending on the pathways between the initial and the final location of the Li-ion, the resultant activation barrier values E_a vary between 0.57eV and 1.07eV. This happens since all the six pathways shown on Figure 7-3 are symmetrically non-equivalent, although to different extents. For example, Li-ion following paths 1 and 5 must jump between two adjacent oxygen ions moving them apart which demands an appreciable amount of energy resulting in the activation barriers to be approximately 1.1 eV for both pathways. On the other hand, paths 2, 3, 4, and 6 do not run through the narrow spaces between the two oxygen ions but only envelope one oxygen ion which is much more energetically favorable compared to paths 1 and 5. This therefore explains the presence of two groups of pathways characterized by

substantially different barriers E_a as shown in Figure 7-4. The calculated E_a values allow one to determine the most favorable pathways for Li-migration requiring the minimal energy needed for hopping between adjacent Li-ion sites. For the particular atomic configuration shown in Figure 7-3, there are four paths with similar activation barrier values lying between 0.57eV and 0.65eV which is within the computational error of the model used in the present study. Thus, E_a = 0.6eV can be chosen as a very reasonable value for estimation of the diffusion coefficient for pure Li_4SiO_4. From equation 7-1 at room temperature T=~300^oK the diffusion coefficient is calculated to be approximately ~ 7.2 x$10^{-13}cm^2/s$. This value will be compared with corresponding numbers for the ionic mobility determined in d Li_4SiO_4 as explained in the manuscript in the various sections to follow below.

7.3.4 Ionic mobility of Li_4SiO_4 with Ca, Mg, V, Nb, and F

As discussed above, incorporation of different aliovalent elements may help create ionic vacancies in the crystal structure of the material, thus facilitating Li migration and improving the overall ionic conductivity. This is an obvious consideration for enhancing the conductivity since a more open crystal structure favors a higher ionic mobility to be expected in the material. On the other hand, the presence of additional elements could hinder the Li-ion mobility due to larger ionic sizes and correspondingly, increased electric charges in the vicinity of the substituent elements. Qualitative evaluation of these factors and assessing their effects on the overall Li-ion mobility and ionic conductivity will be extremely useful in the identification of substituent elements for generating high Li-ion conducting materials. Figure 7-3 shows the atoms in the Li_4SiO_4 structure which will be substituted with different elements considered in the present study. Accordingly, Ca and Mg are placed at the Li-type sites, while V and Nb are placed at the

Si-sites and F-ions substitute for O in the crystal lattice. It is obvious, that there are numerous positions the substituent elements can occupy in the structure and a rigorous study of all those atomic configurations should be considered for calculating the activation barriers. However, such a task will be very time consuming from the computational point of view and thus, only selected ionic configurations have been considered herein to qualitatively evaluate the role of substitute elements in improving the Li-ion diffusivity and mobility. Since the most important parameter for evaluating the ionic diffusion of the specific element considered is calculation of the activation barrier, E_a of the paths between the initial and final Li-ion position, only E_a for the different atomic configurations considered are presented in Figure 7-5 wherein the four different local environments of Li-ion are shown in the insets of the corresponding graphs.

It can be seen that introduction of different elements results in different changes in heights of the activation barriers. Introduction of Mg, Ca and F consistently decreases the E_a values, thus improving the Li-ion diffusivity, while introduction of V and Nb renders the Li-hopping event more energetically demanding which deteriorates the overall ionic mobility. This could be qualitatively explained by considering two factors: (1) the ionic radii of the substituent elements in comparison to the values of the corresponding ionic radii of the unsubstituted Li_4SiO_4 and (2) change in the electrostatic interactions between Li^+ and the corresponding substituted elemental ions. The elements that contribute to improving the mobility, such as Mg^{2+} and F^-, have much smaller ionic sizes compared to the parent ions, Li^+ and O^{2-} (0.72 Å vs. 0.76 Å and 1.33 Å vs 1.4 Å for Mg, Li, F and O, respectively)[419], which help lower the activation barriers due to the larger structural channels available for Li-hopping between the two adjacent sites. The opposite effect appears to be prevalent in the case of V^{5+} and Nb^{5+} ions due to their significantly larger ionic sizes in comparison to Si^{4+} (0.355Å and 0.48 Å vs. 0.26 Å for V, Nb,

and Si, respectively)[419]. Additionally, the electrostatic interactions between the migrating Li-ion and its neighboring atoms can influence the ionic conductivity. Correspondingly, an increase in the ionic charge of the substituent elements from +2 to +3 or from +4 to +5 is expected to raise the electrostatic repulsion and thus, make the movement of the Li^+ ion more energetically demanding resulting in reducing the Li-mobility.

It can also be noticed, that these two factors work synergistically for F^- (smaller size, lower ionic charge), and for V^{5+}, Nb^{5+}, and Ca^{2+} (larger size, higher ionic charge). And only for Mg^{2+} the factors work agnostically (smaller size, higher the charge). Indeed, an introduction of F definitely decreases the activation barrier E_a as shown in Figure 7-5. Also, V and Nb noticeably increase E_a, thus proving the above mentioned concept of the two factors. Although Mg^{2+} has a higher ionic charge, it still has a smaller ionic radius than Li^+ which most likely becomes the decisive factor in determining the overall ionic mobility. In the case of Ca^{2+}, its ionic radius and charge are larger than that of Li^+ and its introduction into Li_4SiO_4 lattice should not facilitate the energetics of the Li-mobility according to the above described analysis. However, the calculated results shown in Figure 7-5 clearly contradict the above analysis.

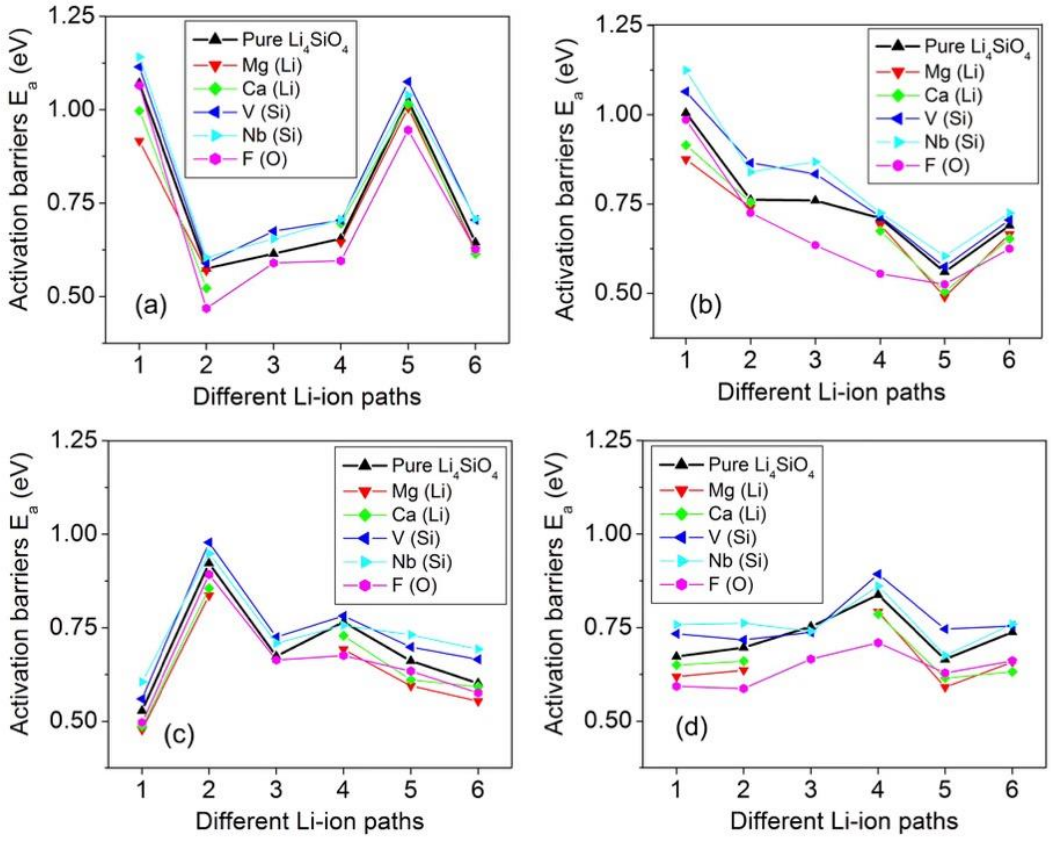

Figure 7-5 Calculated activation barriers E_a in eV for different crystallographic environments and the different migration paths for the Li-ions in pure and ion substituted Li_4SiO_4.

Using equation 7-1 for estimation of the diffusivity coefficient with the different substituent elements, the lowest calculated activation barriers E_a among all the four minimal values shown in Figure 7-5 a-d, should be chosen. For three out of the four different atomic configurations, the minimal E_a value is ~ 0.45eV, which gives the diffusion coefficient D(T) to be ~ 2.4×10^{-10} cm^2/s at room temperature T=300°K, which is 300 fold higher than the corresponding D(T) calculated for unsubstituted Li_4SiO_4 (~$7.2 \times 10^{-13} cm^2/s$). Thus, the theoretical study conducted herein suggests the use of Mg, Ca, and F as preferred substitute elements for improving the Li-ion mobility and ionic conductivity when introduced into the lattice of Li_4SiO_4

by at least 2-3 orders of magnitude. In order to validate the results of these calculations, pure and ion-substituted lithium orthosilicates were experimentally synthesized using Mg, Ca and F as the preferred substituents for ionic substitutions, and the corresponding ionic conductivity was measured. The details are described in the sections below.

7.4 Experimental

7.4.1 Chemical Synthesis

The raw materials used in this work, lithium acetate dihydrate ($CH_3COOLi.2H_2O$, 99.99%), calcium acetate hydrate ($(CH_3COO)_2Ca.xH_2O$, 99.99%), magnesium acetate tetrahydrate ($(CH_3COO)_2Mg.4H_2O$, 99.99% trace metals basis, Silica (SiO_2, fumed) and lithium Fluoride (LiF, ≥99.99%), Copper(II) sulfate pentahydrate ($CuSO_4.5H_2O$, ≥98.0%,), 4,4′-bipyridine (4,4′-bpy, $C_{10}H_8N_2$, ≥98.0%), l-aspartic acid (l-asp, $C_4H_7NO_4$, ≥98%) and sulfur (S, ≥99.5%, Sigma Aldrich) were purchased from Sigma Aldrich and used in the as received form without any further purification.

In order to synthesize calcium and magnesium substituted Li_4SiO_4, stoichiometric quantities of the raw materials were dispersed in methanol, the quantity of which was adjusted to obtain 1M Li-ion concentration. The solution was then slowly heated at 60ºC under continuous stirring to evaporate methanol. The resulting powder was then heated at 950ºC for 12h in an alumina crucible. The heating and cooling rates were set at 5ºC/min and 1ºC/min respectively. Li_4SiO_4 was substituted with fluorine using similar methods except that the final temperature was set at 850ºC.

S-Cu-bpy-CFM was synthesized by the method adapted in our previous publication[410] following the original work by Shi et al[228]. Cu-bpy-CFM was synthesized by the microwave-assisted hydrothermal reaction of $CuSO_4.5H_2O$ (4.6 mM), 4,4′-bpy (6.6 mM) and l-asp (5.9 mM) at 120°C for 4 h in 160 mL of deionized water. Sulfur was infiltrated in the Cu-pyz-CFM at a weight ratio of 70 wt% S:30 wt% Cu-bpy-CFM under vacuum at 300 °C for 24 h inside a quartz tube. The substituted-Li_4SiO_4 coated S-Cu-bpy-CFM cathode architecture was prepared by pressing 10 mg of the ion substituted Li_4SiO_4 onto a pre-pressed 10 mg pellet of S-Cu-bpy, super-P and poly-vinylidene fluoride (PVDF) in a weight ratio of (50:40:10 wt%) using a 1.3 cm diameter stainless steel (Carver Inc.) die employing a 10 ton load following the procedure similar to our previously published work[30]. The S-Cu-bpy-CFM pellets without Li_4SiO_4 coating had an average thickness of ~250-350μm while the unsubstituted and substituted Li_4SiO_4 coated S-Cu-bpy-CFM pellets were ~400-500μm thick.

The Li_4SiO_4 coated S-Cu-bpy-CFM cathodes (3.8 mg/cm^2-S loading) were then assembled into 2032-coin cell against lithium metal anode (200μm thickness) using polypropylene (PP) separator and 1.8 M LiTFSI + 0.2 M $LiNO_3$ in DOL/DME (1:1 vol%) in an Ar-filled glovebox. The assembled batteries were cycled in an Arbin Inc., battery cycler at 0.1 C rate between 1.6 – 2.6 V.

7.4.2 X-Ray Characterization

XRD analysis of the powder samples was performed using the Philips XPERT PRO system equipped with a monochromator that employs CuK_α (λ = 0.15406 nm) with a 45kV operating voltage and 40mA operating current. The 2θ value was varied from 10 to 90° with a step size of 0.04°.

7.4.3 Electrochemical Impedance Analysis

For ionic conductivity measurements, Li_4SiO_4 and the ion substituted silicate were made into 2mm thick pellets using a 13mm diameter die by applying a uniform pressure of 5MPa for 5 minutes. The pellets were then sintered at 950ºC for 4 h. The CR 2032 type coin cell set up was used for determining the Li-ion conductivity. Accordingly, the cells were assembled by embedding these pellets between two Lithium foils. The AC impedance measurements were performed at 25ºC, over a frequency range of 0.01Hz to 100 kHz at 10mA amplitude using a Gamry potentiostat. The impedance spectra obtained experimentally were interpreted and analyzed using the Z-View software (Scribner Associates, Inc.; version 3.3c). The impedance spectra were measured at the open circuit voltage for all the ion substituted systems (OCV) (2.2 – 2.4 V).

7.5 Experimental Results and Discussion

Figure 7-6a-c shows the XRD patterns of calcium, magnesium, and fluorine substituted lithium orthosilicate. It can be seen that introduction of the substituents does not alter the monoclinic lattice structure of Li_4SiO_4 at low substituent concentrations similar to reports on $LaFeO_3$[403]. A maximum of 7.5% lithium sites was successfully substituted by the divalent cations of calcium and magnesium. Further increase in the substituent concentration results in the formation of CaO secondary phases when Li was substituted with Ca (Figure 7-6a) and Mg_2SiO_3 and MgO were observed as the secondary phases when Li was substituted with magnesium (Figure 7-6b). On the other hand, up to 10% oxygen sites were replaced with monovalent

fluoride ions maintaining the single-phase purity of the crystal. At 10% F substituting, secondary phases of Li_4SiO_3 and LiF begin to appear upon excessive addition of F. The systems with more than 7.5% Ca and Mg substituents and 10% F as an ion substituent contain impurity phases. As such, further analysis was only done on the samples with pure Li_4SiO_4 phase.

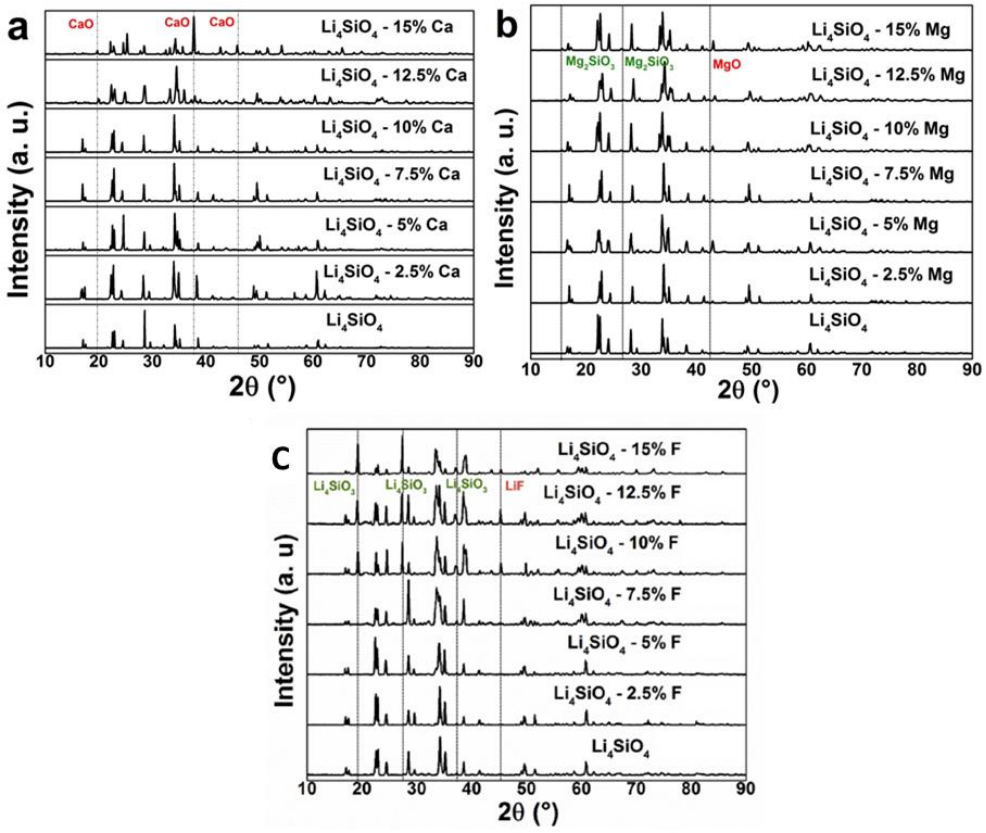

Figure 7-6 XRD spectra of (a) Calcium, (b) Magnesium and (c) fluorine substituted Lithium Orthosilicate.

To confirm the presence of Ca^{2+} and Mg^{2+} ion is in the Li^+ sites of Li_4SiO_4 structure, Rietveld analysis was performed on the pure Li_4SiO_4 phases using the X'pert Highscore Plus suite 4.5 provided by Malvern Panalytical**.** The results of Rietveld analysis show that the values of a, b and V increase and the value of c and β decrease with insertion of Ca^{2+} ions (see Table 7-1). The increase in the unit cell volume is mostly related to the insertion of Ca^{2+} into the

Li_4SiO_4 structure, which can be attributed to the larger ionic size of Ca^{2+} (114 pm) compared to that of Li^+ (90 pm). On the other hand, the oxide structures with Mg^{2+} substituted on Li^+ sites and F^- substituted on O^{2-} sites shows a decrease in the lattice parameters and unit cell volume due to the smaller ionic size of Mg^{2+} (86 pm) and F^- (119 pm) as compared to Li^+ and O^{2-} (126 pm), respectively. The values of R factors (R_p, R_{wp}, R_B) and χ^2(Goodness of Fit/Chi squared) obtained from the Rietveld refinement analysis are also tabulated in Table 7-1.

Table 7-1 Lattice parameter of the substituted Li4SiO4 obtained from Rietveld Refinement.

Li_4SiO_4	a (Å)	b (Å)	c (Å)	β (°)	V (Å^3)	R_p (%)	R_{wp} (%)	R_B (%)	χ^2
Unsubstituted	5.147	6.094	5.293	90.33	166.019	8.43	9.61	3.83	1.39
Substitution of 2.5% Ca	5.206	6.134	5.206	90.26	166.246	7.36	8.72	4.25	1.42
Substitution of 5% Ca	5.247	6.172	5.183	90.18	166.624	9.20	7.82	5.46	1.18
Substitution of 7.5% Ca	5.286	6.189	5.145	90.02	168.318	7.82	7.56	6.06	1.35
Substitution of 2.5% Mg	5.132	6.081	5.252	90.42	163.902	8.72	6.42	3.27	1.29
Substitution of 5% Mg	5.118	6.067	5.224	90.67	162.209	6.24	8.12	4.12	1.56
Substitution of 7.5% Mg	5.112	6.054	5.208	90.85	161.177	8.53	9.25	3.71	1.42

Table 7-1 (continued)

Substitution of 2.5% F	5.114	6.074	5.274	90.37	163.82	9.73	7.57	4.57	1.09
Substitution of 5% F	5.063	6.053	5.242	90.52	160.648	7.19	9.20	4.22	1.27
Substitution of 7.5% F	5.018	6.024	5.215	90.71	157.641	6.72	8.94	5.82	1.16
Substitution of 10% F	5.012	6.022	5.212	90.84	157.309	8.91	6.75	6.53	1.43

The Cole-Cole plot of the complex impedance of the samples is plotted with real and imaginary axes. Figure 7-7a-c shows the experimental impedance results obtained for the three substituted orthosilicates. As can be clearly seen in Figure 7-7a-c, the impedance data of calcium, magnesium, and fluorine substituted orthosilicates are very similar.

The semicircle in the impedance plots at higher frequencies correspond to the conduction of bulk ions and the perturbations observed at the low frequencies are generally due to secondary ionic carriers [420], grain-boundary diffusion observed in the powdered samples [421] or due to ion diffusion at the surface[422]. In general, the perturbations observed at low the frequencies are due to effects at the electrode surface which are commonly observed in impedance measurements of single crystalline samples[422].

The equivalent circuit for the Cole–Cole plots obtained from the impedance measurements is a RC parallel circuit whose impedance is summarized by Equation 7-2[422]: in which ω is the angular frequency (ω = 2πf).

$$Z_{R\|C} = \frac{R - i\omega CR}{1 + \omega^2 C^2 R^2} \tag{7-2}$$

The Cole–Cole plot is a semicircle, whose diameter is equal to R, and the angular frequency ω_p at which the semicircle peak occurs is governed by the equation: $\omega_p = 1/RC$. The Cole–Cole plots are in general partial semicircles, which could be fit by using a simple RC circuit. However, typically when the Cole–Cole plots show curves at lower frequency, the curves are usually attributed to the surface roughness. The Cole–Cole plots in case of samples with surface roughness could be simulated by an RC circuit in series with a Constant Phase element (CPE), whose complex impedance is given by Equation 7-3[422]: which produces a straight line with angle of $n\pi/2$ with the R axis in the Cole–Cole plot.

$$Z_{CPE} = Af^{-n}(cos\frac{n\pi}{2} - i\ sin\frac{n\pi}{2}) \quad (7\text{-}3)$$

In this work, the numerical fitting of the experimental and the simulated curves are achieved by using the Zview software package in the frequency range of 12 Hz to 10000 Hz. The fit resulting from the real and the imaginary components are very close. Figure 7-7d shows the simple equivalent circuit used to fit the experimental results[423], where R_s represents the contact resistance inside the cell, R_p represents the resistance to lithium ion mobility and CPE is the constant phase element arising from the dielectric capacitance across the solid electrolyte. The fitted values of R_s, R_p, CPE-T and CPE-P are tabulated in Appendix E Table 1**,** Appendix E Table 2**,** Appendix E Table 3 (Appendix E).

The fitted value of R_p was used to calculate the lithium ionic conductivity(σ) of the substituted orthosilicates using Equation 7-4 [396, 424], where R_p is the resistance, t is the thickness and S is the surface area of the orthosilicate samples, respectively.

$$\sigma = \frac{1}{R_p} \times \frac{t}{S} \quad (7\text{-}4)$$

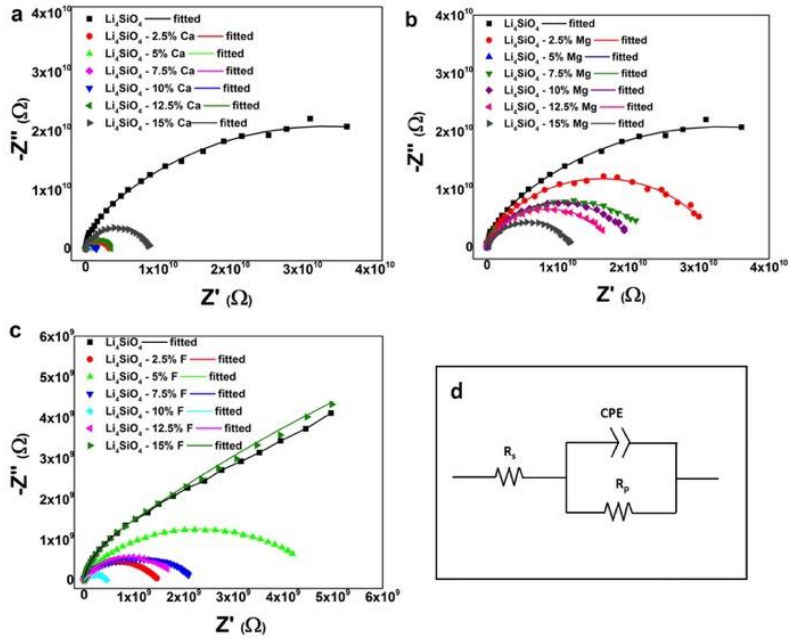

Figure 7-7 (a-c) Nyquist plots of Calcium, Magnesium and fluorine substituted Lithium Orthosilicate, (d) Equivalent circuit used to fit the impedance data.

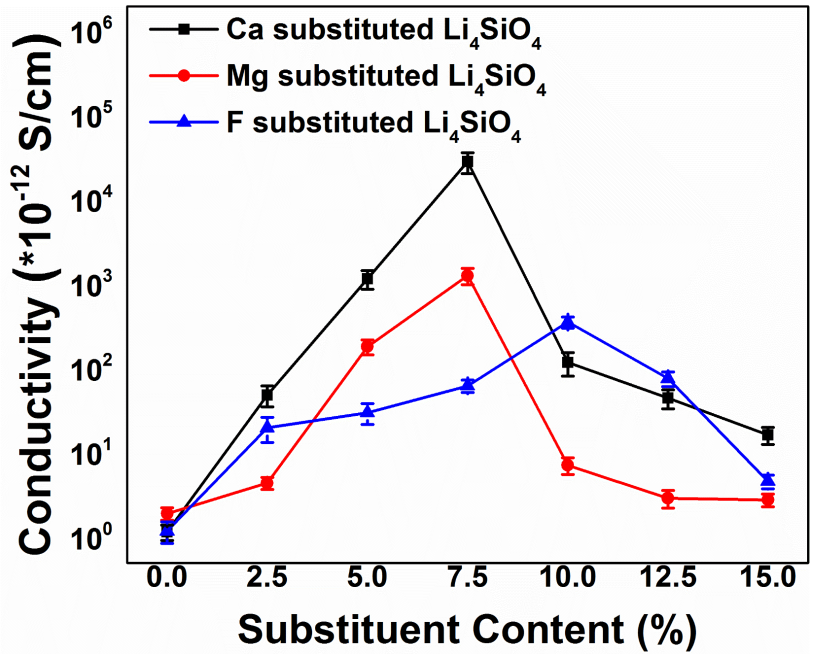

Figure 7-8 Comparison of the effect of Calcium, Magnesium and Fluorine substitution on the ionic conductivity of Lithium Orthosilicate (Each datum represents an average of three independent tests run on three different samples under identical conditions).

The lithium ion conductivities of calcium, magnesium and fluorine substituted orthosilicates at ambient temperature are plotted in Figure 7-8. The lithium ion conductivity of pristine Li_4SiO_4 is 1.2 * 10^{-12} S/cm which is closer to the values reported by West et al[397] in his work on similar systems. Upon substitution, the ionic conductivity increased by 3 – 4 orders of magnitude due to the introduction of Li^+ vacancies as previously explained by the density functional theory calculations. The substituted orthosilicates show increase in ionic conductivity with up to 7.5% calcium and magnesium additions and 10% fluorine incorporations. The ionic conductivity of lithium orthosilicates increased to 2.9 * 10^{-8} S/cm and 1.3* 10^{-9} S/cm upon 7.5% introduction of calcium and magnesium ions, respectively. Upon 10% addition of fluorine, the lithium ionic conductivity increases to 3.6 * 10^{-10} S/cm. The ionic conductivities decreased at higher substituent concentrations due to the likely formation of impure secondary phases as shown by XRD. The formation of secondary phases within the grains as intra-granular precipitates or at the grain boundaries in the form of inter-granular precipitates formed at higher substituent concentrations could very well add to the barriers posed for Li-ion migration resulting in a reduction in the overall Li-ion conductivity[403]. In order to evaluate the influence of the substituted orthosilicates on the electrochemical cycling response of Li-S batteries, the electrochemical cycling performance of substituted-Li_4SiO_4 pellet coated S-Cu-bpy-CFM cathodes were evaluated and the corresponding performance is shown in Figure 7-9a. The objective of our previous work by Jampani et al[30] was to understand the effect of unsubstituted pure orthosilicate on the prevention of polysulfide dissolution by trapping them within the orthosilicate serving as an effective solvent impermeable membrane allowing only Li-ion migration.

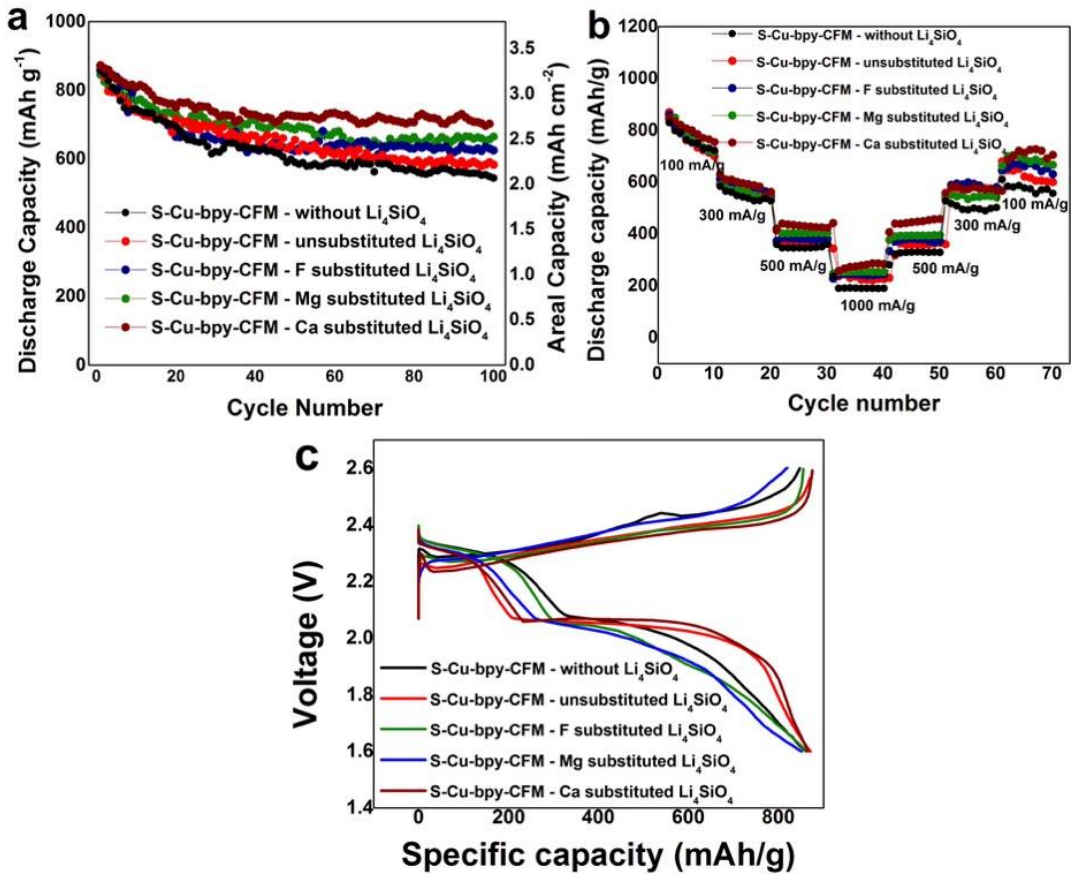

Figure 7-9 a) Electrochemical cycling performance, b) Rate capability and c) First cycle charge-discharge profiles of the S-Cu-bpy-CFM system with and without the ion substituted Li4SiO4 coating. (The cycling and rate capability data is verified in three independent tests runon three different samples under identical conditions).

In the current work, the authors have further explored the effect of substituted orthosilicate on the cycling stability and rate capability without compromising the solvent impermeability of the pristine orthosilicate by introducing the ion-substituted orthosilicate as a coating membrane in the S-Cu-bpy-CFM[410] system. We have previously studied this system extensively and have shown its improved electrochemical performance as opposed to commercial sulfur cathodes[410]. The pellet pressing procedure shown in our earlier publication[30] aids in preparing very thick electrodes (~400-500μm) consisting of S-Cu-bpy-CFM, carbon and PVDF binder and the

compaction yielded by the pressing procedure results in better cycling stability as observed in Figure 7-9a. The initial and 100th cycle discharge capacity of the different cathodes are tabulated in Table 7-2. The S-Cu-bpy-CFM electrode without the Li_4SiO_4 pellet covering having a thickness of ~250-350μm showed an average initial capacity of 863±15.5 mAh/g S and a stable capacity 544±12.5 mAh/g S after 100 charge-discharge cycles at a fade rate of 0.40±0.06 %/cycle exhibiting an areal capacity of 2.07±0.04 mAh/cm^2. The S-Cu-bpy-CFM electrode with the pristine Li_4SiO_4 pellet cover exhibited an average initial capacity of 873±13.7 mAh/g S and a stable capacity 583±10.2 mAh/g S after 100 charge-discharge cycles yielding a fade rate of 0.33±0.05 %/cycle exhibiting an areal capacity of 2.21±0.04 mAh/cm^2. The F, Mg and Ca substituted Li_4SiO_4 pellet covered S-Cu-bpy-CFM electrode on the other hand, showed an average initial capacity of 858±18.2 mAh/g S, 845±16.4 mAh/g S and 871±19.2 mAh/g S, respectively and a discharge capacity of 625±7.6 mAh/g S, 665±9.4 mAh/g S and 702±8.5 mAh/g S after 100 cycles. In addition, the F, Mg and Ca substituted Li_4SiO_4 pellet covered S-Cu-bpy-CFM electrode showed a fade rate of 0.27±0.05 %/cycle, 0.21±0.03%/cycle and 0.19±0.03%/cycle, respectively and areal capacities of 2.38±0.03 mAh/cm^2, 2.53±0.03 mAh/cm^2 and 2.67±0.02 mAh/cm^2 after 100 cycles. The improved Li-ion conductivity of the substituted orthosilicates leads to an improvement in the discharge capacity of the cathodes as is evident from the values displayed in Table 7-2. Accordingly, the corresponding areal capacities of the substituted orthosilicate coated S-Cu-bpy CFM cathodes also shows significant improvement as compared to unsubstituted orthosilicate coated S-Cu-bpy-CFM cathodes.

Table 7-2 Electrochemical cycling performance of bare S-Cu-bpy-CFM and the S-Cu-bpy-CFM with a Li_4SiO_4 coating.

Cathode loading (3.8 mg S/cm^2)	Initial discharge capacity (mAh/g S)	100nd cycle discharge capacity (mAh/g S)	Fade rate (%/cycle)	Areal capacity (mAh/cm^2) (100th cycle)
S-Cu-bpy-CFM –without Li_4SiO_4 coating	863±15.5	544±12.5	0.40±0.06	2.07±0.04
S-Cu-bpy-CFM –with unsubstituted pure Li_4SiO_4 coating	873±13.7	583±10.2	0.33±0.05	2.21±0.04
S-Cu-bpy-CFM – with F substituted Li_4SiO_4 coating	858±18.2	625±7.6	0.27±0.05	2.38±0.03
S-Cu-bpy-CFM – with Mg substituted Li_4SiO_4 coating	845±16.4	665±9.4	0.21±0.03	2.53±0.03
S-Cu-bpy-CFM – with Ca substituted Li_4SiO_4 coating	871±19.2	702±8.5	0.19±0.03	2.67±0.02

The improved cycling performance in the S-Cu-bpy-CFM cathodes is attributed to the thick nature of the electrode which is in the range of ~250-350μm in case of the S-Cu-bpy-CFM pellets without Li_4SiO_4 coating and ~400-500μm in unsubstituted and substituted Li_4SiO_4 coated S-Cu-bpy-CFM pellets with the Li_4SiO_4 membrane serving as an additional protective layer as explained by Hanumantha et al[30]. The pellet pressing procedure ensures good contact between the sulfur and the conductive carbon additive (Sup-P) preventing the sulfur from becoming

inactive over the continued charge-discharge process. Also, though there may be a contact between electrolyte and sulfur, the thick electrode architecture ensures that the dissolved polysulfides have an increased residence time due to the close proximity with the carbon as explained by Hanumantha et al[30]. As is evident from the electrochemical cycling data, therefore, the fade rate of the S-Cu-bpy-CFM electrode directly correlates with the Li-ion conductivity of the substituted Li_4SiO_4 pellet covering the electrode. As the conductivity of the substituted Li_4SiO_4 increased, the fade rate in the cycling performance decreased consistently from 0.33%/cycle in the case of pristine Li_4SiO_4 as opposed to 0.19% in Ca substituted Li_4SiO_4. This increase in electrochemical stability from pristine Li_4SiO_4 to the Ca substituted Li_4SiO_4 is evidently due to the increase in room-temperature Li-ion conductivity of Li_4SiO_4 as a result of incorporation of various substituents (Figure 7-8). The improved performance may also be attributed to the thick nature of the electrode (~400-500um) due to the proximity of the sulfur and conducting carbon additive and the high residence time of polysulfides as discussed earlier and the inclusion of an additional protective layer of Li_4SiO_4 membrane.

All of the substituted Li_4SiO_4 coated S-Cu-bpy-CFM cathodes show improved rate capability as well due to the improved Li-ion conductivity. Correspondingly, Ca substituted Li_4SiO_4 coated S-Cu-bpy-CFM cathodes show capacity of ~800 mAh/g @ 100 mA/g while the pristine Li_4SiO_4 coated S-Cu-bpy-CFM cathodes show a capacity of ~700 mAh/g at the same rate. At high currents of 1000 mA/g, the Ca substituted Li_4SiO_4 coated S-Cu-bpy-CFM cathodes show stable capacity of ~300 mAh/g while the pristine Li_4SiO_4 coated S-Cu-bpy-CFM cathodes show a capacity of ~200 mAh/g. Upon reverting the currents back to 100 mA/g, the Ca substituted Li_4SiO_4 coated S-Cu-bpy-CFM cathodes still retain a capacity of ~700 mAh/g without exhibiting any significant degradation in capacity again justifying the positive influence

of the improved Li-ion conductivity brought about by Ca substitution. The first cycle charge-discharge profiles of the substituted-Li_4SiO_4 pellet covered electrode and uncovered S-Cu-bpy-CFM cathodes is shown in Figure 7-9c. The charge-discharge profiles of all the systems showed the typical characteristic plateaus corresponding to Li_2S_x (x=4-8) formation at 2.3 V[31] and Li_2S at 2.0 V[30] as observed in various publications on Li-S systems[24, 31, 226, 308, 425].

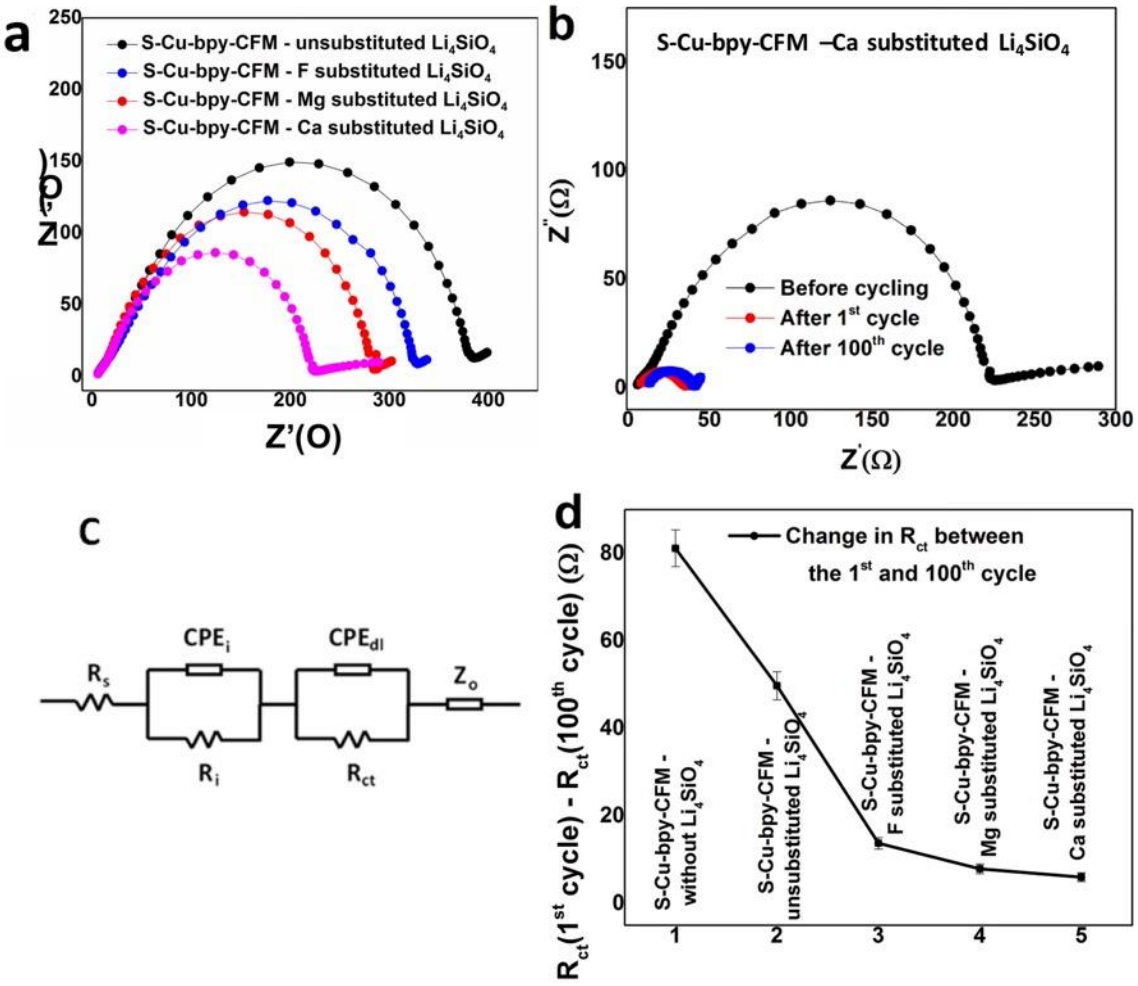

Figure 7-10 a) Nyquist plot of the different substituted and unsubstituted Li4SiO4 coated S-Cu-bpy-CFM electrodes at the OCV (2.2-2.4 V); b) Nyquist plot of the S-Cu-bpy-CFM – Ca substituted $Li4SiO_4$ coated electrode before and after 1st and 100th cycles; c) Randal equivalent circuit used to fit the EIS data (figure 7-10 b inset) d) Difference in Rct between the 1st and 100th cycle.

To further understand the improved electrochemical cycling stability and rate capability performance, the pristine as well as F, Mg and Ca substituted Li_4SiO_4 were analyzed using EIS at the OCV (~2.2-2.4 V), the results of which are shown in Figure 7-10. Figure 7-10a represents the Nyquist plot of the batteries assembled using the pristine and F, Mg and Ca substituted Li_4SiO_4 coated Cu-bpy-CFM cathodes (w.r.t Li/Li^+), fitted using the Randall's equivalent circuit model shown in Figure 7-10c. As evident from the Nyquist plot, the experimental data fits well with the fitted data. The equivalent circuit used to fit the EIS data consists of two R-CPE (resistance – constant phase elements) in series with the R_s (solution resistance) and Warburg component (Z_o). The first R-CPE element consists of the R_i (interfacial resistance) and CPE_i (interfacial constant phase element) and is the resistance attributed by the coating in addition to any resistances at the interface during cycling. The second R-CPE element consists of the R_{ct} (charge-transfer resistance) and CPE_{ct} (charge-transfer constant phase element) developed as a result of the charge transfer process that accompanies the electrochemical cycling.

The interfacial resistance R_i of the pristine as well as F, Mg and Ca substituted Li_4SiO_4 covered S-Cu-bpy-CFM cathodes are almost constant at around ~20 Ω (Fitted values are shown in Appendix E Table 4), however, the charge transfer resistance decreases consistently from the Cu-bpy-CFM - pristine Li_4SiO_4 cathode to the Cu-bpy-CFM – Ca substituted Li_4SiO_4 due to the improved Li-ion conductivity of the substituted Li_4SiO_4. Figure 7-10b compares the Nyquist plots of the Cu-bpy-CFM – Ca substituted CFM before and after 1^{st} and 100^{th} cycles. The Nyquist plots for other substituted systems is given in Appendix E Figure 2(Appendix E). It can be seen in Figure 7-10b and Appendix E Table 4 that the R_i remained constant before and after the first cycle while the charge transfer resistance (R_{ct}) undergoes significant change with lithiation (after first cycle). This is because R_{ct} is a measure of kinetics of the reaction and the

initial kinetics of polysulfide formation is rapid while the kinetics of conversion of lithium polysulfides to Li_2S is a sluggish process under normal conditions[31]. However, due to the increased ionic conductivity of the substituted Li_4SiO_4, in the case of the coated S-Cu-bpy-CFM cathodes with the substituted Li_4SiO_4 contrasted with electrode coated with pristine Li_4SiO_4, the kinetics of the polysulfide reaction is expected to be improved. This is therefore, reflected in the cycling stability and rate capability of the ion substituted Li_4SiO_4 coated cathodes.

In addition, lithiated species become successively difficult to further lithiate as is commonly observed in lithium ion batteries. Figure 7-10d shows the change in R_{ct} between the first and the 100^{th} cycle for all the various electrodes of S-Cu-bpy-CFM cathodes with no orthosilicate pellet covering along with pristine orthosilicate and progressively substituted orthosilicate pellet covering. The change in charge transfer resistance (R_{ct}) between the 1^{st} and the 100^{th} cycle decreased from 49.7Ω in case of pristine Li_4SiO_4 coated S-Cu-bpy-CFM to 2.14Ω in the case of calcium substituted Li_4SiO_4 coated S-Cu-bpy-CFM cathodes. This change in R_{ct} between the first and 100^{th} cycle conceivably correlates with the cycling stability of the cathodes due to the higher Li-ion conductivity of the substituted Li_4SiO_4. Additionally, it is reported that the stability could occur by the possible formation of stable interface as explained by Deng et al[426] in his EIS study of lithium sulfur batteries. Therefore, in the current work, additionally, the improved ionic conductivity of the substituted Li_4SiO_4 further likely aids in the formation of a stable interface. This observation, hence, further explains the improvement in cycling performance in the substituted Li_4SiO_4 coated cathode. It can thus be concluded that the high Li-ion conductivity of Li_4SiO_4 brought about by able substitution of substituents determined by DFT studies and the subsequent generation of the substituted Li_4SiO_4 serves to act as a protective solvent impermeable barrier aiding only in facilitating higher Li-ion migration. As a result, the

substituted Li_4SiO_4 coating serves to improve the performance of the system with promoting enhanced shuttling of lithium ions thus validating the proposed novel Li-ion conducting barrier concept of heterostructure composite Li-S electrodes.

7.6 Conclusions

Density functional theory calculations suggest that substituting the Li and O sites in Li_4SiO_4 with different aliovalent elements help create ionic vacancies in the crystal structure, facilitating Li-ion migration and thus, improving the overall Li-ionic conductivity. The theoretical study also suggests the use of Mg, Ca, and F as preferred substituents for improving the Li-ion mobility and ionic conductivity of Li_4SiO_4 by 2-3 orders of magnitude. In order to validate the theoretical calculations, Li_4SiO_4 was accordingly substituted with six different concentrations of each substituent using a high temperature solid-state diffusion technique. A maximum of 7.5 atomic % of Li^+ sites were substituted with Ca^{2+} and Mg^{2+} ions and 10% of the O^{2-} sites were substituted with F^- ions while maintaining the crystallographic and phase purity. Electrochemical Impedance Spectroscopy (EIS) analysis results clearly show that the introduction of the substituents improved the ionic conductivity of Li_4SiO_4 by 3 – 4 orders of magnitude. In fact, Ca^{2+} introduction as a substituent showed the maximum improvement in ionic conductivity from 1.2×10^{-12} S cm^{-1} to 2.9×10^{-8} S cm^{-1}. This strategy can easily be implemented for improving the lithium ion conductivity following introduction of substituents paving the way for developing an all solid-state lithium-ion battery utilizing oxide based solid electrolytes. The substituted Li_4SiO_4 further serve to act as an impermeable barrier to solvent molecules only enabling faster transport of Li ions adding to the cycling stability. High loading

sulfur cathodes (~3.8 mg S/cm^2) of S-Cu-bpy-CFM were thus tested by coating a layer of the substituted Li_4SiO_4 and their cycling performance and rate capability were evaluated. The substituted Li_4SiO_4 S-Cu-bpy-CFM electrodes demonstrated high areal capacities of (~2.21-2.67 mAh/cm^2) along with good capacity retention (~0.19-0.33%/cycle) and rate capabilities (~800 mAh/g-700 mAh/g @100 mA/g, 600 mAh/g- 500 mAh/g @300 mA/g, 400 mAh/g-300 mAh/g @ 500 mA/g and ~250mAh/g – 190 mAh/g @1000 mA/g) in comparison to pristine Li_4SiO_4. Post cycle EIS (electrochemical impedance spectroscopy) analysis of the batteries shows that the difference in charge-transfer resistance (R_{ct}) between the 1st and the 100th cycle is 49.7Ω in case of pristine Li_4SiO_4 coated S-Cu-bpy-CFM and 2.14Ω in the case of calcium substituted Li_4SiO_4 coated S-Cu-bpy-CFM cathodes explaining the improvement in cycling performance of aliovalent ion substituted Li_4SiO_4 coated cathodes. Such a strategy may well be incorporated in stabilizing the cycling performance of Li-S batteries even further in the future by using Li-ion conductors displaying even higher Li-ion conductivities matching that of liquid electrolyte systems.

7.7 Acknowledgements

U.S. Department of Energy grant OVT-DE-EE0006825 and OVT-DE-EE0008199 supported the research. Authors thank the Edward R. Weidlein Chair Professorship Funds and the Center for Complex Engineered Multifunctional Materials (CCEMM) for helping procure the electrochemical equipment and facilities used in this research work. The authors also gratefully acknowledge the National Science Foundation, CBET-1511390 for partial support of this research. The authors also acknowledge the Extreme Science and Engineering Discovery

Environment (XSEDE)[427] supported by National Science Foundation grant number ACI-1053575, for providing the computational resources needed to complete the theoretical component of the present study.

8.0 Specific Aim 4: Develop Novel Composite Sulfur Cathodes Comprising High Sulfur Loadings on Electronically Conducting Platforms with Polysulfide Trapping Agents (PTA) and Understand the Mechanisms Related to Prevention of Polysulfide Dissolution Contributing to High Energy Density - Directly Deposited Sulfur Architectures with Polysulfide Trapping Agents (DDSA-PTA) for Lithium-Sulfur Batteries

The results of the work in this specific aim has been prepared as a communication that is to be submitted to the Journal of The Electrochemical Society.

Pavithra M Shanthi[a], Ramalinga Kuruba[b], Bharat Gattu[a], Moni Datta[b], Prashant N Kumta[a, b, c, d, *]

[a]Department of Chemical and Petroleum Engineering,

University of Pittsburgh, Pittsburgh, PA 15261 (USA)

[b]Department of Bioengineering,

University of Pittsburgh, Pittsburgh, PA 15261 (USA)

[c]Department of Mechanical Engineering and Materials Science,

University of Pittsburgh, Pittsburgh, PA 15261 (USA)

[d]Center for Complex Engineered Multifunctional Materials,

University of Pittsburgh, Pittsburgh, PA 15261 (USA)

8.1 Synopsis

Lithium-Sulfur (Li-S) batteries has the potential to meet the increased energy density requirements of electric vehicle (EV) technologies. However, the Li-S system is plagued by polysulfide shuttling. In this work, Directly Deposited Sulfur Architectures (DDSA) containing Polysulfide Trapping Agent (PTA) were investigated as cathodes in Li-S battery. The PTA-DDSA cathodes exhibited high sulfur loadings (~8-18 mg/cm^2) and significantly reduced polysulfide dissolution in addition to excellent cycling stability. The DDSA-PTA electrode exhibits an initial capacity of 1188 mAh/g (14.62 mAh/cm^2 areal capacity) and a stable capacity of 870 mAh/g (10.71 mAh/cm^2 areal capacity) after 100 cycles at 0.1 C rate. The DDSA-PTA electrode 1 shows an initial capacity of 1152 mAh/g (14.06 mAh/cm^2 areal capacity) and a stable capacity of 925 mAh/g (11.29 mAh/cm^2 areal capacity) after 100 cycles at 0.1C rate when tested under lean electrolyte (4μl/mg-S) testing conditions outlined by the Department of Energy's (DOE's) Battery500 consortium aimed at developing batteries with 500Wh/kg energy density.

8.2 Introduction

Developments in portable electronic devices (PEDs) and electric vehicles (EVs) is largely limited by the gravimetric and volumetric energy densities of the Li-ion battery systems (Wh/kg and Wh/L). Improvements in energy density are therefore imperative to exploit the complete potenetial of these novel environmentally benign technologies. Li-S battery systems uses sulfur which has a theoretical specific capacity of 1675mAh/g[192] as cathode and exhibits a thermodynamic specific energy density of 2600Wh/kg[51]. The abundance (0.07% of the Earth's

crust) and eco-friendliness, in addition to the cost-effective characteristics of sulfur[11] make it a promising cathode material for large scale and EV energy storage applications. Nevertheless, the insulating behavior of sulfur results in incomplete utilization of active material in Li-S batteries[12, 13]. In addition, formation of highly soluble polysulfide intermediates (Li_2S_n; n = 2-8) during electrochemical cycling is a major limitation leading to active material loss and eventual battery failure.

Various strategies have been explored to address these challenges. Conductive carbon was introduced into the sulfur cathodes to increase the conductivity and active material utilization of the electrodes with overall reduction in cathode resistance by high conductivity carbon black incorporation in the active material mixture. [39] The active carbon possesses nanopores (~2-10nm) with a high surface area (~500-2000m^2/g) absorbing the polysulfide species thereby preventing their dissolution into the electrolyte[40]. Mesoporous carbon acts as an ordered encapsulation substrate for sulfur. [26, 44] Li et al. [26] systematically tuned and investigated the pore sizes and pore volumes of several mesoporous carbon materials and showed that the large pore size (~3-22nm) of mesoporous carbon can accommodate higher sulfur loading (>80% S) and can exhibit enhanced cell performance under higher sulfur loading situations. Transition metal silicates, aluminum oxides, vanadium oxides, and transition-metal chalcogenides have been utilized with sulfur cathodes to decrease the polysulfide diffusion and migration [24, 25 26-29]. However, their electron transport property was limited by large particle size which tend to decrease the electrochemical performance. In addition to limitations in sulfur cathodes, the lithium anode side is also plagued with limitations of dendrite formation posing a safety hazard[428]**.** Replacing the commonly used Li-S battery organic electrolyte (dioxolane(DOL)/dimethoxyeethane(DME)) with a PVdF-HFP based composite polymer

electrolyte (CPE) has shown ability to trap the polysulfides due to the very low electrolyte content of the CPE (~1-2µl electrolyte/mg sulfur)[255]. The safety and cyclic life of the anode was improved using polymer and solid-state electrolytes that protect lithium metal and minimize dendrite formation on the anode, hence leading to enhanced performance of Li-S batteries. Nevertheless, polymer and solid-state electrolytes generally suffer from low Li-ion conductivity due to the high viscous nature of polymers hindering the lithium ion transport due to high energy barrier in solid state electrolytes. [79, 255, 317, 329] These approaches however, lead to an increase in the utilization of active material in sulfur cathodes although, they lack complete prevention of the dissolution of polysulfide species into the electrolyte. [30].

In this work, Directly Deposited Sulfur Architectures (DDSA) with sulfur loadings of ~8-18mg/cm^2 were created using simple electrodeposition technique. The DDSA electrodes were then coated with a Polysulfide Trapping Agent (PTA) to chemically prevent the dissolution of polysulfides. These free-standing cathodes were studied chemically and electrochemically to understand the mechanism of polysulfide dissolution in these structures. These PTA coated DDSA showed a high initial capacity of 1170±18mAh/g and stable capacity of 897±27mAh/cm^2 for over 100 cycles. The mechanism by which the PTA prevents the dissolution of polysulfide has also been studied in detail.

8.3 Experimental

The synthesis of DDSA was accomplished by electrochemically depositing sulfur onto a conducting carbon nano fiber (CNF) matt. The CNF matt was prepared by electrospinning 1 M solution of polyacrylonitrile (PAN) into a nanofiber (~200nm) matt at a high voltage of 25kV

and flow rate of 1 ml/h using an in-house-built electrospinning setup. The electro spun PAN matt was subsequently carbonized at 700°C for 4h in (ultra-high purity (UHP)-argon atmosphere (Matheson; 99.99%, flow rate of 100 cm^3/min) to form the CNF matt. Sulfur was electrodeposited onto the CNF matt under aqueous electrolyte-conditions using a two-electrode setup originally reported by Zhang et al.[167] The electrolyte consisted of 4.8g of sulfuric acid (98%, Sigma Aldrich), 0.3 g of KOH (99.9%, Sigma Aldrich), 0.5 M thiourea (99.9%, Sigma Aldrich) dissolved in 100ml of deionized water. The CNF matt was used as the working electrode and a Pt foil was used as the counter electrode and by applying a constant voltage of 5V[167] between the electrodes for 24 hours using a current limiting AC to DC transformer (25A) from McMaster-Carr. According to Zhang et al.[167], during the electrodeposition process, the sulfate (SO_4^{2-}) and hydroxy (OH^-) ions are intercalated into the CNF, while the thiourea molecules infiltrates into the CNF and are converted into elemental sulfur particles. The DDSA electrodes have an average sulfur loading of ~ 8-18 mg/cm^2. The DDSA on CNF matt was then electrochemically coated with gold (Au) which was selected as the polysulfide trapping agent (PTA). The PTA was electrodeposited onto the DDSA using gold chloride (200mg/dL deionized water) (Sigma Aldrich) solution by applying a potential of **5V** between Pt foil working electrode and DDSA counter electrode.

The X-ray diffraction patterns of the DDSA-PTA were collected using the Philips XPERT PRO system employing Cu-K_α (λ=0.15406nm) between 2Θ (10-40°) at 40mA and 45kV respectively. The microstructure and elemental composition of the DDSA-PTA was analyzed using JEOL JSM 6610 LV low-vac Scanning Electron Microscope (SEM) equipped with an Energy Dispersion Spectrometer (EDS). The surface chemistry of the DDSA-PTA was probed by X-ray photoelectron spectroscopy (XPS) using an ESCALAB250Xi system (Thermo Scientific)

equipped with a mono-chromated Al-K_a X-ray source. Uniform charge neutralization was provided by beams of low-energy (≤10eV) Ar^+ ions and low-energy electrons guided by magnetic lens. The UV-VIS spectroscopic measurements were performed in UV-VIS Evol 600 using the organic electrolyte as the reference. The electrochemical performance of the DDSA-PTA was evaluated in 2032 coin-cell. The coin cells for the electrochemical cycling were assembled inside an Argon-filled glovebox using the DDSA-PTA electrode as the cathode, lithium foil as anode and 1.8 M lithium trifluoro methane sulfonamide (LiTFSI) and 0.4 M $LiNO_3$ dissolved in Dioxolane/Dimethoxyethane (1:1 vol%) as electrolyte. The DOE's guidelines for lean electrolyte testing conditions, electrolyte to sulfur (E/S) ratio of 4µl/mg-S was employed. The coin cells were tested in an Arbin BT200 battery cycler between 1.6-2.6 V (w.r.t. Li^+/Li) at 0.1 C current rate. Electrochemical Impedance Spectroscopy (EIS) analysis were performed using a Gamry 600 potentiostat by varying the frequency between 100kHz and 10mHz at an amplitude of 10mV w.r.t the open circuit potential of ~2.2-2.4V. The obtained EIS data were then fitted using the ZView software (Scribner and Associates).

8.4 Results and Discussion

The XRD analysis of the DDSA-PTA electrode (Appendix F Figure 1) shows peaks corresponding to crystalline sulfur confirming crystalline deposits of sulfur on the CNF matt. The microstructure of the CNF samples, DDSA samples before and after PTA electrodeposition were characterized by scanning electron microscopy (SEM). Figure 8-1 shows a typical SEM image of the CNF matt and PTA-DDSA matt along with the sulfur, carbon and gold elemental mapping combined with the EDS and elemental composition results of the DDSA-PTA matt.

Appendix F Figure 2 shows SEM images of the DDSA matt including elemental mapping of carbon and sulfur showing 60 wt.% carbon and 36 wt.% S. The CNF fibers (Figure 8-1a) were smooth and of uniform thickness (1-2μm). The empty regions between the CNF fibers provides room for accommodating sulfur via sulfur electrodeposition.

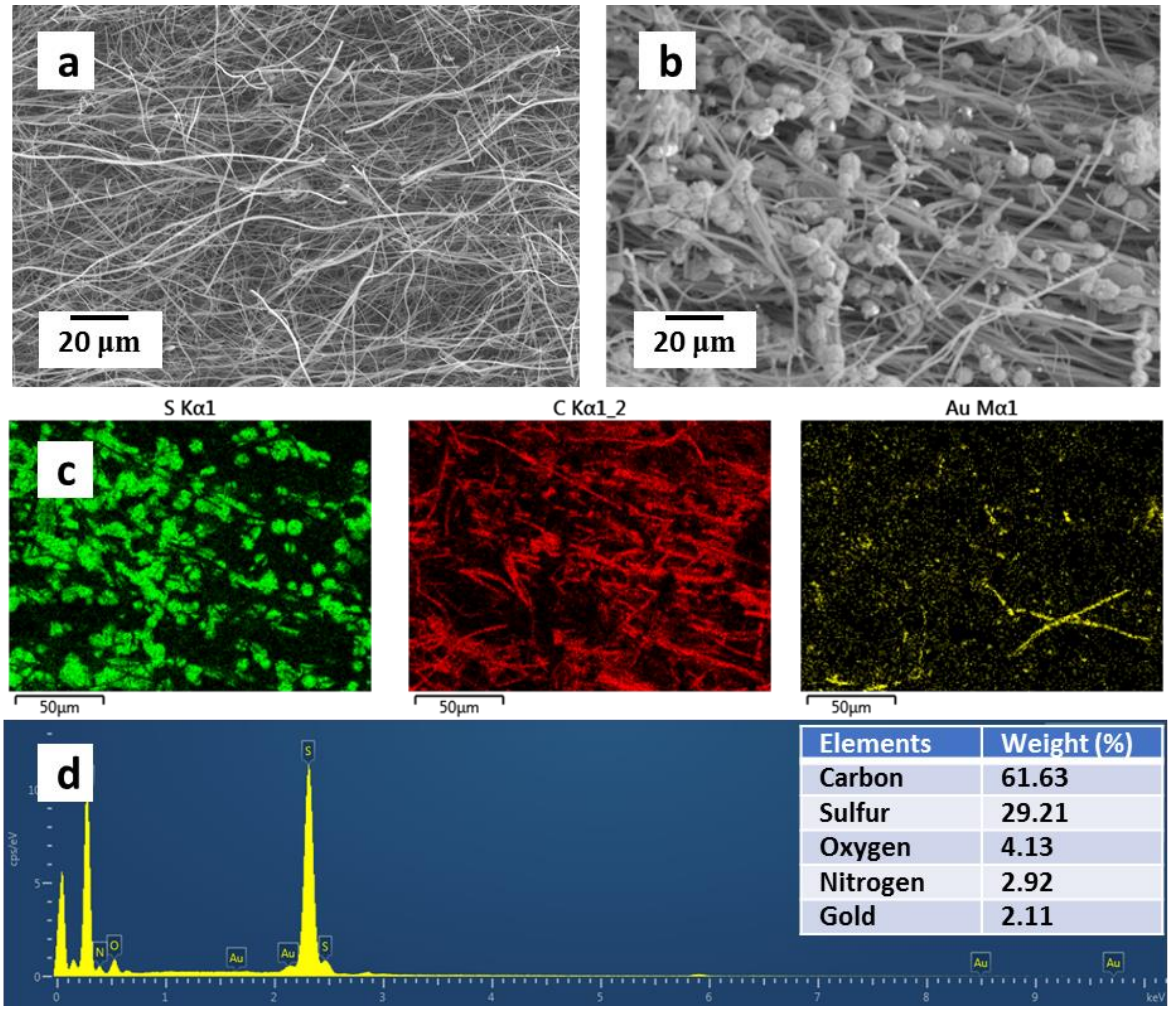

Figure 8-1 (a) SEM image of the CNF matt, (b) SEM images of PTA-DDSA matt, (d) Sulfur, carbon and gold mapping of the DDSA-PTA matt and d) EDS and elemental composition results of the DDSA-PTA matt.

Figure 8-1b shows the STEM image of the CNF matt after sulfur electrodeposition (DDSA-PTA). The sulfur particles are of uniform size with an average diameter of 5–7 μm and the CNF matt is uniformly coated with the sulfur particles. The use of electrodeposition aids in

preparing uniform sulfur deposits on the CNF matt. The sulfur, carbon and gold mappings of the DDSA-PTA (Figure 8-1c) shows that they match well with the STEM image Figure 8-1b, indicating that sulfur, carbon and gold are distributed homogeneously throughout the CNF-S composites. The elemental composition analysis (Figure 8-1d) shows the presence of ~30 wt.% sulfur and ~2 wt.% gold in the CNF matt comprising ~62 wt.% carbon.

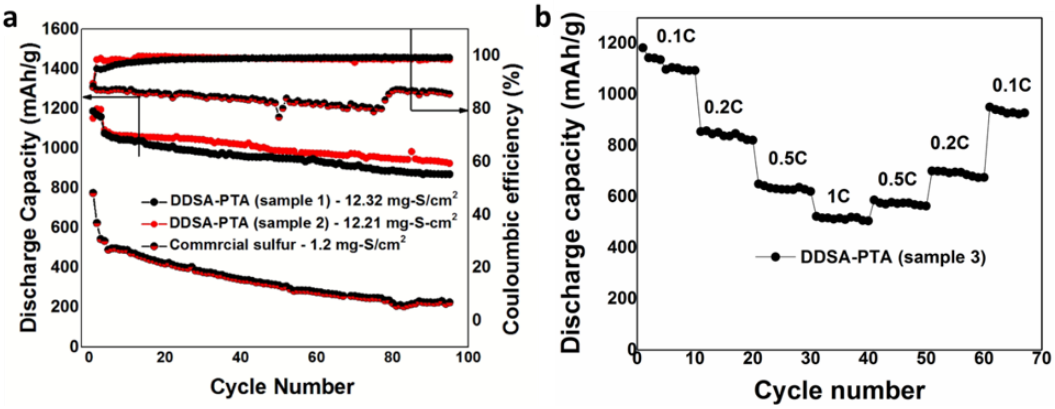

Figure 8-2 a) Electrochemical cycling plot of two DDSA-PTA samples (sample 1 and sample 2) from two batches synthesized under identical deposition conditions, (b) Rate capability measurements on the DDSA-PTA sample 3.

Figure 8-2 shows the cycling performance and rate-capability of the DDSA electrodes cycled at 0.1 C rate. The discharge capacity is calculated based on the weight of sulfur in the electrode measured from EDS. The DDSA-PTA electrodes exhibits a relatively stable discharge capacity during electrochemical charge–discharge cycling (cycling data from DDSA-PTA electrodes cycled under different E/S ratio are shown in Appendix F Figure 3and Appendix F Figure 5). The first and 100th cycle discharge capacity of the DDSA-PTA (sample 1) is 1152 mAh/g and 925 mAh/g, respectively corresponding to an areal capacity of ~11.29 mAh/cm^2. On the other hand, the first and 100th cycle discharge capacity of the DDSA-PTA (sample 2) is 1188

mAh/g and 870 mAh/g, respectively giving an area capacity of ~10.71 mAh/cm^2. Correspondingly the DDSA-PTA (sample 1) and DDSA-PTA (sample 2) electrodes exhibit very low fade rate of 0.20%/cycle and 0.26%/cycle, respectively while additionally exhibiting very high coulombic efficiency of ~99.6%. The observation of slight fade in capacity is due to the formation of insulating Li_2S that is not completely oxidized upon charging and not due to polysulfide dissolution, as explained by Zhang et al., in his work on sulfur electrodeposition onto graphite. It is deduced that the sulfur electrodeposited onto CNF matts by the electrochemical method is responsible for the stable electrochemical cycling performance due to its physical and chemical interactions with polysulfides. In addition, the sulfur electrodeposition at the solid/liquid (CNF/aqueous thiourea solution) interface can ensure intimate contact of sulfur particles with the CNF matts, effectively confining lithium polysulfides from dissolving into the organic liquid electrolyte. Figure 8-2b shows the rate capability of the DDSA-PTA (sample 3) electrode at different current densities from 0.1C to 1C rate. A reversible capacity of ~ 825 mAh/g is obtained at a current density of 0.2C rate, owing to the good electrical conductivity of the CNF ($1.81 \pm 0.17 \times 10^{-5}$ S/cm) and the uniformly dispersed S. The value of the discharge capacity is ~ 589 and 492 mAh/g for 0.5C and 1C rate, respectively and the discharge capacity returns to ~918 mAh/g at 0.1C rate, the electrode almost recovering its original capacity. This value to the best of our knowledge for discharge capacity at high sulfur loading is comparable to the best performance of sulfur cathode materials prepared by solution-based deposition technique and other methods. X-ray photoelectron spectroscopy (XPS) was used to characterize the chemical state of sulfur in the DDSA-PTA separators and electrodes post cycling. The XPS spectra obtained from the DDSA-PTA separators and electrodes were compared with those obtained from corresponding separators and electrodes cycled with commercial sulfur cathode.

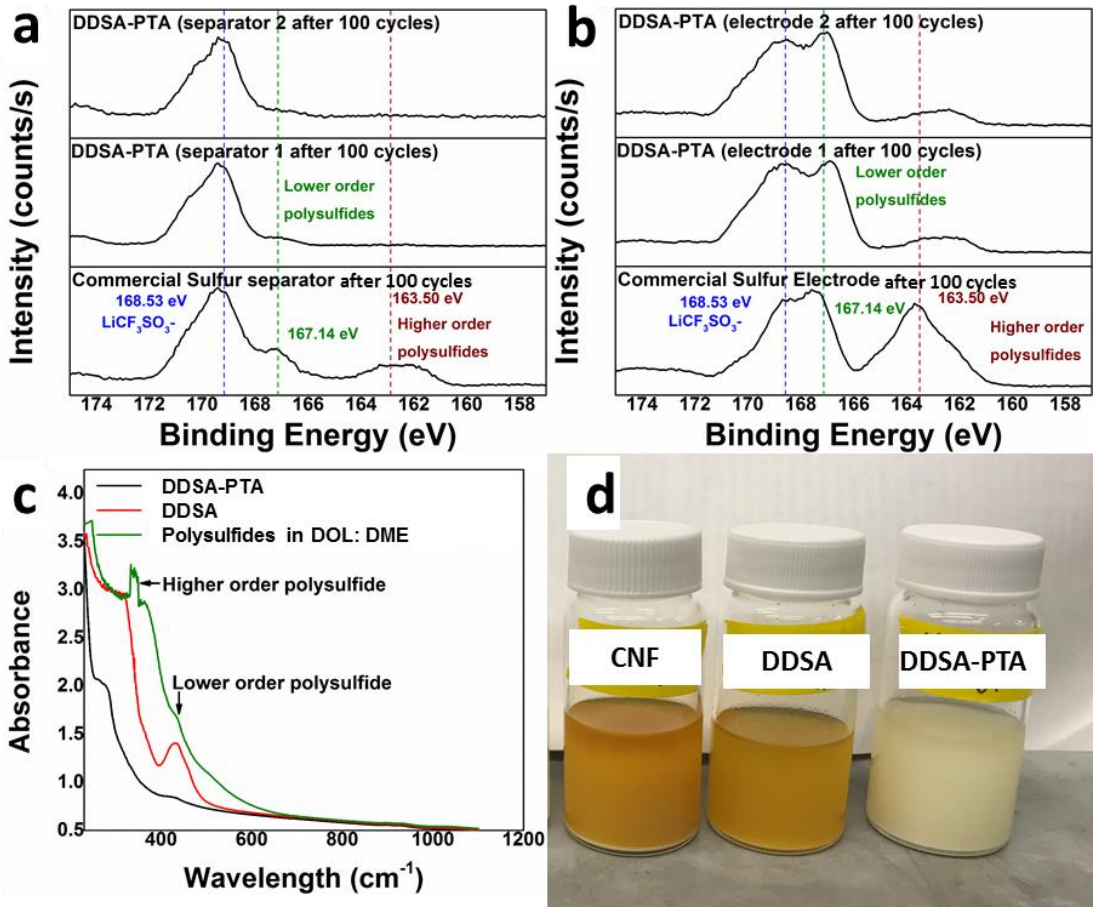

Figure 8-3 (a) XPS analysis of the separators, (b) electrodes from the two DDSA-PTA batteries, (c) UV-Vis spectroscopy analysis on the DDSA and DDSA-PTA samples and (d) polysulfide solutions treated with CNF, DDSA and DDSA-PTA.

Figure 8-3a shows the S2p XPS spectra of the DDSA-PTA (sample 1 and sample 2) separators collected after 100 cycles. The commercial sulfur separator after 100 cycles exhibits S2p peaks at 168.53eV[250], 167.14eV[192, 429] and 163.50eV[430] corresponding to $CF_3SO_3^-$ groups from the LiTFSI salt, lower and higher order polysulfides, respectively. However, the DDSA-PTA separators after cycling shows significant reduction in peak intensities at 167.14eV and 163.50eV confirming that there is almost negligible polysulfide dissolution in the DDSA-PTA system. Similarly, the commercial sulfur electrodes (sample 1 and sample 2) after cycling

(Figure 8-3b) exhibits S2p peaks at 168.53eV, 167.14eV and 163.50eV corresponding to $CF_3SO_3^-$ groups from the LiTFSI salt, lower and higher order polysulfides respectively. However, the DDSA-PTA electrodes after cycling shows significant reduction in peak intensities at 163.50eV indicating the absence of higher order polysulfides on the DDSA-PTA cathode, which could be attributed to the polysulfide reduction property of Au as explained by Fan et al., in his work on Au-S at the sulfur cathode[431]. Appendix F Figure 6 shows XPS results on the separators collected after 100 cycles of other DDSA-PTA electrodes compared to the commercial sulfur cycled separator after 100 cycles. The UV-VIS spectroscopic analysis conducted on the DOL-DME solvent containing polysulfides added to the CNF matt, the DDSA and DDSA-PTA samples correspondingly also reveals the absence of higher order polysulfides in the polysulfide solution immersed in DDSA-PTA electrode (Figure 8-3c).

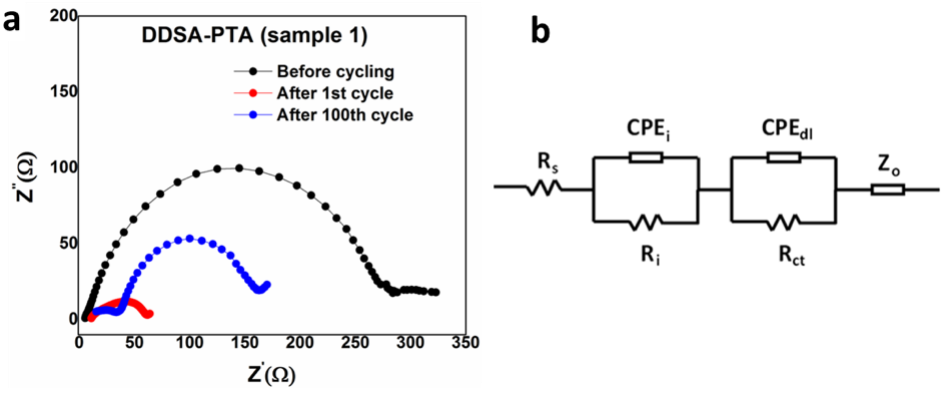

Figure 8-4 (a) Nyquist plot of the DDSA-PTA battery before cycling, after 1st cycle and 100th charge-discharge cycles and (b) the equivalent circuit used to fit the Nyquist plots.

The DDSA-PTA electrodes were further studied using electrochemical impedance spectroscopy (EIS) analysis before and after cycling to further understand their enhanced electrochemical performance. Figure 8-4a&b shows the Nyquist plot and the equivalent circuit

used to fit the data (Appendix F Figure 7 shows the impedance data from DDSA-PTA (sample 2 and sample 3)). As is evident from the Nyquist plots, the experimental data fits well with the fitted data using the equivalent circuit. The Nyquist plots shows two semicircles, corresponding to the resistance of passivation film (interface resistance-R_i) of the discharge product in the high-frequency region and the charge transfer resistance R_{ct} in the medium-frequency area. The R_{ct} decreases considerably after cycling due to complete wetting of the electrode by the electrolyte and the rearrangement of the migrated active materials to the electrochemically favorable position.

The interfacial resistance R_i of the pristine as well as the cells after 1st and 100th cycle remained almost constant at ~20 Ω (Fitted values are shown in Appendix F Table 1), before and after the first cycle while the charge transfer resistance (R_{ct}) undergoes significant change with lithiation (after first cycle) similar to that observed by Fan et al., in his work on using Au nanoparticles as sulfur immobilizers in Li-S batteries[431]. This reduction in R_{ct} is likely due to the immobilization of polysulfides by the Au nanoparticles similar to the results of Fan et al., thereby restricting the formation of the solid electrolyte interface (SEI) on the anode arising from the deposition of the low order polysulfides. All these electrochemical characterizations further suggest that the modest decoration of the cathode by the electrodeposition of Au nanoparticles has a profound influence on the improvement of the electrochemical performance of Li–S batteries.

8.5 Summary

A simple electrodeposition technique was implemented to prepare PTA coated DDSA electrodes that were used as free-standing cathodes in Li-S batteries. The PTA-DDSA cathodes exhibited significantly reduced polysulfide dissolution as is evident from the XPS analysis in addition to displaying excellent cycling stability. The DDSA-PTA electrode exhibits an initial capacity of 1188 mAh/g (14.62 mAh/cm2 areal capacity) and a stable capacity of 870 mAh/g (10.71 mAh/cm2 areal capacity) after 100 cycles at 0.1 C rate. The DDSA-PTA electrode 1 shows an initial capacity of 1152 mAh/g (14.06 mAh/cm2 areal capacity) and a stable capacity of 925 mAh/g (11.29 mAh/cm2 areal capacity) after 100 cycles at 0.1C rate when tested under the lean electrolyte (4µl/mg-S) testing conditions. The PTA-DDSA electrodes exhibited very low fade rate of 0.23±0.03%/cycle and significantly reduced polysulfides when examined by XPS and UV-VIS spectroscopy. The EIS impedance analysis of the DDSA-PTA before and after cycling also suggests polysulfide immobilization by Au nanoparticles. The development PTA-DDSA electrodes will enable the use of high energy density battery systems consisting of sulfur cathodes with superior capacity retention and stability. The success of this approach should help expedite developments in high energy lithium-sulfur battery systems and help achieve the DOE's target of 500 Wh/kg.

8.6 Acknowledgments

The authors acknowledge the research support by the U.S. Department of Energy (OVT-DE-EE0006825, OVT-DE-EE0007797 and Battery500 consortium DE-EE0008199) Edward R. Weidlein Chair Professorship Funds and the Center for Complex Engineered Multifunctional Materials (CCEMM) for assistance and help with procuring the electrochemical equipment and facilities used in this research work. The authors also acknowledge Dr. Joel Gillespie, PPG Materials Characterization Laboratory, and the Department of Chemistry, University of Pittsburgh for graciously providing access to the use of XPS instrumentation.

9.0 Conclusions

The design and development of novel materials for energy storage is urgent for addressing electric vehicle (EV) energy storage demands. Materials for Li-S battery cathodes and electrolytes were developed as a part of this dissertation. Nanoporous non-carbonized MOF were synthesized using a simple, scalable room temperature method. Sulfur was directly infiltrated into the as-synthesized MOF with no subsequent carbonization and tested as cathodes for Li – S batteries. The resultant S – MOF display very high initial capacity (1476 mAh/g) that is rendered stable at 609 mAh/g for over 200 cycles with an impressive very minimal fade rate (0.0014 %/cycle). The study reveals that the use of non-carbonized MOF resulting in Lewis acid-base interactions is vital for ensuring the carbon-sulfur bonding with the MOF architecture resulting in complete retention of lithiated polysulfide species within the porous MOF structure.

Metal sulfate containing, nanoporous CFMs (Cu-bpy-CFM and Cu-pyz-CFM) were synthesized using microwave-assisted hydrothermal synthesis, infiltrated with sulfur, and used as cathodes to study their performance in Li-S battery. The S-Cu-bpy-CFM shows an initial discharge capacity of 1565 mAh/g and stabilizes at a discharge capacity of 975 mAh/g after 200 cycles (fade rate of 0.19%/ cycle). The S-Cu-pyz-CFM also shows a high initial discharge capacity of 1626 mAh/g and a stable 1020 mAh/g discharge capacity after 200 cycles (fade rate of 0.18%/cycle). These CFMs interacts with polysulfides via Lewis acid-base interactions and thereby effectively restrain the polysulfides from diffusing and dissolving into the electrolyte. In addition, the carbon atoms of the CFMs bind with sulfur during the sulfur infiltration process, further aiding in preventing the polysulfides from dissolving into the electrolyte. XPS analysis of the CFM separators further confirms the absence of polysulfide dissolution.

A sulfonic acid-based complex framework material (CFM), termed as SCFM was effectively synthesized at room temperature and infiltrated with sulfur using a vapor-phase infiltration technique to form S-SCFM. The S-SCFM electrode was then tested as a cathode for Li-S batteries. The S-SCFM electrode demonstrated a high initial capacity of 1190 mAh/g, with stable capacity of 1044 mAh/g for up to 100 cycles when cycled at 0.1C rate while also exhibiting reversible capacity of 669 mAh/g at 1C rate. The electrode regains the capacity of 1066 mAh/g when cycled back at 0.1C. The S-SCFM also exhibited good cycling stability along with a low fade rate of ~0.0012%/cycle. The higher discharge capacity along with impressive cycling stability makes the sulfonic acid-based CFM namely, SCFM an appealing sulfur host to form S-SCFM structures serving as effective operational electrodes for Li-S batteries.

f-SiO_2, nm-SiO_2, and nm-TiO_2 incorporated novel electrospun PVdF-HFP CPEs were tested as electrolytes in Li–S battery. The 10 wt % f- SiO_2 CPE exhibited an initial discharge capacity of 895 mAh/g and very low fade rate of 0.055%/cycle when cycled for over 100 cycles at 0.1 C rate against commercial sulfur cathode. The study also conclusively indicates that the electrospinning technique improves the mechanical properties of the CPEs which in turn help suppress dendrite formation on the lithium anode. The nanofiller incorporated CPEs also exhibit excellent room-temperature ionic conductivity of 9.48×10^{-3} S/cm, with values comparable to that of liquid electrolytes. The CPEs also exhibit excellent chemical stability upon cycling for over 100 cycles, confirmed using FTIR and XPS analysis.

Li_4SiO_4 was substituted with six different concentrations of each substituent using a high temperature solid-state diffusion technique. A maximum of 7.5 atomic % of Li^+ sites were substituted with Ca^{2+} and Mg^{2+} ions and 10% of the O^{2-} sites were substituted with F^- ions while maintaining the crystallographic and phase purity. Electrochemical Impedance Spectroscopy

(EIS) analysis results clearly show that the introduction of the substituents improved the ionic conductivity of Li_4SiO_4 by 3 – 4 orders of magnitude. In fact, Ca^{2+} introduction as a substituent showed the maximum improvement in ionic conductivity from 1.2×10^{-12} S cm^{-1} to 2.9×10^{-8} S/cm. The substituted Li_4SiO_4 further serve to act as an impermeable barrier to solvent molecules only enabling faster transport of Li ions adding to the cycling stability. High loading sulfur cathodes (~3.8 mg S/cm^2) of S-Cu-bpy-CFM were thus tested by coating a layer of the substituted Li_4SiO_4 and their cycling performance and rate capability were evaluated. The substituted Li_4SiO_4 S-Cu-bpy-CFM electrodes demonstrated high areal capacities of (~2.21-2.67 mAh/cm^2) along with good capacity retention (~0.19-0.33%/cycle) and rate capabilities (~800 mAh/g-700 mAh/g @100 mA/g, 600 mAh/g- 500 mAh/g @300 mA/g, 400 mAh/g-300 mAh/g @ 500 mA/g and ~250mAh/g – 190 mAh/g @1000 mA/g) in comparison to pristine Li_4SiO_4.

DDSA-PTA electrodes were synthesized using a simple electrodeposition technique and were used as free-standing cathodes in Li-S batteries. The PTA-DDSA cathodes exhibited significantly reduced polysulfide dissolution as is evident from the XPS analysis in addition to displaying excellent cycling stability. The DDSA-PTA electrode1 exhibits an initial capacity of 1188 mAh/g (14.62 mAh/cm^2 areal capacity) and a stable capacity of 870 mAh/g (10.71 mAh/cm^2 areal capacity) after 100 cycles at 0.1 C rate. The DDSA-PTA electrode 2 shows an initial capacity of 1152 mAh/g (14.06 mAh/cm^2 areal capacity) and a stable capacity of 925 mAh/g (11.29 mAh/cm^2 areal capacity) after 100 cycles at 0.1C rate. The PTA-DDSA electrodes exhibited very low fade rate of 0.23±0.03%/cycle and significantly reduced polysulfides when examined by XPS and UV-VIS spectroscopy. The success of this approach should help expedite developments in high energy lithium-sulfur battery systems and help achieve the DOE's target of 500 Wh/kg.

Appendix A Supporting Information: Understand the Origin of Irreversible Capacity Loss in Li-S Batteries and Address the Mechanisms of Polysulfide Dissolution Using Structurally Distinct Metal Organic Framework (MOF) Based Sulfur Cathodes – (i) Understanding the Origin of Irreversible Capacity Loss in Non-carbonized Carbonate – based Metal Organic Framework (MOF) Sulfur Hosts for Lithium – Sulfur Battery

Pavithra M Shanthi[a], Prashanth J Hanumantha[b], Matthew Sweeney[c], Bharat Gattu[a], Moni K Datta[b], Prashant N Kumta[a, b, d, e]

[a]Department of Chemical and Petroleum Engineering,
University of Pittsburgh, Pittsburgh, PA 15261 (USA)

[b]Department of Bioengineering
University of Pittsburgh, Pittsburgh, PA 15261 (USA)

[c]Department of Chemical Engineering,
University of Maryland- Baltimore County, Baltimore, MD 21250 (USA)

[d]Department of Mechanical Engineering and Materials Science
University of Pittsburgh, Pittsburgh, PA 15261 (USA)

[e]Center for Complex Engineered Multifunctional Materials
University of Pittsburgh, Pittsburgh, PA 15261 (USA)

TGA/DTA analysis

Thermo-Gravimetric Analysis/ Differential Thermal Analysis was performed on the as-prepared-damp Zn MOF-5 materials on a Netzsch STA 09PC/4/H/Luxx TG-DTA analyzer under Argon atmosphere using a temperature sweep of 5°C/min.

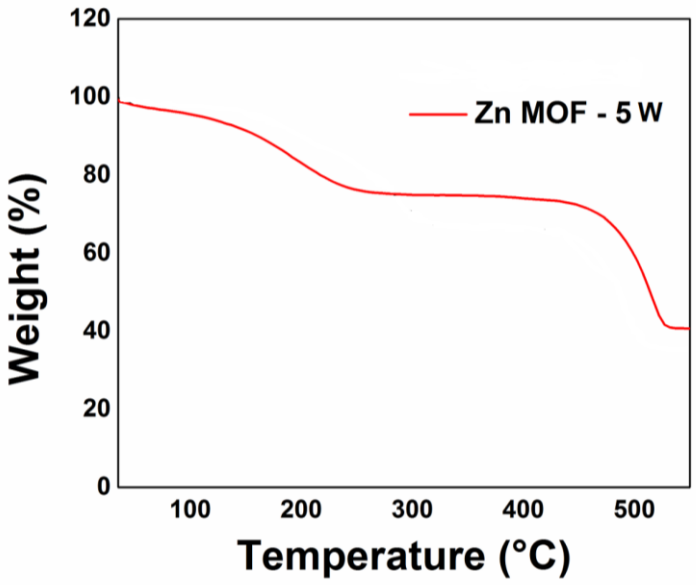

Appendix A Figure 1 TGA curves of Zn MOF – 5W under Argon at 5°C/min heating rate.

The TGA results (Appendix A Figure 1) show that both Zn MOF – 5 (as prepared-damp are stable at temperatures up to 450°C[157, 158, 432, 433]. The initial weight loss between 25 – 200°C is attributed to the loss of solvent molecules entrapped into the pores of the MOF. The stable plateau observed up to 450°C shows the temperature stability of the MOF. The weight loss observed above 420°C is due to the onset of the decomposition of the organic framework. This indicates that the infiltration of sulfur into the MOF structures at 300°C would not cause any decomposition of the same and would result in stable sulfur-containing MOF structures (S-MOF).

SEM Images of the MOF:

Scanning electron microscopy (SEM) was carried out to investigate the microscopic structure of Zn MOF – 5W (Appendix A Figure 2). Philips XL-30FEG equipped with an EDAX detector system comprised of an ultrathin beryllium window and Si(Li) detector operating at 10 kV was used for the SEM analysis. The SEM images show the microscopic structure of Zn MOF – 5W which is in accordance with these reported in literature[145, 434, 435].

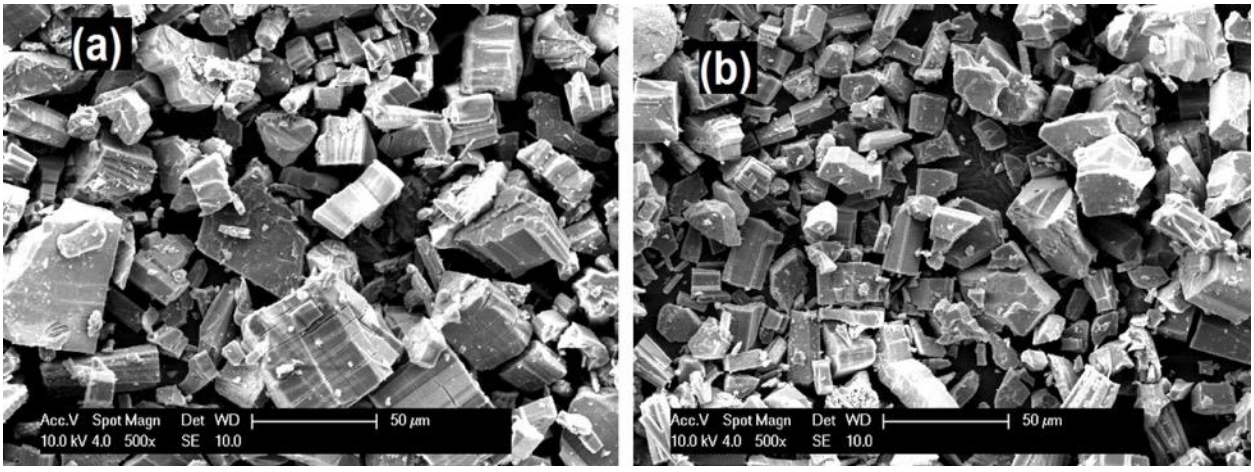

Appendix A Figure 2 SEM images of (a&b) Zn MOF – 5W.

Electrochemical Behavior of S-MOF Materials:

To understand the charge storage behavior of the S-MOF and identify possible sources of the initial irreversible capacity loss observed therein, the charge-discharge profiles of the S-Zn-MOF during different cycles were evaluated as depicted in Appendix A Figure 3. Appendix A Figure 3 corresponds to the specific capacity plots of 1^{st}, 2^{nd}, 10^{th}, 100^{th} and 200^{th} charge – discharge profiles of S – MOF at 0.2C rate. The smaller plateau in the specific capacity plots at 2.4 V corresponds to the formation of the higher order polysulfide during the initial stages of

lithiation Li_2S_n (n = 4-8) and the plateau at 2.1 V corresponds to the formation of lower order lithium sulfides Li_2S_n (n<4) also represented by the larger plateau in the specific capacity plots (Appendix A Figure 3) [87, 140, 436-440]. Similar plateaus at 2.45 V and 2.2 V are observed in the charge cycles corresponding to the delithiation of Li_2S to lower polysulfide and higher order polysulfide respectively, resulting in the formation of sulfur.

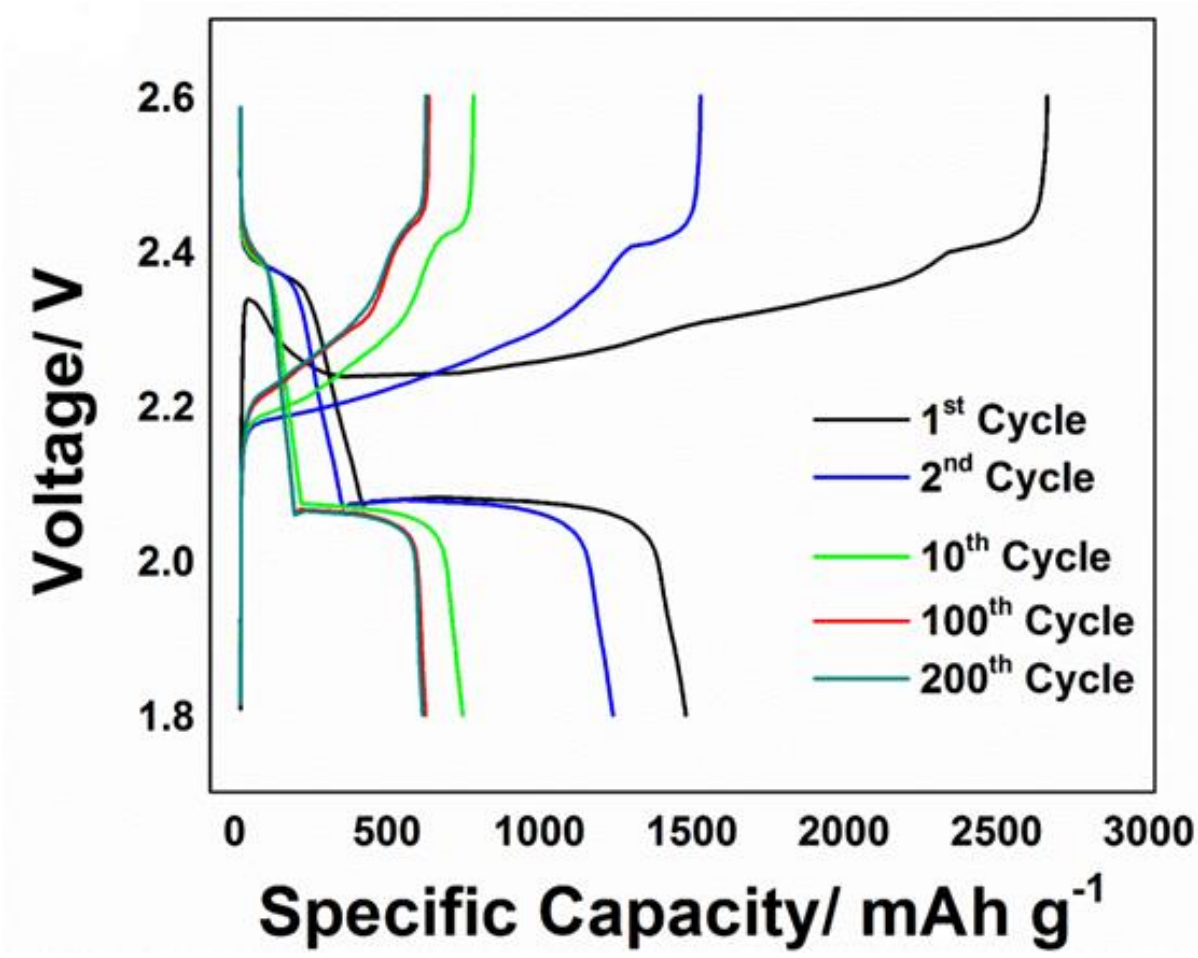

Appendix A Figure 3 Charge-discharge plots at various stages of cycling of S – Zn – MOF.

Appendix A Table 1 Reaction voltages (V w.r.t. Li^+/Li) in cyclic voltammograms of S-Zn-MOF.

S-Zn-MOF						
	Anodic scan			Cathodic scan		
Cycle number	Possible Reactions (S1& S2) voltage/ V	Reaction (i) voltage/ V	Reaction (ii) voltage/ V	Reaction (iii) voltage/ V		Reaction (iv) voltage/ V
1st cycle	2.38	2.45		2.03	2.07	2.35
2nd cycle	2.28	2.35	2.41	2.04	2.08	2.36
5th cycle	2.28	2.36	2.41	2.04	2.08	2.36
10th cycle	2.28	2.35	2.41	2.04	2.07	2.36
20th cycle	2.28	2.35	2.41	2.03	2.07	2.36

XPS Spectra of MOF and S – MOF:

In order to confirm that the initial fade in capacity was indeed a result of the electrochemical oxidation of sulfur and that the state of the electrode does not change subsequent to the initial phase transformation, X-ray photoelectron spectroscopy was performed on the separator and electrode after the 1st and 20th cycle (cycling performed at 0.1 mV/s between 1.7 and 2.6 V- voltammograms seen in Figure 3-9). It can be seen in Appendix A Figure 4 that the S2p peak profiles of the separator retrieved from the S-Zn-MOF cells do not show any noticeable change indicating the absence of sulfur containing polysulfides in the separator during the 1st and 20th cycles in addition to the 200th cycle. This confirms the primary hypothesis of this work-that the presence of sulfur-carbon bonding in the MOF structure ensures polysulfide retention within

the electrode and prevents dissolution and cross-over across the separator to the anode. Appendix A Figure 5 and Appendix A Figure 6 compare the C1s and S2p profiles of the S-Zn-MOF electrodes before cycling and subsequent to 1^{st}, 20^{th} and 200^{th} cycle. It can be seen in Appendix A Figure 5 that the peak positions of carbon bonding in the S-Zn-MOF electrodes does not undergo any change from the 1^{st} to the 200^{th} cycle indicating that the predominating species in the electrode structure remain near identical during cycling. Similar to this is the case with S2p profiles seen in Appendix A Figure 6. However, as indexed in Appendix A Figure 6, the presence of polysulfides, sulfates and sulfites within the electrode structure can be observed during the 1^{st} and 20^{th} cycle. This is to be expected and it is a testament to the superior polysulfide retention capability of the S-Zn-MOF materials, especially since no polysulfides are seen in the separator at the same stage of cycling (Appendix A Figure 4). This is further confirmed by examining the S2p profile of the lithium anode post-cycling where no presence of polysulfides or deposited sulfur is observed (Appendix A Figure 7).

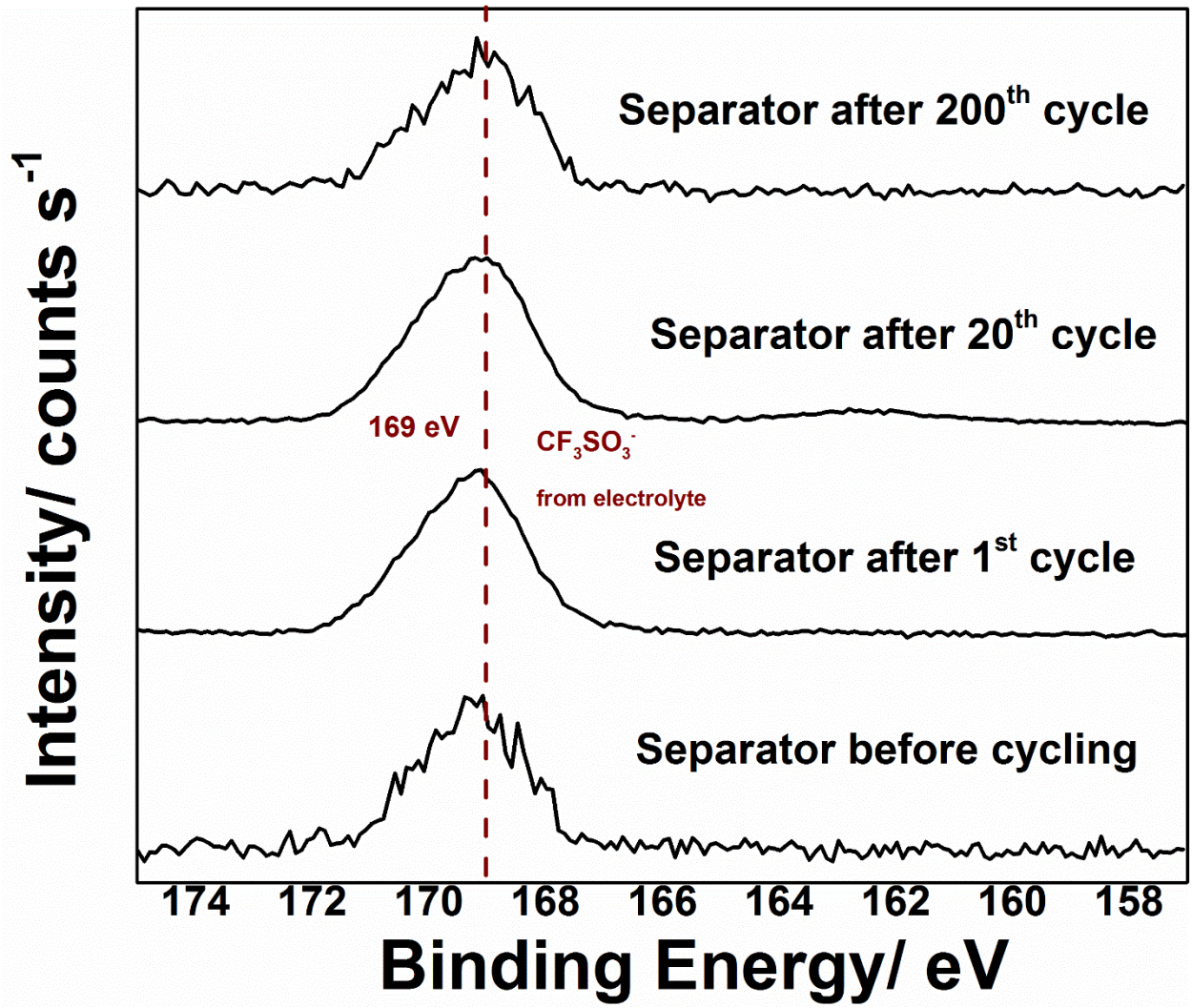

Appendix A Figure 4 S2p profiles of the S-Zn-MOF cell separators before cycling, after the 1st, 20th and 200th cycle.

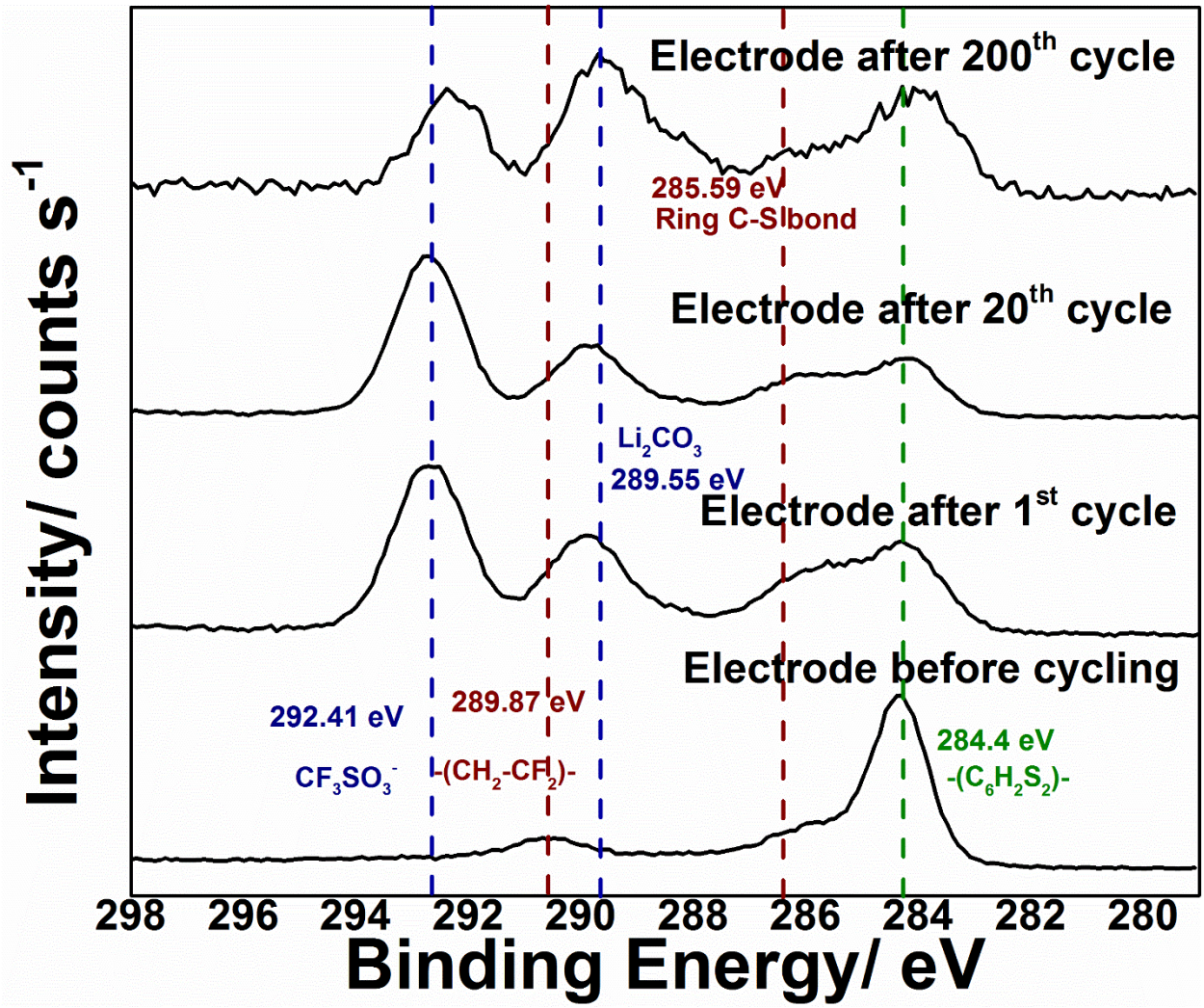

Appendix A Figure 5 C1s profiles of S-Zn-MOF electrodes before cycling, after 1st, 20th and 200th cycle.

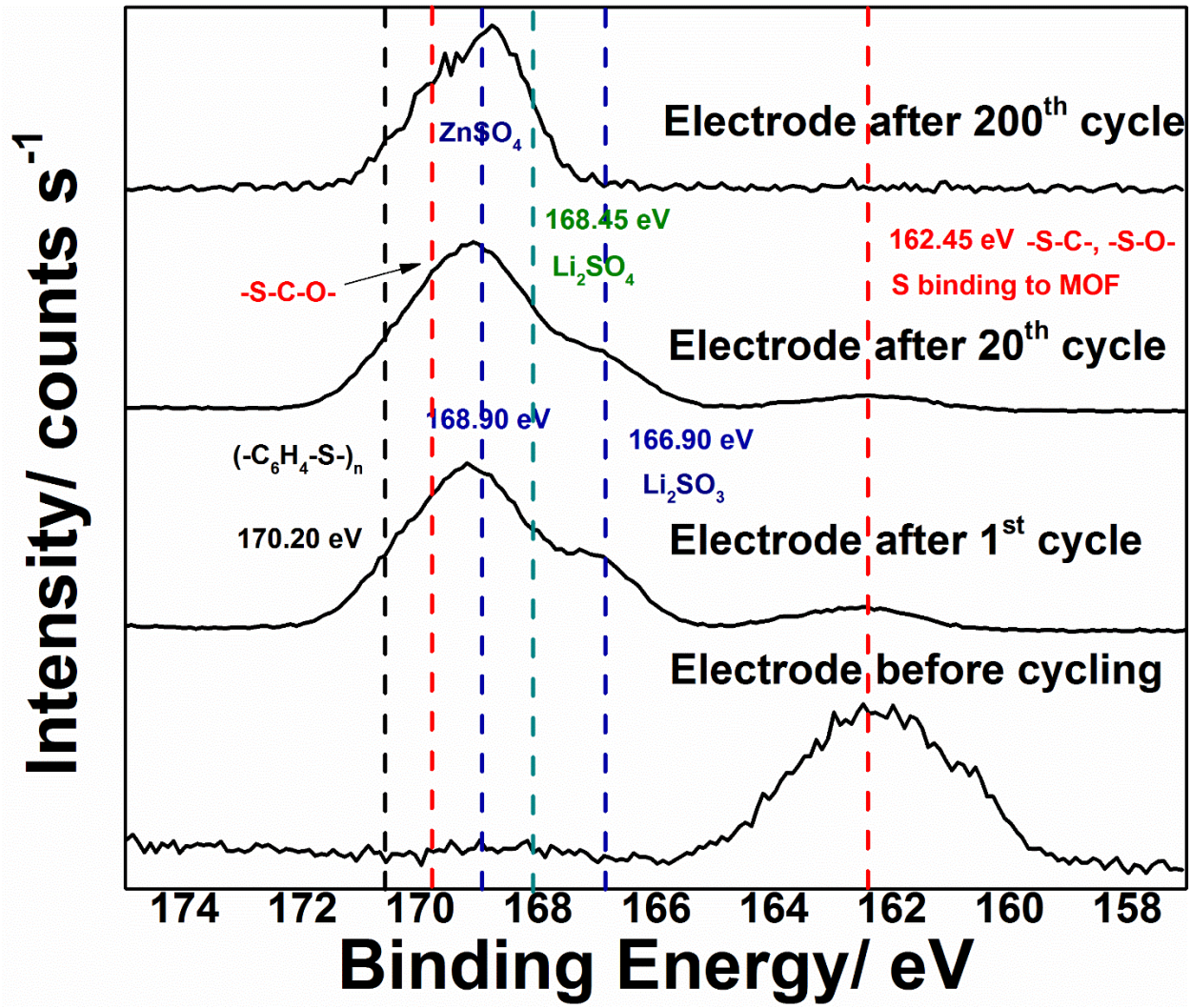

Appendix A Figure 6 S2p profiles of S-Zn-MOF electrodes before cycling, after 1st, 20th and 200th cycle.

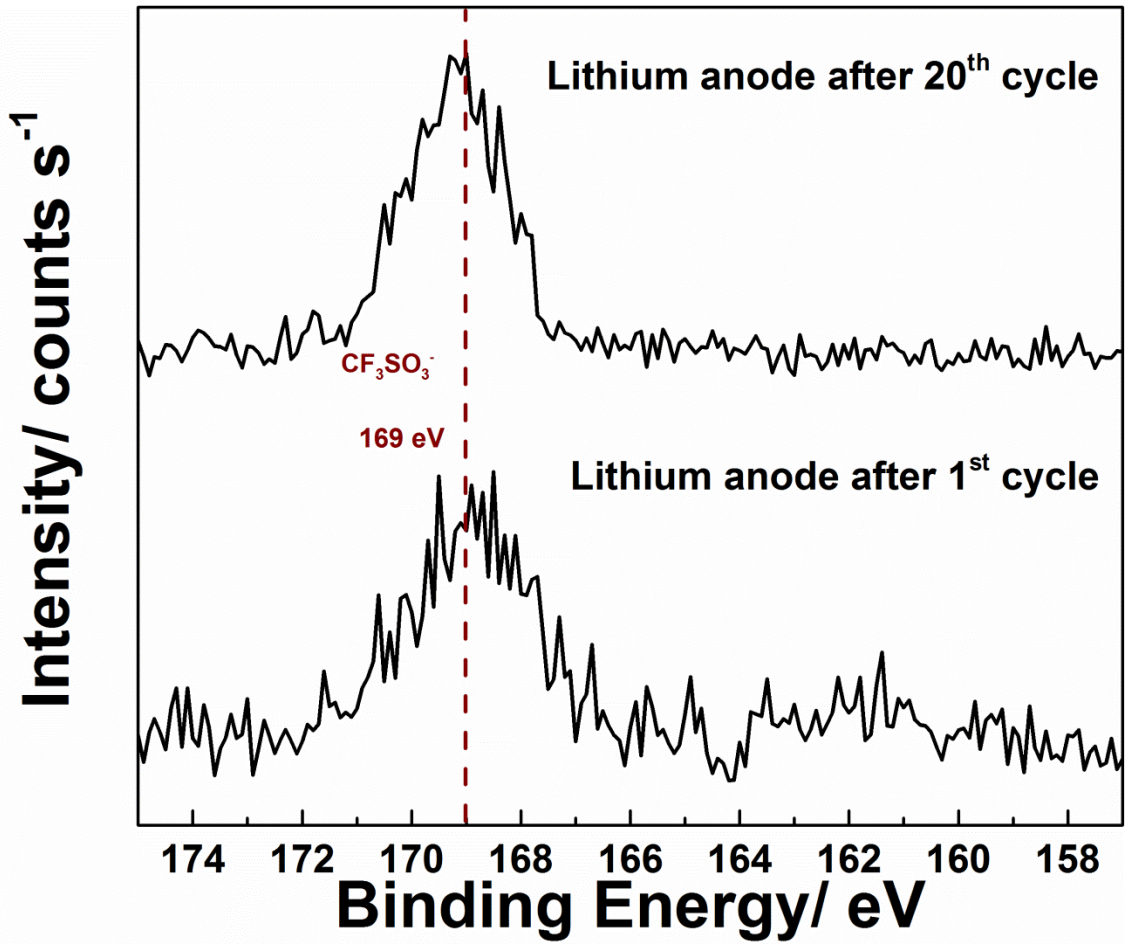

Appendix A Figure 7 S2p profiles of the lithium counter electrode in a cell containing S-Zn-MOF electrodes subsequent to 1st and 20th cycle.

C1s Spectra of MOF and S – MOF:

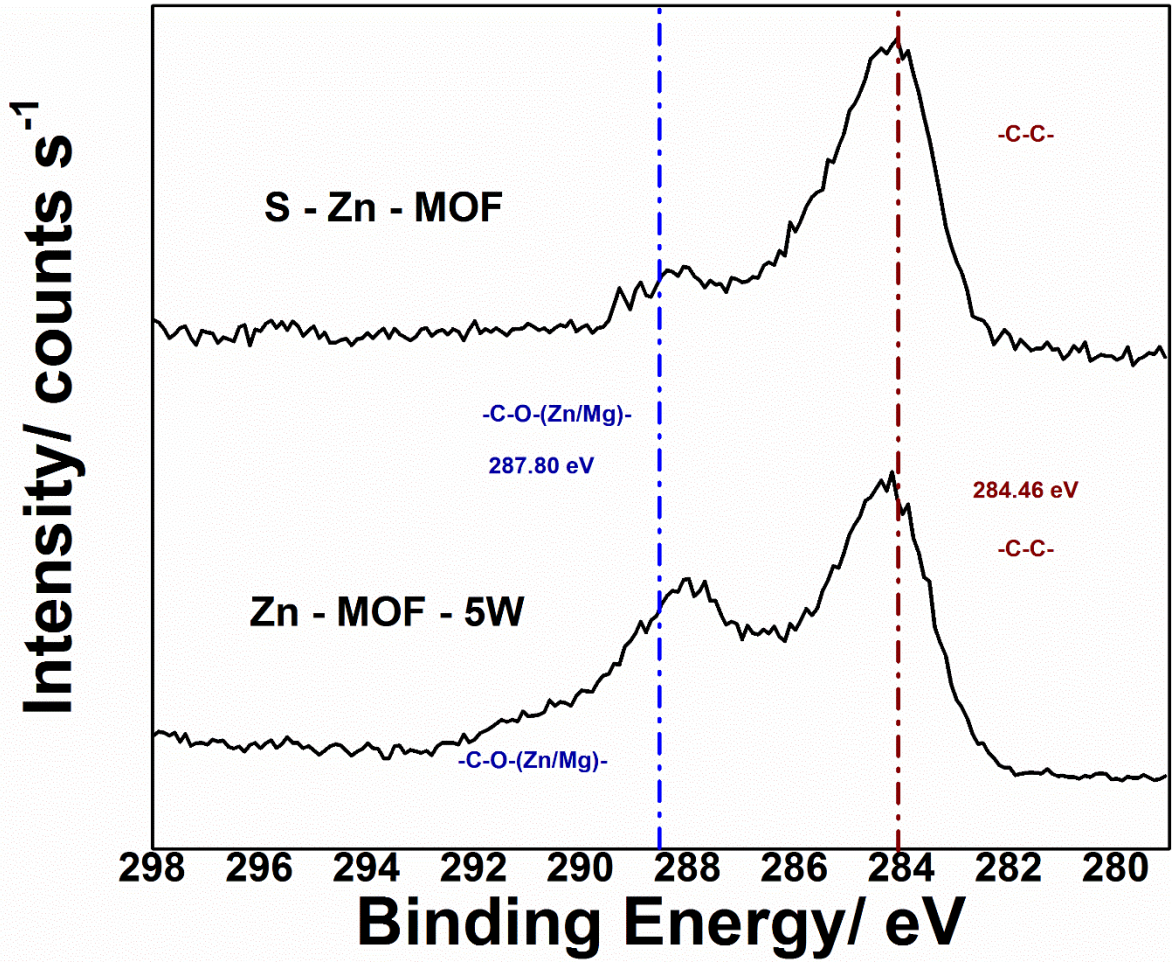

Appendix A Figure 8 C1s spectra of MOF before and after Sulfur infiltration.

The C1s spectra of the MOF-Ws and S – MOF are shown in Appendix A Figure 8. The broad C1s peak around 284.46 eV is due to –C – C – bonds in the MOF structures[441-443]. materials. The C1s peak spread around 287.80 eV is attributed to the binding of C to –O-Mg/Zn –[444, 445] through the formation of –(CO_3)- moieties in the MOF. In addition, it can be observed that the relative peak intensity of the 284.46 eV peak increases with respect to the peak at 287.80 eV. This could be attributed to contribution from the overlapping nature of C-S binding peaks[446] in S – MOF with the C-C peaks in the MOF structure.

Irreversible Loss of Capacity in the 1st ten Cycles:

The observed loss in sulfur capacity through binding with carbonate species could proceed through the mechanism proposed below:

Proposed mechanism: (Results in consumption of 10 moles of S/mole of MOF to form irreversible sulfate-like byproduct)

Reaction S1: $Zn_4O(C_6H_4(COO)_2)_3 + 4S + 6Li \rightarrow Zn_4(S_4)\ O^{2-} + (C_6H_4(COOLi)_2)_3$[447]

Reaction S2: $(C_6H_4(COOLi)_2)_3 + 8S \rightarrow 3Li_2S_2O_3 + C_6H_4C\text{-}S\text{-}S\text{-}$ **(active)**[179]

The formation of such metal cluster complexes has been reported in chemical reactions between Zn-cage like structures and sulfur[447]. Further studies however are warranted to understand the exact nature of electrochemical oxidation of sulfur by the carbonate MOF structures. Appendix A Table 2 shows the calculation of the amount of sulfur lost by the reaction of sulfur with MOF. The calculation is based on the moles of sulfur in S – Zn – MOF electrode based on the initial weight of sulfur and MOF (50:50wt%).

Appendix A Table 2 Calculation of amount of sulfur consumed by the irreversible reactions S1 and S2.

	Proposed mechanism (mole)
Nominal sulfur content during synthesis/mole of MOF (M.W = 32.065 g/mole)	17
Nominal MOF content during synthesis/mole of MOF (M.W = 769.90 g/mole)	1
Number of moles of sulfur lost during initial cycles	10
Active sulfur remaining that cycles stably after initial capacity loss	7

Appendix A Figure 9 represents the recalculated cathode capacity based on the active unreacted sulfur remaining after accounting for the irreversible loss processes described above. It can thus be seen that sulfur accounted for cycling is indeed restricted by the MOF structure at the electrode surface after the initial reaction causing retention of capacity close to the theoretical capacity of sulfur. This nevertheless is not observed due to the loss processes occurring during the 1st ten cycles.

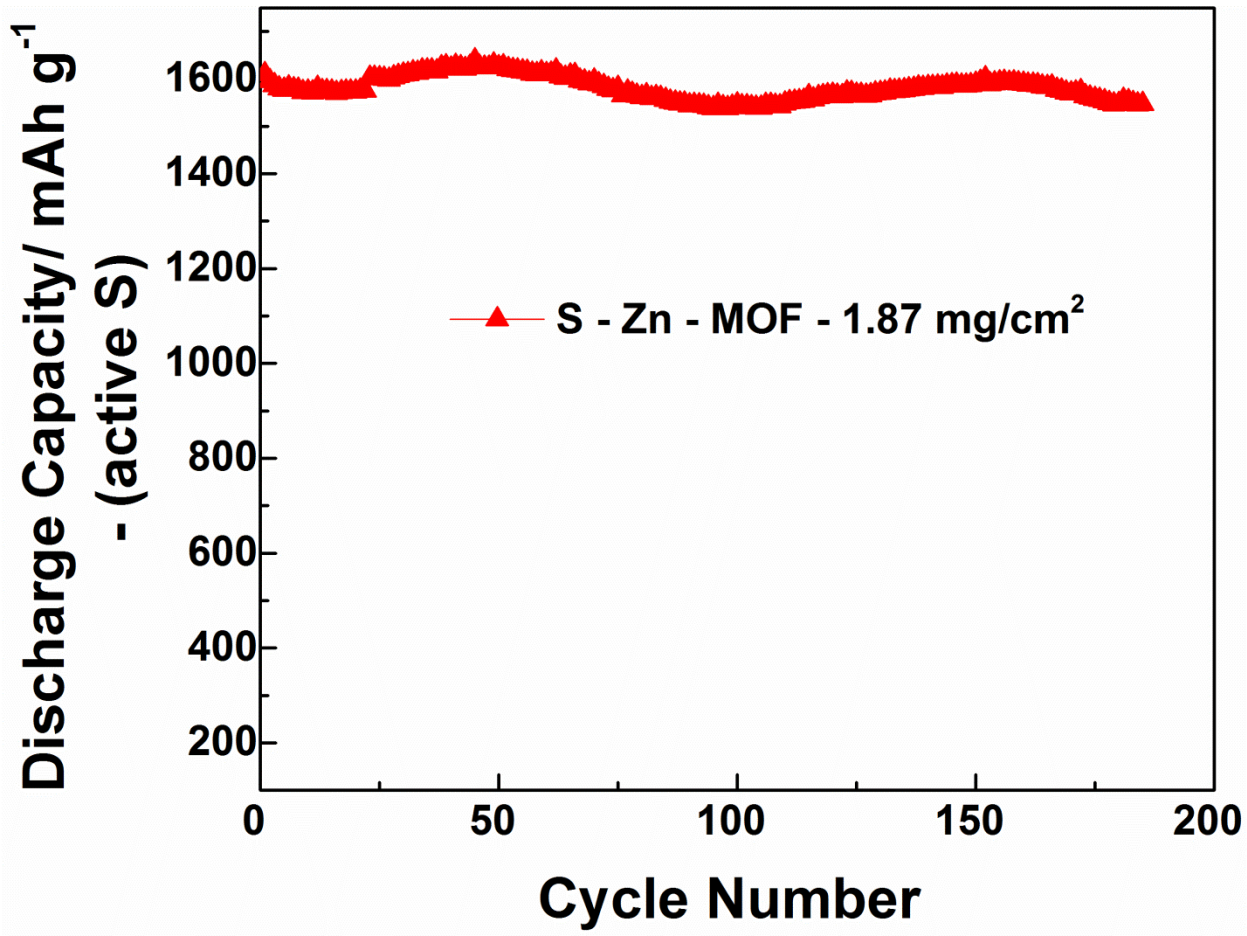

Appendix A Figure 9 Cycling performance of S – Zn-MOF at 0.2C rate with capacity adjusted to reflect the initial loss consuming ~59% of the initial sulfur content through formation of irreversible sulfate-like products (see Reactions S1-S2 and Appendix A Table 2) as seen in Figure 3-8, Figure 3-9 and Figure 3-10.

Appendix B Supporting Information: Understand the Origin of Irreversible Capacity Loss in Li-S Batteries and Address the Mechanisms of Polysulfide Dissolution Using Structurally Distinct Metal Organic Framework (MOF) Based Sulfur Cathodes - (ii) Effective Bipyridine and Pyrazine-based Polysulfide Dissolution Resistant Complex Framework Materials (CFM) Systems for High Capacity Rechargeable Lithium – Sulfur Battery

Pavithra M Shanthi[a], Prashanth J Hanumantha[b], Ramalinga Kuruba[b], Bharat Gattu[a], Moni K Datta[b], Prashant N Kumta[a, b, c, d*]

[a]Department of Chemical and Petroleum Engineering,

University of Pittsburgh, Pittsburgh, PA 15261 (USA)

[b]Department of Bioengineering,

University of Pittsburgh, Pittsburgh, PA 15261 (USA)

[c]Department of Mechanical Engineering and Materials Science,

University of Pittsburgh, Pittsburgh, PA 15261 (USA)

[d]Center for Complex Engineered Multifunctional Materials,

University of Pittsburgh, Pittsburgh, PA 15261 (USA)

Calculation for Sulfur Infiltration:

Molecular weight of sulfur: 32.06 g/mole

Density of sulfur: 2.07 g/cm^3

Pore volume of the Cu-bpy-CFM: 0.31cm^3/g

For every 1 g of Cu-bpy-CFM, **the amount of sulfur that could be infiltrated,**

= 0.31 cm^3/g (Cu-bpy-CFM) × 1 g (Cu-bpy-CFM) × 2.07 g/cm^3 (sulfur) = 0.64 g sulfur

Weight % of sulfur that could be infiltrated into the Cu-bpy-CFM

= 0.64g sulfur/1g Cu-bpy-CFM = **64 wt%**

Pore volume of the Cu-pyz-CFM: 0.32cm^3/g

For every 1 g of Cu-pyz-CFM, **the amount of sulfur that could be infiltrated,**

= 0.32 cm^3/g (Cu-pyz-CFM) × 1 g (Cu-pyz-CFM) × 2.07 g/cm^3 (sulfur) = 0.66 g sulfur

Weight % of sulfur that could be infiltrated into the Cu-pyz-CFM

= 0.66g sulfur/1g Cu-pyz-CFM = **66 wt%**

For further ensuring adequate sulfur infiltration into the synthesized CFMs, an additional 10 wt% of sulfur was added to the calculated amounts, hence both CFMs essentially contain 70 wt% of sulfur infiltrated.

BET Adsorption Isotherms:

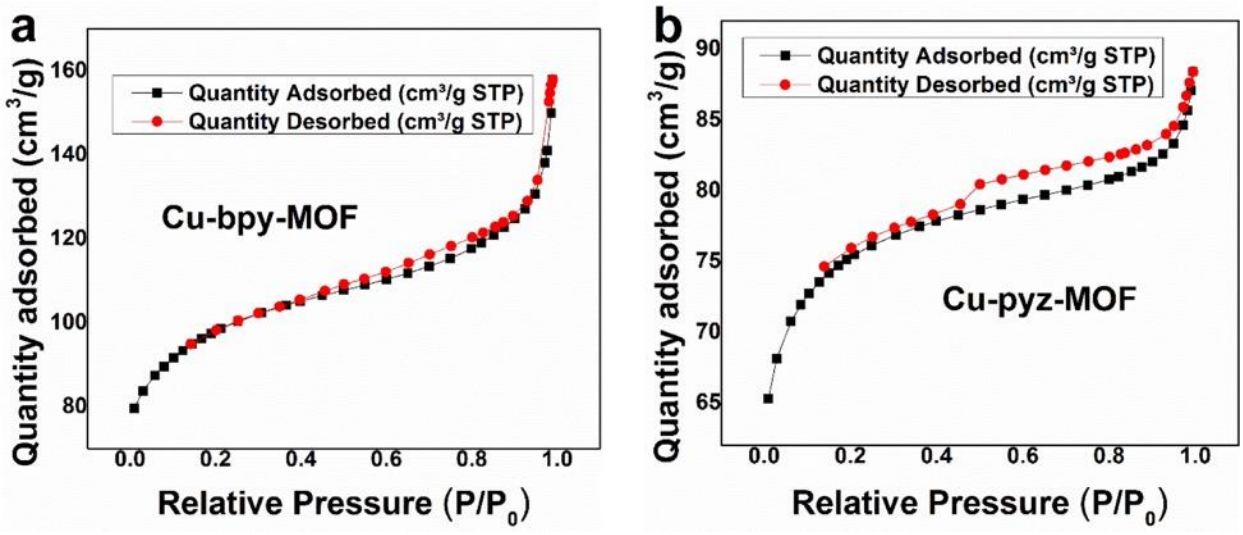

Appendix B Figure 1 BET adsorption isotherm of the a) Cu-bpy-CFM and b) Cu-pyz-CFM.

The BET adsorption isotherm of the Cu-bpy-CFM and Cu-pyz-SCF are shown in Appendix B Figure 1. The S-CFM displays a type II isotherm curve following IUPAC classification[448], confirming its microporous and nanoporous structure.

Standard Deviation Calculation:

The pore size and surface area of the Cu-bpy-CFM and Cu-pyz-CFM is the average of three measurements performed on three independently prepared samples.

The value of standard deviation was calculated using the following formula:

$$\sigma = \sqrt{\frac{1}{N}\sum_{i=1}^{N}(x_i - \mu)^2}$$

where, μ is the mean of the three values and N=3.

SEM images of synthesized Cu-bpy-CFM and Cu-pyz-CFM along with S-Cu-bpy-CFM and S-Cu-pyz-CFM after sulfur infiltration and EDS pattern collected on the S-Cu-bpy-CFM and S-Cu-pyz-CFM after sulfur infiltration.

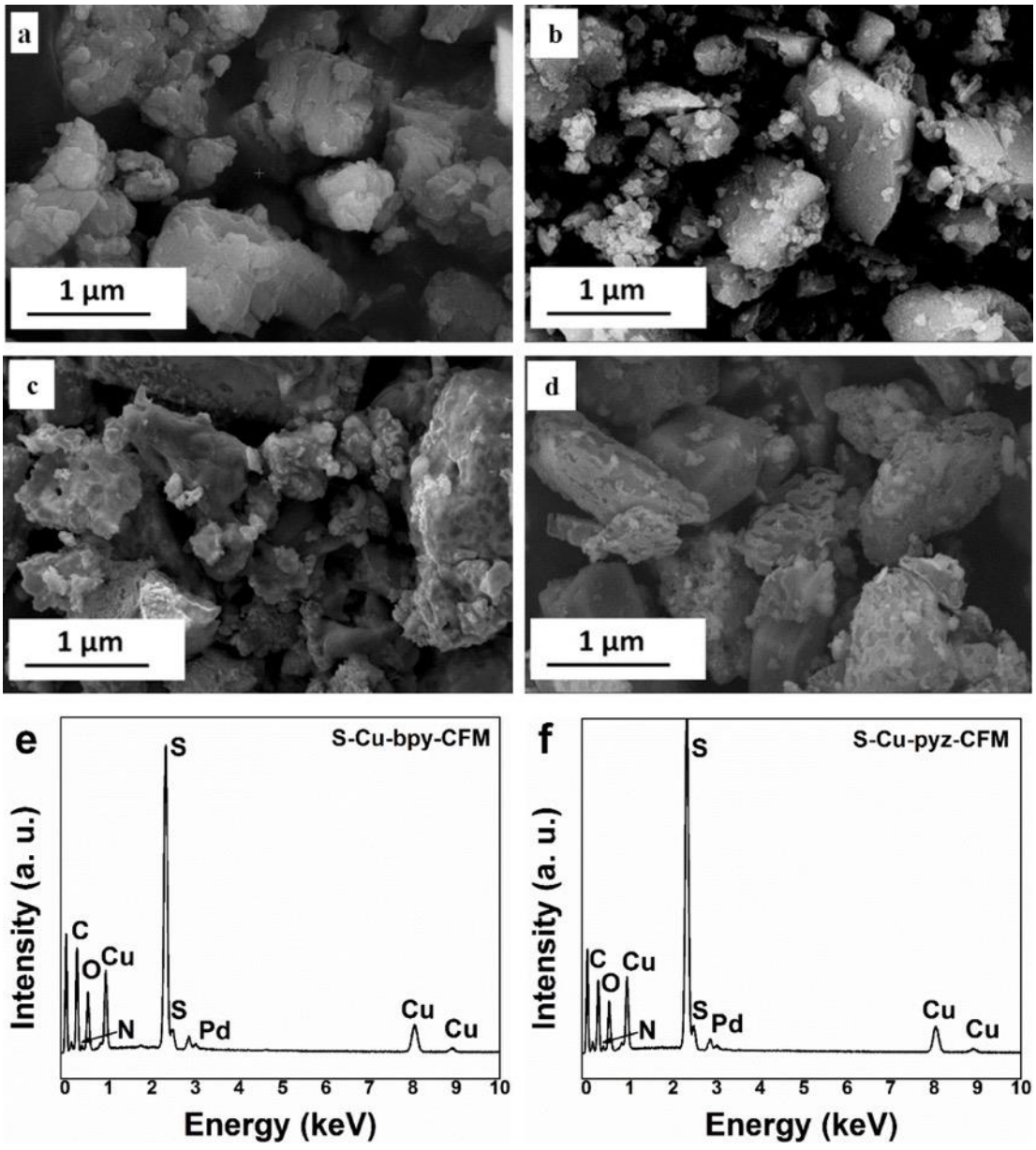

Appendix B Figure 2 SEM images of (a) S-Cu-bpy-CFM and (b) S-Cu-pyz-CFM before sulfur infiltration, SEM images of (c) S-Cu-bpy-CFM and (d) S-Cu-pyz-CFM after sulfur infiltration and EDS pattern of the (e) S-Cu-bpy-CFM and (f) S-Cu-pyz-CFM after sulfur infiltration.

Appendix B Table 1 Experimental and calculated elemental composition of the S-Cu-bpy-CFM and Cu-pyz-CFM.

	S-Cu-bpy-CFM		S-Cu-pyz-CFM	
	Experimental (wt%)	Calculated (wt%)	Experimental (wt%)	Calculated (wt%)
Sulfur	71.76	72.69	70.92	72.86
Carbon	15.21	13.46	8.72	7.60
Oxygen	3.83	3.59	4.92	5.06
Nitrogen	2.88	3.14	4.72	4.43
Copper	6.32	7.12	10.72	10.05

Scanning Electron Microscopy (SEM) and Energy Dispersive X-Ray Spectroscopy (EDS) analysis were performed on the S-Cu-bpy-CFM and S-Cu-pyz-CFM samples after sulfur infiltration to confirm the presence of sulfur infiltrated inside the CFMs and determine the elemental composition of the CFMs. ZEISS Sigma 500 VP SEM equipped with an Oxford Aztec X-EDS detector system operating at 20 kV was used for the SEM analysis. From the SEM images (Appendix B Figure 2a&c), the microstructure of the S-Cu-bpy-CFM and S-Cu-pyz-CFM are in accordance with those reported in literature[227, 228]. Also, the SEM images (Appendix B Figure 2b&d) collected on the S-Cu-bpy-CFM and S-Cu-pyz-CFM after sulfur infiltration appear very similar to the SEM micrographs collected on the S-Cu-bpy-CFM and S-Cu-pyz-CFM before sulfur infiltration (Appendix B Figure 2a&b) indicating no change in morphology of the CFMs after sulfur infiltration. The EDS pattern of the S-Cu-bpy-CFM and S-Cu-pyz-CFM.

(Appendix B Figure 2e&f) confirms the presence of sulfur and the corresponding elemental composition of the CFMs (Appendix B Table 1) are in accordance with that calculated from the molar formula of the CFMs and the weight of sulfur infiltrated into the CFMs.

Measurement of the Amount of Sulfur Infiltrated into the Cu-bpy-CFM and Cu-pyz-CFM:

In order to validate the chemical composition results from the EDS analysis conducted on the experimentally synthesized S-Cu-bpy-CFM and S-Cu-pyz-CFM and to verify the amount of sulfur infiltrated into both of the CFMs, a simple solvation experiment was performed. Accordingly, ~200mg of the sulfur infiltrated CFMs (70wt% S/30 wt% CFM), S-Cu-bpy-CFM and S-Cu-pyz-CFM were dispersed in 20 ml of carbon disulfide (CS_2), the typical solvent used for dissolution of sulfur. The dispersion was sonicated for 30 minutes followed by centrifuging the dispersion to recover the insoluble residue. The S-Cu-bpy-CFM and S-Cu-pyz-CFM were washed in CS_2 three more times before weighing the residue. The results of one such experiment is shown in Appendix B Table 2**.** The experiment was repeated three times on three different S-CFM samples prepared from three different batches of CFMs and the results are in close agreement within a ±2% error limit.

Appendix B Table 2 Results of the measurement of sulfur composition of the S-Cu-bpy-CFM and Cu-pyz-CFM.

S/CFM 70 wt% S/30 wt% CFM	Initial weight (~200 mg)	Final weight (after dissolving sulfur)	% Sulfur in the S/CFM composite
S-Cu-bpy-CFM	207	65	68.59
S-Cu-pyz-CFM	198	61	69.19

The results of this experiment confirm the total infiltration of the measured quantities of sulfur into the pores of the nanoporous CFMs. Also, these results cast a new light into the nature of the chemical bonds between the CFMs and infiltrated sulfur. Almost all the ~70 wt% sulfur infiltrated into the CFMs is soluble in CS_2, implying the nature of the -C-S- binding between the CFMs and sulfur as is evident from the XPS results (Figure 4-5) confirming the weaker chemical binding of sulfur with carbon rather than a strong covalent bonding. This result is similar to that of Zhou et al[204] who reported their work related to loading of sulfur into three-dimensional nitrogen/sulphur-co-doped graphene sponge. In their work, the authors also observed -C-S- binding at 163.7 eV similar to our observation at 164.4 eV in the S2p XPS spectrum of the N, S-co-doped graphene material. The authors further used computational methods to explain the origin of this binding to be due to weak chemical interaction of S and C rather than fully formed strong covalent bonds. This result thus explains and confirms that the total amount of sulfur infiltrated into the CFMs matches the nominal composition of the sulfur in the chemically synthesized CFMs following the complete dissolution of the infiltrated sulfur into CS_2 in our S-Cu-bpy-CFM and S-Cu-pyz-CFM samples.

Appendix B Table 3 Summary of the performances of the currently studied S-Cu-bpy-CFM and S-Cu-pyz-CFM cathode systems compared to reported work in the literature.

CFM	Electrode sulfur loading (wt%)	Initial Capacity (mAh/g)	Capacity after 100 cycles (mAh/g)	C-rate (mA/g)	Fade rate (%)	Voltage range (V)	Reference
S-Cu-bpy-CFM	49	1565	975 (200 cycles)	0.2	0.19	1.7-2.6	Present work
S-Cu-pyz-CFM	49	1626	1020 (200 cycles)	0.2	0.18	1.7-2.6	Present work
Zn-MOF-S/MOF-5	35	1476	609	0.2	0.14	1.7-2.6	Present authors [29]
Ppy-S-in-PCN-224	44	1330	780	0.5	0.3	1.7-2.7	[449]
Ppy-S-in-MIL-53	44	960	900	0.5	0.06	1.7-2.7	[449]
MIL-53	30	1,125	436	0.1	0.72	1.8-2.8	[135]
NH2-MIL-53	30	526	313	0.1	0.45	1.8-2.8	[135]
HKUST-1	30	1,055	710	0.1	0.43	1.8-2.8	[135]
ZIF-8	30	738	654	0.5	0.11	1.8-2.8	[135]
ZIF-8-M	30	556	476	0.5	0.15	1.8-2.8	[135]
MIL-100	30	491	410	0.5	0.17	1.8-2.8	[135]
MIL-100	19	1,100	420	0.1	0.83	1.0-3.0	[450]
HKUST-1	16	1,498	500	0.1	0.39	1.0-3.0	[134]
ZIF-8	12	1,200	420	0.1	0.33	1.0-3.0	[425]
MIL-101	58.8	869	695	0.1	0.17	1.0-3.0	[252]
DUT-23	60	689	550	0.1	0.10	1.5-3.0	[137]
MOF-525	50	1190	602	0.5	0.43	1.5-3.0	[133]

Appendix B Table 4 Reaction voltages (V w.r.t. Li^+/Li) from cyclic voltammograms of S-Cu-bpy-CFM and S-Cu-pyz-CFM.

S-Cu-bpy-CFM					
Cycle number	**Anodic scan**			**Cathodic scan**	
1^{st} cycle	2.43	2.38	2.19	2.01	2.36
2^{nd} cycle	2.42	2.30	2.19	2.02	2.37
5^{th} cycle	2.41	2.28	2.19	2.02	2.37
10^{th} cycle	2.41	2.28	2.19	2.02	2.37
20^{th} cycle	2.41	2.28	2.19	2.02	2.37
25^{th} cycle	2.41	2.28	2.19	2.02	2.37
S-Cu-pyz-CFM					
Cycle number	**Anodic scan**			**Cathodic scan**	
1^{st} cycle	2.43	2.38	2.19	2.01	2.35
2^{nd} cycle	2.41	2.29	2.19	2.02	2.36
5^{th} cycle	2.41	2.28	2.19	2.03	2.36
10^{th} cycle	2.41	2.29	2.19	2.02	2.37
20^{th} cycle	2.41	2.29	2.19	2.02	2.37
25^{th} cycle	2.41	2.29	2.19	2.02	2.37

Extended cycling of the S-Cu-bpy-CFM and S-Cu-pyz-CFM at 0.2 rate:

The S-Cu-bpy-CFM and S-Cu-pyz-CFM were cycled for an extended 200 charge-discharge cycles at 0.2C rate and the results are shown in Appendix B Figure 3. The S-Cu-bpy-CFM shows an initial discharge capacity of 1565 mAh/g and stabilizes at a discharge capacity of 975 mAh/g after 200 cycles with a fade rate of (0.19%/ cycle). The S-Cu-pyz-CFM also shows a high initial discharge capacity of 1626 mAh/g and a stable 1020 mAh/g discharge capacity after 200 cycles (fade-rate of 0.18%/cycle).

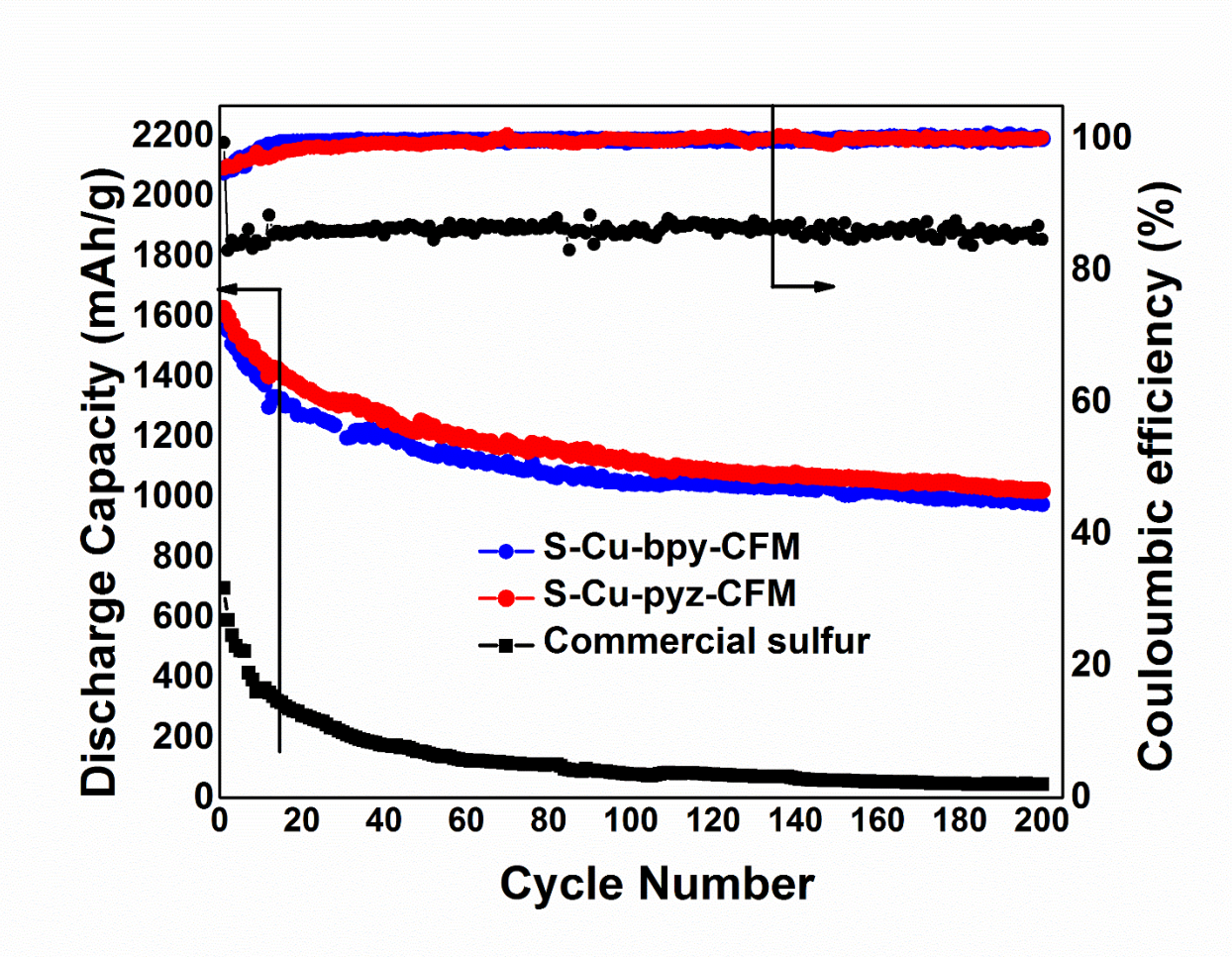

Appendix B Figure 3 Cycling performance of S-Cu-bpy-CFM and S-Cu-pyz-CFM cycled at 0.2C rate for 200 cycles.

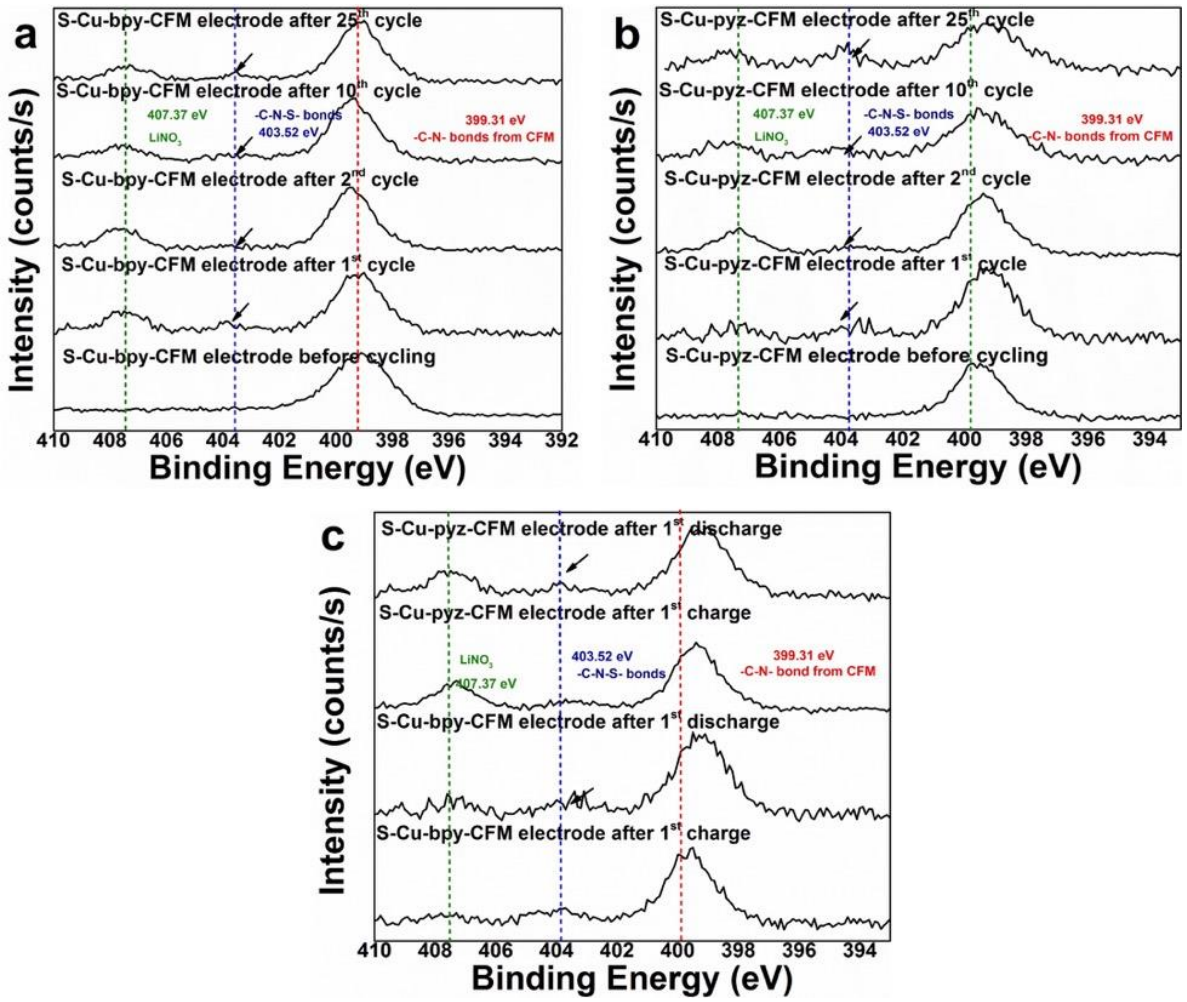

Appendix B Figure 4 N1s spectra of (a) S-Cu-bpy-CFM and (b) S-Cu-pyz-CFM before cycling and after 1st, 2nd, 10th and 25th cycles (c) S-Cu-bpy-CFM and S-Cu-pyz-CFM after 1st charge and discharge cycle at 0.2C rate.

The N1s spectra of both S-Cu-bpy-OF and S-Cu-pyz-CFM corresponding electrodes after 1st, 2nd, 10th and 25th cycles (Appendix B Figure 4a&b) shows a peak at 399.31 eV that corresponds to the binding of carbon to nitrogen arising from the -C-N-[258-260] bonds of pyrazine and bipyridine. A peak at 407.37 eV corresponding to $LiNO_3$[261] added to the electrolyte is observed in electrodes cycled for 1, 2, 10 and 25 cycles. In addition to these peaks, the cycled electrodes show a peak at 403.52 eV, analysis of which indicates its origin from -N-S- bonds

bonds[262, 263]. The peak at 403.52 eV is observed in electrodes after 1st charge and 1st discharge (Appendix B Figure 4c) confirming the irreversible nature of the -N-S- bonds. Appendix B Figure 5a&b represents the XPS S2p spectra of the S-Cu-bpy-CFM and S-Cu-pyz-CFM electrode before cycling and after 1st, 2nd, 10th and 25th cycles.

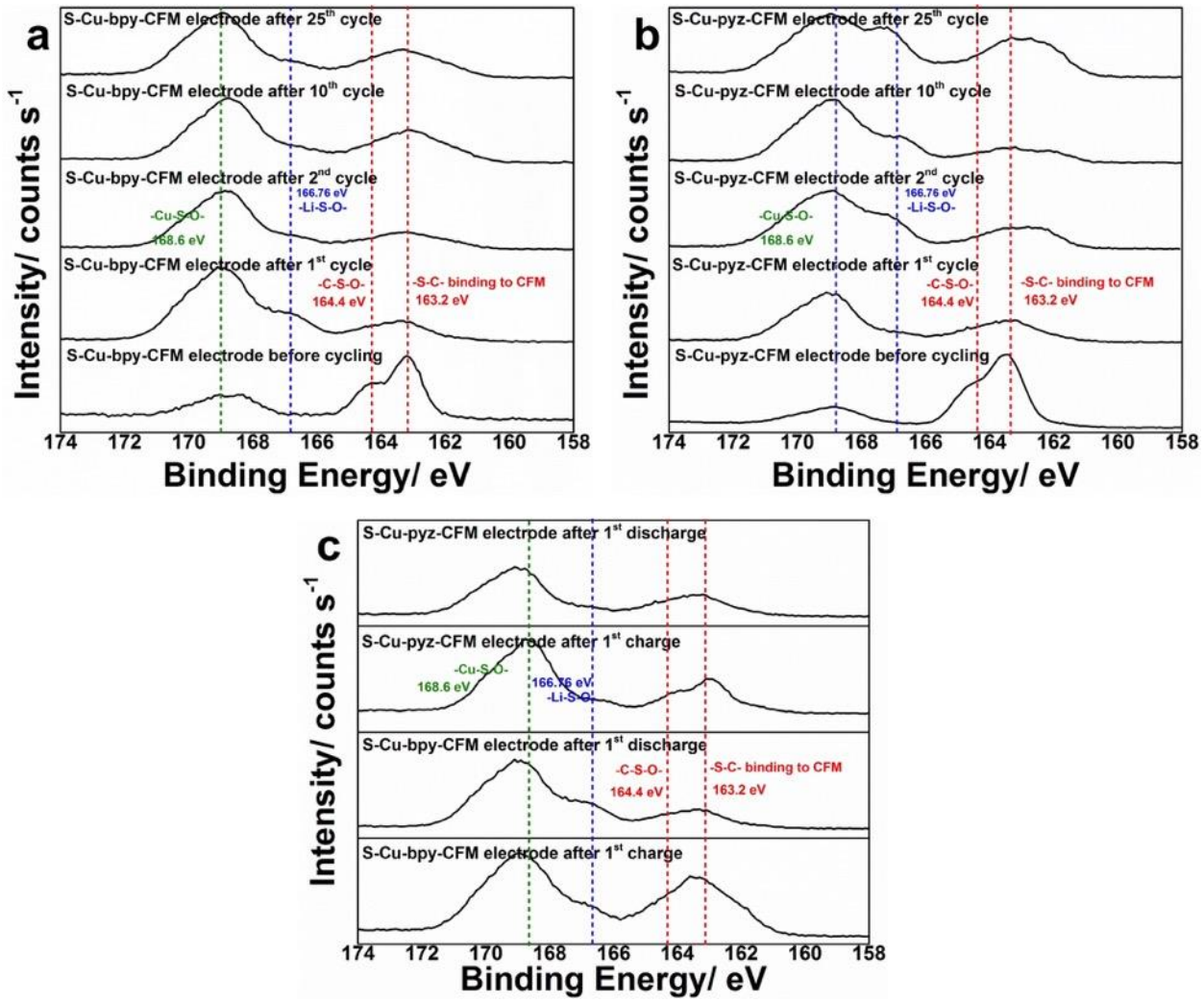

Appendix B Figure 5 S2p spectra of (a) S-Cu-bpy-CFM and (b) S-Cu-pyz-CFM before cycling and after 1st, 2nd, 10th and 25th cycles and (c) S-Cu-bpy-CFM and S-Cu-pyz-CFM after 1st charge and discharge at 0.2C rate.

The S2p spectra of the S-Cu-bpy-CFM and S-Cu-pyz-CFM electrode before cycling shows peaks at 168.6 eV corresponding to the -Cu-S-O-[264] which is characteristic of the CFMs. The peaks observed at 163.2 eV and 164.4 eV in the spectra of S-Cu-bpy-CFM and S-Cu-pyz-CFM corresponds to -C-S- bonds[265] and -C-S-O-[170, 266, 267] bonds respectively formed due to the chemical interaction of sulfur with the carbon in the CFMs. The S2p spectra both the CFMs after1st, 2nd, 10th and 25th cycles (Appendix B Figure 5a&b) shows all the peaks observed before cycling, along with one additional peak at 166.76 eV corresponding to -Li-S-O-[268, 269]. This peak at 166.76 eV is likely due to the loss in active sulfur from the electrode due to formation of SEI layer, which could explain the extra ~10% loss in capacity in addition to the ~25% loss due to -N-S- bonds. The peak at 166.76 eV is observed in both S-Cu-bpy-CFM and S-Cu-pyz-CFM electrodes after 1st charge and 1st discharge (Appendix B Figure 5c) confirming the irreversible nature of the SEI formed.

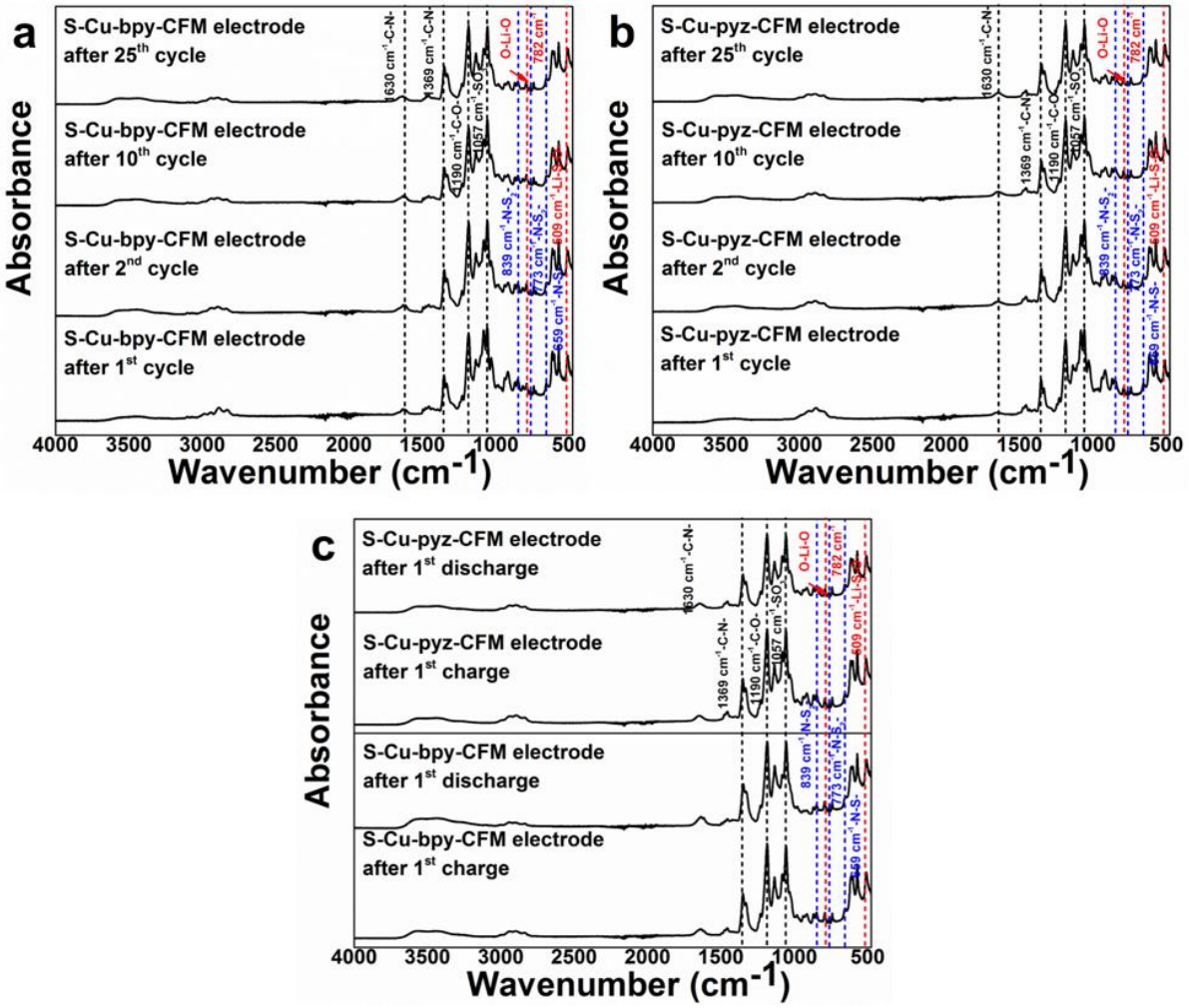

Appendix B Figure 6 FT-IR spectra of a) S-Cu-bpy-CFM and b) S-Cu-pyz-CFM after 1st, 2nd, 10th and 25th cycles and c) S-Cu-bpy-CFM and S-Cu-pyz-CFM after 1st charge and discharge at 0.2C rate.

Appendix B Figure 6a&b represents the FT-IR spectra of the S-Cu-bpy-CFM and S-Cu-pyz-CFM electrode before and after 1st, 2nd, 10th and 25th cycles. The FT-IR spectra of the S-Cu-bpy-CFM and S-Cu-pyz-CFM electrodes before cycling shows peaks characteristic of the CFMs at 1027 cm^{-1}, 1079 cm^{-1}, 1395 cm^{-1} and 1470 cm^{-1} corresponding to C-H rocking[270], C-C stretching[271], C-N[272] bond stretching and C-H bending vibrations[273] respectively. The S-Cu-bpy-CFM and S-Cu-pyz-CFM electrodes after 1st, 2nd, 10th and 25th cycles shows peaks at 574 cm^{-1} and 1057 cm^{-1} corresponding to CF_2 bending vibrations[274], [275], [276] from the PVdF binder and -

SO_3 groups from the $LiCF_3SO_3$ salt respectively[277] in addition to the peaks characteristic of the CFMs. Additionally, the electrodes after cycling shows peaks at 659 cm^{-1}, 773 cm^{-1} and 839 cm^{-1} corresponding to the N-S symmetric stretching[278], N-S_2 asymmetric stretching[278] and N-S_2 stretching vibrations[279] respectively arising from the binding of sulfur to nitrogen from the CFMs. Two peaks are observed at 782 cm^{-1} and 509 cm^{-1} that corresponds to O-Li-O stretching[280] and Li-S-O from cationic interaction with -SO_4 groups[281] respectively. The occurrence of peaks corresponding to Li-S-O bonds in the FT-IR spectra confirms the formation of SEI. The occurrence of the peaks corresponding to -N-S- and Li-S-O bonds in the FT-IR spectra of the S-Cu-bpy-CFM and S-Cu-pyz-CFM electrode after 1st charge and 1st discharge (Appendix B Figure 6c) confirms the irreversible nature of the SEI formed.

Appendix B Table 5 FT-IR peak profiling of the S-Cu-bpy-CFM and S-Cu-pyz-CFM before and after 150 cycles at 0.2C rate.

Sample	Wavenumber (cm^{-1})	Peak assignment	Reference
S-Cu-pyz-CFM electrode before cycling	851	asymmetric CH bending	[248]
	872	C-O stretching mode	[451]
	914	C-H out of plane	[452]
	1027	CH rocking	[270]
	1079	C-C stretching	[271]
	1192	O-C rocking vibrations	[453, 454, 455]
	1239	Stretching of -C-N-	[456, 272, 457]
	1369, 1395	C-N bond stretching	[273]
	1434	C-H deformation	[458, 459, 460, 461]
	1470	C-H bending	
	2827, 2879, 2946	C-H stretching	

Appendix B Table 5 (Continued)

S-Cu-pyz-CFM electrode after cycling	851	asymmetric CH_2 bending	[248]
	872	C-O stretching mode	[451]
	914	C-H out of plane	[452]
	1027	CH rocking	[270]
	1079	C-C stretching	[271]
	1192	O-C rocking vibrations	[453, 454]
	1239	Stretching of -C-N-	[455]
	1369, 1395	C-N bond stretching	[456, 272]
	1434	C-H deformation	[457]
	1470	C-H bending	[273]
	2827, 2879, 2946	C-H stretching	[458, 459, 460, 374]
	574	CF_2 bending	[274, 275, 276]
	655	N-H bending	[462]
	737	C-H wagging	[463]
	758	Out of plane C-H bending vibration	[464]
	787	NH_2 wagging vibration	[465]
	939	CH wag absorption	[466]
	977	C-C stretching vibration	[467]
	1057	$–SO_3–$ groups	[277]
	1133	C-N stretching band	[468]
	1331	C-C ring stretching	[469]
	659	N-S symmetric stretching	[278]
	773	N-S_2 asymmetric stretching	[278]
	839	N-S_2 stretching vibration	[279]
	782	O-Li-O stretching	[280]
	509	Li-S-O cationic interaction with SO_4	[281]

Appendix B Table 5 (Continued)

S-Cu-bpy-CFM electrode before cycling	574	CF_2 bending	[274], [275], [276]
	610	C-C ring bending	[470]
	655	N-H bending	[462]
	737	C-H wagging	[463]
	758	Out of plane C-H bending vibration	[464]
	872		[451]
	939	C-O stretching mode	[466]
	977	CH_2 wag absorption	[467]
	1027	C-C stretching vibration	[270]
	1057	CH rocking	[277]
	1079	$–SO_3–$ groups	[271]
	1133	C-C stretching	[468]
	1192	C-N stretching band	[453], [454]
	1395	O-C rocking vibrations	[456], [272]
	1411	C-N bond stretching	[240]
	1470	C-H bending	[273]
	1605, 1630	C-H bending C-N stretching vibration	[471], [472]

Appendix B Table 5 (Continued)

S-Cu-bpy-CFM electrode after cycling	851	asymmetric CH_2 bending	[248]
	872	C-O stretching mode	[451]
	914	C-H out of plane	[452]
	1027	CH rocking	[270]
	1079	C-C stretching	[271]
	1192	O-C rocking vibrations	[453, 454]
	1239	Stretching of -C-N-	[455]
	1369	C-N bond stretching	[456, 272]
	1470	C-H bending	[273]
	2827, 2879, 2946	C-H stretching	[458, 459, 460, 461]
	574	CF_2 bending	[274, 275, 276]
	655	N-H bending	[462]
	737	C-H wagging	[463]
	758	Out of plane C-H bending vibration	[464]
	787	NH_2 wagging vibration	[465]
	939	CH_2 wag absorption	[466]
	977	C-C stretching vibration	[467]
	1057	$–SO_3–$ groups	[277]
	1133	C-N stretching band	[468]
	1331	C-C ring stretching	[469]
	602	S-O bond stretching	[473]
	610	C-C ring bending	[470]
	1630	C-N stretching vibration	[471, 472]
	659	$N-S_2$ symmetric stretching	[278]
	773	$N-S_2$ asymmetric stretching	[278]
	839	N-S stretching vibration	[279]
	782	O-Li-O stretching	[280]
	509	Li-S-O cationic interaction with SO_4	[281]

Irreversible Loss of Capacity in the Initial 25 Cycles:

The observed loss in sulfur capacity through binding with carbonate species could proceed through the mechanism proposed below:

Proposed mechanism: (Results in consumption of 2 mole of S/mole of CFM to form irreversible -N-S- bonds)

Reaction S1: $Cu_2(C_4H_4N_2)_2(SO_4) + 4S \rightarrow Cu_2(C_4H_4(N\text{-}S)_2)_2(SO_4)$

Reaction S2: $Cu_2(C_{10}H_8N_2)_2(SO_4) + 4S \rightarrow Cu_2(C_{10}H_8(N\text{-}S)_2)_2(SO_4)$

Appendix B Table 6 shows the calculation of the amount of sulfur lost by the reaction of sulfur with nitrogen from the CFM. The calculation is based on the moles of sulfur in S-Cu-bpy/pyzCFM electrode based on the initial weight of sulfur and CFM (70:30wt%).

Appendix B Table 6 Calculation of the amount of sulfur consumed by the irreversible reactions S1 and S2.

S-Cu-pyz-CFM	Proposed mechanism 1 (mole)
Nominal sulfur content during synthesis/mole of CFM (M.W = 32.065 g/mole)	28
Nominal CFM content during synthesis/mole of CFM (M.W = 383.33 g/mole)	1
Number of moles of sulfur lost during initial cycles/ mole of CFM	4
Active sulfur remaining that cycles stably after initial capacity loss	24 (~15% initial capacity loss)

Appendix B Table 6 (Continued)

S-Cu-bpy-CFM	Proposed mechanism 2 (mole)
Nominal sulfur content during synthesis/mole of CFM (M.W = 32.065 g/mole)	39
Nominal CFM content during synthesis/mole of CFM (M.W = 535.52 g/mole)	1
Number of moles of sulfur lost during initial cycles/ mole of CFM	4
Active sulfur remaining that cycles stably after initial capacity loss	35 (~10% initial capacity loss)

Calculations:

S-Cu-pyz-CFM

MW of Cu-pyz-CFM $Cu_2(C_4H_4N_2)_2(SO_4)$ = **383.33 g/mole**

MW of sulfur = **32.065 g/mole**

Assuming 1g of S-Cu-pyz-CFM; we have **0.3g CFM and 0.7g sulfur**

Moles of CFM in 0.3g CFM = **0.3(g)/383.33(g/mole) = 0.000782 mole CFM**

Moles of sulfur in 0.7g sulfur = **0.7(g)/32.065(g/mole) = 0.0218 mole sulfur**

Nominal content of sulfur/mole of CFM = **0.0218/0.000782 = 27.877 (~28)**

Active sulfur remaining after initial capacity loss = **28 – 4** = **24 moles**

Loss in capacity due to loss in sulfur **= 4/28 = 14.285% (~15%)**

S-Cu-bpy-CFM

MW of Cu-bpy-CFM $Cu_2(C_{10}H_8N_2)_2(SO_4)$ = **535.52 g/mole**

MW of sulfur **= 32.065 g/mole**

Assuming 1g of S-Cu-bpy-CFM; we have **0.3g CFM and 0.7g sulfur**

Moles of CFM in 0.3g CFM = **0.3(g)/535.52(g/mole) = 0.0005602 mole CFM**

Moles of sulfur in 0.7g sulfur = **0.7(g)/32.065(g/mole) = 0.0218 mole sulfur**

Nominal content of sulfur/mole of CFM = **0.0218/0.0005602 = 38.914 (~39)**

Active sulfur remaining after initial capacity loss = **39 – 4** = **35 moles**

Loss in capacity due to loss in sulfur **= 4/39 = 10.256% (~10%)**

Appendix C Supporting Information: Understand the Origin of Irreversible Capacity Loss in Li-S batteries and Address the Mechanisms of Polysulfide Dissolution Using Structurally Distinct Metal Organic Framework (MOF) Based Sulfur Cathodes - (iii) Sulfonic Acid Based Complex Framework Materials (CFM) – New Nanostructured Polysulfide Immobilization Systems for Rechargeable Lithium – Sulfur Battery

Pavithra M Shanthi[a], Prashanth J Hanumantha[b], Kuruba Ramalinga[b], Bharat Gattu[a], Moni K Datta[b], Prashant N Kumta[a, b, c, d]

[a]Department of Chemical and Petroleum Engineering,

University of Pittsburgh, Pittsburgh, PA 15261 (USA)

[b]Department of Bioengineering,

University of Pittsburgh, Pittsburgh, PA 15261 (USA)

[c]Department of Mechanical Engineering and Materials Science,

University of Pittsburgh, Pittsburgh, PA 15261 (USA)

[d]Center for Complex Engineered Multifunctional Materials,

University of Pittsburgh, Pittsburgh, PA 15261 (USA)

BET Adsorption Isotherms

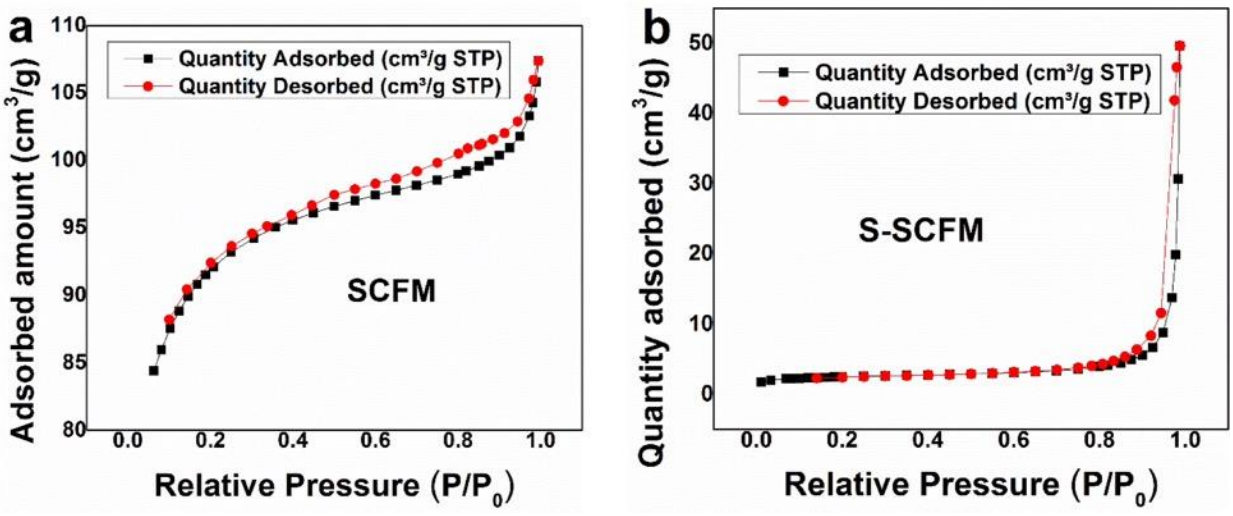

Appendix C Figure 1 BET adsorption isotherm of the a) SCFM and b) S-SCFM.

The BET adsorption isotherm of the sulfonic acid based complex framework materials (CFM) derived SCFM and sulfur infiltrated, S-SCFM architectures are shown in Appendix C Figure 1. The SCFM displays a type II isotherm curve following IUPAC classification[448], confirming their microporous and mesoporous structure. The almost vertical rise in adsorption in the low-pressure range (P/P_0) indicates the presence of micropores and nanopores which is in accordance with that observed in the literature[474, 475]. The S-SCFM shows a type III isotherm due to multilayer adsorption rather than monolayer type interaction, which explains the complete filling and closure of the CFM derived CFM pores after the sulfur infiltration process.

SEM Images of the SCFM Before and After Sulfur Infiltration

Scanning electron microscopy (SEM) was carried out to investigate the microscopic structure of the chemically derived SCFM and sulfur infiltrated S-SCFM. Philips XL-30FEG equipped with an EDAX detector system comprised of an ultrathin beryllium window and Si (Li) detector operating at 20 kV was used for the SEM analysis. The samples for SEM analysis were

prepared by grinding the CFM derived SCFM and S-SCFM before casting onto a conducting carbon tape. The SEM images show the microscopic structure of SCFM (Appendix C Figure 2a) which is in accordance with literature reports of other similar metal organic framework (MOF) structures [145, 434, 435]. The CFM derived SCFM after sulfur infiltration (S-SCFM) (Appendix C Figure 2b) shows slight change in the surface structure due to sulfur infiltration into the SCFM crystals. Accordingly, the surface of the samples shows slight charging effect due to the insulating nature of sulfur. Appendix C Figure 2c shows the SEM image of a single SCFM particle at a higher magnification. The surface and microstructure of the particle remains greatly unchanged upon sulfur infiltration process as seen from the SEM image (Appendix C Figure 2d) corresponding to the SCFM post sulfur infiltration (S-SCFM). Appendix C Figure 2e and Appendix C Table 1 shows the EDS pattern and the composition of S-SCFM respectively. The experimental composition is in accordance with the calculated value confirming the total infiltration of sulfur.

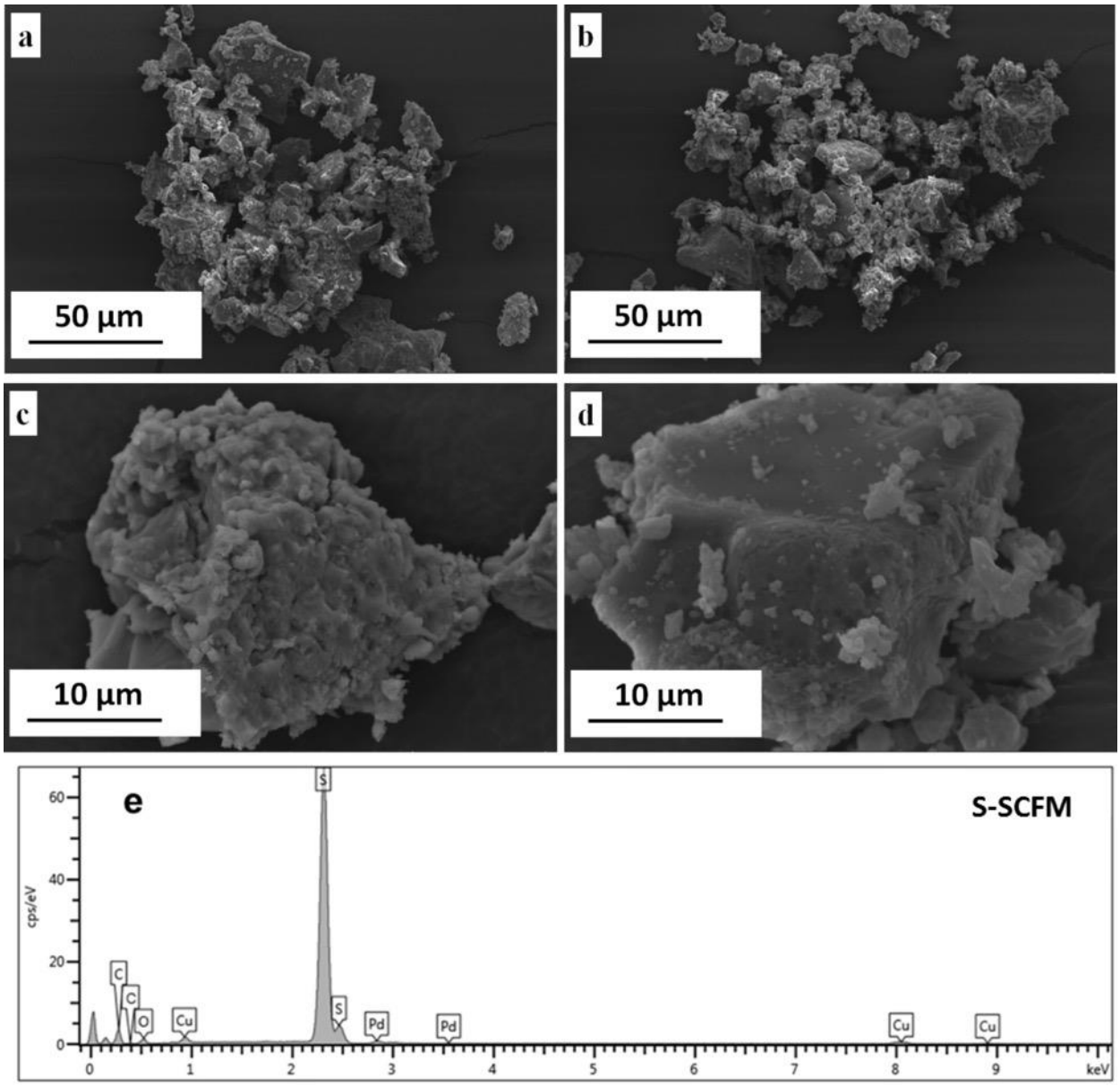

Appendix C Figure 2 Low and high magnification SEM images of the SCFM before (a&c) and after (b&d) infiltration of sulfur and e) EDS pattern of S-SCFM.

Appendix C Table 1 Experimental and calculated elemental composition of the S-SCFM.

	S-SCFM	
	Experimental (wt%)	Calculated (wt%)
Sulfur	77.70	76.83
Carbon	7.95	8.12
Oxygen	10.04	10.35
Copper	7.06	7.67

Electrochemical Cycling Plot of Commercial Sulfur

Appendix C Figure 3 represented the results of the electrochemical cycling experiment performed on commercial sulfur cathodes. The electrodes used for this testing has a sulfur/super P/PVdF ratio of 70/20/10 and a loading of 1.5-2 mg/cm^2. The cells containing commercial sulfur cathode cycled with liquid electrolyte exhibits an initial capacity of 557 mAhg^{-1}, which rapidly faded to a value of 81 mAhg^{-1} after 100 cycles accompanied with a high fade rate of 0.85%cycle^{-1}. The cell with commercial sulfur cathode also exhibits an initial Coulombic efficiency of 94.6%, which quickly fades to less than 80% after 100 cycles, clearly indicating the presence of polysulfide dissolution resulting in the characteristic loss in capacity and Coulombic efficiency. The presence of polysulfide dissolution is also evident from the XPS analysis of the separators collected from this cell (see Figure 5-6).

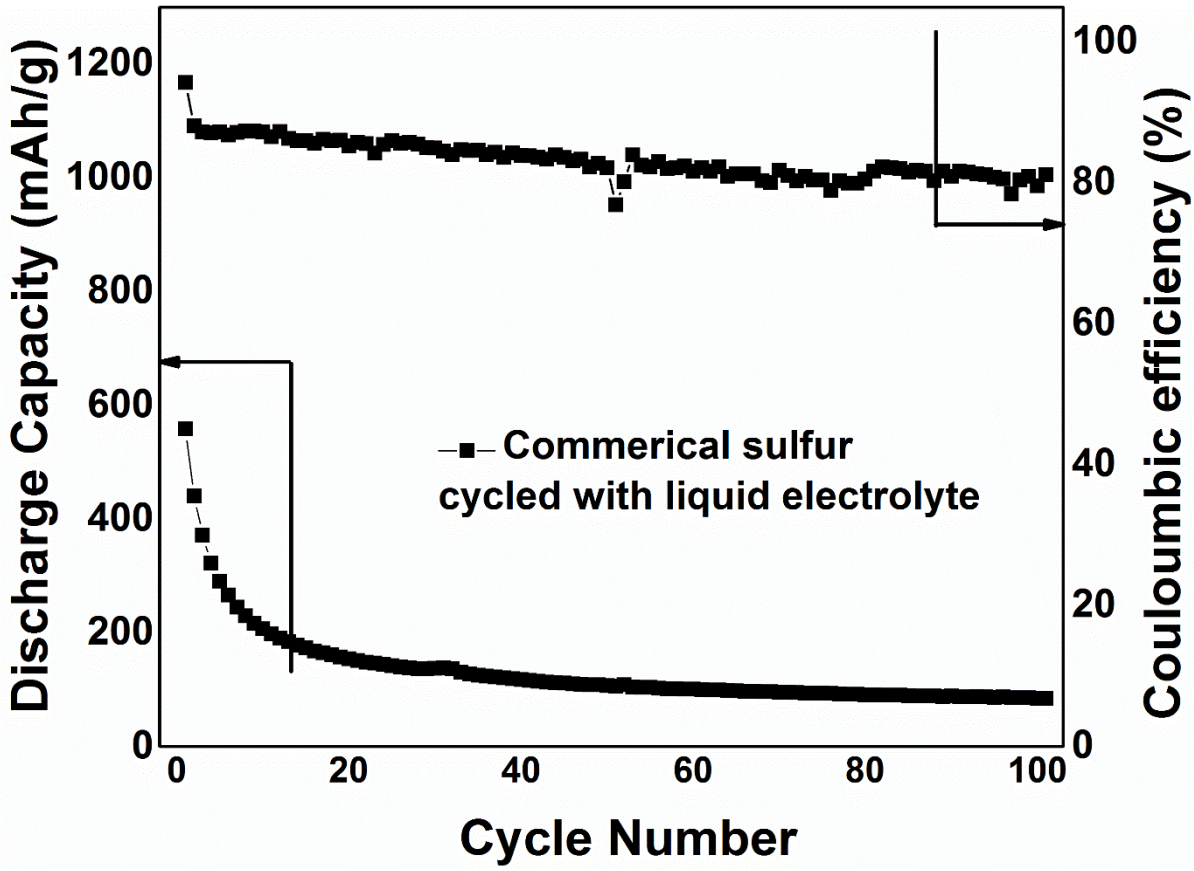

Appendix C Figure 3 Electrochemical cycling performance of commercial sulfur cathode cycled at 0.1C rate.

XPS of Lithium Counter Electrode Before and After Cycling:

Following confirmation of the absence of polysulfide species on the CFM derived S-SCFM separator post cycling, XPS analysis was conducted on the lithium metal counter electrode before and after cycling to confirm the absence of polysulfide species (Appendix C Figure 4). A lithium anode before cycling (a foil of lithium metal dipped in electrolyte (1 M $LiCF_3SO_3$, 0.2 M $LiNO_3$ in 50:50 vol% DOL:DME)), showed a peak at 168.93 eV corresponding to the -CF_3SO_3 group arising from the lithium salt $LiCF_3SO_3$ used in the electrolyte[170]. The lithium anode post-cycling also shows peak at 168.93 eV (-CF_3SO_3). The absence of any anomalous peaks clearly confirms the absence of any polysulfide dissolution.

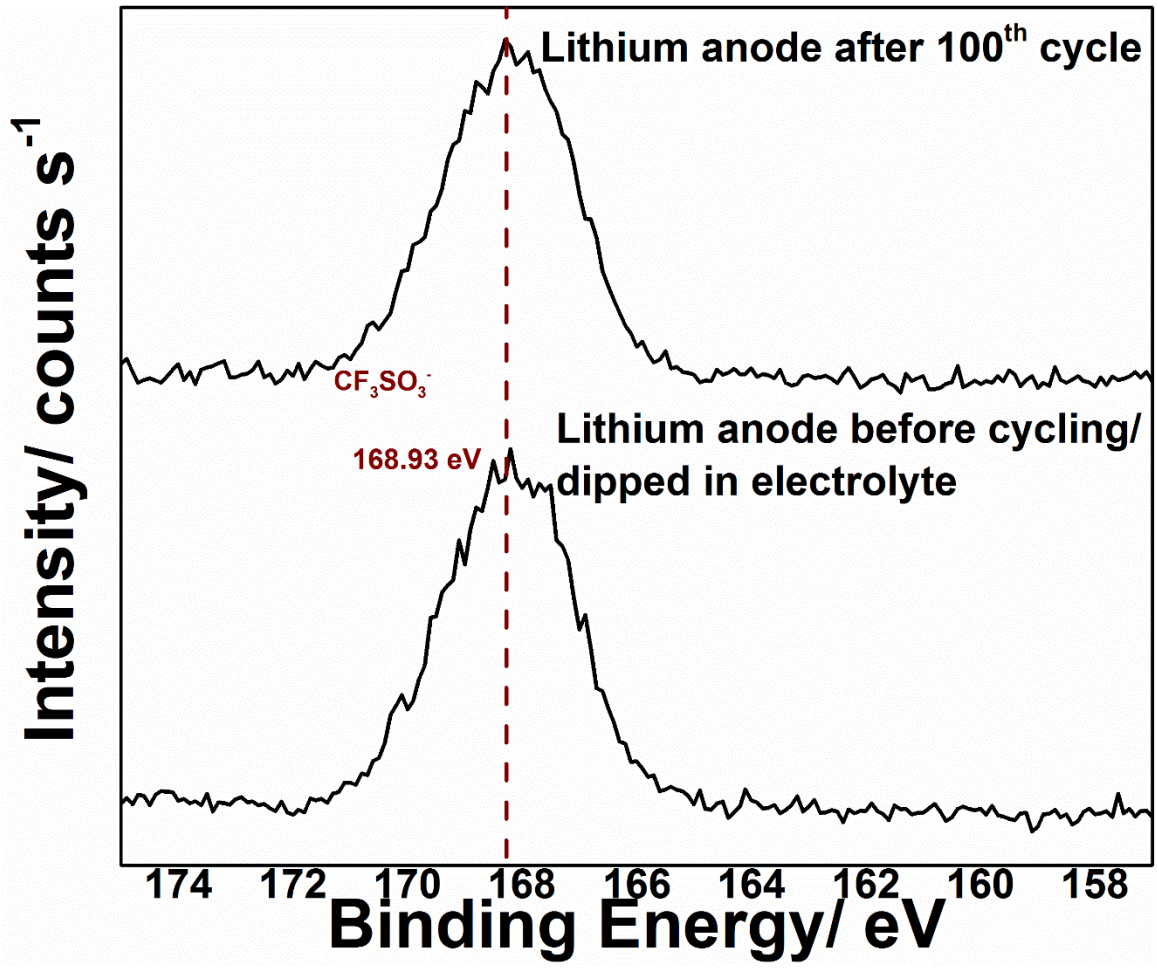

Appendix C Figure 4 S2p profiles of the lithium counter electrode in a cell containing the CFM derived S-CFM electrodes before cycling and after 100th cycles.

Appendix C Table 2 Electrical and Ionic conductivity data of Sulfur, CFMs, and S-CFMs. (Each datum is an average of the conductivities measured from three different samples made from three independent batches of the MOF-5, S-MOF-5, SCFM and S-SCFM systems).

Sample	Electrical conductivity (Scm^{-1})	Ionic conductivity (Scm^{-1})
Sulfur	$1.62 \pm 0.07 \times 10^{-13}$	$8.88 \pm 0.72 \times 10^{-10}$
MOF-5	$6.45 \pm 0.43 \times 10^{-6}$	$7.26 \pm 0.24 \times 10^{-8}$
S – MOF-5	$1.83 \pm 0.21 \times 10^{-8}$	$1.37 \pm 0.08 \times 10^{-9}$
SCFM	$2.48 \pm 0.18 \times 10^{-9}$	$3.42 \pm 0.28 \times 10^{-10}$
S – SCFM	$7.64 \pm 0.73 \times 10^{-10}$	$4.03 \pm 0.12 \times 10^{-10}$

The electrical and ionic conductivity of the MOF-5 systems, from our previous publication is compared with the CFM derived SCFM to understand the difference in the first discharge capacity of the two different chemically derived MOF and CFM structures, respectively. The electrical conductivity measurements were carried out in a Jandel Micro position Probe employing the four-point probe technique. The samples for the electrical conductivity measurements were accordingly prepared by pressing ~200 mg of the MOF and S-CFM materials into pellets of average thickness (t) ~1-1.5 mm and a diameter of 13 mm (d). The pellet was positioned between the four-probes of the instrument and the voltage (V) response for a known value of supplied current (I) was measured. The electrical resistance of the material was then calculated using the following formula.

$$\text{Resistance of the pellet, } R_s = 4.532 \times V/I$$

$$\text{Bulk resistivity of the pellet, } \rho = R_s \times t$$

Electrical conductivity, $\sigma = 1/\rho$

Ionic conductivity of the samples was also studied by the AC impedance spectroscopy technique using a Gamry potentiostat in the frequency range (10 mHz−100 kHz) at an amplitude of 10 mV. The samples for AC impedance-based conductivity measurements were prepared by sandwiching ~1.5-2 mm thick (t) pellets with a diameter of 13 mm (d) (obtained by pressing ~200 mg sample material) between two 200 μm thick lithium metal foils in a 2025-coin cell assembled in a glovebox. Equivalent circuit modeling was performed using the Z-view 2.0 (Scribner Associates Inc.) software to obtain R_p, the resistance to lithium ion mobility. The lithium ion conductivity values were then calculated using the following formula, where, 'Rp' is the resistance, 't' is the thickness and 'S' is the surface area of the pellets, respectively.

$$\text{Lithium ionic conductivity, } \sigma = \frac{1}{R_p} \times \frac{t}{S}$$

$$\text{Surface area of the pellets, } S = \Pi \times \left(\frac{d}{2}\right)^2$$

The S-Zn-MOF from our previous publication showed an initial capacity of 1476 $mAhg^{-1}$ [129] while the CFM derived S-SCFM shows an initial capacity of 1190 $mAhg^{-1}$. This difference in the initial capacity is attributed to the poor ionic and electrical conductivity of the CFM derived SCFM as compared with MOF-5. Each data point is an average of the conductivities measured from three different samples made from three independent batches of the MOF-5, S-MOF-5, SCFM and S-SCFM systems.

Appendix C Table 3 Summary of the performances of the currently studied CFM derived S-CFM cathode systems compared to reported work in the literature.

MOF	Electrode sulfur loading (wt%)	Initial Capacity (mAh/g)	Capacity after 100 cycles (mAh/g)	C-rate (mA/g)	Fade rate (%)	Voltage range (V)	Reference
S-SCFM	56	1190	1044	0.1	0.12 **0.0012 (%/cycle)**	1.7-2.6	Present work
Zn-MOF-S/ MOF-5	35	1476	609	0.2	0.14 **0.0014 (%/cycle)**	1.7-2.6	Present authors [29]
Ppy-S-in-PCN-224	44	1330	780	0.5	0.3	1.7-2.7	[449]
Ppy-S-in-MIL-53	44	960	900	0.5	0.06	1.7-2.7	[449]
MIL-53	30	1,125	436	0.1	0.72	1.8-2.8	[135]
NH2-MIL-53	30	526	313	0.1	0.45	1.8-2.8	[135]
HKUST-1	30	1,055	710	0.1	0.43	1.8-2.8	[135]
ZIF-8	30	738	654	0.5	0.11	1.8-2.8	[135]
ZIF-8-M	30	556	476	0.5	0.15	1.8-2.8	[135]
MIL-100	30	491	410	0.5	0.17	1.8-2.8	[135]
MIL-100	19	1,100	420	0.1	0.83	1.0-3.0	[450]
HKUST-1	16	1,498	500	0.1	0.39	1.0-3.0	[134]
ZIF-8	12	1,200	420	0.1	0.33	1.0-3.0	[425]
MIL-101	58.8	869	695	0.1	0.17	1.0-3.0	[252]
DUT-23	60	689	550	0.1	0.10	1.5-3.0	[137]
MOF-525	50	1190	602	0.5	0.43	1.5-3.0	[133]

Appendix C Table 4 Reaction voltages (V Vs Li^+/Li) observed in the cyclic voltammograms of the CFM derived S-SCFM.

S-SCFM				
	Charge/ anodic scan		Discharge/ cathodic scan	
Cycle number	Peak 1 Voltage (V)	Peak 2 Voltage (V)	Peak 3 Voltage (V)	Peak 4 Voltage (V)
1^{st} cycle	2.30	2.41	2.35	2.02
2^{nd} cycle	2.29	2.40	2.36	2.03
10^{th} cycle	2.29	2.40	2.36	2.03
100^{th} cycle	2.29	2.40	2.36	2.03

Appendix C Table 5 Charge transfer parameters before and after 1st, 2nd and 100th cycles of the S-SCFM, Figure 7b.

S-SCFM	R_s/ ohm cm^{-2}	CPE_i		R_i/ ohm cm^{-2}	CPE_{dl}		R_{ct} / ohm cm^{-2}	Wo		
		(*10^6)			T(*10^5)	P		R	T(*10^8)	P
Before cycling	7.8	3.2	0.71	16.2	18.6	0.71	107.2	0.02	1.33	0.20
After 1st cycle	2.4	55.2	0.82	8.8	1.02	0.83	89.5	0.001	0.2	0.43
After 2nd cycle	6.6	1.5	0.83	27.5	77.1	0.58	70.1	0.005	0.11	0.32
After 100th cycle	4.3	17.5	0.72	32.3	6.4	0.49	68.8	0.02	0.08	0.16

Appendix D Supporting Information: Investigate the Mechanisms of Composite Polymer Electrolytes (CPEs) to suppress solid electrolyte Interphase (SEI) Formation and Prevention of Polysulfide Dissolution in Li-S Batteries – Novel Composite Polymer Electrolytes (CPEs) of PVdF – HFP Derived by Electrospinning with Enhanced Li-ion Conductivities for Rechargeable Lithium – Sulfur Batteries

Pavithra M Shanthi[a], Prashanth J Hanumantha[b], Taciana Albuquerque[c], Bharat Gattu[a], Prashant N Kumta[a, c, d, e]

[a]Department of Chemical and Petroleum Engineering,
University of Pittsburgh, Pittsburgh, PA 15261 (USA)

[b]Department of Bioengineering,
University of Pittsburgh, Pittsburgh, PA 15261 (USA)

[c]Department of Chemical Engineering,
Arizona State University, Tempe, AZ 85287 (USA)

[d]Department of Mechanical Engineering and Materials Science,
University of Pittsburgh, Pittsburgh, PA 15261 (USA)

[e]Center for Complex Engineered Multifunctional Materials,
University of Pittsburgh, Pittsburgh, PA 15261 (USA)

XRD Analysis of Nano-fillers

The crystal structure of fumed silica (f-SiO_2) and nanoparticulate TiO_2, SiO_2 (nm-TiO_2 and nm-SiO_2) synthesized using solution based method were studied using X – ray diffraction (XRD). Appendix D Figure 1 shows the XRD patterns collected on the samples. Both fumed SiO_2 and nm-SiO_2 show an amorphous XRD pattern. However, nm-TiO_2 shows a crystalline structure with peaks at 101, 110, 004, 200 and 211 planes corresponding to anatase phase.[343, 344, 476]

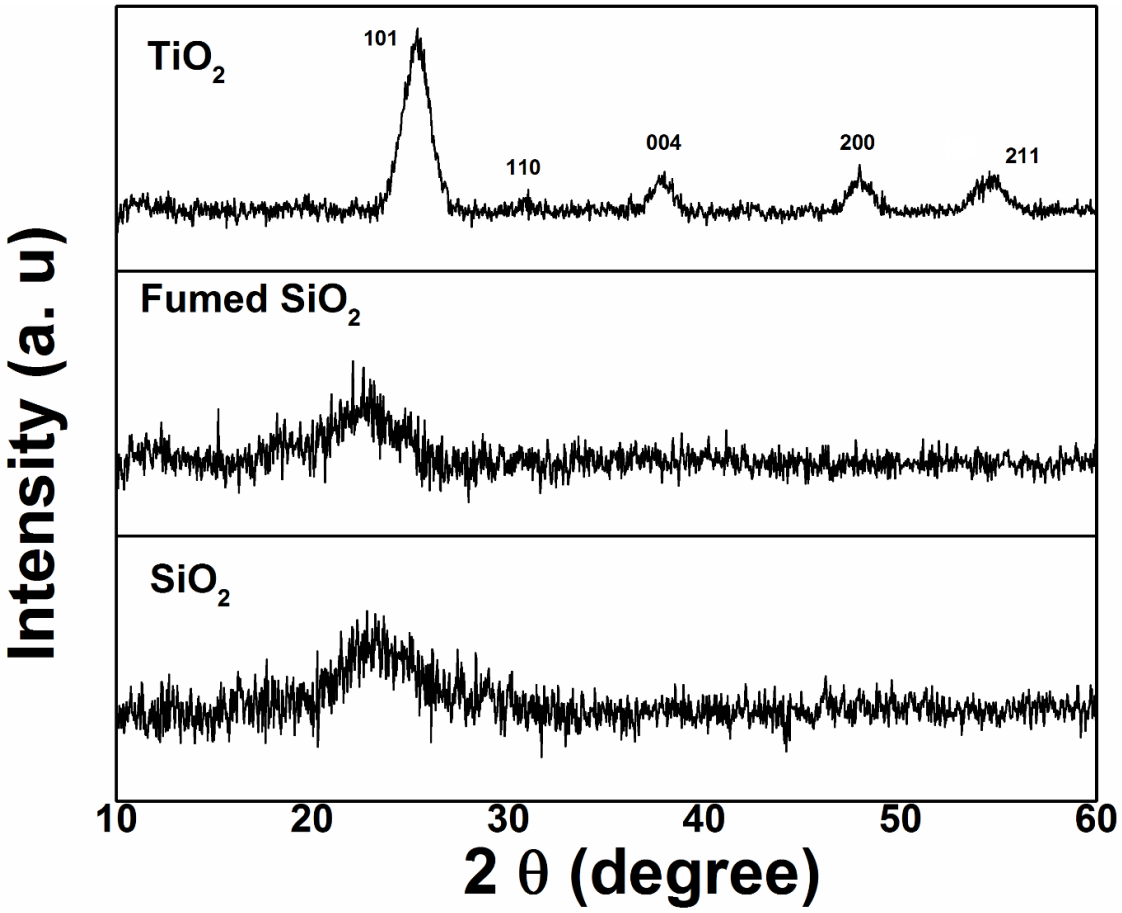

Appendix D Figure 1 XRD patterns of SiO_2, fumed SiO_2 and TiO_2.

SEM – EDS analysis

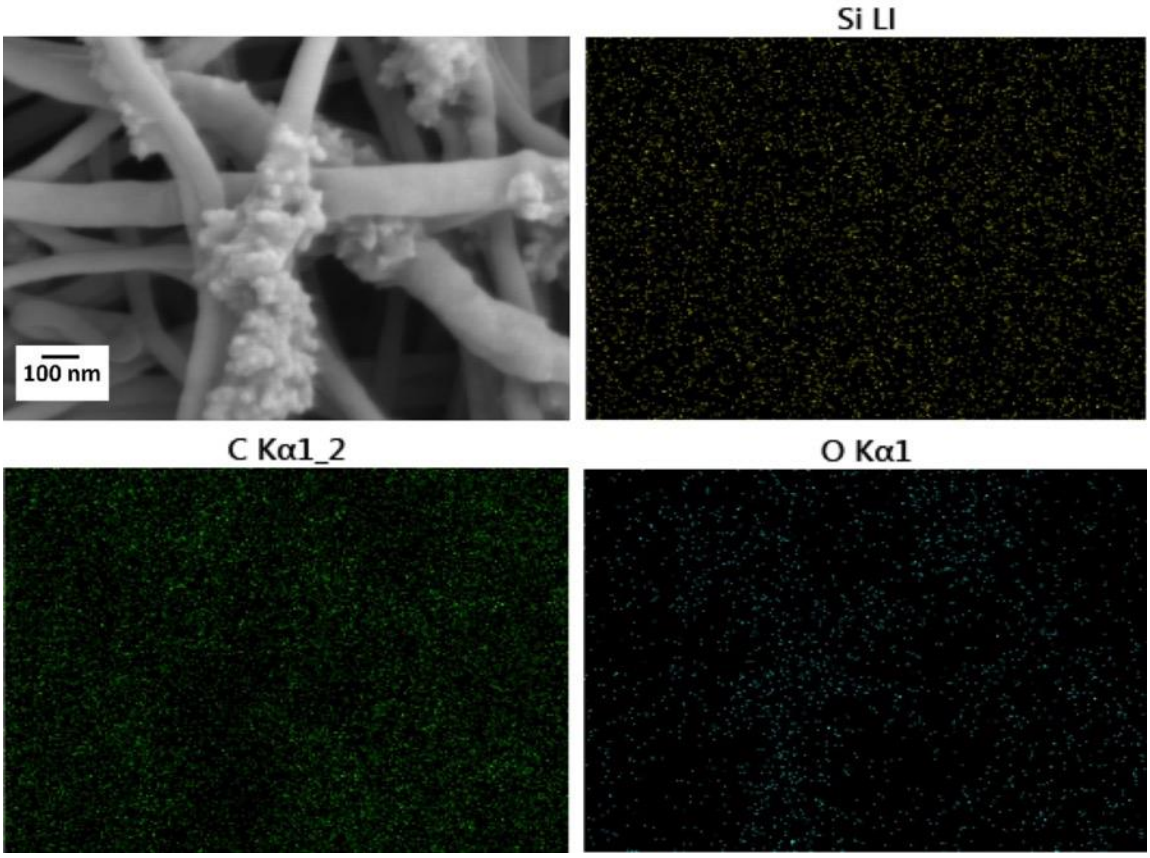

Appendix D Figure 2 SEM micrograph of f-SiO2 incorporated PVDF – HFP membrane with silicon, carbon and oxygen mapping spectra obtained by Energy Dispersive X-ray analysis (EDAX).

The SEM image along with elemental mapping of silicon, carbon and oxygen obtained by EDXA are shown in Appendix D Figure 2. The SEM image shows nanofibers with visibly observable agglomerates of f-SiO_2. Carbon mapping of the SEM image shows a uniform distribution, apparently due to the carbon backbone of the fibers. Elemental mapping of Si and O also shows a uniform distribution, suggesting that f-SiO_2 is uniformly embedded into the fibers along with the agglomerates present on the surface[349].

FTIR Analysis:

The spectrum of PVdF-HFP (Appendix D Figure 3) contains peaks at 760, 850, 872, 973, 1060, 1146, 1292, 1381, and 1404 cm^{-1} corresponding to CF_3 group, CH_2 rocking, CH_2 wagging of the vinylidene, out of plane C–H bending, symmetric C–F stretching, CF_2 stretching, symmetrical stretching CF_3, CH_2 wagging and scissoring vibration of vinylidene[369]. The vibrational frequencies appearing at 1060 and 850 cm^{-1} tend to show the respective crystalline and amorphous phase of PVdF. The peaks at 515 and 574 cm^{-1} are due to symmetric bending mode of LiTFSI[327]. The peaks between 600 to 620 cm^{-1} corresponds to the deformation mode of SO_2[327]. The peaks at 740, 789, 1058, 1140, 1195, 1332 and 1354 cm^{-1} corresponds to overlapping of symmetric bending modes of CF_3 and S-N stretching, S-N symmetric stretching, S-N-S symmetric stretching, C-F stretching and C-CO_2-N bonding mode, CF_3 symmetric stretching, C-SO_2-N bonding mode of LiTFSI and SO_2 asymmetric stretching of LiTFSI, respectively.

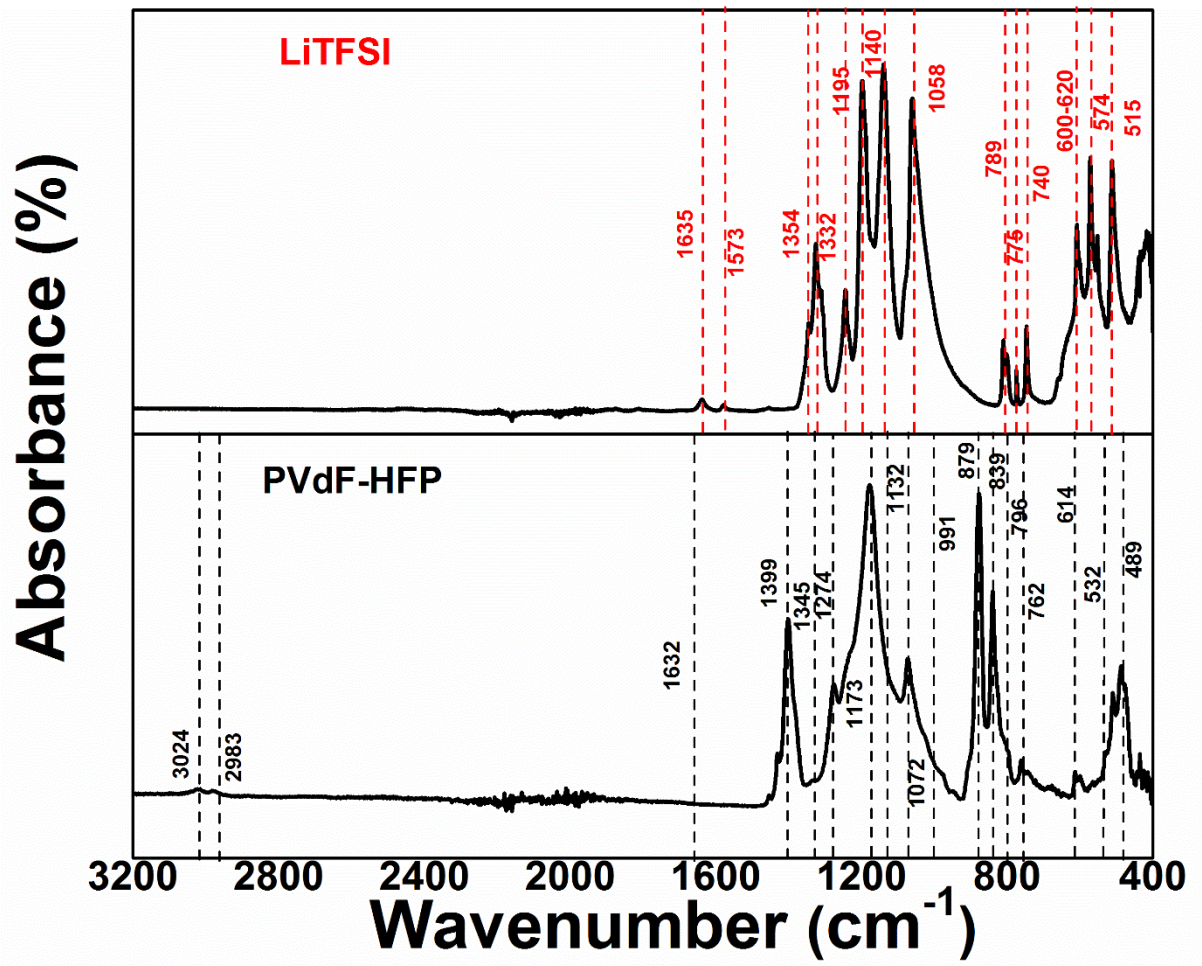

Appendix D Figure 3 FTIR spectra of pure PVdF-HFP and LiTFSI salt.

Appendix D Table 1 Peak assignment for pure PVdF-HFP, LiTFSI, PVdF-HFP with LiTFSI and different nanofillers.

Sample	Wavenumber (cm^{-1})	Peak assignment	Reference
PVdF – HFP membrane	762, 760	CH_2 rocking vibration, CF_3 group	327
	614	CF2 and -C-C-C- skeletal vibration	327
	762	CH_2 rocking vibrations	327
	796	CF_3 stretching vibration	327
	839	Mixed CH_2 rocking modes	327
	489	Bending vibrations of CF_2 group	327
	532	Wagging vibrations of CF_2 group	327
	879	Combined -C-C- and CF_2 symmetric stretching vibrations	327
			327
	976	C-F stretching vibrations	327
	1060	C-F symmetric stretching vibrations	369
	1146	-CF_2 stretching vibrations	369
	1174	-C-C-C- bond symmetric stretching	369
	1292	-CF_3 symmetric stretching	369
	1381	-CH_2 wagging	369
	1404	Scissoring vibration of vinylidene	369
	2983	Symmetric stretching of CH_2	327
	3024	Asymmetric stretching of CH_2	327

Appendix D Table 1 (Continued)

LiTFSI	515, 574 600-620 740 789 1058 1140 1195 1332 1354 1573 1635	CF_3 asymmetric bending mode Deformation mode of SO_2 Overlapping of symmetric bending modes of CF_3 and S-N stretching of LiTFSI S-N symmetric stretching S-N-S symmetric stretching C-F stretching and C-CO_2-N bonding mode CF_3 symmetric stretching C-SO_2-N bonding mode of LiTFSI SO_2 asymmetric stretching -S-N-S- bending vibration -S-N-S- stretching vibration	327, 477 327, 478 477 327, 478 327, 478 327, 479 327, 478 327, 479、 327, 478 327, 480 481
PVdF – HFP + LiTFSI	1058 1630 574	Asymmetric S–N–S stretching of LiTFSI Complexation formed between polymer backbone and LiTFSI salt CF_3 asymmetric bending mode of LiTFSI	327 327 327
PVdF – HFP + LiTFSI + nm-SiO_2 and f-SiO_2	1070 (peak intensity increase)	Overlap of F-C-F symmetric stretching vibrations and Si-O-Si asymmetric stretching vibrations	356
PVdF – HFP + LiTFSI + TiO_2	1580 (shifts from 1600)	Greater number of ions coordinate with –NH_2	357

Flame test:

To confirm the thermal stability of the polymer membranes, flame test was performed on the membranes and commercial separator membranes. The distance between the separators and the source of flame was set at 5 cm. Appendix D Figure 4 shows the results of flame test on commercial separator and polymer electrolyte membranes. While the commercial separator shrunk within 5 seconds, the polymer membranes was not affected even after exposing to flame for over 60 seconds[482].

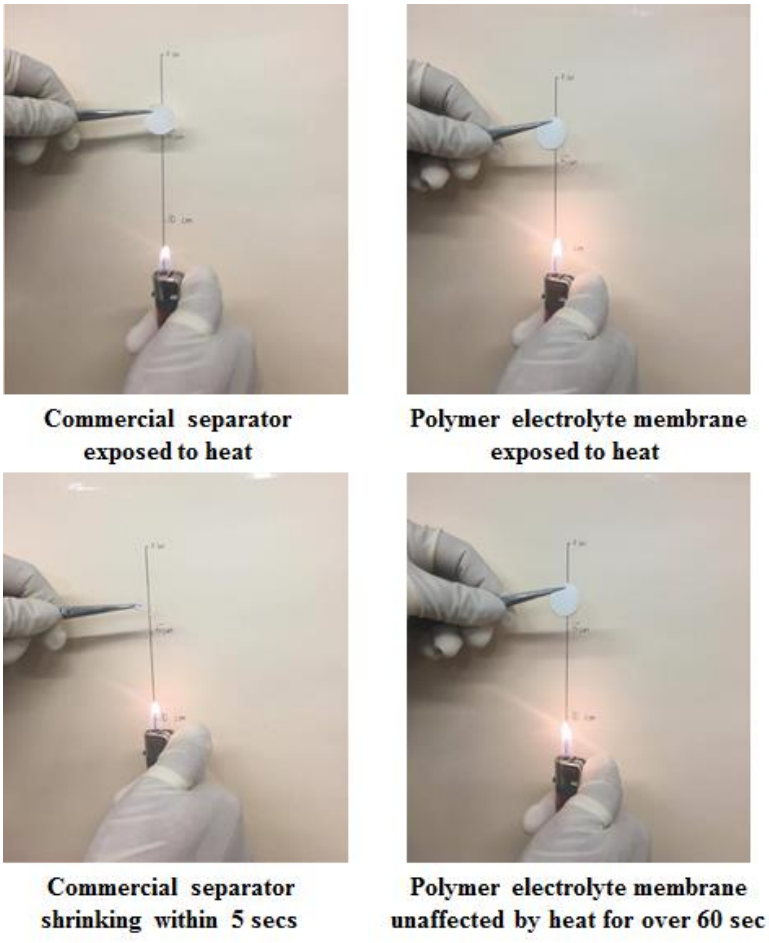

Appendix D Figure 4 Commercial separator and polymer membrane exposed to flame for 5 seconds and 60 seconds, respectively.

Electrolyte Uptake of the CPE Separators

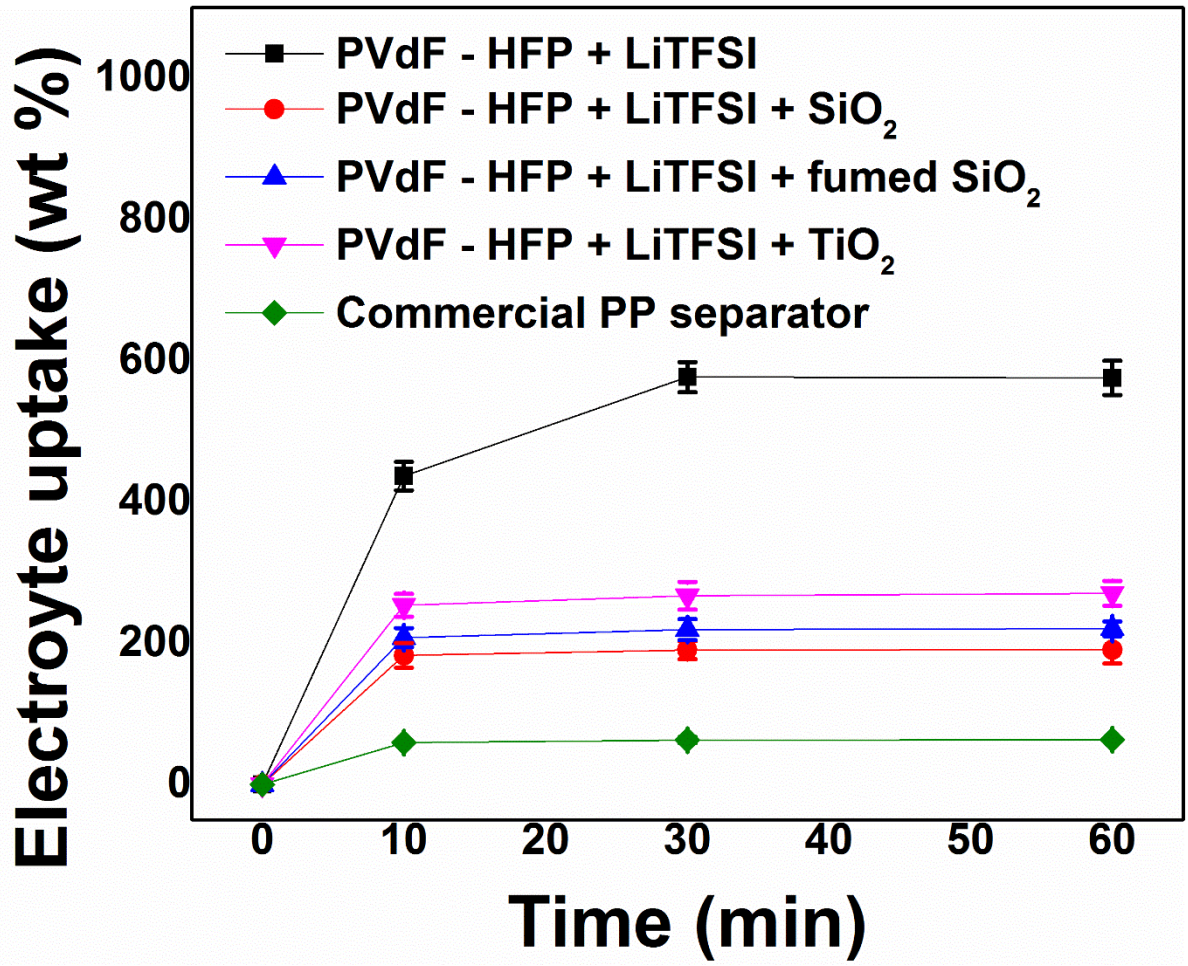

Appendix D Figure 5 Electrolyte uptake of the CPEs. Each data represents an average of three independent tests run on three different samples under identical conditions.

To determine the E/S ratio in the CPEs, electrolyte uptake test was performed in the CPEs and the results are shown in Appendix D Figure 5. The uptake increases linearly and then stabilizes after 10 min.

Electrochemical Charge – Discharge Profiles of the CPEs

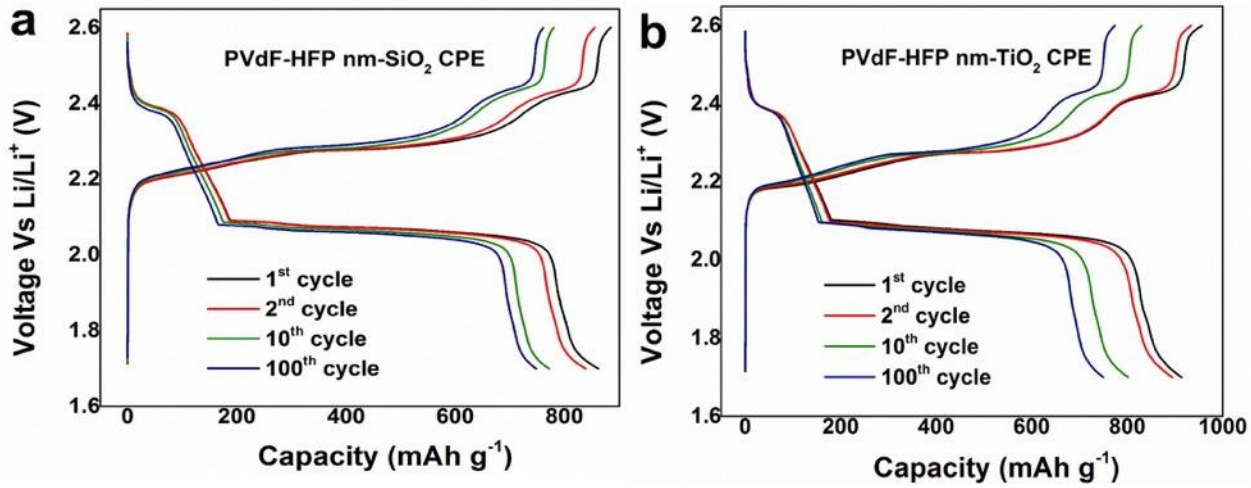

Appendix D Figure 6 a) electrochemical charge – discharge profile of PVdF-HFP+LiTFSI+nm-SiO_2 polymer membrane and b) PVdF-HFP+LiTFSI+nm-TiO_2 polymer membrane.

The voltage profiles of both the CPE membranes at 1st, 2nd, 10th and 100th cycles feature the two discharge plateaus characteristic of Li-S batteries. The plateau at around 2.4 V corresponds to the transformation from the S_8 molecular forms to a series of soluble polysulfides. On the other hand, the plateau at 2.1 V corresponds to the transformation of L_2S_4 species to insoluble Li_2S_2 and Li_2S[100, 254].

FTIR Comparison of Separators Before and After Cycling

The FTIR spectrum of nanofiller incorporated PVDF – HFP + LiTFSI membrane soaked in electrolyte shows peaks corresponding to PVdF – HFP at wavenumbers 489, 614, 839, 879, 1060, 1174, 1292, 1381 and 1404 cm^{-1} representing bending vibrations of CF_2 group, CF_2 and -C-C-C- skeletal vibration, mixed CH_2 rocking modes, combined -C-C and CF_2 symmetric stretching vibrations, C-F symmetric stretching vibration, -C-C-C- bond symmetric stretching, -CF_3 symmetric stretching, -CH_2 wagging and scissoring vibration of CH_2[369, 483].

Appendix D Table 2 Peak assignment for polymer electrolyte membranes before and after electrochemical cycling.

Sample	Wavenumber (cm^{-1})	Peak assignment
PVdF – HFP + LiTFSI + f-SiO_2, nm-SiO_2 and nm-TiO_2 + membranes before cycling	489	Bending vibration of CF_2 group
	509	Out of plane -C-C- bending of the ring structure of dioxane
	570	Symmetric deformation mode of -CF_3 group from interaction with dioxane
	614	CF_2 and -C-C-C- skeletal vibrations
	684	-N-H bending vibrations from the imide group of LiTFSI
	762	
	839	-C=O vibrations (ester)
	879	Mixed CH_2 rocking modes
	1032	Combined -C-C- and CF_2 symmetric stretching
	1060	Introduction of SO_3^- C-F symmetric stretching vibration
	1070	Overlap of F-C-F symmetric stretching vibrations and Si-O-Si asymmetric stretching vibrations
	1174	-C-C-C- bond symmetric stretching
	1229	-C-N- stretching vibration
	1292	-CF_3 symmetric stretching
	1355	-CH_2 wagging
	1381	Scissoring vibration of vinylidene
	1404	-CH_2 symmetric stretching vibrations
	2829	-C-H stretching vibrations

Appendix D Table 2 (Continued)

PVdF – HFP + LiTFSI + nm-SiO_2 and f-SiO_2 membranes after cycling (side facing lithium metal and sulfur cathode)	3680-3310	Indicates the presence of exchangeable protons, typically from amide group
	1630, 1500	-C=O bond from carbonyl group of dimethoxyethane
	1333	-C-H ring bending vibrations of dioxane ring
	1134	Stretching vibrations of carbonate group formed during cycling
	1008	-Si-O stretching vibrations
	793	-SO_3 from LITFSI
	683	Si–O–Si stretching vibrations
PVdF – HFP + LiTFSI + nm-TiO_2 membrane after cycling (side facing lithium metal and sulfur cathode)	1630, 1500	C=O bond from carbonyl group of dimethoxyethane
	1333	-C-H ring bending vibrations of dioxane ring
	1134	Stretching vibrations of carbonate group formed during cycling
	1580	Greater number of ions coordinate with –NH_2

Appendix E Supporting Information: Study the Electrochemical Stability and Room Temperature Li-ion Conductivity of New Substituted Solid-state Oxide and Non-oxide Li-ion Conductors - Theoretical and Experimental Strategies for New Heterostructures with Improved Stability for Rechargeable Lithium Sulfur Batteries

Pavithra M Shanthi[a], Oleg I. Velikokhatnyi[b], Prashanth J Hanumantha[b], Bharat Gattu[a], Moni K Datta[b], Prashant N Kumta[a, b, c, d,*]

[a]Department of Chemical and Petroleum Engineering,
University of Pittsburgh, Pittsburgh, PA 15261 (USA)

[b]Department of Bioengineering,
University of Pittsburgh, Pittsburgh, PA 15261 (USA)

[c]Department of Mechanical Engineering and Materials Science,
University of Pittsburgh, Pittsburgh, PA 15261 (USA)

[d]Center for Complex Engineered Multifunctional Materials,
University of Pittsburgh, Pittsburgh, PA 15261 (USA)

Appendix E Table 1 Fitted results of Ca substituted Orthosilicate (Each datum represents an average of three independent tests run on three different samples under identical conditions.)

% Ca substitution	R_s (Ohm)	CPE-T$\times 10^{11}$	CPE-P	R_p (Ohm)	Conductivity $\times 10^{12}$ (S/cm)
0	1.70±0.21	5.26±0.32	0.78±0.05	1.29±0.21 E+11	1.17±0.25
2.5	2.57±0.35	5.14±0.27	0.79±0.05	3.07±0.42 E+09	49.14±13.62
5	3.06±0.26	3.87±0.46	0.94±0.09	1.29±0.17 E+08	1169.55±292.65
7.5	8.47±0.76	5.19±0.28	0.70±0.12	5.25±0.73 E+06	28706.07±8000.53
10	1.12±0.08	4.11±0.54	0.81±0.04	1.26±0.20 E+09	119.27±37.34
12.5	9.85±0.62	4.15±0.63	0.82±0.05	3.34±0.45 E+09	45.08±11.4
15	1.40±0.07	4.29±0.54	0.79±0.03	9.12±1.12 E+09	16.54±3.8

Appendix E Table 2 Fitted results of Mg substituted Orthosilicate (Each datum represents an average of three independent tests run on three different samples under identical conditions)

% Mg substitution	R_s (Ohm)	CPE-T$\times 10^{11}$	CPE-P	R_p (Ohm)	Conductivity $\times 10^{12}$ (S/cm)
0	1.91±0.09	3.59±0.29	0.79±0.06	7.82±0.82 E+10	1.19±0.32
2.5	5.24±0.46	9.53±1.02	0.76±0.04	3.39±0.28 E+10	4.45±0.72
5	1.36±0.05	5.67±0.84	0.85±0.05	8.22±0.96 E+08	183.51±37.40
7.5	7.44±0.82	7.16±0.68	0.84±0.10	1.18±0.15 E+08	1277.59±275.72
10	1.39±0.23	9.80±1.16	0.83±0.09	2.09±0.26 E+10	7.23±1.62
12.5	1.69±0.07	8.20±0.85	0.83±0.07	5.14±0.35 E+10	2.94±0.70
15	1.78±0.03	4.96±0.28	0.86±0.04	5.37±0.42 E+10	2.81±0.48

Appendix E Table 3 Fitted results of F substituted Orthosilicate (Each datum represents an average of three independent tests run on three different samples under identical conditions)

% F substitution	R_s (Ohm)	CPE-T$\times 10^{10}$	CPE-P	R_p (Ohm)	Conductivity $\times 10^{12}$ (S/cm)
0	3.54±0.54	1.16±0.09	0.76±0.04	1.26±0.20 E+11	1.19±0.32
2.5	2.40±0.12	1.59±0.21	0.79±0.06	7.52±0.63 E+09	20.04±6.60
5	1.32±0.06	1.67±0.08	0.81±0.06	4.96±0.55 E+09	30.41±8.50
7.5	1.01±0.02	2.06±0.29	0.76±0.08	2.39±0.19 E+09	63.13±10.41
10	3.08±0.21	2.01±0.08	0.71±0.02	4.19± 0.32E+08	359.63±54.34
12.5	1.43±0.07	1.63±0,12	0.70±0.06	1.96±0.19 E+09	76.95±15.42
15	1.27±0.08	1.47±0.06	0.79±0.04	3.23±0.42 E+10	4.66±0.87

Charge-discharge Profiles of the Cu-bpy-CFM – without Li_4SiO_4 and with Substituted and Unsubstituted Li_4SiO_4:

The charge-discharge profiles of the Cu-bpy-CFM – without Li_4SiO_4, Cu-bpy-CFM – Unsubstituted Li_4SiO_4, Cu-bpy-CFM – F substituted Li_4SiO_4, Cu-bpy-CFM – Mg substituted Li_4SiO_4, Cu-bpy-CFM – Ca substituted Li_4SiO_4 after 1^{st}, 2^{nd} and 100^{th} cycles are shown in Appendix E Figure 1 a, b, c, d and e respectively.

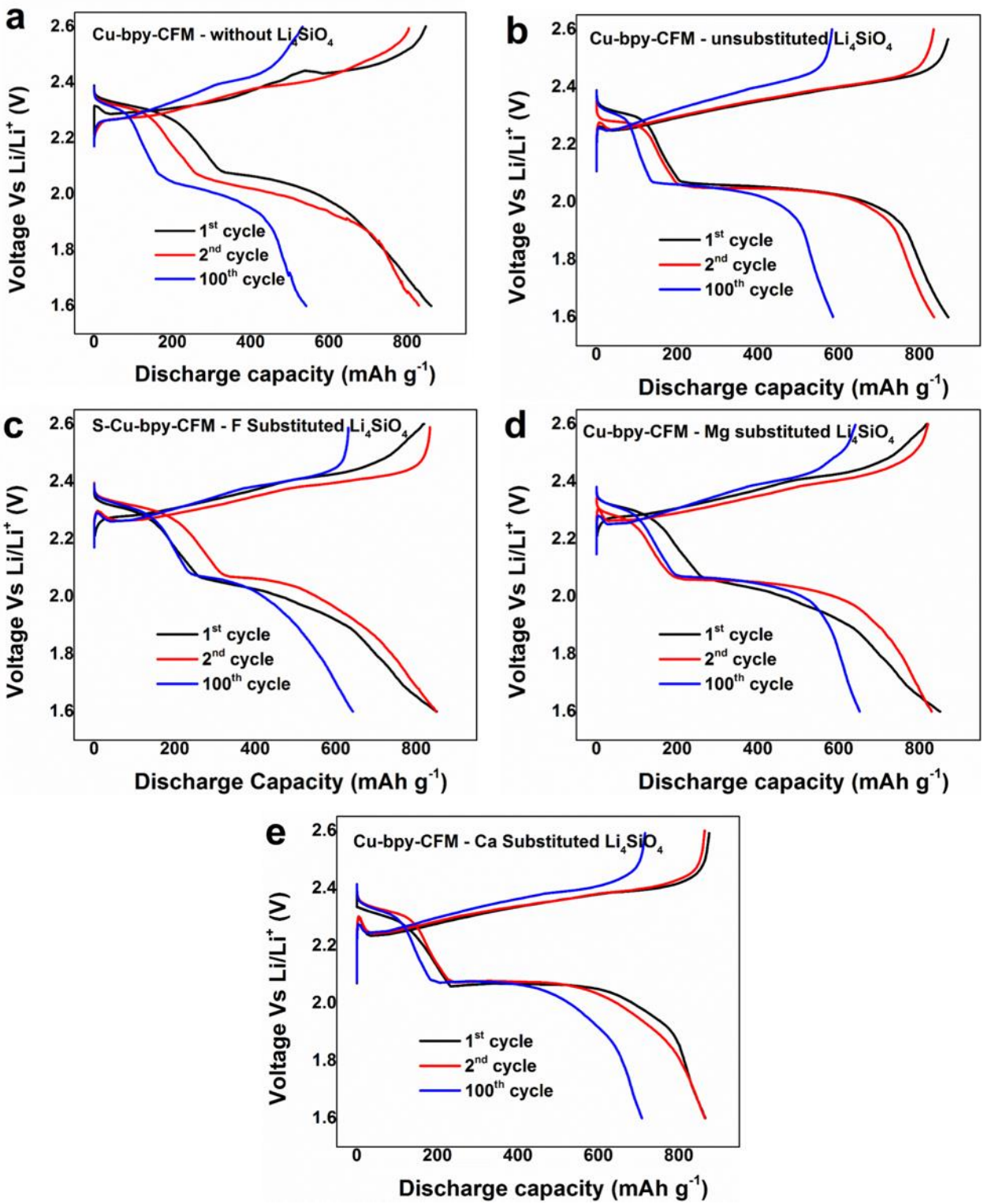

Appendix E Figure 1 Charge-discharge profiles of the Cu-bpy-CFM – without Li4SiO4, b) Cu-bpy-CFM – Unsubstituted Li4SiO4, c) Cu-bpy-CFM – F substituted Li4SiO4, d) Cu-bpy-CFM – Mg substituted Li4SiO4, e) Cu-bpy-CFM – Ca substituted Li4SiO4 after 1st, 2nd and 100th cycles.

Nyquist plots of the Cu-bpy-CFM – without Li_4SiO_4 and with Substituted and Unsubstituted Li_4SiO_4:

The Nyquist plots of the Cu-bpy-CFM – without Li_4SiO_4, Cu-bpy-CFM – Unsubstituted Li_4SiO_4, Cu-bpy-CFM – F substituted Li_4SiO_4 and Cu-bpy-CFM – Mg substituted Li_4SiO_4 before and after first and 100^{th} cycles are shown inf Appendix E Figure 2 a, b, c and d respectively. The fitted values for R_s, CPE_i, R_i, CPE_{dl}, R_{ct} and Z_o are shown in Appendix E Table 4.

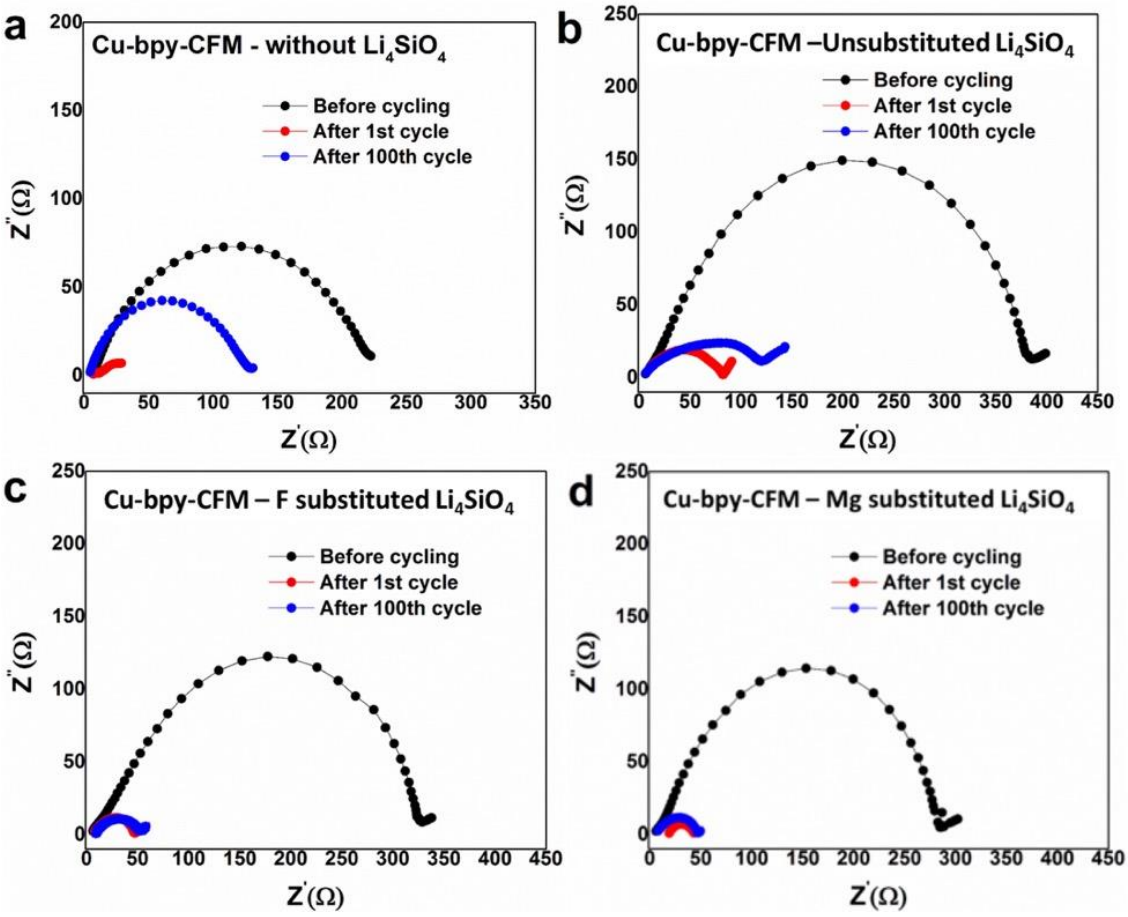

Appendix E Figure 2 a) Nyquist plots of the Cu-bpy-CFM – without Li_4SiO_4, b) Cu-bpy-CFM – Unsubstituted Li_4SiO_4, c) Cu-bpy-CFM – F substituted Li_4SiO_4, d) Cu-bpy-CFM – Mg substituted Li_4SiO_4 before and after first and 100^{th} cycles at the OCV (22-2.4 V).

Appendix E Table 4 Charge transfer parameters before and after 1st, 2nd and 100th cycles of the substituted and unsubstituted Li_4SiO_4 coated S-Cu-bpy-CFM electrodes.

S-SCFM	R_s/ ohm cm^{-2}	CPE_i		R_i/ ohm cm^{-2}	CPE_{dl}		R_{ct} / ohm cm^{-2}	Zo		
		T	P		T	P		R	T	P
S-Cu-bpy-CFM – without Li_4SiO_4 coating										
Before cycling	6.806	1.01*10^{-5}	0.78	20.81	1.60*10^{-2}	0.52	184.21	18.41	1.30*10^{-2}	0.53
After 1st cycle	6.70	2.60*10^{-5}	0.81	22.08	2.0*10^{-2}	0.45	13.42	22.08	0.19	0.39
After 100th cycle	3.85	1.02*10^{-5}	0.81	25.44	4.56*10^{-4}	0.64	94.56	4.79	4.95*10^{-4}	0.60
S-Cu-bpy-CFM – pristine Li_4SiO_4 coating										
Before cycling	3.55	3.01*10^{-4}	0.58	19.40	1.85*10^{-5}	0.92	354.5	10.34	1.0*10^{-4}	0.34
After 1st cycle	5.94	8.11*10^{-4}	0.55	19.68	1.59*10^{-5}	0.69	52.92	7.48	7.07*10^{-6}	0.48
After 100th cycle	5.67	1.52*10^{-5}	0.64	22.29	8.03*10^{-5}	o.69	102.6	2.06	1.88*10^{-2}	0.31

Appendix E Table 4 (Continued)

S-Cu-bpy-CFM – F substituted Li_4SiO_4 coating										
Before cycling	4.01	1.32*10^{-4}	0.63	20.51	2.29*10^{-5}	0.89	292.6	6.21	2.83*10^{-5}	0.44
After 1st cycle	3.18	1.64*10^{-4}	0.57	20.89	5.83*10^{-5}	0.78	20.29	7.02	1.82*10^{-8}	0.46
After 100th cycle	7.28	1.30*10^{-4}	0.73	19.23	3.05*10^{-4}	0.64	33.98	3.34	0.02	0.41
S-Cu-bpy-CFM – Mg substituted Li_4SiO_4 coating										
Before cycling	5.16	6.34*10^{-5}	0.68	23.67	2.68*10^{-5}	0.86	270.5	1.19*10^{-6}	1.16	0.59
After 1st cycle	6.35	8.10*10^{-5}	0.63	22.33	6.61*10^{-5}	0.65	16.92	0.47	4.87*10^{-6}	0.64
After 100th cycle	4.57	8.86*10^{-6}	0.89	21.67	9.7*20^{-5}	0.63	24.78	2.31	0.36	0.51
S-Cu-bpy-CFM – Ca substituted Li_4SiO_4 coating										
Before cycling	4.68	1.8*10^{-4}	0.67	25.45	2.26*10^{-5}	0.91	186	5.52	3.20*10^{-5}	0.48
After 1st cycle	6.56	2.0*10^{-2}	0.64	26.08	6.61*10^{-5}	0.65	15.98	0.66	4.90*10^{-6}	0.62
After 100th cycle	6.01	2.13*10^{-4}	0.65	23.39	4.92*10^{-4}	0.77	18.12	6.61	1.72*10^{-8}	1.59*10^{-6}

Appendix F Supporting Information: Develop Novel Composite Sulfur Cathodes Comprising High Sulfur Loadings on Electronically Conducting Platforms with Polysulfide Trapping Agents (PTA) and Understand the Mechanisms Related to Prevention of Polysulfide Dissolution Contributing to High Energy Density - Directly Deposited Sulfur Architectures with Polysulfide Trapping Agents (DDSA-PTA) for Lithium-Sulfur Batteries

Pavithra M Shanthi[a], Ramalinga Kuruba[b], Bharat Gattu[a], Moni Datta[b], Prashant N Kumta[a, b, c, d, *]

[a]Department of Chemical and Petroleum Engineering,

University of Pittsburgh, Pittsburgh, PA 15261 (USA)

[b]Department of Bioengineering,

University of Pittsburgh, Pittsburgh, PA 15261 (USA)

[c]Department of Mechanical Engineering and Materials Science,

University of Pittsburgh, Pittsburgh, PA 15261 (USA)

[d]Center for Complex Engineered Multifunctional Materials,

University of Pittsburgh, Pittsburgh, PA 15261 (USA)

XRD Analysis:

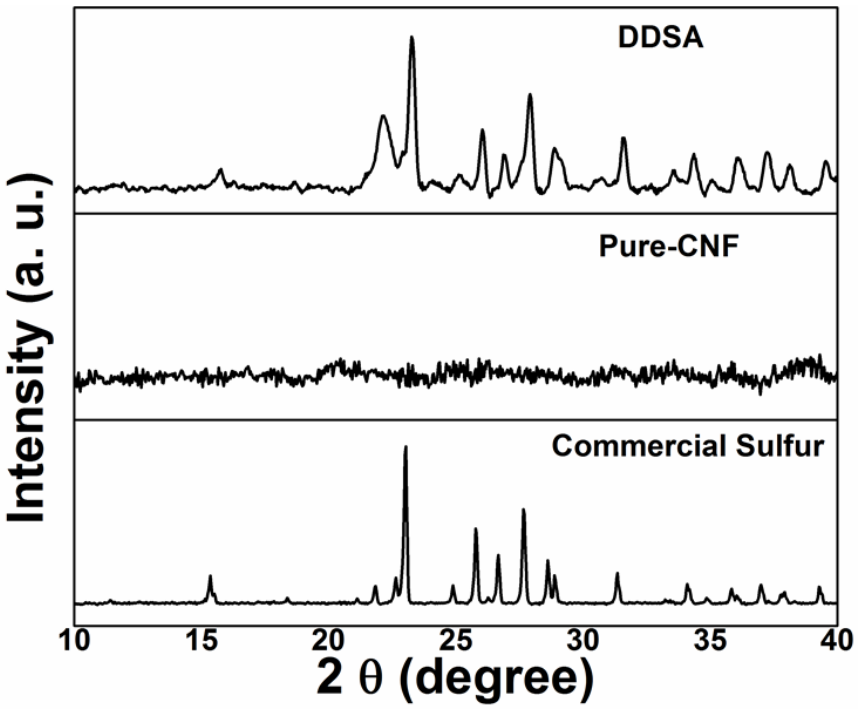

Appendix F Figure 1 Comparison of the XRD patterns of commercial sulfur, CNF and DDSA matt

SEM of DDSA:

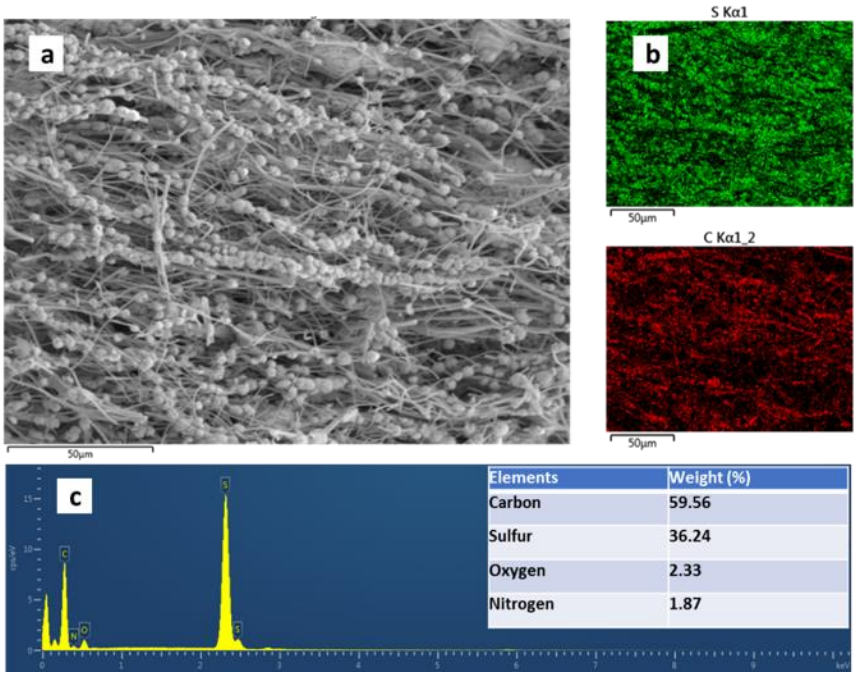

Appendix F Figure 2 (a) SEM image of the DDSA matt, (b) Sulfur and carbon mapping of the DDSA- matt and c) EDS and elemental composition results of the DDSA matt.

Electrochemical Cycling Data of DDSA-PTA Electrodes:

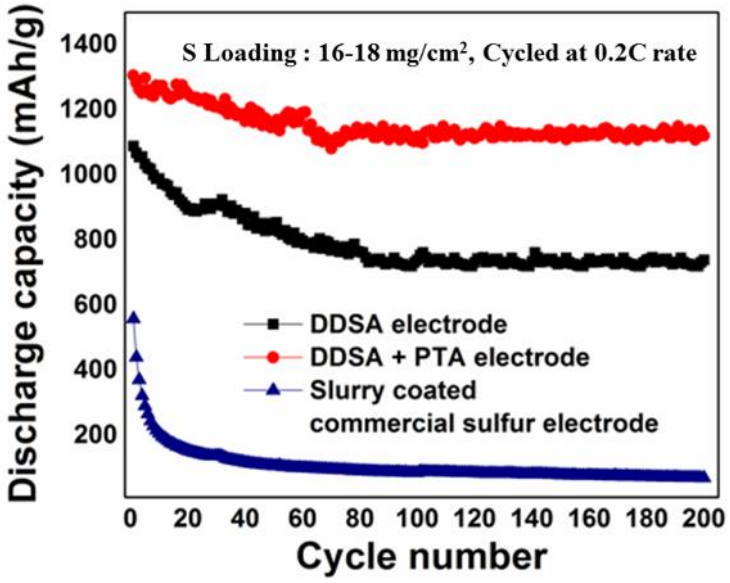

Appendix F Figure 3 Cycling performance of PTA coated DDSA electrode under flooded electrolyte conditions (20ul/mg-S E/S ratio) commonly used in Li-S coin cell testing.

The PTA coated DDSA electrode, when tested in a flooded electrolyte system shows excellent electrochemical cycling performance with an initial capacity of 1305 mAh/g that stabilized at 1112 mAh/g to 200 cycles with less than 0.0014% when cycled at 0.2C rate (Appendix F Figure 3).

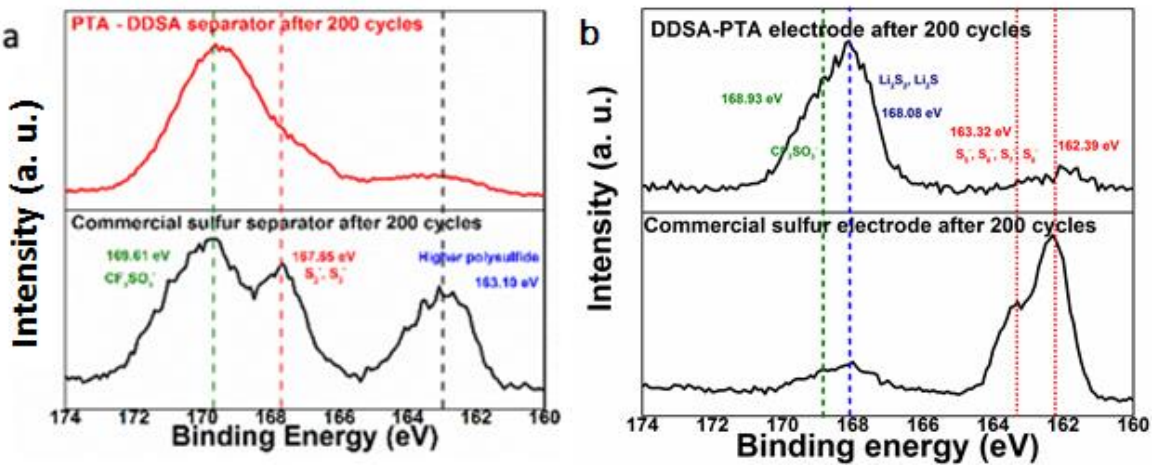

Appendix F Figure 4 (a) Comparison of XPS patterns of commercial sulfur and PTA - DDSA separators after 200 cycles and (b) Comparison of XPS patterns of commercial sulfur and PTA - DDSA electrodes after 200 cycles

XPS study of the electrodes and separators from the commercial sulfur and DDSA-PTA cathodes after 200 electrochemical charge – discharge cycles (Appendix F Figure 4a&b) clearly shows the absence of polysulfide peaks showing the efficacy of the polysulfide trapping agents in completing eliminating polysulfide dissolution.

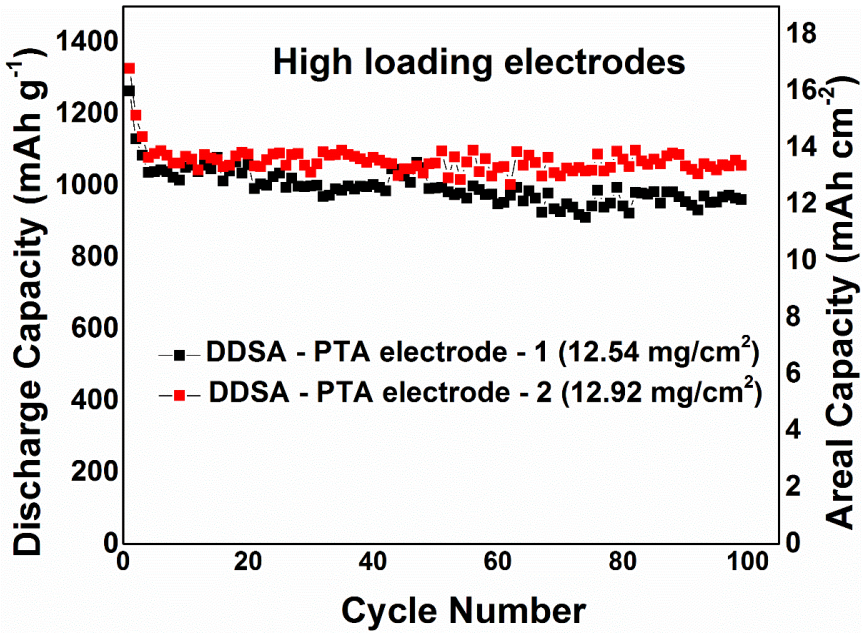

Appendix F Figure 5 Electrochemical cycling of PTA-DDSA electrode using the Batt 500 lean electrolyte (3ul/mg-S E/S ratio) protocol

The PTA coated DDSA electrodes showed good electrochemical performance when tested using the Batt 500 protocol is shown by the results of electrochemical cycling experiments in Appendix F Figure 5**.** The electrodes PTA-DDSA-1 and PTA-DDSA-2 showed an initial capacity of 1263 mAh/g and 1326 mAh/g respectively, when cycled at C/20 rate. Upon prolonged cycling, the PTA-DDSA-1 and PTA-DDSA-2 shows a capacity of 1023 mAh/g and 986 mAh/g respectively after 100 cycles at C/5 rate.

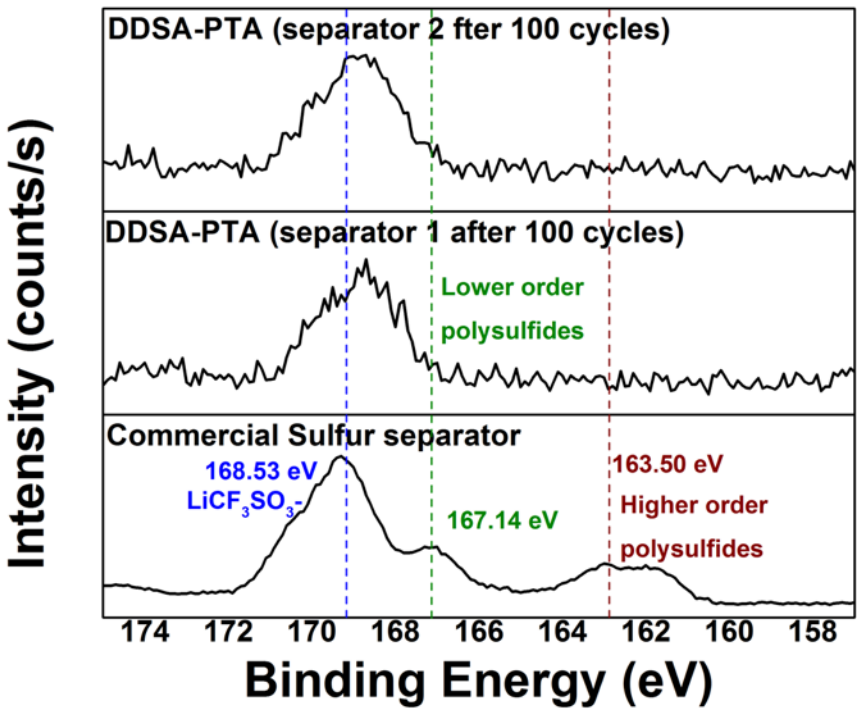

Appendix F Figure 6 (a) Comparison of XPS patterns of commercial sulfur and PTA - DDSA separators after 200 cycles

XPS study of the separators from the commercial sulfur and DDSA-PTA cathodes after 100 electrochemical charge – discharge cycles (Appendix F Figure 6) clearly shows the absence of polysulfide peaks showing the efficacy of the polysulfide trapping agents in completing eliminating polysulfide dissolution.

EIS Nyquist plot

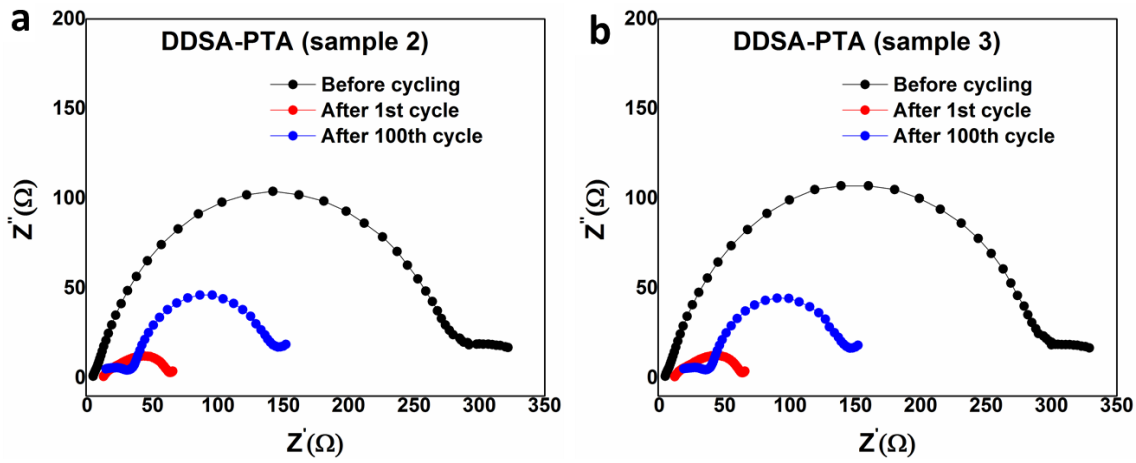

Appendix F Figure 7 Nyquist plot of the DDSA-PTA (sample 2 and sample 3) battery before cycling, after 1st cycle and 100th charge-discharge cycles.

Appendix F Table 1 EIS data fitting of the samples

DDSA-PTA	R_s/ ohm cm^{-2}	CPE_i		R_i/ ohm cm^{-2}	CPE_{dl}		R_{ct} / ohm cm^{-2}	Zo		
		T	P		T	P		R	T	P
DDSA-PTA (sample 1)										
Before cycling	5.42	1.05* 10^{-5}	0.84	19.36	1.32* 10^{-2}	0.34	264.19	5.63	1.73 *10^{-2}	0.82
After 1st cycle	4.92	3.20* 10^{-5}	0.76	18.22	1.62* 10^{-2}	0.52	123.20	12.82	0.26	0.45
After 100th cycle	5.22	2.12* 10^{-5}	0.86	20.63	5.68* 10^{-4}	0.81	38.52	9.23	2.50 *10^{-4}	0.56

Bibliography

1. Song, D.; Ikuta, H.; Uchida, T.; Wakihara, M., The spinel phases LiAlyMn2−yO4 (y=0, 1/12, 1/9, 1/6, 1/3) and Li(Al,M)1/6Mn11/6O4 (M=Cr, Co) as the cathode for rechargeable lithium batteries. *Solid State Ionics* **1999,** *117* (1–2), 151-156.

2. Kang, B.; Ceder, G., Battery materials for ultrafast charging and discharging. *Nature* **2009,** *458* (7235), 190-193.

3. Croce, F.; Appetecchi, G. B.; Persi, L.; Scrosati, B., Nanocomposite polymer electrolytes for lithium batteries. *Nature* **1998,** *394* (6692), 456-458.

4. Manuel Stephan, A.; Nahm, K. S., Review on composite polymer electrolytes for lithium batteries. *Polymer* **2006,** *47* (16), 5952-5964.

5. Whittingham, M. S., Lithium Batteries and Cathode Materials. *Chemical Reviews* **2004,** *104* (10), 4271-4302.

6. Sun, Y.-K.; Myung, S.-T.; Park, B.-C.; Prakash, J.; Belharouak, I.; Amine, K., High-energy cathode material for long-life and safe lithium batteries. *Nat Mater* **2009,** *8* (4), 320-324.

7. Bruce, P. G.; Freunberger, S. A.; Hardwick, L. J.; Tarascon, J.-M., Li-O2 and Li-S batteries with high energy storage. *Nat Mater* **2012,** *11* (1), 19-29.

8. Janek, J.; Zeier, W. G., A Solid Future for Battery Development. *Nat. Energy* **2016,** *1*, 16141.

9. Fotouhi, A.; Auger, D. J.; O'Neill, L.; Cleaver, T.; Walus, S., Lithium-Sulfur Battery Technology Readiness and Applications—A Review. *Energies* **2017,** *10* (12), 1937.

10. Berckmans, G.; Messagie, M.; Smekens, J.; Omar, N.; Vanhaverbeke, L.; Van Mierlo, J., Cost Projection of State of the Art Lithium-Ion Batteries for Electric Vehicles Up to 2030. *Energies* **2017,** *10* (9), 1314.

11. Raanan, R.; Gunier, R. B.; Balmes, J. R.; Beltran, A. J.; Harley, K. G.; Bradman, A.; Eskenazi, B., Elemental sulfur use and associations with pediatric lung function and respiratory symptoms in an agricultural community (California, USA). *Environmental health perspectives* **2017,** *87007*, 087007-1.

12. Yamin, H.; Peled, E., Electrochemistry of a nonaqueous lithium/sulfur cell. *Journal of Power Sources* **1983,** *9* (3), 281-287.

13. Marmorstein, D.; Yu, T. H.; Striebel, K. A.; McLarnon, F. R.; Hou, J.; Cairns, E. J., Electrochemical performance of lithium/sulfur cells with three different polymer electrolytes. *Journal of Power Sources* **2000,** *89* (2), 219-226.

14. Kolosnitsyn, V. S.; Karaseva, E. V., Lithium-sulfur batteries: Problems and solutions. *Russian Journal of Electrochemistry* **2008,** *44* (5), 506-509.

15. Zhang, S. S., Liquid electrolyte lithium/sulfur battery: Fundamental chemistry, problems, and solutions. *Journal of Power Sources* **2013,** *231*, 153-162.

16. Wang, J.; Chew, S. Y.; Zhao, Z. W.; Ashraf, S.; Wexler, D.; Chen, J.; Ng, S. H.; Chou, S. L.; Liu, H. K., Sulfur–mesoporous carbon composites in conjunction with a novel ionic liquid electrolyte for lithium rechargeable batteries. *Carbon* **2008,** *46* (2), 229-235.

17. Yuan, L.; Yuan, H.; Qiu, X.; Chen, L.; Zhu, W., Improvement of cycle property of sulfur-coated multi-walled carbon nanotubes composite cathode for lithium/sulfur batteries. *Journal of Power Sources* **2009,** *189* (2), 1141-1146.

18. Zheng, W.; Liu, Y. W.; Hu, X. G.; Zhang, C. F., Novel nanosized adsorbing sulfur composite cathode materials for the advanced secondary lithium batteries. *Electrochimica Acta* **2006,** *51* (7), 1330-1335.

19. Han, S.-C.; Song, M.-S.; Lee, H.; Kim, H.-S.; Ahn, H.-J.; Lee, J.-Y., Effect of Multiwalled Carbon Nanotubes on Electrochemical Properties of Lithium/Sulfur Rechargeable Batteries. *Journal of The Electrochemical Society* **2003,** *150* (7), A889-A893.

20. Sun, M.; Zhang, S.; Jiang, T.; Zhang, L.; Yu, J., Nano-wire networks of sulfur–polypyrrole composite cathode materials for rechargeable lithium batteries. *Electrochemistry Communications* **2008,** *10* (12), 1819-1822.

21. Wang, J.; Chen, J.; Konstantinov, K.; Zhao, L.; Ng, S. H.; Wang, G. X.; Guo, Z. P.; Liu, H. K., Sulphur-polypyrrole composite positive electrode materials for rechargeable lithium batteries. *Electrochimica Acta* **2006,** *51* (22), 4634-4638.

22. Wang, J.; Yang, J.; Wan, C.; Du, K.; Xie, J.; Xu, N., Sulfur Composite Cathode Materials for Rechargeable Lithium Batteries. *Advanced Functional Materials* **2003,** *13* (6), 487-492.

23. Hanumantha, P. J.; Gattu, B.; Shanthi, P. M.; Damle, S. S.; Basson, Z.; Bandi, R.; Datta, M. K.; Park, S.; Kumta, P. N., Flexible sulfur wires (Flex-SWs)—A new versatile platform for lithium-sulfur batteries. *Electrochimica Acta* **2016,** *212*, 286-293.

24. Liang, X.; Kwok, C. Y.; Lodi-Marzano, F.; Pang, Q.; Cuisinier, M.; Huang, H.; Hart, C. J.; Houtarde, D.; Kaup, K.; Sommer, H.; Brezesinski, T.; Janek, J.; Nazar, L. F., Tuning Transition Metal Oxide–Sulfur Interactions for Long Life Lithium Sulfur Batteries: The "Goldilocks" Principle. *Advanced Energy Materials* **2016,** *6* (6), 1501636-n/a.

25. Tao, X.; Wang, J.; Liu, C.; Wang, H.; Yao, H.; Zheng, G.; Seh, Z. W.; Cai, Q.; Li, W.; Zhou, G.; Zu, C.; Cui, Y., Balancing surface adsorption and diffusion of lithium-polysulfides on nonconductive oxides for lithium–sulfur battery design. *Nature Communications* **2016,** *7*, 11203.

26. Li, X.; Cao, Y.; Qi, W.; Saraf, L. V.; Xiao, J.; Nie, Z.; Mietek, J.; Zhang, J.-G.; Schwenzer, B.; Liu, J., Optimization of mesoporous carbon structures for lithium-sulfur battery applications. *Journal of Materials Chemistry* **2011,** *21* (41), 16603-16610.

27. Jin, J.; Wen, Z.; Ma, G.; Lu, Y.; Rui, K., Mesoporous carbon/sulfur composite with polyaniline coating for lithium sulfur batteries. *Solid State Ionics* **2014,** *262*, 170-173.

28. Gong, Z.; Wu, Q.; Wang, F.; Li, X.; Fan, X.; Yang, H.; Luo, Z., A hierarchical micro/mesoporous carbon fiber/sulfur composite for high-performance lithium-sulfur batteries. *RSC Advances* **2016,** *6* (44), 37443-37451.

29. Shanthi, P. M.; Hanumantha, P. J.; Gattu, B.; Sweeney, M.; Datta, M. K.; Kumta, P. N., Understanding the Origin of Irreversible Capacity loss in Non-Carbonized Carbonate − based Metal Organic Framework (MOF) Sulfur hosts for Lithium − Sulfur battery. *Electrochimica Acta* **2017,** *229*, 208-218.

30. Hanumantha, P. J.; Gattu, B.; Velikokhatnyi, O.; Datta, M. K.; Damle, S. S.; Kumta, P. N., Heterostructures for Improved Stability of Lithium Sulfur Batteries. *Journal of The Electrochemical Society* **2014,** *161* (6), A1173-A1180.

31. Manthiram, A.; Fu, Y.; Chung, S.-H.; Zu, C.; Su, Y.-S., Rechargeable Lithium–Sulfur Batteries. *Chemical Reviews* **2014,** *114* (23), 11751-11787.

32. Skotheim, T. A., High capacity cathodes for secondary cells. Google Patents: 1995.

33. Dahl, C.; Prange, A.; Steudel, R., *Biopolymers Online*. 2005; p 35.

34. Mikhaylik, Y. V.; Akridge, J. R., *J. Electrochem. Soc.* **2004,** *151*, A1969.

35. Mikhaylik, Y. V.; Akridge, J. R., Polysulfide Shuttle Study in the Li/S Battery System. *Journal of The Electrochemical Society* **2004,** *151* (11), A1969-A1976.

36. Su, Y. S.; Fu, Y.; Guo, B.; Dai, S.; Manthiram, A., Fast, Reversible Lithium Storage with a Sulfur/Long-Chain-Polysulfide Redox Couple. *Chemistry – A European Journal* **2013,** *19* (26), 8621-8626.

37. Peled, E.; Sternberg, Y.; Gorenshtein, A.; Lavi, Y., Lithium-Sulfur Battery: Evaluation of Dioxolane-Based Electrolytes. *Journal of The Electrochemical Society* **1989,** *136* (6), 1621-1625.

38. Rauh, R. D.; Abraham, K. M.; Pearson, G. F.; Surprenant, J. K.; Brummer, S. B., A Lithium/Dissolved Sulfur Battery with an Organic Electrolyte. *Journal of The Electrochemical Society* **1979,** *126* (4), 523-527.

39. Shim, J.; Striebel, K. A.; Cairns, E. J., The Lithium/Sulfur Rechargeable Cell: Effects of Electrode Composition and Solvent on Cell Performance. *Journal of The Electrochemical Society* **2002,** *149* (10), A1321-A1325.

40. Wang, J. L.; Yang, J.; Xie, J. Y.; Xu, N. X.; Li, Y., Sulfur–carbon nano-composite as cathode for rechargeable lithium battery based on gel electrolyte. *Electrochemistry Communications* **2002,** *4* (6), 499-502.

41. Wang, J.; Yang, J.; Xie, J.; Xu, N., A Novel Conductive Polymer–Sulfur Composite Cathode Material for Rechargeable Lithium Batteries. *Advanced Materials* **2002,** *14* (13-14), 963-965.

42. Chen, S.-R.; Zhai, Y.-P.; Xu, G.-L.; Jiang, Y.-X.; Zhao, D.-Y.; Li, J.-T.; Huang, L.; Sun, S.-G., Ordered mesoporous carbon/sulfur nanocomposite of high performances as cathode for lithium–sulfur battery. *Electrochimica Acta* **2011,** *56* (26), 9549-9555.

43. Ding, B.; Yuan, C.; Shen, L.; Xu, G.; Nie, P.; Zhang, X., Encapsulating Sulfur into Hierarchically Ordered Porous Carbon as a High-Performance Cathode for Lithium–Sulfur Batteries. *Chemistry – A European Journal* **2013,** *19* (3), 1013-1019.

44. Li, D.; Han, F.; Wang, S.; Cheng, F.; Sun, Q.; Li, W.-C., High Sulfur Loading Cathodes Fabricated Using Peapodlike, Large Pore Volume Mesoporous Carbon for Lithium–Sulfur Battery. *ACS Applied Materials & Interfaces* **2013,** *5* (6), 2208-2213.

45. Wei, S.; Zhang, H.; Huang, Y.; Wang, W.; Xia, Y.; Yu, Z., Pig bone derived hierarchical porous carbon and its enhanced cycling performance of lithium-sulfur batteries. *Energy & Environmental Science* **2011,** *4* (3), 736-740.

46. Xi, K.; Cao, S.; Peng, X.; Ducati, C.; Vasant Kumar, R.; Cheetham, A. K., Carbon with hierarchical pores from carbonized metal-organic frameworks for lithium sulphur batteries. *Chemical Communications* **2013,** *49* (22), 2192-2194.

47. Schuster, J.; He, G.; Mandlmeier, B.; Yim, T.; Lee, K. T.; Bein, T.; Nazar, L. F., Spherical Ordered Mesoporous Carbon Nanoparticles with High Porosity for Lithium–Sulfur Batteries. *Angewandte Chemie International Edition* **2012,** *51* (15), 3591-3595.

48. Ji, X.; Lee, K. T.; Nazar, L. F., A highly ordered nanostructured carbon–sulphur cathode for lithium–sulphur batteries. *Nature Materials* **2009,** *8*, 500.

49. Liang, C.; Dudney, N. J.; Howe, J. Y., Hierarchically Structured Sulfur/Carbon Nanocomposite Material for High-Energy Lithium Battery. *Chemistry of Materials* **2009,** *21* (19), 4724-4730.

50. Li, L.; Jiang, Z.; Li, M.; Li, R.; Fang, T., Hierarchically structured PMMA fibers fabricated by electrospinning. *RSC Advances* **2014,** *4* (95), 52973-52985.

51. Kim, J.; Lee, D. J.; Jung, H. G.; Sun, Y. K.; Hassoun, J.; Scrosati, B., An Advanced Lithium-Sulfur Battery. *Advanced Functional Materials* **2013,** *23* (8), 1076-1080.

52. Shin, J. H.; Kim, K. W.; Ahn, H. J.; Ahn, J. H., Electrochemical properties and interfacial stability of (PEO)10LiCF3SO3–TinO2n−1 composite polymer electrolytes for lithium/sulfur battery. *Materials Science and Engineering: B* **2002,** *95* (2), 148-156.

53. Hassoun, J.; Scrosati, B., Moving to a Solid-State Configuration: A Valid Approach to Making Lithium-Sulfur Batteries Viable for Practical Applications. *Advanced Materials* **2010,** *22* (45), 5198-5201.

54. Liang, X.; Wen, Z.; Liu, Y.; Zhang, H.; Huang, L.; Jin, J., Highly dispersed sulfur in ordered mesoporous carbon sphere as a composite cathode for rechargeable polymer Li/S battery. *Journal of Power Sources* **2011,** *196* (7), 3655-3658.

55. Kanno, R.; Murayama , M., Lithium Ionic Conductor Thio-LISICON: The Li2 S - GeS2 - P 2 S 5 System. *Journal of The Electrochemical Society* **2001,** *148* (7), A742-A746.

56. Deng, Y.; Eames, C.; Fleutot, B.; David, R.; Chotard, J.-N.; Suard, E.; Masquelier, C.; Islam, M. S., Enhancing the Lithium Ion Conductivity in Lithium Superionic Conductor (LISICON) Solid Electrolytes through a Mixed Polyanion Effect. *ACS Applied Materials & Interfaces* **2017,** *9* (8), 7050-7058.

57. Hayashi, A.; Ohtomo, T.; Mizuno, F.; Tadanaga, K.; Tatsumisago, M., All-solid-state Li/S batteries with highly conductive glass–ceramic electrolytes. *Electrochemistry Communications* **2003,** *5* (8), 701-705.

58. Hakari, T.; Nagao, M.; Hayashi, A.; Tatsumisago, M., Preparation of composite electrode with Li2S–P2S5 glasses as active materials for all-solid-state lithium secondary batteries. *Solid State Ionics* **2014,** *262*, 147-150.

59. Hayashi, A.; Ohtsubo, R.; Ohtomo, T.; Mizuno, F.; Tatsumisago, M., All-solid-state rechargeable lithium batteries with Li2S as a positive electrode material. *Journal of Power Sources* **2008,** *183* (1), 422-426.

60. Nagao, M.; Hayashi, A.; Tatsumisago, M., High-capacity Li2S-nanocarbon composite electrode for all-solid-state rechargeable lithium batteries. *Journal of Materials Chemistry* **2012,** *22* (19), 10015-10020.

61. Kobayashi, T.; Imade, Y.; Shishihara, D.; Homma, K.; Nagao, M.; Watanabe, R.; Yokoi, T.; Yamada, A.; Kanno, R.; Tatsumi, T., All solid-state battery with sulfur electrode and thio-LISICON electrolyte. *Journal of Power Sources* **2008,** *182* (2), 621-625.

62. Yersak, T. A.; Son, S.-B.; Cho, J. S.; Suh, S.-S.; Kim, Y.-U.; Moon, J.-T.; Oh, K. H.; Lee, S.-H., An All-Solid-State Li-Ion Battery with a Pre-Lithiated Si-Ti-Ni Alloy Anode. *Journal of The Electrochemical Society* **2013,** *160* (9), A1497-A1501.

63. Lin, Z.; Liu, Z.; Fu, W.; Dudney, N. J.; Liang, C., Lithium Polysulfidophosphates: A Family of Lithium-Conducting Sulfur-Rich Compounds for Lithium–Sulfur Batteries. *Angewandte Chemie International Edition* **2013,** *52* (29), 7460-7463.

64. Kamaya, N.; Homma, K.; Yamakawa, Y.; Hirayama, M.; Kanno, R.; Yonemura, M.; Kamiyama, T.; Kato, Y.; Hama, S.; Kawamoto, K., A Lithium Superionic Conductor. *Nat. Mater.* **2011,** *10*, 682.

65. Jin, Z.; Xie, K.; Hong, X.; Hu, Z.; Liu, X., Application of lithiated Nafion ionomer film as functional separator for lithium sulfur cells. *Journal of Power Sources* **2012,** *218*, 163-167.

66. Jin, Z.; Xie, K.; Hong, X., Electrochemical performance of lithium/sulfur batteries using perfluorinated ionomer electrolyte with lithium sulfonyl dicyanomethide functional groups as functional separator. *RSC Advances* **2013,** *3* (23), 8889-8898.

67. Gorkovenko, A.; Skotheim, T. A.; Xu, Z.-S., Cathodes comprising electroactive sulfur materials and secondary batteries using same. Google Patents: 2005.

68. Song, M.-S.; Han, S.-C.; Kim, H.-S.; Kim, J.-H.; Kim, K.-T.; Kang, Y.-M.; Ahn, H.-J.; Dou, S. X.; Lee, J.-Y., Effects of Nanosized Adsorbing Material on Electrochemical Properties of Sulfur Cathodes for Li/S Secondary Batteries. *Journal of The Electrochemical Society* **2004,** *151* (6), A791-A795.

69. Evers, S.; Yim, T.; Nazar, L. F., Understanding the Nature of Absorption/Adsorption in Nanoporous Polysulfide Sorbents for the Li–S Battery. *The Journal of Physical Chemistry C* **2012,** *116* (37), 19653-19658.

70. Choi, Y.; Jung, B.; Lee, D.; Jeong, J.; Kim, K.; Ahn, H.; Cho, K.; Gu, H., Electrochemical properties of sulfur electrode containing nano Al2O3 for lithium/sulfur cell. *Physica Scripta* **2007,** *2007* (T129), 62.

71. Ji, X.; Evers, S.; Black, R.; Nazar, L. F., Stabilizing lithium–sulphur cathodes using polysulphide reservoirs. *Nature communications* **2011,** *2*, 325.

72. Wei Seh, Z.; Li, W.; Cha, J. J.; Zheng, G.; Yang, Y.; McDowell, M. T.; Hsu, P.-C.; Cui, Y., Sulphur–TiO2 yolk–shell nanoarchitecture with internal void space for long-cycle lithium–sulphur batteries. *Nature Communications* **2013,** *4*, 1331.

73. Marca, M. D., Battery Cathodes. In *Batteries for Sustainability*, Springer: 2013.

74. Nazar, L. F.; Cuisinier, M.; Pang, Q., Lithium-sulfur batteries. *MRS Bulletin* **2014,** *39* (05), 436-442.

75. Yang, Y.; Zheng, G.; Cui, Y., Nanostructured sulfur cathodes. *Chemical Society Reviews* **2013,** *42* (7), 3018-3032.

76. Bruce, P. G.; Freunberger, S. A.; Hardwick, L. J.; Tarascon, J.-M., Li-O-2 and Li-S batteries with high energy storage. *Nature Materials* **2012,** *11* (1), 19-29.

77. Cabana, J.; Monconduit, L.; Larcher, D.; Rosa Palacin, M., Beyond Intercalation-Based Li-Ion Batteries: The State of the Art and Challenges of Electrode Materials Reacting Through Conversion Reactions. *Advanced Materials* **2010,** *22* (35), E170-E192.

78. Scrosati, B.; Garche, J., Lithium batteries: Status, prospects and future. *Journal of Power Sources* **2010,** *195* (9), 2419-2430.

79. Jeddi, K.; Sarikhani, K.; Qazvini, N. T.; Chen, P., Stabilizing lithium/sulfur batteries by a composite polymer electrolyte containing mesoporous silica particles. *Journal of Power Sources* **2014,** *245*, 656-662.

80. Liang, X.; Hart, C.; Pang, Q.; Garsuch, A.; Weiss, T.; Nazar, L. F., A highly efficient polysulfide mediator for lithium–sulfur batteries. *Nat Commun* **2015,** *6*.

81. Lin, C.-N.; Chen, W.-C.; Song, Y.-F.; Wang, C.-C.; Tsai, L.-D.; Wu, N.-L., Understanding dynamics of polysulfide dissolution and re-deposition in working lithium–sulfur battery by in-operando transmission X-ray microscopy. *Journal of Power Sources* **2014,** *263*, 98-103.

82. Vijayakumar, M.; Govind, N.; Walter, E.; Burton, S. D.; Shukla, A.; Devaraj, A.; Xiao, J.; Liu, J.; Wang, C.; Karim, A.; Thevuthasan, S., Molecular structure and stability of dissolved lithium polysulfide species. *Physical Chemistry Chemical Physics* **2014,** *16* (22), 10923-10932.

83. Wujcik, K. H.; Pascal, T. A.; Pemmaraju, C.; Devaux, D.; Stolte, W. C.; Balsara, N. P.; Prendergast, D., Characterization of Polysulfide Radicals Present in an Ether-Based Electrolyte of a Lithium–Sulfur Battery During Initial Discharge Using In Situ X-Ray Absorption Spectroscopy Experiments and First-Principles Calculations. *Advanced Energy Materials* **2015,** *5* (16).

84. Pascal, T. A.; Wujcik, K. H.; Velasco-Velez, J.; Wu, C.; Teran, A. A.; Kapilashrami, M.; Cabana, J.; Guo, J.; Salmeron, M.; Balsara, N., X-ray absorption spectra of dissolved polysulfides in lithium–sulfur batteries from first-principles. *The Journal of Physical Chemistry Letters* **2014,** *5* (9), 1547-1551.

85. Wujcik, K. H.; Velasco-Velez, J.; Wu, C. H.; Pascal, T.; Teran, A. A.; Marcus, M. A.; Cabana, J.; Guo, J.; Prendergast, D.; Salmeron, M., Fingerprinting Lithium-Sulfur Battery Reaction Products by X-ray Absorption Spectroscopy. *Journal of the Electrochemical Society* **2014,** *161* (6), A1100-A1106.

86. Xiao, J.; Hu, J. Z.; Chen, H.; Vijayakumar, M.; Zheng, J.; Pan, H.; Walter, E. D.; Hu, M.; Deng, X.; Feng, J.; Liaw, B. Y.; Gu, M.; Deng, Z. D.; Lu, D.; Xu, S.; Wang, C.; Liu, J., Following the Transient Reactions in Lithium–Sulfur Batteries Using an In Situ Nuclear Magnetic Resonance Technique. *Nano Letters* **2015,** *15* (5), 3309-3316.

87. Ahn, W.; Kim, K.-B.; Jung, K.-N.; Shin, K.-H.; Jin, C.-S., Synthesis and electrochemical properties of a sulfur-multi walled carbon nanotubes composite as a cathode material for lithium sulfur batteries. *Journal of Power Sources* **2012,** *202*, 394-399.

88. Chen, R.; Zhao, T.; Tian, T.; Cao, S.; Coxon, P. R.; Xi, K.; Fairen-Jimenez, D.; Vasant Kumar, R.; Cheetham, A. K., Graphene-wrapped sulfur/metal organic framework-derived microporous carbon composite for lithium sulfur batteries. *APL Materials* **2014,** *2* (12), 124109.

89. Duan, X.; Han, Y.; Huang, L.; Li, Y.; Chen, Y., Improved rate ability of low cost sulfur cathodes by using ultrathin graphite sheets with self-wrapped function as cheap conductive agent. *Journal of Materials Chemistry A* **2015,** *3* (15), 8015-8021.

90. Jeddi, K.; Zhao, Y.; Zhang, Y.; Konarov, A.; Chen, P., Fabrication and Characterization of an Effective Polymer Nanocomposite Electrolyte Membrane for High Performance Lithium/Sulfur Batteries. *Journal of The Electrochemical Society* **2013,** *160* (8), A1052-A1060.

91. Jia-jia, C.; Xin, J.; Qiu-jie, S.; Chong, W.; Qian, Z.; Ming-sen, Z.; Quan-feng, D., The preparation of nano-sulfur/MWCNTs and its electrochemical performance. *Electrochimica Acta* **2010,** *55* (27), 8062-8066.

92. Ji, X.; Lee, K. T.; Nazar, L. F., A highly ordered nanostructured carbon-sulphur cathode for lithium-sulphur batteries. *Nature Materials* **2009,** *8* (6), 500-506.

93. Liang, X.; Wen, Z.; Liu, Y.; Zhang, H.; Jin, J.; Wu, M.; Wu, X., A composite of sulfur and polypyrrole–multi walled carbon combinatorial nanotube as cathode for Li/S battery. *Journal of Power Sources* **2012,** *206* (0), 409-413.

94. Wang, J.; Lu, L.; Shi, D.; Tandiono, R.; Wang, Z.; Konstantinov, K.; Liu, H., A Conductive Polypyrrole-Coated, Sulfur–Carbon Nanotube Composite for Use in Lithium–Sulfur Batteries. *ChemPlusChem* **2013,** *78* (4), 318-324.

95. Zheng, G.; Zhang, Q.; Cha, J. J.; Yang, Y.; Li, W.; Seh, Z. W.; Cui, Y., Amphiphilic Surface Modification of Hollow Carbon Nanofibers for Improved Cycle Life of Lithium Sulfur Batteries. *Nano Letters* **2013,** *13* (3), 1265-1270.

96. Park, Y.; Shin, D. S.; Woo, S. H.; Choi, N. S.; Shin, K. H.; Oh, S. M.; Lee, K. T.; Hong, S. Y., Sodium terephthalate as an organic anode material for sodium ion batteries. *Advanced Materials* **2012,** *24* (26), 3562-3567.

97. Evers, S.; Nazar, L. F., New Approaches for High Energy Density Lithium–Sulfur Battery Cathodes. *Accounts of Chemical Research* **2012,** *46* (5), 1135-1143.

98. Wang, C.; Su, K.; Wan, W.; Guo, H.; Zhou, H.; Chen, J.; Zhang, X.; Huang, Y., High sulfur loading composite wrapped by 3D nitrogen-doped graphene as a cathode material for lithium–sulfur batteries. *Journal of Materials Chemistry A* **2014,** *2* (14), 5018-5023.

99. Li, W.; Zheng, G.; Yang, Y.; Seh, Z. W.; Liu, N.; Cui, Y., High-performance hollow sulfur nanostructured battery cathode through a scalable, room temperature, one-step, bottom-up approach. *Proceedings of the National Academy of Sciences* **2013,** *110* (18), 7148-7153.

100. Huang, J.-Q.; Zhang, Q.; Peng, H.-J.; Liu, X.-Y.; Qian, W.-Z.; Wei, F., Ionic shield for polysulfides towards highly-stable lithium-sulfur batteries. *Energy & Environmental Science* **2014,** *7* (1), 347-353.

101. Xu, C.; Wu, Y.; Zhao, X.; Wang, X.; Du, G.; Zhang, J.; Tu, J., Sulfur/three-dimensional graphene composite for high performance lithium–sulfur batteries. *Journal of Power Sources* **2015,** *275*, 22-25.

102. Li, B.; Li, S.; Liu, J.; Wang, B.; Yang, S., Vertically Aligned Sulfur–Graphene Nanowalls on Substrates for Ultrafast Lithium–Sulfur Batteries. *Nano Letters* **2015,** *15* (5), 3073-3079.

103. Lu, S.; Chen, Y.; Wu, X.; Wang, Z.; Li, Y., Three-dimensional sulfur/graphene multifunctional hybrid sponges for lithium-sulfur batteries with large areal mass loading. *Scientific reports* **2014,** *4*.

104. Jeong, S. S.; Lim, Y. T.; Choi, Y. J.; Cho, G. B.; Kim, K. W.; Ahn, H. J.; Cho, K. K., Electrochemical properties of lithium sulfur cells using PEO polymer electrolytes prepared under three different mixing conditions. *Journal of Power Sources* **2007,** *174* (2), 745-750.

105. Zhang, S. S.; Tran, D. T., A simple approach for superior performance of lithium/sulphur batteries modified with a gel polymer electrolyte. *Journal of Materials Chemistry A* **2014,** *2* (20), 7383-7388.

106. Zhao, Y.; Zhang, Y.; Gosselink, D.; Doan, T. N. L.; Sadhu, M.; Cheang, H.-J.; Chen, P., Polymer Electrolytes for Lithium/Sulfur Batteries. *Membranes* **2012,** *2* (3), 553-564.

107. Zhou, G.; Li, L.; Wang, D. W.; Shan, X. y.; Pei, S.; Li, F.; Cheng, H. M., A Flexible Sulfur-Graphene-Polypropylene Separator Integrated Electrode for Advanced Li–S Batteries. *Advanced Materials* **2015,** *27* (4), 641-647.

108. Yao, H.; Yan, K.; Li, W.; Zheng, G.; Kong, D.; Seh, Z. W.; Narasimhan, V. K.; Liang, Z.; Cui, Y., Improved lithium–sulfur batteries with a conductive coating on the separator to prevent the accumulation of inactive S-related species at the cathode–separator interface. *Energy & Environmental Science* **2014,** *7* (10), 3381-3390.

109. Chang, C.-H.; Chung, S.-H.; Manthiram, A., Ultra-lightweight PANiNF/MWCNT-functionalized separators with synergistic suppression of polysulfide migration for Li–S batteries with pure sulfur cathodes. *Journal of Materials Chemistry A* **2015,** *3* (37), 18829-18834.

110. Bauer, I.; Thieme, S.; Brückner, J.; Althues, H.; Kaskel, S., Reduced polysulfide shuttle in lithium–sulfur batteries using Nafion-based separators. *Journal of Power Sources* **2014,** *251*, 417-422.

111. Chung, S. H.; Manthiram, A., Bifunctional Separator with a Light-Weight Carbon-Coating for Dynamically and Statically Stable Lithium-Sulfur Batteries. *Advanced Functional Materials* **2014,** *24* (33), 5299-5306.

112. Zhang, Y.; Zhao, Y.; Bakenov, Z.; Gosselink, D.; Chen, P., Poly (vinylidene fluoride-co-hexafluoropropylene)/poly (methylmethacrylate)/nanoclay composite gel polymer

electrolyte for lithium/sulfur batteries. *Journal of Solid State Electrochemistry* **2014,** *18* (4), 1111-1116.

113. Agostini, M.; Hassoun, J., A lithium-ion sulfur battery using a polymer, polysulfide-added membrane. *Scientific reports* **2015,** *5*.

114. Lin, Z.; Liang, C., Lithium-sulfur batteries: from liquid to solid cells. *Journal of Materials Chemistry A* **2015,** *3* (3), 936-958.

115. Yu, X.; Bi, Z.; Zhao, F.; Manthiram, A., Hybrid Lithium–Sulfur Batteries with a Solid Electrolyte Membrane and Lithium Polysulfide Catholyte. *ACS Applied Materials & Interfaces* **2015,** *7* (30), 16625-16631.

116. Su, Y.-S.; Manthiram, A., Lithium–sulphur batteries with a microporous carbon paper as a bifunctional interlayer. *Nat Commun* **2012,** *3*, 1166.

117. Wang, D.-W.; Zeng, Q.; Zhou, G.; Yin, L.; Li, F.; Cheng, H.-M.; Gentle, I. R.; Lu, G. Q. M., Carbon-sulfur composites for Li-S batteries: status and prospects. *Journal of Materials Chemistry A* **2013,** *1* (33), 9382-9394.

118. Wang, H.; Yang, Y.; Liang, Y.; Robinson, J. T.; Li, Y.; Jackson, A.; Cui, Y.; Dai, H., Graphene-Wrapped Sulfur Particles as a Rechargeable Lithium–Sulfur Battery Cathode Material with High Capacity and Cycling Stability. *Nano Letters* **2011,** *11* (7), 2644-2647.

119. Xin, S.; Gu, L.; Zhao, N.-H.; Yin, Y.-X.; Zhou, L.-J.; Guo, Y.-G.; Wan, L.-J., Smaller Sulfur Molecules Promise Better Lithium–Sulfur Batteries. *Journal of the American Chemical Society* **2012,** *134* (45), 18510-18513.

120. Qiu, L.; Zhang, S.; Zhang, L.; Sun, M.; Wang, W., Preparation and enhanced electrochemical properties of nano-sulfur/poly(pyrrole-co-aniline) cathode material for lithium/sulfur batteries. *Electrochimica Acta* **2010,** *55* (15), 4632-4636.

121. Zhang, Y.; Zhao, Y.; Konarov, A.; Gosselink, D.; Soboleski, H. G.; Chen, P., A novel nano-sulfur/polypyrrole/graphene nanocomposite cathode with a dual-layered structure for lithium rechargeable batteries. *Journal of Power Sources* **2013,** *241*, 517-521.

122. Tarascon, J. M.; Armand, M., Issues and challenges facing rechargeable lithium batteries. *Nature* **2001,** *414* (6861), 359-367.

123. Rao, M.; Geng, X.; Li, X.; Hu, S.; Li, W., Lithium-sulfur cell with combining carbon nanofibers–sulfur cathode and gel polymer electrolyte. *Journal of Power Sources* **2012,** *212* (0), 179-185.

124. Mo, Y.; Ong, S. P.; Ceder, G., First Principles Study of the Li10GeP2S12 Lithium Super Ionic Conductor Material. *Chemistry of Materials* **2012,** *24* (1), 15-17.

125. Rice, M. J.; Roth, W. L., Ionic transport in super ionic conductors: a theoretical model. *Journal of Solid State Chemistry* **1972,** *4* (2), 294-310.

126. Guo, J.; Xu, Y.; Wang, C., Sulfur-Impregnated Disordered Carbon Nanotubes Cathode for Lithium–Sulfur Batteries. *Nano Letters* **2011,** *11* (10), 4288-4294.

127. Jayaprakash, N.; Shen, J.; Moganty, S. S.; Corona, A.; Archer, L. A., Porous Hollow Carbon@Sulfur Composites for High-Power Lithium–Sulfur Batteries. *Angewandte Chemie* **2011,** *123* (26), 6026-6030.

128. Ji, X.; Lee, K. T.; Nazar, L. F., A highly ordered nanostructured carbon-sulphur cathode for lithium-sulphur batteries. *Nat Mater* **2009,** *8* (6), 500-506.

129. Zhang, C.; Wu, H. B.; Yuan, C.; Guo, Z.; Lou, X. W., Confining Sulfur in Double-Shelled Hollow Carbon Spheres for Lithium–Sulfur Batteries. *Angewandte Chemie* **2012,** *124* (38), 9730-9733.

130. Zheng, G.; Yang, Y.; Cha, J. J.; Hong, S. S.; Cui, Y., Hollow Carbon Nanofiber-Encapsulated Sulfur Cathodes for High Specific Capacity Rechargeable Lithium Batteries. *Nano Letters* **2011,** *11* (10), 4462-4467.

131. Wu, H. B.; Wei, S.; Zhang, L.; Xu, R.; Hng, H. H.; Lou, X. W., Embedding Sulfur in MOF-Derived Microporous Carbon Polyhedrons for Lithium–Sulfur Batteries. *Chemistry – A European Journal* **2013,** *19* (33), 10804-10808.

132. Park, J. H.; Choi, K. M.; Lee, D. K.; Moon, B. C.; Shin, S. R.; Song, M.-K.; Kang, J. K., Encapsulation of redox polysulphides via chemical interaction with nitrogen atoms in the organic linkers of metal-organic framework nanocrystals. *Scientific Reports* **2016,** *6*, 25555.

133. Wang, Z.; Wang, B.; Yang, Y.; Cui, Y.; Wang, Z.; Chen, B.; Qian, G., Mixed-metal–organic framework with effective lewis acidic sites for sulfur confinement in high-performance lithium–sulfur batteries. *ACS applied materials & interfaces* **2015,** *7* (37), 20999-21004.

134. Wang, Z.; Li, X.; Cui, Y.; Yang, Y.; Pan, H.; Wang, Z.; Wu, C.; Chen, B.; Qian, G., A Metal–Organic Framework with Open Metal Sites for Enhanced Confinement of Sulfur and Lithium–Sulfur Battery of Long Cycling Life. *Crystal Growth & Design* **2013,** *13* (11), 5116-5120.

135. Zhou, J.; Li, R.; Fan, X.; Chen, Y.; Han, R.; Li, W.; Zheng, J.; Wang, B.; Li, X., Rational design of a metal-organic framework host for sulfur storage in fast, long-cycle Li-S batteries. *Energy & Environmental Science* **2014,** *7* (8), 2715-2724.

136. Wang, Z.; Dong, Y.; Li, H.; Zhao, Z.; Bin Wu, H.; Hao, C.; Liu, S.; Qiu, J.; Lou, X. W., Enhancing lithium–sulphur battery performance by strongly binding the discharge products on amino-functionalized reduced graphene oxide. *Nat Commun* **2014,** *5*.

137. Zheng, J.; Tian, J.; Wu, D.; Gu, M.; Xu, W.; Wang, C.; Gao, F.; Engelhard, M. H.; Zhang, J.-G.; Liu, J.; Xiao, J., Lewis Acid–Base Interactions between Polysulfides and Metal Organic Framework in Lithium Sulfur Batteries. *Nano Letters* **2014,** *14* (5), 2345-2352.

138. Li, H.; Eddaoudi, M.; O'Keeffe, M.; Yaghi, O. M., Design and synthesis of an exceptionally stable and highly porous metal-organic framework. *Nature* **1999,** *402* (6759), 276-279.

139. Ji, X.; Nazar, L. F., Advances in Li-S batteries. *Journal of Materials Chemistry* **2010,** *20* (44), 9821-9826.

140. Miao, L.-X.; Wang, W.-K.; Wang, A.-B.; Yuan, K.-G.; Yang, Y.-S., A high sulfur content composite with core-shell structure as cathode material for Li-S batteries. *Journal of Materials Chemistry A* **2013,** *1* (38), 11659-11664.

141. Li, J.; Cheng, S.; Zhao, Q.; Long, P.; Dong, J., Synthesis and hydrogen-storage behavior of metal–organic framework MOF-5. *International Journal of Hydrogen Energy* **2009,** *34* (3), 1377-1382.

142. Tranchemontagne, D. J.; Hunt, J. R.; Yaghi, O. M., Room temperature synthesis of metal-organic frameworks: MOF-5, MOF-74, MOF-177, MOF-199, and IRMOF-0. *Tetrahedron* **2008,** *64* (36), 8553-8557.

143. Fujimori, T.; Morelos-Gómez, A.; Zhu, Z.; Muramatsu, H.; Futamura, R.; Urita, K.; Terrones, M.; Hayashi, T.; Endo, M.; Young Hong, S.; Chul Choi, Y.; Tománek, D.; Kaneko, K., Conducting linear chains of sulphur inside carbon nanotubes. *Nat Commun* **2013,** *4*.

144. Liu, Y.; Ng, Z.; Khan, E. A.; Jeong, H.-K.; Ching, C.-b.; Lai, Z., Synthesis of continuous MOF-5 membranes on porous α-alumina substrates. *Microporous and Mesoporous Materials* **2009,** *118* (1–3), 296-301.

145. Son, W.-J.; Kim, J.; Kim, J.; Ahn, W.-S., Sonochemical synthesis of MOF-5. *Chemical Communications* **2008,** (47), 6336-6338.

146. Zheng, C.; Greer, H. F.; Chiang, C.-Y.; Zhou, W., Microstructural study of the formation mechanism of metal-organic framework MOF-5. *CrystEngComm* **2014,** *16* (6), 1064-1070.

147. Chmelik, C.; Freude, D.; Bux, H.; Haase, J., Ethene/ethane mixture diffusion in the MOF sieve ZIF-8 studied by MAS PFG NMR diffusometry. *Microporous and Mesoporous Materials* **2012,** *147* (1), 135-141.

148. Zacharia, R.; Cossement, D.; Lafi, L.; Chahine, R., Volumetric hydrogen sorption capacity of monoliths prepared by mechanical densification of MOF-177. *Journal of Materials Chemistry* **2010,** *20* (11), 2145-2151.

149. Klementev, K. V., Extraction of the fine structure from x-ray absorption spectra. *Journal of Physics D: Applied Physics* **2001,** *34* (2), 209.

150. Guillerm, V.; Gross, S.; Serre, C.; Devic, T.; Bauer, M.; Ferey, G., A zirconium methacrylate oxocluster as precursor for the low-temperature synthesis of porous zirconium(iv) dicarboxylates. *Chemical Communications* **2010,** *46* (5), 767-769.

151. Rodriguez, N. A.; Parra, R.; Grela, M. A., Structural characterization, optical properties and photocatalytic activity of MOF-5 and its hydrolysis products: implications on their excitation mechanism. *RSC Advances* **2015,** *5* (89), 73112-73118.

152. Ming, Y.; Purewal, J.; Yang, J.; Xu, C.; Soltis, R.; Warner, J.; Veenstra, M.; Gaab, M.; Müller, U.; Siegel, D. J., Kinetic Stability of MOF-5 in Humid Environments: Impact of Powder Densification, Humidity Level, and Exposure Time. *Langmuir* **2015,** *31* (17), 4988-4995.

153. Ren, J.; Rogers, D. E. C.; Segakweng, T.; Langmi, H. W.; North, B. C.; Mathe, M.; Bessarabov, D., Thermal treatment induced transition from Zn3(OH)2(BDC)2 (MOF-69c) to Zn4O(BDC)3 (MOF-5). *International Journal of Materials Research* **2013,** *105* (1), 89-93.

154. Ravon, U.; Domine, M. E.; Gaudillere, C.; Desmartin-Chomel, A.; Farrusseng, D., MOFs as acid catalysts with shape selectivity properties. *New Journal of Chemistry* **2008,** *32* (6), 937-940.

155. First, E. L.; Floudas, C. A., MOFomics: Computational pore characterization of metal–organic frameworks. *Microporous and Mesoporous Materials* **2013,** *165*, 32-39.

156. Gadipelli, S.; Guo, Z., Postsynthesis Annealing of MOF-5 Remarkably Enhances the Framework Structural Stability and CO2 Uptake. *Chemistry of Materials* **2014,** *26* (22), 6333-6338.

157. Liu, B.; Wong-Foy, A. G.; Matzger, A. J., Rapid and enhanced activation of microporous coordination polymers by flowing supercritical CO2. *Chemical Communications* **2013,** *49* (14), 1419-1421.

158. Wu, C.-M.; Rathi, M.; Ahrenkiel, S. P.; Koodali, R. T.; Wang, Z., Facile synthesis of MOF-5 confined in SBA-15 hybrid material with enhanced hydrostability. *Chemical Communications* **2013,** *49* (12), 1223-1225.

159. Yu, X.-R.; Liu, F.; Wang, Z.-Y.; Chen, Y., Auger parameters for sulfur-containing compounds using a mixed aluminum-silver excitation source. *Journal of Electron Spectroscopy and Related Phenomena* **1990,** *50* (2), 159-166.

160. Hollinger, G.; Kumurdjian, P.; Mackowski, J. M.; Pertosa, P.; Porte, L.; Duc, T. M., ESCA study of molecular GeS3-x Tex As2 glasses. *Journal of Electron Spectroscopy and Related Phenomena* **1974,** *5* (1), 237-245.

161. Thomas, J. M.; Adams, I.; Williams, R. H.; Barber, M., Valence band structures and core-electron energy levels in the monochalcogenides of gallium. Photoelectron spectroscopic study. *Journal of the Chemical Society, Faraday Transactions 2: Molecular and Chemical Physics* **1972,** *68* (0), 755-764.

162. Chehimi, M. M.; Delamar, M., X-ray photoelectron spectroscopy of merocyanine dyes. *Journal of Electron Spectroscopy and Related Phenomena* **1990,** *50* (2), C25-C32.

163. Morris, R. E.; Wheatley, P. S., Gas Storage in Nanoporous Materials. *Angewandte Chemie International Edition* **2008,** *47* (27), 4966-4981.

164. Rosi, N. L.; Eckert, J.; Eddaoudi, M.; Vodak, D. T.; Kim, J.; O'Keeffe, M.; Yaghi, O. M., Hydrogen Storage in Microporous Metal-Organic Frameworks. *Science* **2003,** *300* (5622), 1127-1129.

165. Perez, E. V.; Balkus Jr, K. J.; Ferraris, J. P.; Musselman, I. H., Mixed-matrix membranes containing MOF-5 for gas separations. *Journal of Membrane Science* **2009,** *328* (1–2), 165-173.

166. Ma, S.; Zhou, H.-C., Gas storage in porous metal-organic frameworks for clean energy applications. *Chemical Communications* **2010,** *46* (1), 44-53.

167. Zhang, L.; Huang, H.; Yin, H.; Xia, Y.; Luo, J.; Liang, C.; Gan, Y.; Tao, X.; Zhang, W., Sulfur synchronously electrodeposited onto exfoliated graphene sheets as a cathode material for advanced lithium-sulfur batteries. *Journal of Materials Chemistry A* **2015,** *3* (32), 16513-16519.

168. Munch, A. S.; Mertens, F. O. R. L., The Lewis acidic and basic character of the internal HKUST-1 surface determined by inverse gas chromatography. *CrystEngComm* **2015,** *17* (2), 438-447.

169. Akimbekov, Z.; Wu, D.; Brozek, C. K.; Dinca, M.; Navrotsky, A., Thermodynamics of solvent interaction with the metal-organic framework MOF-5. *Physical Chemistry Chemical Physics* **2016,** *18* (2), 1158-1162.

170. Lindberg, B. J.; Hamrin, K.; Johansson, G.; Gelius, U.; Fahlman, A.; Nordling, C.; Siegbahn, K., Molecular Spectroscopy by Means of ESCA II. Sulfur compounds. Correlation of electron binding energy with structure. *Physica Scripta* **1970,** *1* (5-6), 286.

171. Zu, C.; Fu, Y.; Manthiram, A., Highly reversible Li/dissolved polysulfide batteries with binder-free carbon nanofiber electrodes. *Journal of Materials Chemistry A* **2013,** *1* (35), 10362-10367.

172. Su, Y.-S.; Fu, Y.; Cochell, T.; Manthiram, A., A strategic approach to recharging lithium-sulphur batteries for long cycle life. *Nat Commun* **2013,** *4*.

173. Zu, C.; Azimi, N.; Zhang, Z.; Manthiram, A., Insight into lithium-metal anodes in lithium-sulfur batteries with a fluorinated ether electrolyte. *Journal of Materials Chemistry A* **2015,** *3* (28), 14864-14870.

174. Dapoz, S.; Betz, N.; Guittet, M.-J.; Le Moël, A., ESCA characterization of heparin-like fluoropolymers obtained by functionalization after grafting induced by swift heavy ion irradiation. *Nuclear Instruments and Methods in Physics Research Section B: Beam Interactions with Materials and Atoms* **1995,** *105* (1–4), 120-125.

175. Riga, J.; Snauwaert, P.; De Pryck, A.; Lazzaroni, R.; Boutique, J. P.; Verbist, J. J.; Brédas, J. L.; André, J. M.; Taliani, C., Electronic structure of sulphur-containing conducting polymers. *Synthetic Metals* **1987,** *21* (1), 223-228.

176. Huntley, D. R., The mechanism of the desulfurization of benzenethiol by nickel (110). *The Journal of Physical Chemistry* **1992,** *96* (11), 4550-4558.

177. Cavanagh, A. S.; Lee, Y.; Yoon, B.; George, S., Atomic Layer Deposition of LiOH and Li2CO3 Using Lithium t-Butoxide as the Lithium Source. *ECS Transactions* **2010,** *33* (2), 223-229.

178. Rao, M.; Li, W.; Cairns, E. J., Porous carbon-sulfur composite cathode for lithium/sulfur cells. *Electrochemistry Communications* **2012,** *17*, 1-5.

179. Gobeltz, N.; Demortier, A.; Lelieur, J. P.; Duhayon, C., Identification of the Products of the Reaction between Sulfur and Sodium Carbonate. *Inorganic Chemistry* **1998,** *37* (1), 136-138.

180. Yim, T.; Park, M.-S.; Yu, J.-S.; Kim, K. J.; Im, K. Y.; Kim, J.-H.; Jeong, G.; Jo, Y. N.; Woo, S.-G.; Kang, K. S.; Lee, I.; Kim, Y.-J., Effect of chemical reactivity of polysulfide toward carbonate-based electrolyte on the electrochemical performance of Li–S batteries. *Electrochimica Acta* **2013,** *107*, 454-460.

181. Gardella, J. A.; Ferguson, S. A.; Chin, R. L., $\pi^* \leftarrow \pi$ Shakeup Satellites for the Analysis of Structure and Bonding in Aromatic Polymers by X-Ray Photoelectron Spectroscopy. *Appl. Spectrosc.* **1986,** *40* (2), 224-232.

182. Abraham, K. M.; Chaudhri, S. M., The Lithium Surface Film in the Li / SO 2 Cell. *Journal of The Electrochemical Society* **1986,** *133* (7), 1307-1311.

183. Strohmeier, B. R.; Hercules, D. M., Surface spectroscopic characterization of the interaction between zinc ions and γ-alumina. *Journal of Catalysis* **1984,** *86* (2), 266-279.

184. Nefedov, V. I., A comparison of results of an ESCA study of nonconducting solids using spectrometers of different constructions. *Journal of Electron Spectroscopy and Related Phenomena* **1982,** *25* (1), 29-47.

185. Gao, J.; Lowe, M. A.; Kiya, Y.; Abruña, H. D., Effects of Liquid Electrolytes on the Charge–Discharge Performance of Rechargeable Lithium/Sulfur Batteries:

Electrochemical and in-Situ X-ray Absorption Spectroscopic Studies. *The Journal of Physical Chemistry C* **2011,** *115* (50), 25132-25137.

186. Hu, Z.; Zhang, K.; Zhu, Z.; Tao, Z.; Chen, J., FeS2 microspheres with an ether-based electrolyte for high-performance rechargeable lithium batteries. *Journal of Materials Chemistry A* **2015,** *3* (24), 12898-12904.

187. Song, M.-K.; Zhang, Y.; Cairns, E. J., A Long-Life, High-Rate Lithium/Sulfur Cell: A Multifaceted Approach to Enhancing Cell Performance. *Nano Letters* **2013,** *13* (12), 5891-5899.

188. Ehsani, M.; Gao, Y.; Longo, S.; Ebrahimi, K., *Modern electric, hybrid electric, and fuel cell vehicles*. CRC press: 2018.

189. Zhang, L.; Hu, X.; Wang, Z.; Sun, F.; Deng, J.; Dorrell, D. G., Multiobjective optimal sizing of hybrid energy storage system for electric vehicles. *IEEE Transactions on Vehicular Technology* **2018,** *67* (2), 1027-1035.

190. Nitta, N.; Wu, F.; Lee, J. T.; Yushin, G., Li-ion battery materials: present and future. *Materials Today* **2015,** *18* (5), 252-264.

191. Manthiram, A.; Chung, S. H.; Zu, C., Lithium–sulfur batteries: progress and prospects. *Advanced materials* **2015,** *27* (12), 1980-2006.

192. Manthiram, A.; Chung, S. H.; Zu, C., Lithium–Sulfur Batteries: Progress and Prospects. *Adv. Mater.* **2015,** *27*, 1980.

193. Hofer, U., New diversity in the sulfur cycle. *Nature Reviews Microbiology* **2018,** *16*, 260.

194. Fang, R.; Zhao, S.; Sun, Z.; Wang, D. W.; Cheng, H. M.; Li, F., More Reliable Lithium-Sulfur Batteries: Status, Solutions and Prospects. *Adv. Mater.* **2017,** *29*, 1606823.

195. Yin, Y. X.; Xin, S.; Guo, Y. G.; Wan, L. J., Lithium–sulfur batteries: electrochemistry, materials, and prospects. *Angewandte Chemie International Edition* **2013,** *52* (50), 13186-13200.

196. Wang, L.; Liu, J.; Yuan, S.; Wang, Y.; Xia, Y., To mitigate self-discharge of lithium-sulfur batteries by optimizing ionic liquid electrolytes. *Energy & Environmental Science* **2016,** *9* (1), 224-231.

197. Edeling, M.; Schmutzler, R. W.; Hensel, F., The electrical conductivity of liquid sulphur. *Philosophical Magazine Part B* **1979,** *39* (6), 547-550.

198. Seh, Z. W.; Sun, Y.; Zhang, Q.; Cui, Y., Designing High-Energy Lithium-Sulfur Batteries. *Chem. Soc. Rev.* **2016,** *45*, 5605.

199. Ding, N.; Zhou, L.; Zhou, C.; Geng, D.; Yang, J.; Chien, S. W.; Liu, Z.; Ng, M. F.; Yu, A.; Hor, T. S. A., Building Better Lithium-Sulfur Batteries: From LiNO3 to Solid Oxide Catalyst. *Sci. Rep.* **2016,** *6*, 33154.

200. Ming, L.; Qing, L.; Xianying, Q.; Gemeng, L.; Wenjie, H.; Dong, Z.; Yan-Bing, H.; Baohua, L.; Feiyu, K., Suppressing Self-Discharge and Shuttle Effect of Lithium–Sulfur Batteries with V2O5-Decorated Carbon Nanofiber Interlayer. *Small* **2017,** *13* (12), 1602539.

201. Fu, Y.; Su, Y. S.; Manthiram, A., Highly Reversible Lithium/Dissolved Polysulfide Batteries with Carbon Nanotube Electrodes. *Angew. Chem., Int. Ed.* **2013,** *52*, 6930.

202. Zheng, J.; Gu, M.; Chen, H.; Meduri, P.; Engelhard, M. H.; Zhang, J.-G.; Liu, J.; Xiao, J., Ionic liquid-enhanced solid state electrolyte interface (SEI) for lithium-sulfur batteries. *Journal of Materials Chemistry A* **2013,** *1* (29), 8464-8470.

203. Bucur, C. B.; Muldoon, J.; Lita, A., A layer-by-layer supramolecular structure for a sulfur cathode. *Energy & Environmental Science* **2016,** *9* (3), 992-998.

204. Zhou, G.; Paek, E.; Hwang, G. S.; Manthiram, A., Long-life Li/polysulphide batteries with high sulphur loading enabled by lightweight three-dimensional nitrogen/sulphur-codoped graphene sponge. *Nature Communications* **2015,** *6*, 7760.

205. Liang, X.; Rangom, Y.; Kwok, C. Y.; Pang, Q.; Nazar, L. F., Interwoven Mxene Nanosheet/Carbon-Nanotube Composites as Li–S Cathode Hosts. *Adv. Mater.* **2017,** *29*, 1603040.

206. Liu, S.; Li, G. R.; Gao, X. P., Lanthanum Nitrate as Electrolyte Additive to Stabilize the Surface Morphology of Lithium Anode for Lithium–Sulfur Battery. *ACS Appl. Mater. Interfaces* **2016,** *8*, 7783.

207. Cheng, X. B.; Yan, C.; Huang, J. Q.; Li, P.; Zhu, L.; Zhao, L.; Zhang, Y.; Zhu, W.; Yang, S. T.; Zhang, Q., The Gap between Long Lifespan Li-S Coin and Pouch Cells: The Importance of Lithium Metal Anode Protection. *Energy Storage Mater.* **2017,** *6*, 18.

208. Peng, H. J.; Xu, W. T.; Zhu, L.; Wang, D. W.; Huang, J. Q.; Cheng, X. B.; Yuan, Z.; Wei, F.; Zhang, Q., 3D Carbonaceous Current Collectors: The Origin of Enhanced Cycling Stability for High-Sulfur-Loading Lithium–Sulfur Batteries. *Adv. Funct. Mater.* **2016,** *26*, 6351.

209. Li, Q.; Zhu, S.; Lu, Y., 3D Porous Cu Current Collector/Li-Metal Composite Anode for Stable Lithium-Metal Batteries. *Adv. Funct. Mater.* **2017,** *27*, 1606422.

210. Rao, M.; Geng, X.; Li, X.; Hu, S.; Li, W., Lithium-sulfur cell with combining carbon nanofibers–sulfur cathode and gel polymer electrolyte. *Journal of Power Sources* **2012,** *212*, 179-185.

211. Liu, M.; Zhou, D.; He, Y.-B.; Fu, Y.; Qin, X.; Miao, C.; Du, H.; Li, B.; Yang, Q.-H.; Lin, Z.; Zhao, T. S.; Kang, F., Novel gel polymer electrolyte for high-performance lithium–sulfur batteries. *Nano Energy* **2016,** *22*, 278-289.

212. Murata, K.; Izuchi, S.; Yoshihisa, Y., An overview of the research and development of solid polymer electrolyte batteries. *Electrochimica Acta* **2000,** *45* (8–9), 1501-1508.

213. Guo, Q.; Han, Y.; Wang, H.; Hong, X.; Zheng, C.; Liu, S.; Xie, K., Safer Lithium Metal Battery based on Advanced Ionic Liquid Gel Polymer Nonflammable Electrolytes. *RSC Adv.* **2016,** *6*, 101638.

214. Hong, X.-J.; Tan, T.-X.; Guo, Y.-K.; Tang, X.-Y.; Wang, J.-Y.; Qin, W.; Cai, Y.-P., Confinement of polysulfides within bi-functional metal-organic frameworks for high performance lithium-sulfur batteries. *Nanoscale* **2018,** *10* (6), 2774-2780.

215. Zhang, X.; Wang, W.; Wang, A.; Huang, Y.; Yuan, K.; Yu, Z.; Qiu, J.; Yang, Y., Improved Cycle Stability and High Security of Li-B Alloy Anode for Lithium-Sulfur Battery. *J. Mater. Chem. A* **2014,** *2*, 11660.

216. Huang, J. Q.; Zhang, Q.; Peng, H. J.; Liu, X. Y.; Qian, W. Z.; Wei, F., Ionic Shield for Polysulfides Towards Highly-Stable Lithium-Sulfur Batteries. *Energy Environ. Sci.* **2014,** *7*, 347.

217. Ma, G.; Wen, Z.; Wu, M.; Shen, C.; Wang, Q.; Jin, J.; Wu, X., A Lithium Anode Protection Guided Highly-Stable Lithium-Sulfur Battery. *Chem. Commun.* **2014,** *50*, 14209.

218. Kim, J. S.; Hwang, T. H.; Kim, B. G.; Min, J.; Choi, J. W., A Lithium-Sulfur Battery with a High Areal Energy Density. *Adv. Funct. Mater.* **2014,** *24*, 5359.

219. Borchardt, L.; Oschatz, M.; Kaskel, S., Carbon Materials for Lithium Sulfur Batteries—Ten Critical Questions. *Chem. - Eur. J.* **2016,** *22*, 7324.

220. Wu, H. B.; Wei, S.; Zhang, L.; Xu, R.; Hng, H. H.; Lou, X. W., Embedding Sulfur in MOF-Derived Microporous Carbon Polyhedrons for Lithium–Sulfur Batteries. *Chemistry – A European Journal* **2013,** *19* (33), 10804-10808.

221. Juan, Z.; Chun-Peng, Y.; Ya-Xia, Y.; Li-Jun, W.; Yu-Guo, G., Sulfur Encapsulated in Graphitic Carbon Nanocages for High-Rate and Long-Cycle Lithium–Sulfur Batteries. *Advanced Materials* **2016,** *28* (43), 9539-9544.

222. Sohn, H.; Gordin, M. L.; Xu, T.; Chen, S.; Lv, D.; Song, J.; Manivannan, A.; Wang, D., Porous Spherical Carbon/Sulfur Nanocomposites by Aerosol-Assisted Synthesis: The Effect of Pore Structure and Morphology on Their Electrochemical Performance As Lithium/Sulfur Battery Cathodes. *ACS Applied Materials & Interfaces* **2014,** *6* (10), 7596-7606.

223. Zheng, J.; Guo, G.; Li, H.; Wang, L.; Wang, B.; Yu, H.; Yan, Y.; Yang, D.; Dong, A., Elaborately Designed Micro–Mesoporous Graphitic Carbon Spheres as Efficient Polysulfide Reservoir for Lithium–Sulfur Batteries. *ACS Energy Letters* **2017,** *2* (5), 1105-1114.

224. Peng, H. J.; Huang, J. Q.; Zhao, M. Q.; Zhang, Q.; Cheng, X. B.; Liu, X. Y.; Qian, W. Z.; Wei, F., Nanoarchitectured graphene/CNT@ porous carbon with extraordinary electrical conductivity and interconnected micro/mesopores for lithium-sulfur batteries. *Advanced functional materials* **2014,** *24* (19), 2772-2781.

225. Xu, G.; Ding, B.; Shen, L.; Nie, P.; Han, J.; Zhang, X., Sulfur embedded in metal organic framework-derived hierarchically porous carbon nanoplates for high performance lithium-sulfur battery. *Journal of Materials Chemistry A* **2013,** *1* (14), 4490-4496.

226. Park, H.; Siegel, D. J., Tuning the Adsorption of Polysulfides in Lithium–Sulfur Batteries with Metal–Organic Frameworks. *Chemistry of Materials* **2017,** *29* (11), 4932-4939.

227. Amo-Ochoa, P.; Givaja, G.; Miguel, P. J. S.; Castillo, O.; Zamora, F., Microwave assisted hydrothermal synthesis of a novel CuI-sulfate-pyrazine MOF. *Inorganic Chemistry Communications* **2007,** *10* (8), 921-924.

228. Shi, F.-N.; Silva, A. R.; Rocha, J., Metal-organic framework based on copper(I) sulfate and 4,4′-bipyridine catalyzes the cyclopropanation of styrene. *Journal of Solid State Chemistry* **2011,** *184* (8), 2196-2203.

229. Farha, O. K.; Eryazici, I.; Jeong, N. C.; Hauser, B. G.; Wilmer, C. E.; Sarjeant, A. A.; Snurr, R. Q.; Nguyen, S. T.; Yazaydın, A. Ö.; Hupp, J. T., Metal–Organic Framework Materials with Ultrahigh Surface Areas: Is the Sky the Limit? *Journal of the American Chemical Society* **2012,** *134* (36), 15016-15021.

230. Li, B.; Wen, H.-M.; Zhou, W.; Xu, Jeff Q.; Chen, B., Porous Metal-Organic Frameworks: Promising Materials for Methane Storage. *Chem* **2016,** *1* (4), 557-580.

231. Liang, L.; Liu, C.; Jiang, F.; Chen, Q.; Zhang, L.; Xue, H.; Jiang, H.-L.; Qian, J.; Yuan, D.; Hong, M., Carbon dioxide capture and conversion by an acid-base resistant metal-organic framework. *Nature Communications* **2017,** *8* (1), 1233.

232. Lim, C.-H.; Holder, A. M.; Hynes, J. T.; Musgrave, C. B., Roles of the Lewis Acid and Base in the Chemical Reduction of CO2 Catalyzed by Frustrated Lewis Pairs. *Inorganic Chemistry* **2013,** *52* (17), 10062-10066.

233. Zhao, X.; Xiao, B.; Fletcher, A. J.; Thomas, K. M.; Bradshaw, D.; Rosseinsky, M. J., Hysteretic adsorption and desorption of hydrogen by nanoporous metal-organic frameworks. *Science* **2004,** *306* (5698), 1012-1015.

234. Lin, X.; Telepeni, I.; Blake, A. J.; Dailly, A.; Brown, C. M.; Simmons, J. M.; Zoppi, M.; Walker, G. S.; Thomas, K. M.; Mays, T. J.; Hubberstey, P.; Champness, N. R.; Schröder, M., High Capacity Hydrogen Adsorption in Cu(II) Tetracarboxylate

Framework Materials: The Role of Pore Size, Ligand Functionalization, and Exposed Metal Sites. *Journal of the American Chemical Society* **2009,** *131* (6), 2159-2171.

235. Snurr, R. Q.; Hupp, J. T.; Nguyen, S. T., Prospects for nanoporous metal-organic materials in advanced separations processes. *AIChE journal* **2004,** *50* (6), 1090-1095.

236. Fletcher, A. J.; Cussen, E. J.; Bradshaw, D.; Rosseinsky, M. J.; Thomas, K. M., Adsorption of Gases and Vapors on Nanoporous Ni2(4,4‘-Bipyridine)3(NO3)4 Metal−Organic Framework Materials Templated with Methanol and Ethanol: Structural Effects in Adsorption Kinetics. *Journal of the American Chemical Society* **2004,** *126* (31), 9750-9759.

237. Fujimori, T.; Morelos-Gómez, A.; Zhu, Z.; Muramatsu, H.; Futamura, R.; Urita, K.; Terrones, M.; Hayashi, T.; Endo, M.; Hong, S. Y., Conducting linear chains of sulphur inside carbon nanotubes. *Nature communications* **2013,** *4*, 2162.

238. Zhang, Y.; Gao, Z.; Song, N.; Li, X., High-performance supercapacitors and batteries derived from activated banana-peel with porous structures. *Electrochimica Acta* **2016,** *222*, 1257-1266.

239. Brudler, R.; de Groot, H. J. M.; van Liemt, W. B. S.; Gast, P.; Hoff, A. J.; Lugtenburg, J.; Gerwert, K., FTIR spectroscopy shows weak symmetric hydrogen bonding of the QB carbonyl groups in Rhodobacter sphaeroides R26 reaction centres. *FEBS Letters* **1995,** *370* (1), 88-92.

240. Lewis, P. D.; Lewis, K. E.; Ghosal, R.; Bayliss, S.; Lloyd, A. J.; Wills, J.; Godfrey, R.; Kloer, P.; Mur, L. A., Evaluation of FTIR spectroscopy as a diagnostic tool for lung cancer using sputum. *BMC cancer* **2010,** *10* (1), 640.

241. Parthasarthy, G.; Sevegney, M.; Kannan, R. M., Rheooptical Fourier transform infrared spectroscopy of the deformation behavior in quenched and slow-cooled isotactic polypropylene films. *Journal of Polymer Science Part B: Polymer Physics* **2002,** *40* (22), 2539-2551.

242. Colom, X.; Carrillo, F.; Nogués, F.; Garriga, P., Structural analysis of photodegraded wood by means of FTIR spectroscopy. *Polymer Degradation and Stability* **2003,** *80* (3), 543-549.

243. Tang, J.; Jing, X.; Wang, B.; Wang, F., Infrared spectra of soluble polyaniline. *Synthetic Metals* **1988,** *24* (3), 231-238.

244. Yuen, S.-N.; Choi, S.-M.; Phillips, D. L.; Ma, C.-Y., Raman and FTIR spectroscopic study of carboxymethylated non-starch polysaccharides. *Food Chemistry* **2009,** *114* (3), 1091-1098.

245. Duarte, M. L.; Ferreira, M. C.; Marvão, M. R.; Rocha, J., An optimised method to determine the degree of acetylation of chitin and chitosan by FTIR spectroscopy. *International Journal of Biological Macromolecules* **2002,** *31* (1), 1-8.

246. Devi, T. R.; Gayathri, S., FTIR and FT-Raman spectral analysis of paclitaxel drugs. *International Journal of Pharmaceutical Sciences Review and Research* **2010,** *2* (2), 106-110.

247. Seoudi, R.; El-Bahy, G. S.; El Sayed, Z. A., FTIR, TGA and DC electrical conductivity studies of phthalocyanine and its complexes. *Journal of Molecular Structure* **2005,** *753* (1), 119-126.

248. Wen, S. J.; Richardson, T. J.; Ghantous, D. I.; Striebel, K. A.; Ross, P. N.; Cairns, E. J., FTIR characterization of PEO + LiN(CF3SO2)2 electrolytes. *Journal of Electroanalytical Chemistry* **1996,** *408* (1), 113-118.

249. Logacheva, N. M.; Baulin, V. E.; Tsivadze, A. Y.; Pyatova, E. N.; Ivanova, I. S.; Velikodny, Y. A.; Chernyshev, V. V., Ni(II), Co(II), Cu(II), Zn(II) and Na(I) complexes of a hybrid ligand 4[prime or minute]-(4[triple prime]-benzo-15-crown-5)-methyloxy-2,2[prime or minute]:6[prime or minute],2[double prime]-terpyridine. *Dalton Transactions* **2009,** (14), 2482-2489.

250. Lindberg, B.; Hamrin, K.; Johansson, G.; Gelius, U.; Fahlman, A.; Nordling, C.; Siegbahn, K., Molecular spectroscopy by means of ESCA II. Sulfur compounds. Correlation of electron binding energy with structure. *Physica Scripta* **1970,** *1* (5-6), 286.

251. Gardella Jr, J. A.; Ferguson, S. A.; Chin, R. L., $\pi^* \leftarrow \pi$ shakeup satellites for the analysis of structure and bonding in aromatic polymers by X-Ray Photoelectron Spectroscopy. *Applied spectroscopy* **1986,** *40* (2), 224-232.

252. Zhao, Z.; Wang, S.; Liang, R.; Li, Z.; Shi, Z.; Chen, G., Graphene-wrapped chromium-MOF (MIL-101)/sulfur composite for performance improvement of high-rate rechargeable Li–S batteries. *Journal of Materials Chemistry A* **2014,** *2* (33), 13509-13512.

253. Xiao, M.; Huang, M.; Zeng, S.; Han, D.; Wang, S.; Sun, L.; Meng, Y., *Sulfur@graphene oxide core–shell particles as a rechargeable lithium–sulfur battery cathode material with high cycling stability and capacity*. 2013; Vol. 3, p 4914-4916.

254. Ma, G.; Huang, F.; Wen, Z.; Wang, Q.; Hong, X.; Jin, J.; Wu, X., Enhanced performance of lithium sulfur batteries with conductive polymer modified separators. *Journal of Materials Chemistry A* **2016,** *4* (43), 16968-16974.

255. Murugavel Shanthi, P.; Jampani Hanumantha, P.; Albuquerque, T.; Gattu, B.; Kumta, P. N., Novel Composite Polymer Electrolytes (CPEs) of PVdF – HFP derived by Electrospinning with Enhanced Li-ion Conductivities for Rechargeable Lithium – Sulfur batteries. *ACS Applied Energy Materials* **2018**.

256. Qin, F.; Zhang, K.; Fang, J.; Lai, Y.; Li, Q.; Zhang, Z.; L, J., *High performance lithium sulfur batteries with a cassava-derived carbon sheet as a polysulfides inhibitor*. 2014; Vol. 38.

257. Li, Z.; Yuan, L.; Yi, Z.; Liu, Y.; Xin, Y.; Zhang, Z.; Huang, Y., A dual coaxial nanocable sulfur composite for high-rate lithium-sulfur batteries. *Nanoscale* **2014,** *6* (3), 1653-1660.

258. Barber, M.; Connor, J. A.; Guest, M. F.; Hillier, I. H.; Schwarz, M.; Stacey, M., Bonding in some donor-acceptor complexes involving boron trifluoride. Study by means of ESCA and molecular orbital calculations. *Journal of the Chemical Society, Faraday Transactions 2: Molecular and Chemical Physics* **1973,** *69* (0), 551-558.

259. Feng, D.; Zhou, Z.; Bo, M., An investigation of the thermal degradation of melamine phosphonite by XPS and thermal analysis techniques. *Polymer degradation and stability* **1995,** *50* (1), 65-70.

260. Nakayama, T.; Inamura, K.; Inoue, Y.; Ikeda, S.; Kishi, K., Adsorption of benzonitrile and alkyl cyanides on evaporated nickel and palladium films studied by XPS. *Surface science* **1987,** *179* (1), 47-58.

261. Aduru, S.; Contarini, S.; Rabalais, J. W., Electron-, x-ray-, and ion-stimulated decomposition of nitrate salts. *The Journal of Physical Chemistry* **1986,** *90* (8), 1683-1688.

262. Hummel, H. U.; Förner, W.; Krogmann, K., Untersuchungen der Ladungsverteilung in freiem und gebundenem 1, 1-Dicyanoethylen-2, 2-dithiolat Eine ab initio-HF-MO-und XPS-Studie. *Zeitschrift für anorganische und allgemeine Chemie* **1986,** *540* (9-10), 300-306.

263. Lalitha, S.; Manoharan, P., X-ray photoelectron spectroscopic studies on some dithiolate complexes. *Journal of Electron Spectroscopy and Related Phenomena* **1989,** *49* (1), 61-75.

264. Kurmaev, E. Z.; Fedorenko, V. V.; Galakhov, V. R.; Bartkowski, S.; Uhlenbrock, S.; Neumann, M.; Slater, P. R.; Greaves, C.; Miyazaki, Y., Analysis of oxyanion (BO 3 3− , CO 3 2− , SO 4 2− , PO 4 3− , SeO 4 4-) substitution in Y123 compounds studied by X-ray photoelectron spectroscopy. *Journal of Superconductivity* **1996,** *9* (1), 97-100.

265. Wagner, C. D.; Taylor, J. A., Contributions to screening in the solid state by electron systems of remote atoms: Effects to photoelectron and Auger transitions. *Journal of Electron Spectroscopy and Related Phenomena* **1982,** *28* (2), 211-217.

266. Bellitto, C.; Bonamico, M.; Fares, V.; Imperatori, P.; Patrizio, S., Tetrathiafulvalenium salts of planar Pt, Pd, and Cu 1,2-dithio-oxalato-S,S[prime or minute] anions. Synthesis, chemistry and molecular structures of bis(tetrathiafulvalenium) bis(1,2-dithio-oxalato-S,S[prime or minute])palladate(II), [ttf]2[Pd(S2C2O2)2], and of bis(tetrathiafulvalenium)tetrathiafulvalene bis(1,2-dithio-oxalato-S,S[prime or minute])platinate(II), [ttf]3[Pt(S2C2O2)2]. *Journal of the Chemical Society, Dalton Transactions* **1989,** (4), 719-727.

267. Chehimi, M. M.; Delamar, M., X-ray photoelectron spectroscopy of merocyanine dyes: Part VII. Partial charge and conjugation of heteroatoms in the electrodonor rings11For preceding papers in this series, see refs. (25–30). *Journal of Electron Spectroscopy and Related Phenomena* **1989,** *49* (2), 231.

268. Yao, W.; Zhang, Z.; Gao, J.; Li, J.; Xu, J.; Wang, Z.; Yang, Y., Vinyl ethylene sulfite as a new additive in propylene carbonate-based electrolyte for lithium ion batteries. *Energy & Environmental Science* **2009,** *2* (10), 1102-1108.

269. Li, X.; Yin, Z.; Li, X.; Wang, C., Ethylene sulfate as film formation additive to improve the compatibility of graphite electrode for lithium-ion battery. *Ionics* **2014,** *20* (6), 795-801.

270. Liao, L.-F.; Lien, C.-F.; Lin, J.-L., FTIR study of adsorption and photoreactions of acetic acid on TiO 2. *Physical Chemistry Chemical Physics* **2001,** *3* (17), 3831-3837.

271. Pereira, L.; Sousa, A.; Coelho, H.; Amado, A. M.; Ribeiro-Claro, P. J. A., Use of FTIR, FT-Raman and 13C-NMR spectroscopy for identification of some seaweed phycocolloids. *Biomolecular Engineering* **2003,** *20* (4), 223-228.

272. Strawn, S.; White, J.; Marshall, G.; Gee, L.; Goodis, H.; Marshall, S., Spectroscopic changes in human dentine exposed to various storage solutions—short term. *Journal of Dentistry* **1996,** *24* (6), 417-423.

273. Li, Z.; Jiang, W.-T.; Hong, H., An FTIR investigation of hexadecyltrimethylammonium intercalation into rectorite. *Spectrochimica Acta Part A: Molecular and Biomolecular Spectroscopy* **2008,** *71* (4), 1525-1534.

274. Mohammadi, B.; Yousefi, A. A.; Bellah, S. M., Effect of tensile strain rate and elongation on crystalline structure and piezoelectric properties of PVDF thin films. *Polymer Testing* **2007,** *26* (1), 42-50.

275. Peng, Y.; Wu, P., A two dimensional infrared correlation spectroscopic study on the structure changes of PVDF during the melting process. *Polymer* **2004,** *45* (15), 5295-5299.

276. Yang, H.; Zhuang, G. V.; Ross, P. N., Thermal stability of LiPF6 salt and Li-ion battery electrolytes containing LiPF6. *Journal of Power Sources* **2006,** *161* (1), 573-579.

277. Ludvigsson, M.; Lindgren, J.; Tegenfeldt, J., FTIR study of water in cast Nafion films. *Electrochimica Acta* **2000,** *45* (14), 2267-2271.

278. Hassanzadeh, P.; Andrews, L., Infrared spectra of new sulfur-nitrogen species in solid argon. *Journal of the American Chemical Society* **1992,** *114* (1), 83-91.

279. Rao, C.; Venkataraghavan, R.; Kasturi, T., Contribution to the infrared spectra of organosulphur compounds. *Canadian journal of chemistry* **1964,** *42* (1), 36-42.

280. Yadav, H.; Sinha, N.; Kumar, B., Growth and characterization of new semiorganic nonlinear optical and piezoelectric lithium sulfate monohydrate oxalate single crystals. *Materials Research Bulletin* **2015,** *64*, 194-199.

281. Slavkova, Z.; Kostadinova, O.; Avdeev, G.; Petkova, T., Structure and Thermal Behaviour of Lithium Sodium Sulphate. In *Advanced Nanotechnologies for Detection and Defence against CBRN Agents*, Springer: 2018; pp 87-93.

282. Etacheri, V.; Marom, R.; Elazari, R.; Salitra, G.; Aurbach, D., Challenges in the development of advanced Li-ion batteries: a review. *Energy & Environmental Science* **2011,** *4* (9), 3243-3262.

283. Goodenough, J. B.; Kim, Y., Challenges for Rechargeable Li Batteries. *Chem. Mater.* **2010,** *22*, 587.

284. Bruce, P. G.; Scrosati, B.; Tarascon, J. M., Nanomaterials for Rechargeable Lithium Batteries. *Angewandte Chemie International Edition* **2008,** *47* (16), 2930-2946.

285. Chung, S.-Y.; Bloking, J. T.; Chiang, Y.-M., Electronically conductive phospho-olivines as lithium storage electrodes. *Nature Materials* **2002,** *1*, 123.

286. Li, J.; Du, Z.; Ruther, R. E.; AN, S. J.; David, L. A.; Hays, K.; Wood, M.; Phillip, N. D.; Sheng, Y.; Mao, C.; Kalnaus, S.; Daniel, C.; Wood, D. L., Toward Low-Cost, High-Energy Density, and High-Power Density Lithium-Ion Batteries. *JOM* **2017,** *69* (9), 1484-1496.

287. Padhi, A. K.; Nanjundaswamy, K. S.; Goodenough, J. B., Phospho-olivines as Positive-Electrode Materials for Rechargeable Lithium Batteries. *Journal of The Electrochemical Society* **1997,** *144* (4), 1188-1194.

288. Yamada, A.; Chung, S. C.; Hinokuma , K., Optimized LiFePO4 for Lithium Battery Cathodes. *Journal of The Electrochemical Society* **2001,** *148* (3), A224-A229.

289. Scrosati, B., Recent advances in lithium ion battery materials. *Electrochimica Acta* **2000,** *45* (15–16), 2461-2466.

290. Chan, C. K.; Peng, H.; Liu, G.; McIlwrath, K.; Zhang, X. F.; Huggins, R. A.; Cui, Y., High-performance lithium battery anodes using silicon nanowires. *Nature Nanotechnology* **2007,** *3*, 31.

291. Holland, H. D.; Turekian, K. K., *Geochemistry of earth surface systems: A derivative of the treatise on geochemistry*. Academic Press: 2010.

292. Pang, Q.; Liang, X.; Kwok, C. Y.; Nazar, L. F., Advances in Lithium–Sulfur Batteries Based on Multifunctional Cathodes and Electrolytes. *Nat. Energy* **2016,** *1*, 16132.

293. Zu, C.; Manthiram, A., Stabilized Lithium–Metal Surface in a Polysulfide-Rich Environment of Lithium–Sulfur Batteries. *J. Phys. Chem. Lett.* **2014,** *5*, 2522.

294. Yuan, Z.; Peng, H. J.; Huang, J. Q.; Liu, X. Y.; Wang, D. W.; Cheng, X. B.; Zhang, Q., Hierarchical Free-Standing Carbon-Nanotube Paper Electrodes with Ultrahigh Sulfur-Loading for Lithium–Sulfur Batteries. *Adv. Funct. Mater.* **2014,** *24*, 6105.

295. Kong, L. L.; Zhang, Z.; Zhang, Y. Z.; Liu, S.; Li, G. R.; Gao, X. P., Porous Carbon Paper as Interlayer to Stabilize the Lithium Anode for Lithium–Sulfur Battery. *ACS Appl. Mater. Interfaces* **2016,** *8*, 31684.

296. Ji, X.; Liu, D. Y.; Prendiville, D. G.; Zhang, Y.; Liu, X.; Stucky, G. D., Spatially Heterogeneous Carbon-Fiber Papers as Surface Dendrite-Free Current Collectors for Lithium Deposition. *Nano Today* **2012,** *7*, 10.

297. Xiong, S.; Xie, K.; Diao, Y.; Hong, X., Properties of Surface Film on Lithium Anode with LiNO3 as Lithium Salt in Electrolyte Solution for Lithium–Sulfur Batteries. *Electrochim. Acta* **2012,** *83*, 78.

298. Zhang, S. S., Role of LiNO3 in Rechargeable Lithium/Sulfur Battery. *Electrochim. Acta* **2012,** *70*, 344.

299. Jin, C.; Sheng, O.; Luo, J.; Yuan, H.; Fang, C.; Zhang, W.; Huang, H.; Gan, Y.; Xia, Y.; Liang, C., 3D Lithium Metal Embedded within Lithiophilic Porous Matrix for Stable Lithium Metal Batteries. *Nano Energy* **2017,** *37*, 177.

300. Li, Y.; Wong, K. W.; Ng, K. M., Ionic Liquid Decorated Mesoporous Silica Nanoparticles: A New High-Performance Hybrid Electrolyte for Lithium Batteries. *Chem. Commun.* **2016,** *52*, 4369.

301. Elazari, R.; Salitra, G.; Garsuch, A.; Panchenko, A.; Aurbach, D., Sulfur-Impregnated Activated Carbon Fiber Cloth as a Binder-Free Cathode for Rechargeable Li-S Batteries. *Advanced Materials* **2011,** *23* (47), 5641-5644.

302. Shin, W. K.; Kannan, A. G.; Kim, D. W., Effective Suppression of Dendritic Lithium Growth Using an Ultrathin Coating of Nitrogen and Sulfur Codoped Graphene Nanosheets on Polymer Separator for Lithium Metal Batteries. *ACS Appl. Mater. Interfaces* **2015,** *7*, 23700.

303. Zhou, G.; Tian, H.; Jin, Y.; Tao, X.; Liu, B.; Zhang, R.; Seh, Z. W.; Zhuo, D.; Liu, Y.; Sun, J., Catalytic Oxidation of Li2S on the Surface of Metal Sulfides for Li–S Batteries. *Proc. Natl. Acad. Sci. U. S. A.* **2017,** *114*, 840.

304. Yan, C.; Cheng, X. B.; Zhao, C. Z.; Huang, J. Q.; Yang, S. T.; Zhang, Q., Lithium Metal Protection through in-situ Formed Solid Electrolyte Interphase in Lithium-Sulfur Batteries: The Role of Polysulfides on Lithium Anode. *J. Power Sources* **2016,** *327*, 212.

305. Li, F.; Zhang, X.; Liu, X.; Zhao, M., Novel Conductive Metal–Organic Framework for a High-Performance Lithium–Sulfur Battery Host: 2D Cu-Benzenehexathial (BHT). *ACS Applied Materials & Interfaces* **2018**.

306. Bao, W.; Zhang, Z.; Zhou, C.; Lai, Y.; Li, J., Multi-walled carbon nanotubes @ mesoporous carbon hybrid nanocomposites from carbonized multi-walled carbon nanotubes @ metal–organic framework for lithium sulfur battery. *Journal of Power Sources* **2014,** *248*, 570-576.

307. Bao, W.; Zhang, Z.; Qu, Y.; Zhou, C.; Wang, X.; Li, J., Confine sulfur in mesoporous metal–organic framework @ reduced graphene oxide for lithium sulfur battery. *Journal of Alloys and Compounds* **2014,** *582*, 334-340.

308. Li, X.; Sun, Q.; Liu, J.; Xiao, B.; Li, R.; Sun, X., Tunable porous structure of metal organic framework derived carbon and the application in lithium–sulfur batteries. *Journal of Power Sources* **2016,** *302*, 174-179.

309. Mietrach, A.; Muesmann, T. W. T.; Christoffers, J.; Wickleder, M. S., Sulfonic Acid Analogs of Terephthalic and Trimesic Acid as Linkers in Metal-Organic Frameworks – Synthesis of Thermally Robust MOFs. *European Journal of Inorganic Chemistry* **2009,** *2009* (35), 5328-5334.

310. Li, Y.; Guan, H.-M.; Chung, T.-S.; Kulprathipanja, S., Effects of novel silane modification of zeolite surface on polymer chain rigidification and partial pore blockage in polyethersulfone (PES)–zeolite A mixed matrix membranes. *Journal of Membrane Science* **2006,** *275* (1), 17-28.

311. Kwon, S.; Pignatello, J. J., Effect of Natural Organic Substances on the Surface and Adsorptive Properties of Environmental Black Carbon (Char): Pseudo Pore Blockage by Model Lipid Components and Its Implications for N2-Probed Surface Properties of Natural Sorbents. *Environmental Science & Technology* **2005,** *39* (20), 7932-7939.

312. Song, M.-K.; Cairns, E. J.; Zhang, Y., Lithium/sulfur batteries with high specific energy: old challenges and new opportunities. *Nanoscale* **2013,** *5* (6), 2186-2204.

313. Lin, Y. X.; Liu, Z.; Leung, K.; Chen, L. Q.; Lu, P.; Qi, Y., Connecting the Irreversible Capacity Loss in Li-Ion Batteries with the Electronic Insulating Properties of Solid Electrolyte Interphase (SEI) Components. *J. Power Sources* **2016,** *309*, 221.

314. Zhang, S. S.; Tran, D. T., A proof-of-concept lithium/sulfur liquid battery with exceptionally high capacity density. *Journal of Power Sources* **2012,** *211*, 169-172.

315. Tischer, R.; Ludwig, F., The sulfur electrode in nonaqueous media. *Advances in Electrochemistry and Electrochemical Engineering* **1977,** *10*, 391-482.

316. Kafizas, A.; Noor, N.; Carmalt, C. J.; Parkin, I. P., TiO 2-based transparent conducting oxides; the search for optimum electrical conductivity using a combinatorial approach. *Journal of Materials Chemistry C* **2013,** *1* (39), 6335-6346.

317. Lin, Y.; Li, J.; Liu, K.; Liu, Y.; Liu, J.; Wang, X., Unique starch polymer electrolyte for high capacity all-solid-state lithium sulfur battery. *Green Chemistry* **2016,** *18* (13), 3796-3803.

318. Sun, Y.; Li, G.; Lai, Y.; Zeng, D.; Cheng, H., High rate lithium-sulfur battery enabled by sandwiched single ion conducting polymer electrolyte. *Scientific Reports* **2016,** *6*, 22048.

319. Li, Y.; Xu, B.; Xu, H.; Duan, H.; Lü, X.; Xin, S.; Zhou, W.; Xue, L.; Fu, G.; Manthiram, A.; Goodenough, J. B., Hybrid Polymer/Garnet Electrolyte with a Small Interfacial Resistance for Lithium-Ion Batteries. *Angewandte Chemie* **2017,** *129* (3), 771-774.

320. Zhou, W.; Li, Y.; Xin, S.; Goodenough, J. B., Rechargeable Sodium All-Solid-State Battery. *ACS Central Science* **2017,** *3* (1), 52-57.

321. Aono, H.; Sugimoto, E.; Sadaoka, Y.; Imanaka, N.; Adachi, G. y., Ionic Conductivity of Solid Electrolytes Based on Lithium Titanium Phosphate. *Journal of The Electrochemical Society* **1990,** *137* (4), 1023-1027.

322. Li, J.; Ma, C.; Chi, M.; Liang, C.; Dudney, N. J., Solid Electrolyte: the Key for High-Voltage Lithium Batteries. *Advanced Energy Materials* **2015,** *5* (4), 1401408-n/a.

323. Kharton, V. V.; Marques, F. M. B.; Atkinson, A., Transport properties of solid oxide electrolyte ceramics: a brief review. *Solid State Ionics* **2004,** *174* (1), 135-149.

324. Manuel Stephan, A., Review on gel polymer electrolytes for lithium batteries. *European Polymer Journal* **2006,** *42* (1), 21-42.

325. Fergus, J. W., Ceramic and polymeric solid electrolytes for lithium-ion batteries. *Journal of Power Sources* **2010,** *195* (15), 4554-4569.

326. Gopalan, A. I.; Santhosh, P.; Manesh, K. M.; Nho, J. H.; Kim, S. H.; Hwang, C.-G.; Lee, K.-P., Development of electrospun PVdF–PAN membrane-based polymer electrolytes for lithium batteries. *Journal of Membrane Science* **2008,** *325* (2), 683-690.

327. Shalu; Singh, V. K.; Singh, R. K., Development of ion conducting polymer gel electrolyte membranes based on polymer PVdF-HFP, BMIMTFSI ionic liquid and the Li-salt with improved electrical, thermal and structural properties. *Journal of Materials Chemistry C* **2015,** *3* (28), 7305-7318.

328. Kim, J. R.; Choi, S. W.; Jo, S. M.; Lee, W. S.; Kim, B. C., Electrospun PVdF-based fibrous polymer electrolytes for lithium ion polymer batteries. *Electrochimica Acta* **2004,** *50* (1), 69-75.

329. Agrawal, R. C.; Pandey, G. P., Solid polymer electrolytes: materials designing and all-solid-state battery applications: an overview. *Journal of Physics D: Applied Physics* **2008,** *41* (22), 223001.

330. Rao, M.; Geng, X.; Liao, Y.; Hu, S.; Li, W., Preparation and performance of gel polymer electrolyte based on electrospun polymer membrane and ionic liquid for lithium ion battery. *Journal of Membrane Science* **2012,** *399–400*, 37-42.

331. Idris, N. H.; Rahman, M. M.; Wang, J.-Z.; Liu, H.-K., Microporous gel polymer electrolytes for lithium rechargeable battery application. *Journal of Power Sources* **2012,** *201*, 294-300.

332. Gray, F. M., *Polymer electrolytes*. Royal Society of Chemistry: 1997.

333. MacCallum, J.; Vincent, C., Polymer electrolytes reviews, vols. 1 and 2Elsevier. *London (1987 and 1989)* **1989**.

334. MacCallum, J. R.; Vincent, C. A., *Polymer electrolyte reviews*. Springer Science & Business Media: 1989; Vol. 2.

335. Scrosati, B., *Applications of electroactive polymers*. Springer: 1993; Vol. 75.

336. Kim, K. M.; Park, N.-G.; Ryu, K. S.; Chang, S. H., Characteristics of PVdF-HFP/TiO2 composite membrane electrolytes prepared by phase inversion and conventional casting methods. *Electrochimica Acta* **2006,** *51* (26), 5636-5644.

337. Adam, D., A fine set of threads. *Nature* **2001,** *411* (6835), 236-236.

338. Manesh, K. M.; Kim, H. T.; Santhosh, P.; Gopalan, A. I.; Lee, K.-P., A novel glucose biosensor based on immobilization of glucose oxidase into multiwall carbon nanotubes–polyelectrolyte-loaded electrospun nanofibrous membrane. *Biosensors and Bioelectronics* **2008,** *23* (6), 771-779.

339. Kim, H. S.; Jin, H.-J.; Myung, S. J.; Kang, M.; Chin, I.-J., Carbon Nanotube-Adsorbed Electrospun Nanofibrous Membranes of Nylon 6. *Macromolecular Rapid Communications* **2006,** *27* (2), 146-151.

340. Huang, X.; Zeng, S.; Liu, J.; He, T.; Sun, L.; Xu, D.; Yu, X.; Luo, Y.; Zhou, W.; Wu, J., High-Performance Electrospun Poly(vinylidene fluoride)/Poly(propylene carbonate) Gel Polymer Electrolyte for Lithium-Ion Batteries. *The Journal of Physical Chemistry C* **2015,** *119* (50), 27882-27891.

341. Li, X.; Cheruvally, G.; Kim, J.-K.; Choi, J.-W.; Ahn, J.-H.; Kim, K.-W.; Ahn, H.-J., Polymer electrolytes based on an electrospun poly(vinylidene fluoride-co-hexafluoropropylene) membrane for lithium batteries. *Journal of Power Sources* **2007,** *167* (2), 491-498.

342. Rao, K. S.; El-Hami, K.; Kodaki, T.; Matsushige, K.; Makino, K., A novel method for synthesis of silica nanoparticles. *Journal of Colloid and Interface Science* **2005,** *289* (1), 125-131.

343. Chen, X.; Mao, S. S., Synthesis of Titanium Dioxide (TiO2) Nanomaterials. *Journal of Nanoscience and Nanotechnology* **2006,** *6* (4), 906-925.

344. Nishiwaki, K.; Kakuta, N.; Ueno, A.; Nakabayashi, H., Generation of acid sites on finely divided TiO2. *Journal of Catalysis* **1989,** *118* (2), 498-501.

345. Zhou, Z. Q.; Xu, H. Y.; Ji, W. J.; Chen, Y., Preparation of Novel Composite VPO/Fumed Silica Catalyst for Partial Oxidation of n-Butane. *Catalysis Letters* **2004,** *96* (3), 221-226.

346. Kumar, B.; Scanlon, L. G., Polymer-ceramic composite electrolytes. *Journal of Power Sources* **1994,** *52* (2), 261-268.

347. Manuel Stephan, A.; Teeters, D., Characterization of PVdF-HFP polymer membranes prepared by phase inversion techniques I. Morphology and charge–discharge studies. *Electrochimica Acta* **2003,** *48* (14–16), 2143-2148.

348. Song, J. Y.; Wang, Y. Y.; Wan, C. C., Conductivity Study of Porous Plasticized Polymer Electrolytes Based on Poly(vinylidene fluoride) A Comparison with Polypropylene Separators. *Journal of The Electrochemical Society* **2000,** *147* (9), 3219-3225.

349. Sethupathy, M.; Sethuraman, V.; Manisankar, P., Preparation of PVDF/SiO₂ Composite Nanofiber Membrane Using Electrospinning for Polymer Electrolyte Analysis. *Soft Nanoscience Letters* **2013,** *Vol.03No.02*, 7.

350. Zhou, R.; Liu, W.; Yao, X.; Leong, Y. W.; Lu, X., Poly(vinylidene fluoride) nanofibrous mats with covalently attached SiO2 nanoparticles as an ionic liquid host: enhanced ion transport for electrochromic devices and lithium-ion batteries. *Journal of Materials Chemistry A* **2015,** *3* (31), 16040-16049.

351. Solarajan, A. K.; Murugadoss, V.; Angaiah, S., High performance electrospun PVdF-HFP/SiO2 nanocomposite membrane electrolyte for Li-ion capacitors. *Journal of Applied Polymer Science* **2017,** *134* (32), 45177-n/a.

352. Stephan, A. M.; Nahm, K. S.; Anbu Kulandainathan, M.; Ravi, G.; Wilson, J., Poly(vinylidene fluoride-hexafluoropropylene) (PVdF-HFP) based composite electrolytes for lithium batteries. *European Polymer Journal* **2006,** *42* (8), 1728-1734.

353. Solarajan, A. K.; Murugadoss, V.; Angaiah, S., Dimensional stability and electrochemical behaviour of ZrO2 incorporated electrospun PVdF-HFP based nanocomposite polymer membrane electrolyte for Li-ion capacitors. *Scientific Reports* **2017,** *7*, 45390.

354. Ding, Y.; Zhang, P.; Long, Z.; Jiang, Y.; Xu, F.; Di, W., The ionic conductivity and mechanical property of electrospun P(VdF-HFP)/PMMA membranes for lithium ion batteries. *Journal of Membrane Science* **2009,** *329* (1–2), 56-59.

355. Li, N.; Xiao, C.; An, S.; Hu, X., Preparation and properties of PVDF/PVA hollow fiber membranes. *Desalination* **2010,** *250* (2), 530-537.

356. Koganti, V. R.; Das, S.; Rankin, S. E., In Situ FTIR Investigation of the Kinetics of Silica Polycondensation in Surfactant Templated, Mesostructured Thin Films. *The Journal of Physical Chemistry C* **2014,** *118* (33), 19450-19461.

357. Prabakaran, K.; Mohanty, S.; Nayak, S. K., Improved electrochemical and photovoltaic performance of dye sensitized solar cells based on PEO/PVDF-HFP/silane modified TiO2 electrolytes and MWCNT/Nafion[registered sign] counter electrode. *RSC Advances* **2015,** *5* (51), 40491-40504.

358. Liao, L.-F.; Lien, C.-F.; Shieh, D.-L.; Chen, F.-C.; Lin, J.-L., FTIR study of adsorption and photochemistry of amide on powdered TiO 2: Comparison of benzamide with acetamide. *Physical Chemistry Chemical Physics* **2002,** *4* (18), 4584-4589.

359. Feuillade, G.; Perche, P., Ion-conductive macromolecular gels and membranes for solid lithium cells. *Journal of Applied Electrochemistry* **1975,** *5* (1), 63-69.

360. Blond, D.; Walshe, W.; Young, K.; Blighe, F. M.; Khan, U.; Almecija, D.; Carpenter, L.; McCauley, J.; Blau, W. J.; Coleman, J. N., Strong, Tough, Electrospun Polymer–Nanotube Composite Membranes with Extremely Low Density. *Advanced Functional Materials* **2008,** *18* (17), 2618-2624.

361. Matsumoto, K.; Sogabe, S.; Endo, T., Conductive networked polymer gel electrolytes composed of poly(meth)acrylate, lithium salt, and ionic liquid. *Journal of Polymer Science Part A: Polymer Chemistry* **2012,** *50* (7), 1317-1324.

362. Li, W.; Pang, Y.; Liu, J.; Liu, G.; Wang, Y.; Xia, Y., A PEO-based gel polymer electrolyte for lithium ion batteries. *RSC Advances* **2017,** *7* (38), 23494-23501.

363. Tang, X.; Cao, Q.; Wang, X.; Peng, X.; Zeng, J., Study of the effect of a novel high-performance gel polymer electrolyte based on thermoplastic polyurethane/poly(vinylidene fluoride)/polystyrene and formed using an electrospinning technique. *RSC Advances* **2015,** *5* (72), 58655-58662.

364. Zhang, H.; Wang, X.; Liang, Y., Preparation and characterization of a Lithium-ion battery separator from cellulose nanofibers. *Heliyon* **2015,** *1* (2), Article e00032.

365. Perera, K.; Dissanayake, M. A. K. L.; Bandaranayake, P. W. S. K., Ionic conductivity of a gel polymer electrolyte based on Mg(ClO4)2 and polyacrylonitrile (PAN). *Materials Research Bulletin* **2004,** *39* (11), 1745-1751.

366. Zhang, R.; Chen, Y.; Montazami, R., Ionic Liquid-Doped Gel Polymer Electrolyte for Flexible Lithium-Ion Polymer Batteries. *Materials* **2015,** *8* (5), 2735.

367. Song, J. Y.; Wang, Y. Y.; Wan, C. C., Review of gel-type polymer electrolytes for lithium-ion batteries. *Journal of Power Sources* **1999,** *77* (2), 183-197.

368. Capuano, F.; Croce, F.; Scrosati, B., Composite Polymer Electrolytes. *Journal of The Electrochemical Society* **1991,** *138* (7), 1918-1922.

369. Mohamed, N. S.; Arof, A. K., Conductivity studies of LiCF3SO3-doped and DMF-plasticized PVDF-based solid polymer electrolytes. *physica status solidi (a)* **2004,** *201* (14), 3096-3101.

370. Tanzi, M. C.; Mantovani, D.; Petrini, P.; Guidoin, R.; Laroche, G., Chemical stability of polyether urethanes versus polycarbonate urethanes. *Journal of biomedical materials research* **1997,** *36* (4), 550-559.

371. Mihály, J.; Sterkel, S.; Ortner, H. M.; Kocsis, L.; Hajba, L.; Furdyga, É.; Mink, J., FTIR and FT-Raman spectroscopic study on polymer based high pressure digestion vessels. *Croatica chemica acta* **2006,** *79* (3), 497-501.

372. Poliskie, M.; Clevenger, J. O., Fourier transform infrared (FTIR) spectroscopy for coating characterization and failure analysis. *Metal Finishing* **2008,** *106* (5), 44-47.

373. Cui, C.; Park, D. H.; Kim, J.; Joo, J.; Ahn, D. J., Oligonucleotide assisted light-emitting Alq3 microrods: energy transfer effect with fluorescent dyes. *Chemical Communications* **2013,** *49* (47), 5360-5362.

374. Prabavathi, N.; Senthil Nayaki, N.; Krishnakumar, V., Spectroscopic Investigation (FT-IR, FT-Raman, NMR and UV-Vis), Conformational Stability, NBO and Thermodynamic Analysis of 1-(2-Methoxyphenyl) Piperazine and 1-(2-Chlorophenyl) Piperazine by DFT Approach. *Pharm Anal Acta* **2015,** *6* (391), 2.

375. Ibrahim, M.; Nada, A.; Kamal, D. E., Density functional theory and FTIR spectroscopic study of carboxyl group. *Indian Journal of Pure and Applied Physics* **2005,** *44* (12), 911-917.

376. Zhang, Z. P.; Rong, M. Z.; Zhang, M. Q.; Yuan, C. e., Alkoxyamine with reduced homolysis temperature and its application in repeated autonomous self-healing of stiff polymers. *Polymer Chemistry* **2013,** *4* (17), 4648-4654.

377. Saikia, B. J.; Parthasarathy, G., Fourier transform infrared spectroscopic characterization of kaolinite from Assam and Meghalaya, Northeastern India. *Journal of Modern Physics* **2010,** *1* (04), 206.

378. El-Bahy, G. M. S., FTIR and Raman spectroscopic study of Fenugreek (Trigonella foenum graecum L.) seeds. *Journal of Applied Spectroscopy* **2005,** *72* (1), 111-116.

379. Biswas, N.; Waring, A. J.; Walther, F. J.; Dluhy, R. A., Structure and conformation of the disulfide bond in dimeric lung surfactant peptides SP-B1–25 and SP-B8–25. *Biochimica et Biophysica Acta (BBA) - Biomembranes* **2007,** *1768* (5), 1070-1082.

380. Park, K.; Cho, J. H.; Jang, J.-H.; Yu, B.-C.; De La Hoz, A. T.; Miller, K. M.; Ellison, C. J.; Goodenough, J. B., Trapping lithium polysulfides of a Li-S battery by forming lithium bonds in a polymer matrix. *Energy & Environmental Science* **2015,** *8* (8), 2389-2395.

381. Thackeray, M. M.; Wolverton, C.; Isaacs, E. D., Electrical energy storage for transportation-approaching the limits of, and going beyond, lithium-ion batteries. *Energy & Environmental Science* **2012,** *5* (7), 7854-7863.

382. Dunn, B.; Kamath, H.; Tarascon, J.-M., Electrical Energy Storage for the Grid: A Battery of Choices. *Science* **2011,** *334* (6058), 928-935.

383. Peled, E.; Menachem, C.; Bar-Tow, D.; Melman, A., Improved Graphite Anode for Lithium-Ion Batteries Chemically: Bonded Solid Electrolyte Interface and Nanochannel Formation. *Journal of The Electrochemical Society* **1996,** *143* (1), L4-L7.

384. Aurbach, D., Review of selected electrode–solution interactions which determine the performance of Li and Li ion batteries. *Journal of Power Sources* **2000,** *89* (2), 206-218.

385. Kim, S.-W.; Seo, D.-H.; Ma, X.; Ceder, G.; Kang, K., Electrode Materials for Rechargeable Sodium-Ion Batteries: Potential Alternatives to Current Lithium-Ion Batteries. *Advanced Energy Materials* **2012,** *2* (7), 710-721.

386. Ravdel, B.; Abraham, K. M.; Gitzendanner, R.; DiCarlo, J.; Lucht, B.; Campion, C., Thermal stability of lithium-ion battery electrolytes. *Journal of Power Sources* **2003,** *119–121*, 805-810.

387. Campion, C. L.; Li, W.; Euler, W. B.; Lucht, B. L.; Ravdel, B.; DiCarlo, J. F.; Gitzendanner, R.; Abraham, K. M., Suppression of Toxic Compounds Produced in the Decomposition of Lithium-Ion Battery Electrolytes. *Electrochemical and Solid-State Letters* **2004,** *7* (7), A194-A197.

388. Vetter, J.; Novák, P.; Wagner, M. R.; Veit, C.; Möller, K. C.; Besenhard, J. O.; Winter, M.; Wohlfahrt-Mehrens, M.; Vogler, C.; Hammouche, A., Ageing mechanisms in lithium-ion batteries. *Journal of Power Sources* **2005,** *147* (1–2), 269-281.

389. Bhattacharyya, R.; Key, B.; Chen, H.; Best, A. S.; Hollenkamp, A. F.; Grey, C. P., In situ NMR observation of the formation of metallic lithium microstructures in lithium batteries. *Nat Mater* **2010,** *9* (6), 504-510.

390. Ohtsuka, H.; Okada, S.; Yamaki, J.-i., Solid state battery with Li2O-V2O5-SiO2 solid electrolyte thin film. *Solid State Ionics* **1990,** *40*, 964-966.

391. Takada, K.; Aotani, N.; Iwamoto, K.; Kondo, S., Proceedings of the 10th International Conference on Solid State IonicsSolid state lithium battery with oxysulfide glass. *Solid State Ionics* **1996,** *86*, 877-882.

392. Inaba, H.; Tagawa, H., Ceria-based solid electrolytes. *Solid State Ionics* **1996,** *83* (1), 1-16.

393. Pratt, J. N., Applications of solid electrolytes in thermodynamic studies of materials: A review. *Metallurgical Transactions A* **1990,** *21* (4), 1223-1250.

394. Huberman, B. A., Cooperative Phenomena in Solid Electrolytes. *Physical Review Letters* **1974,** *32* (18), 1000-1002.

395. Nanjundaswamy, K. S.; Padhi, A. K.; Goodenough, J. B.; Okada, S.; Ohtsuka, H.; Arai, H.; Yamaki, J., Synthesis, redox potential evaluation and electrochemical characteristics of NASICON-related-3D framework compounds. *Solid State Ionics* **1996,** *92* (1), 1-10.

396. AL-RIKABI, A., Ionic Conductivity Measurements of Lithium Iodide-doped Lithium Phosphate. *Jour. Chem. Soc. Pak. Vol* **1989,** *11* (1), 1.

397. West, A. R., Ionic conductivity of oxides based on Li4SiO4. *Journal of Applied Electrochemistry* **1973,** *3* (4), 327-335.

398. Catti, M., First-Principles Modeling of Lithium Ordering in the LLTO (LixLa2/3-x/3TiO3) Superionic Conductor. *Chemistry of Materials* **2007,** *19* (16), 3963-3972.

399. Huang, M.; Dumon, A.; Nan, C.-W., Effect of Si, In and Ge doping on high ionic conductivity of Li7La3Zr2O12. *Electrochemistry Communications* **2012,** *21*, 62-64.

400. Thangadurai, V.; Weppner, W., Li6ALa2Ta2O12 (A = Sr, Ba): Novel Garnet-Like Oxides for Fast Lithium Ion Conduction. *Advanced Functional Materials* **2005,** *15* (1), 107-112.

401. Hu, Y. W.; Raistrick, I. D.; Huggins, R. A., Ionic conductivity of lithium phosphate-doped lithium orthosilicate. *Materials Research Bulletin* **1976,** *11* (10), 1227-1230.

402. Du, M.-H., Effects of impurity doping on ionic conductivity and polarization phenomenon in TlBr. *Applied Physics Letters* **2013,** *102* (8), 082102.

403. Bidrawn, F.; Lee, S.; Vohs, J. M.; Gorte, R. J., The Effect of Ca, Sr, and Ba Doping on the Ionic Conductivity and Cathode Performance of LaFeO3. *Journal of The Electrochemical Society* **2008,** *155* (7), B660-B665.

404. Iskakova, A. A.; Uvarov, N. F.; Bokhonov, B. B., The effect of cationic doping on the ionic conductivity of rubidium nitrate. *Russian Journal of Electrochemistry* **2015,** *51* (6), 508-512.

405. Funahashi, T.; Mineshige, A.; Yoshioka, H.; Kobayashi, K.; Matsushita, Y.; Katsuya, Y.; Tanaka, M.; Sakata, O.; Yazawa, T., Effect of cation doping on ionic conductivity and crystal structure of oxyapatite-type lanthanum silicates. *Solid State Ionics* **2016,** *289*, 106-112.

406. Stafford, R. J.; Rothman, S. J.; Routbort, J. L., Effect of dopant size on the ionic conductivity of cubic stabilised ZrO2. *Solid State Ionics* **1989,** *37* (1), 67-72.

407. Adnan, S. B. R. S.; Mohamed, N. S., Effects of Sn substitution on the properties of Li4SiO4 ceramic electrolyte. *Solid State Ionics* **2014,** *262*, 559-562.

408. Adnan, S. B. R. S.; Mohamed, N. S., Characterization of novel Li4Zr0.06Si0.94O4 and Li3.94Cr0.02Zr0.06Si0.94O4 ceramic electrolytes for lithium cells. *Ceramics International* **2014,** *40* (4), 6373-6379.

409. Kim, H.; Kim, Y.-I., Partial nitridation of Li4SiO4 and ionic conductivity of Li4.1SiO3.9N0.1. *Ceramics International* **2018**.

410. Shanthi, P. M.; Hanumantha, P. J.; Kuruba, R.; Gattu, B.; Datta, M. K.; Kumta, P. N., Effective Bipyridine and Pyrazine-Based Polysulfide Dissolution Resistant Complex Framework Material Systems for High Capacity Rechargeable Lithium–Sulfur Batteries. *Energy Technology 0* (0), 1900141.

411. Tranqui, D.; Shannon, R. D.; Chen, H.-Y.; Iijima, S.; Baur, W. H., Crystal structure of ordered Li4SiO4. *Acta Crystallographica Section B* **1979,** *35* (11), 2479-2487.

412. Xu, W.; Wang, J.; Ding, F.; Chen, X.; Nasybulin, E.; Zhang, Y.; Zhang, J.-G., Lithium metal anodes for rechargeable batteries. *Energy & Environmental Science* **2014,** *7* (2), 513-537.

413. Kresse, G.; Furthmüller, J., Efficiency of ab-initio total energy calculations for metals and semiconductors using a plane-wave basis set. *Computational Materials Science* **1996,** *6* (1), 15-50.

414. Kresse, G.; Joubert, D., From ultrasoft pseudopotentials to the projector augmented-wave method. *Physical Review B* **1999,** *59* (3), 1758-1775.

415. Perdew, J. P.; Yue, W., Accurate and simple density functional for the electronic exchange energy: Generalized gradient approximation. *Physical Review B* **1986,** *33* (12), 8800-8802.

416. Mills, G.; Jónsson, H.; Schenter, G. K., Reversible work transition state theory: application to dissociative adsorption of hydrogen. *Surface Science* **1995,** *324* (2), 305-337.

417. JÓNSSON, H.; MILLS, G.; JACOBSEN, K. W., Nudged elastic band method for finding minimum energy paths of transitions. In *Classical and Quantum Dynamics in Condensed Phase Simulations*, WORLD SCIENTIFIC: 2011; pp 385-404.

418. Tang, T.; Chen, P.; Luo, W.; Luo, D.; Wang, Y., Crystalline and electronic structures of lithium silicates: A density functional theory study. *Journal of Nuclear Materials* **2012,** *420* (1–3), 31-38.

419. Shannon, R., Revised effective ionic radii and systematic studies of interatomic distances in halides and chalcogenides. *Acta Crystallographica Section A* **1976,** *32* (5), 751-767.

420. Park, J.-H.; Kim, C.-S.; Choi, B.-C.; Moon, B. K.; Seo, H.-J., Impedance spectroscopy of KTiOPO4 single crystal in the temperature range –100 to 100 °C. *Applied Physics A* **2004,** *78* (5), 745-748.

421. Prosini, P. P.; Lisi, M.; Zane, D.; Pasquali, M., Determination of the chemical diffusion coefficient of lithium in LiFePO4. *Solid State Ionics* **2002,** *148* (1–2), 45-51.

422. Li, J.; Yao, W.; Martin, S.; Vaknin, D., Lithium ion conductivity in single crystal LiFePO4. *Solid State Ionics* **2008,** *179* (35–36), 2016-2019.

423. Inaguma, Y.; Liquan, C.; Itoh, M.; Nakamura, T.; Uchida, T.; Ikuta, H.; Wakihara, M., High ionic conductivity in lithium lanthanum titanate. *Solid State Communications* **1993,** *86* (10), 689-693.

424. Ricker, H., Solid Electrolytes. General Principles, Characterization, Materials, Applications. Herausgegeben von P. Hagenmuller und W. van Gool. Academic Press, New York 1978. XVII, 549 S., geb. $ 52.00. *Angewandte Chemie* **1979,** *91* (11), 947-947.

425. Wang, Z.; Dou, Z.; Cui, Y.; Yang, Y.; Wang, Z.; Qian, G., Sulfur encapsulated ZIF-8 as cathode material for lithium–sulfur battery with improved cyclability. *Microporous and Mesoporous Materials* **2014,** *185*, 92-96.

426. Deng, Z.; Zhang, Z.; Lai, Y.; Liu, J.; Li, J.; Liu, Y., Electrochemical Impedance Spectroscopy Study of a Lithium/Sulfur Battery: Modeling and Analysis of Capacity Fading. *Journal of The Electrochemical Society* **2013,** *160* (4), A553-A558.

427. Towns, J.; Cockerill, T.; Dahan, M.; Foster, I.; Gaither, K.; Grimshaw, A.; Hazlewood, V.; Lathrop, S.; Lifka, D.; Peterson, G. D.; Roskies, R.; Scott, J. R.; Wilkins-Diehr, N., XSEDE: Accelerating Scientific Discovery. *Computing in Science & Engineering* **2014,** *16* (5), 62-74.

428. Rosso, M.; Brissot, C.; Teyssot, A.; Dollé, M.; Sannier, L.; Tarascon, J. M.; Bouchet, R.; Lascaud, S., Dendrite Short-Circuit and Fuse Effect on Li/Polymer/Li Cells. *Electrochim. Acta* **2006,** *51*, 5334.

429. Su, Y.-S.; Fu, Y.; Cochell, T.; Manthiram, A., A strategic approach to recharging lithium-sulphur batteries for long cycle life. *Nature Communications* **2013,** *4* (1), 2985.

430. Zu, C.; Azimi, N.; Zhang, Z.; Manthiram, A., Insight into lithium–metal anodes in lithium–sulfur batteries with a fluorinated ether electrolyte. *Journal of Materials Chemistry A* **2015,** *3* (28), 14864-14870.

431. Fan, C.-Y.; Xiao, P.; Li, H.-H.; Wang, H.-F.; Zhang, L.-L.; Sun, H.-Z.; Wu, X.-L.; Xie, H.-M.; Zhang, J.-P., Nanoscale polysulfides reactors achieved by chemical Au–S interaction: improving the performance of Li–S batteries on the electrode level. *ACS applied materials & interfaces* **2015,** *7* (50), 27959-27967.

432. Kim, H.; Das, S.; Kim, M. G.; Dybtsev, D. N.; Kim, Y.; Kim, K., Synthesis of Phase-Pure Interpenetrated MOF-5 and Its Gas Sorption Properties. *Inorganic Chemistry* **2011,** *50* (8), 3691-3696.

433. Chen, B.; Wang, X.; Zhang, Q.; Xi, X.; Cai, J.; Qi, H.; Shi, S.; Wang, J.; Yuan, D.; Fang, M., Synthesis and characterization of the interpenetrated MOF-5. *Journal of Materials Chemistry* **2010,** *20* (18), 3758-3767.

434. Mueller, U.; Schubert, M.; Teich, F.; Puetter, H.; Schierle-Arndt, K.; Pastre, J., Metal-organic frameworks-prospective industrial applications. *Journal of Materials Chemistry* **2006,** *16* (7), 626-636.

435. Klinowski, J.; Almeida Paz, F. A.; Silva, P.; Rocha, J., Microwave-Assisted Synthesis of Metal-Organic Frameworks. *Dalton Transactions* **2011,** *40* (2), 321-330.

436. Li, G. C.; Hu, J. J.; Li, G. R.; Ye, S. H.; Gao, X. P., Sulfur/activated-conductive carbon black composites as cathode materials for lithium/sulfur battery. *Journal of Power Sources* **2013,** *240*, 598-605.

437. Li, K.; Wang, B.; Su, D.; Park, J.; Ahn, H.; Wang, G., Enhance electrochemical performance of lithium sulfur battery through a solution-based processing technique. *Journal of Power Sources* **2012,** *202*, 389-393.

438. Xiong, S.; Xie, K.; Diao, Y.; Hong, X., Oxidation process of polysulfides in charge process for lithium–sulfur batteries. *Ionics* **2012,** *18* (9), 867-872.

439. Zhang, S., Understanding of Sulfurized Polyacrylonitrile for Superior Performance Lithium/Sulfur Battery. *Energies* **2014,** *7* (7), 4588.

440. Akridge, J. R.; Mikhaylik, Y. V.; White, N., Li/S fundamental chemistry and application to high-performance rechargeable batteries. *Solid State Ionics* **2004,** *175* (1–4), 243-245.

441. Hantsche, H., High resolution XPS of organic polymers, the scienta ESCA300 database. By G. Beamson and D. Briggs, Wiley, Chichester 1992, 295 pp., hardcover, £ 65.00, ISBN 0-471-93592-1. *Advanced Materials* **1993,** *5* (10), 778-778.

442. Vohs, J. M.; Barteau, M. A., Photoelectron spectroscopy of diethylzinc on the polar surfaces of zinc oxide. *Journal of Electron Spectroscopy and Related Phenomena* **1989,** *49* (1), 87-96.

443. Bournel, F.; Laffon, C.; Parent, P.; Tourillon, G., Adsorption of some substituted ethylene molecules on Pt(111) at 95 K Part 1: NEXAFS, XPS and UPS studies. *Surface Science* **1996,** *350* (1–3), 60-78.

444. Peng, X. D.; Barteau, M. A., Spectroscopic characterization of surface species derived from HCOOH, CH3COOH, CH3OH, C2H5OH, HCOOCH3, and C2H2 on MgO thin film surfaces. *Surface Science* **1989,** *224* (1), 327-347.

445. Kishi, K.; Ehara, Y., Interaction of acetic acid with ethylenediamine on a Ni(111) surface studied by XPS. *Surface Science* **1986,** *176* (3), 567-577.

446. Lalitha, S.; Manoharan, P. T., X-ray photoelectron spectroscopic studies on some dithiolate complexes. *Journal of Electron Spectroscopy and Related Phenomena* **1989,** *49* (1), 61-75.

447. Chaganti, V. R.; Physics, T. U. o. T. a. E. P., *Study of Structural and Spectroscopic Properties of Small Zinc Sulfide Clusters by DFT*. University of Texas at El Paso: 2008.

448. Rehman, S.; Gu, X.; Khan, K.; Mahmood, N.; Yang, W.; Huang, X.; Guo, S.; Hou, Y., 3D Vertically Aligned and Interconnected Porous Carbon Nanosheets as Sulfur Immobilizers for High Performance Lithium-Sulfur Batteries. *Advanced Energy Materials* **2016,** *6* (12), 1502518.

449. Jiang, H.; Liu, X. C.; Wu, Y.; Shu, Y.; Gong, X.; Ke, F. S.; Deng, H., Metal–Organic Frameworks for High Charge–Discharge Rates in Lithium–Sulfur Batteries. *Angewandte Chemie* **2018,** *130* (15), 3980-3985.

450. Demir-Cakan, R.; Morcrette, M.; Nouar, F.; Davoisne, C.; Devic, T.; Gonbeau, D.; Dominko, R.; Serre, C.; Férey, G.; Tarascon, J.-M., Cathode Composites for Li–S Batteries via the Use of Oxygenated Porous Architectures. *Journal of the American Chemical Society* **2011,** *133* (40), 16154-16160.

451. Berzina-Cimdina, L.; Borodajenko, N., Research of calcium phosphates using Fourier transform infrared spectroscopy. In *Infrared Spectroscopy-Materials Science, Engineering and Technology*, InTech: 2012.

452. Tallman, D. E.; Levine, K. L.; Siripirom, C.; Gelling, V. G.; Bierwagen, G. P.; Croll, S. G., Nanocomposite of polypyrrole and alumina nanoparticles as a coating filler for the corrosion protection of aluminium alloy 2024-T3. *Applied Surface Science* **2008,** *254* (17), 5452-5459.

453. Duan, W.; Vemuri, R. S.; Milshtein, J. D.; Laramie, S.; Dmello, R. D.; Huang, J.; Zhang, L.; Hu, D.; Vijayakumar, M.; Wang, W., A symmetric organic-based nonaqueous redox flow battery and its state of charge diagnostics by FTIR. *Journal of Materials Chemistry A* **2016,** *4* (15), 5448-5456.

454. Ahmed, G.; Gilbert, M.; Mainprize, S.; Rogerson, M., FTIR analysis of silane grafted high density polyethylene. *Plastics, Rubber and Composites* **2009,** *38* (1), 13-20.

455. Trchova, M.; Stejskal, J.; Prokeš, J., Infrared spectroscopic study of solid-state protonation and oxidation of polyaniline. *Synthetic Metals* **1999,** *101* (1-3), 840-841.

456. Paradkar, M.; Irudayaraj, J., A rapid FTIR spectroscopic method for estimation of caffeine in soft drinks and total methylxanthines in tea and coffee. *Journal of food science* **2002,** *67* (7), 2507-2511.

457. Patel, G.; Sureshkumar, M.; Singh, N.; Bhattacharya, S., Spectroscopic correlation of mechanical properties of PVC/PMMA polymer blend. *Journal of International Academy of Physical Sciences* **2010,** *14* (1).

458. Katara, S.; Kabra, S.; Sharma, A.; Hada, R.; Rani, A., Surface modification of fly ash by thermal activation: A DR/FTIR study. *International Research Journal of Pure and Applied Chemistry* **2013,** *3* (4), 299.

459. Mianehrow, H.; Moghadam, M. H. M.; Sharif, F.; Mazinani, S., Graphene-oxide stabilization in electrolyte solutions using hydroxyethyl cellulose for drug delivery application. *International Journal of Pharmaceutics* **2015,** *484* (1), 276-282.

460. Glisenti, A., Interaction of formic acid with Fe2O3 powders under different atmospheres: an XPS and FTIR study. *Journal of the Chemical Society, Faraday Transactions* **1998,** *94* (24), 3671-3676.

462. Lü, C.; Cui, Z.; Guan, C.; Guan, J.; Yang, B.; Shen, J., Research on preparation, structure and properties of TiO2/polythiourethane hybrid optical films with high refractive index. *Macromolecular Materials and Engineering* **2003,** *288* (9), 717-723.

463. Radziszewski, J. G.; Hess Jr, B. A.; Zahradnik, R., Infrared spectrum of o-benzyne: experiment and theory. *Journal of the American Chemical Society* **1992,** *114* (1), 52-57.

464. Sharma, S.; Nirkhe, C.; Pethkar, S.; Athawale, A. A., Chloroform vapour sensor based on copper/polyaniline nanocomposite. *Sensors and Actuators B: Chemical* **2002,** *85* (1), 131-136.

465. Klokkenburg, M.; Hilhorst, J.; Erne, B., Surface analysis of magnetite nanoparticles in cyclohexane solutions of oleic acid and oleylamine. *Vibrational spectroscopy* **2007,** *43* (1), 243-248.

466. Medda, S. K.; Kundu, D.; De, G., Inorganic–organic hybrid coatings on polycarbonate.: Spectroscopic studies on the simultaneous polymerizations of methacrylate and silica networks. *Journal of Non-Crystalline Solids* **2003,** *318* (1-2), 149-156.

467. Bloembergen, S.; Holden, D. A.; Hamer, G. K.; Bluhm, T. L.; Marchessault, R. H., Studies of composition and crystallinity of bacterial poly (β-hydroxybutyrate-co-β-hydroxyvalerate). *Macromolecules* **1986,** *19* (11), 2865-2871.

468. Wang, Y. G.; Li, H. Q.; Xia, Y. Y., Ordered whiskerlike polyaniline grown on the surface of mesoporous carbon and its electrochemical capacitance performance. *Advanced Materials* **2006,** *18* (19), 2619-2623.

469. Chandra, V.; Kim, K. S., Highly selective adsorption of Hg 2+ by a polypyrrole–reduced graphene oxide composite. *Chemical Communications* **2011,** *47* (13), 3942-3944.

470. Mozgawa, W., The relation between structure and vibrational spectra of natural zeolites. *Journal of Molecular Structure* **2001,** *596* (1), 129-137.

471. Shao, J.; Zheng, J.; Liu, J.; Carr, C., Fourier transform Raman and Fourier transform infrared spectroscopy studies of silk fibroin. *Journal of Applied Polymer Science* **2005,** *96* (6), 1999-2004.

472. Tang, C. Y.; Kwon, Y.-N.; Leckie, J. O., Effect of membrane chemistry and coating layer on physiochemical properties of thin film composite polyamide RO and NF

membranes: I. FTIR and XPS characterization of polyamide and coating layer chemistry. *Desalination* **2009,** *242* (1-3), 149-167.

473. Grande, C. J.; Torres, F. G.; Gomez, C. M.; Carmen Bañó, M., Nanocomposites of bacterial cellulose/hydroxyapatite for biomedical applications. *Acta Biomaterialia* **2009,** *5* (5), 1605-1615.

474. Shim, W.-G.; Hwang, K.-J.; Chung, J.-T.; Baek, Y.-S.; Yoo, S.-J.; Kim, S.-C.; Moon, H.; Lee, J.-W., Adsorption and thermodesorption characteristics of benzene in nanoporous metal organic framework MOF-5. *Advanced Powder Technology* **2012,** *23* (5), 615-619.

475. Othman, S. Z.; Misran, H.; Affendy, W. A.; Mahadi, N. F., Effect of Synthesis Methods Using Renewable PODFA on Structural Characteristics of Metal-Organic Framework (MOF-5). *IOP Conference Series: Earth and Environmental Science* **2016,** *32* (1), 012060.

476. Lee, C. H.; Rhee, S. W.; Choi, H. W., Preparation of TiO2 nanotube/nanoparticle composite particles and their applications in dye-sensitized solar cells. *Nanoscale Research Letters* **2012,** *7* (1), 48.

477. Hardwick, L. J.; Saint, J. A.; Lucas, I. T.; Doeff, M. M.; Kostecki, R., FTIR and Raman Study of the Li x Ti y Mn1 − y O2 (y = 0 , 0.11) Cathodes in Methylpropyl Pyrrolidinium Bis(fluoro-sulfonyl)imide, LiTFSI Electrolyte. *Journal of The Electrochemical Society* **2009,** *156* (2), A120-A127.

478. Ahmad, S.; Deepa, M.; Agnihotry, S. A., Effect of salts on the fumed silica-based composite polymer electrolytes. *Solar Energy Materials and Solar Cells* **2008,** *92* (2), 184-189.

479. Ali, A. M. M.; Yahya, M. Z. A.; Bahron, H.; Subban, R. H. Y.; Harun, M. K.; Atan, I., Impedance studies on plasticized PMMA-LiX [X: CF3SO3−, N(CF3SO2)2−] polymer electrolytes. *Materials Letters* **2007,** *61* (10), 2026-2029.

480. Silkmoth Chorion. In *The Functional Fold*, Pan Stanford Publishing: 2012; pp 55-72.

481. de Campos Vidal, B.; Mello, M. L. S., Collagen type I amide I band infrared spectroscopy. *Micron* **2011,** *42* (3), 283-289.

482. Zhang, J.; Yue, L.; Kong, Q.; Liu, Z.; Zhou, X.; Zhang, C.; Xu, Q.; Zhang, B.; Ding, G.; Qin, B.; Duan, Y.; Wang, Q.; Yao, J.; Cui, G.; Chen, L., Sustainable, heat-resistant and flame-retardant cellulose-based composite separator for high-performance lithium ion battery. *Scientific Reports* **2014,** *4*, 3935.

483. Ramesh, S.; Ling, O. P., Effect of ethylene carbonate on the ionic conduction in poly(vinylidenefluoride-hexafluoropropylene) based solid polymer electrolytes. *Polymer Chemistry* **2010,** *1* (5), 702-707.